

Dissertation zur Erlangung des Doktorgrades
der Fakultät für Chemie und Pharmazie
der Ludwig-Maximilians-Universität München

Synthesis and characterization of rare-earth oxide transition-metal arsenides and selenides

Simon Friedrich Peschke

aus

Rosenheim, Deutschland

2017

Erklärung

Diese Dissertation wurde im Sinne von § 7 der Promotionsordnung vom 28. November 2011 von Herrn Prof. Dr. Dirk Johrendt betreut.

Eidesstattliche Versicherung

Diese Dissertation wurde eigenständig und ohne unerlaubte Hilfe erarbeitet.

München,

Simon Peschke

Dissertation eingereicht am 16.03.2017

1. Gutachter Prof. Dr. Dirk Johrendt

2. Gutachter Prof. Dr. Oliver Oeckler

Mündliche Prüfung am 06.04.2017

Danksagung

Ganz herzlich möchte ich mich bei meinem Chef, Prof. Dr. Dirk Johrendt, für die Freiheit zur Verfolgung eigener Ideen und die hervorragende Betreuung während dieser Doktorarbeit bedanken. Ebenso möchte ich mich für die Möglichkeiten, eigene Ergebnisse in wissenschaftlichen Zeitschriften zu veröffentlichen, sowie nationale und internationale Tagungen zu besuchen, bedanken.

Prof. Dr. Oliver Oeckler danke ich herzlich für die Übernahme des Zweitgutachtens und damit für das Interesse an meiner Arbeit, sowie für die Zeit und Mühe, die er in den Kurs "Beugungsmethoden in der Festkörperchemie" gesteckt hat.

Herrn Prof. Konstantin Karaghiosoff, Herrn Prof. Thomas Klapötke, Herrn PD Dr. Rudi Hackl und Herrn Prof. Hans-Christian Böttcher danke ich für ihre Bereitschaft, als Teil der Prüfungskommission am Tag der mündlichen Prüfung zur Verfügung zu stehen.

Danke auch an all meine aktuellen und ehemaligen Kollegen: Andreas Binek, Lars Bulthaupt, Beatrix Fischer, Rainer Frankovsky, Gina Friederichs, Arthur Haffner, Franziska Hummel, Christopher Kipp, Lola Lilensten, Catrin Löhnert, Tina Markovic, Fabian Nitsche, Ursula Pachmayr, Roman Pobel, Tobias Rackl, Bettina Rendenbach, Constantin Frhr. Schirndinger von Schirnding, Rudolf Schönmann, Anne Schulz, Evgeniya Shlaen, Juliane Stahl, Christine Stürzer, Tobias Stürzer und Erwin Wiesenmayer. Vielen Dank für eure Unterstützung in Form von zahlreichen Messungen, interessanten Diskussionen und der guten Stimmung, die ihr stets verbreitet habt. Ein ganz besonderer Dank gilt Catrin Löhnert, die die ganze Truppe stets im Griff hat.

Ich möchte der wechselnden Besetzung des Labors D2.061 für den gemeinsamen Stressabbau in jeder erdenklichen Form danken. Im Besonderen Gina für die herzliche Aufnahme und Unterstützung bereits während meiner Masterarbeit. Ein weiteres Dankeschön an Rainer für die Einarbeitung in das Metathese-Thema sowie für unterhaltsame Fahrten ans SQUID. Herzlichen Dank an Fabian für die Hilfe bei inkommensurablen Problemen. Roman danke ich für die gemeinsame Betreuung von "komplizierten" Geräten und vor allem für die abwechslungsreiche Zeit mit vielen Diskussionen rund um unsere gemeinsame Leidenschaft, dem

lifti-lifti. Danke Juliane, dass Du bis spätabends die Stellung hältst. Danke Tobi, dass Dir immer ein "guter" Spruch einfällt. Danke Rudi, dass Du immer mitlachst. Danke Ursi, dass Du trotz unzähliger Einkristallmessungen immer an meiner Seite geblieben bist.

Ein ganz besonderer Dank gilt meinen Praktikanten Leo Diehl, Lisa Gamperl, Bernhard Illes, Christopher Kipp, Sebastian Vogel und Valentin Weippert. Ohne euch wäre diese Arbeit in der Form nicht möglich gewesen.

Vielen Dank auch an meine Kooperationspartner Stefan Holenstein, Dr. Oliver Janka, Dr. Hubertus Luetkens, Dr. Andrea Malagoli, Dr. Martin Mühlbauer, Prof. Dr. Rainer Pöttgen und Dr. Anatoliy Senyshyn. Dr. Andrea Hoffmann und Marina Boyko danke ich recht herzlich für die gute Zusammenarbeit am SQUID in Garching.

Ein riesen Dankeschön an Thomas Miller und Wolfgang Wunschheim für ihre stetige Unterstützung bei allerlei Problem(ch)en.

Ich bedanke mich auch bei allen weiteren Kollegen der Arbeitskreise Schnick, Hoch und Lotsch für die gemeinsame Zeit.

Natürlich danke ich Frank Tambornino, Philipp Schmid und Daniel Terwilliger für den wissenschaftlichen Austausch während den allwöchentlichen Mittagessen.

Zum Schluss möchte ich ganz besonders meiner Familie für die immerwährende Unterstützung und für die Freiheit das tun zu können, was mich interessiert, danken. Meinen Eltern Friedrich und Maria Peschke, meiner Oma Maria Entfellner und meinen Brüdern Christoph und Thomas danke ich für den Zusammenhalt und die schöne gemeinsame Zeit.

"Immer erscheinen die entscheidenden Ideen
nachträglich als einfache und selbstverständliche."

Stefan Zweig

Contents

1	Introduction	1
1.1	References	5
2	Methods	7
2.1	Synthesis methods	7
2.1.1	Starting materials	7
2.1.2	Equipment and conditions	8
2.1.3	Precursor synthesis	8
2.1.4	Solid state metathesis reactions	9
2.1.5	Flux-mediated reactions	9
2.2	Powder diffraction	10
2.2.1	X-ray powder diffraction	10
2.2.2	Neutron powder diffraction	10
2.2.3	Rietveld refinements	10
2.3	Magnetic measurements	11
2.4	Energy-dispersive X-ray analysis	11
2.5	Muon spin rotation	11
2.6	UV-VIS-spectroscopy	11
2.7	Single-crystal X-ray diffraction	11
2.8	References	12
3	Solid State Metathesis of $REFeAsO_{1-x}F_x$ Compounds	13
3.1	$LaFeAsO_{1-x}F_x$	14
3.1.1	Introduction	14
3.1.2	Results and Discussion	16
3.2	$SmFeAsO_{1-x}F_x$	22
3.2.1	Introduction	22
3.2.2	Results and Discussion	23

3.3	<i>REFeAsO</i> _{1-x} <i>F</i> _x (<i>RE</i> = Gd–Dy)	30
3.3.1	Introduction	30
3.3.2	Results and Discussion	30
3.4	Conclusion	35
3.5	References	36
4	Flux Mediated Synthesis of New Quaternary <i>RE-T-Se-O</i> Compounds	39
4.1	Flux Synthesis, Modulated Crystal Structures, and Physical Properties of <i>RE</i> ₂ <i>O</i> ₂ <i>MnSe</i> ₂ (<i>RE</i> = La, Ce)	40
4.1.1	Abstract	40
4.1.2	Introduction	40
4.1.3	Experimental Details	41
4.1.4	Results and Discussion	42
4.1.4.1	<i>La</i> ₂ <i>O</i> ₂ <i>MnSe</i> ₂	42
4.1.4.2	<i>Ce</i> ₂ <i>O</i> ₂ <i>MnSe</i> ₂	53
4.1.5	Conclusion	60
4.2	The Modulated Structures of <i>La</i> _{2-x} <i>Pr</i> _x <i>O</i> ₂ <i>MnSe</i> ₂ and <i>La</i> _{2-x} <i>Nd</i> _x <i>O</i> ₂ <i>MnSe</i> ₂	61
4.2.1	Abstract	61
4.2.2	Introduction	61
4.2.3	Experimental Details	63
4.2.4	Results and Discussion	64
4.2.5	Conclusion	71
4.3	Flux Synthesis, Crystal Structures, and Magnetism of the Series <i>La</i> _{2n+2} <i>MnSe</i> _{n+2} <i>O</i> _{2n+2} (<i>n</i> = 0–2)	72
4.3.1	Abstract	72
4.3.2	Introduction	72
4.3.3	Experimental Details	74
4.3.4	Results	75
4.3.5	Conclusion	82
4.4	Flux Synthesis, Crystal Structures, and Magnetic Ordering of the Rare-Earth Chromium(II) Oxyselenides <i>RE</i> ₂ <i>CrSe</i> ₂ <i>O</i> ₂ (<i>RE</i> = La–Nd)	83
4.4.1	Abstract	83
4.4.2	Introduction	84
4.4.3	Experimental Details	85
4.4.4	Results and Discussion	86
4.4.5	Conclusion	98

4.5 Flux Synthesis, Crystal Structures, and Physical Properties of New Lanthanum Vanadium Oxyselenides	99
4.5.1 Abstract	99
4.5.2 Introduction	100
4.5.3 Experimental Details	100
4.5.4 Results and Discussion	102
4.5.4.1 LaVSe ₂ O	102
4.5.4.2 La ₅ V ₃ Se ₆ O ₇	104
4.5.4.3 La ₅ V ₃ Se ₇ O ₅	108
4.5.4.4 La ₇ VSe ₅ O ₇	112
4.5.4.5 La ₁₃ V ₇ Se ₁₆ O ₁₅	116
4.5.5 Conclusion	124
4.6 Synthesis and Crystal Structures of New Lanthanum Titanium Oxyselenides . . .	126
4.6.1 Introduction	126
4.6.2 Experimental Details	126
4.6.3 Results and Discussion	127
4.6.3.1 La ₁₂ Ti ₁₃ Se ₉ O ₃₂	127
4.6.3.2 La ₁₅ Ti ₆ Se ₁₀ O _{26-x}	132
4.6.4 Conclusion	136
4.7 References	138
5 Summary	141
Appendix A	149
Scientific contributions	179
Curriculum vitae	183

Chapter 1

Introduction

Superconductivity remains a fascinating phenomenon even though it is not fully understood until today, more than 100 years after its first discovery.^[1] It is widely accepted that the formation of electron pairs is one requirement for the emergence of superconductivity. In contrast, magnetism was considered to be detrimental to superconductivity, which was already postulated by *Matthias* in the 1950s.^[2,3] His six rules for a successful search for superconductors include: (1) A high symmetry is good, cubic is best. (2) A high density of electronic states is good. (3) Stay away from oxygen. (4) Stay away from magnetism. (5) Stay away from insulators. (6) Stay away from theorists.^[4] Most of these rules have been disconfirmed by the discovery of new superconducting systems. Probably most impressive by the report of unconventional superconductivity up to 140 K in cuprates, which are *Mott* insulators with an antiferromagnetic ground state at low temperatures. This is only one example that the theory of superconductivity is not fully understood until today and the emergence of superconductivity cannot be predicted by general rules. Another contribution to this paradigm change has been made by the discovery of superconductivity in iron-based superconductors in the early 21st century, which proved that magnetism is essential for high-temperature superconductors. Although the crystal structures of *REFeAsO* (*RE* = rare-earth metal) compounds have been already reported in 2000^[5], superconductivity in LaFeAsO up to 26 K was first observed by electron doping with fluorine in 2008.^[6] Undoped LaFeAsO however, is a poor metal and exhibits a stripe-type antiferromagnetic order of the iron moments, but does not exhibit superconductivity.^[7] In the following years, several types of iron-based superconductors have been characterized, which all consist of layers of edge-sharing $\text{FeX}_{4/4}$ tetrahedra (X = pnictogen (Pn) or chalcogen (Q) atom). These sheets are separated by more or less

complex interlayers leading to compounds, which are abbreviated by their stoichiometry in the following (Fig. 1.1). The simplest representative is the so-called 11 type ($\text{Fe}Q$; $Q = \text{S-Te}$) without any atoms between the sheets. The 111 type ($A\text{Fe}Pn$; $A = \text{alkaline metal}$) consists of double layers of alkaline metals between the sheets, while the 122 type $[(A/AE)\text{Fe}_2Pn_2, (A/AE)\text{Fe}_2Q_2$; $AE = \text{alkaline-earth metal}$] includes single layers of A^+ or AE^{2+} cations as interlayer. The structure type which is primary subject of the present thesis is the 1111 type ($RE\text{Fe}Pn\text{O}$). These compounds adopt the ZrCuSiAs -type structure with slabs of edge-sharing $\text{Fe}Pn_{4/4}$ -tetrahedra in *anti*- PbO -type structure, stacked alternating with slabs of rare-earth oxide tetrahedra with PbO -type structure. Beside these, there exist others - including the 21311, 32522, 1038 and 1048 types - with even more complex structures, which are not shown here.^[8,9]

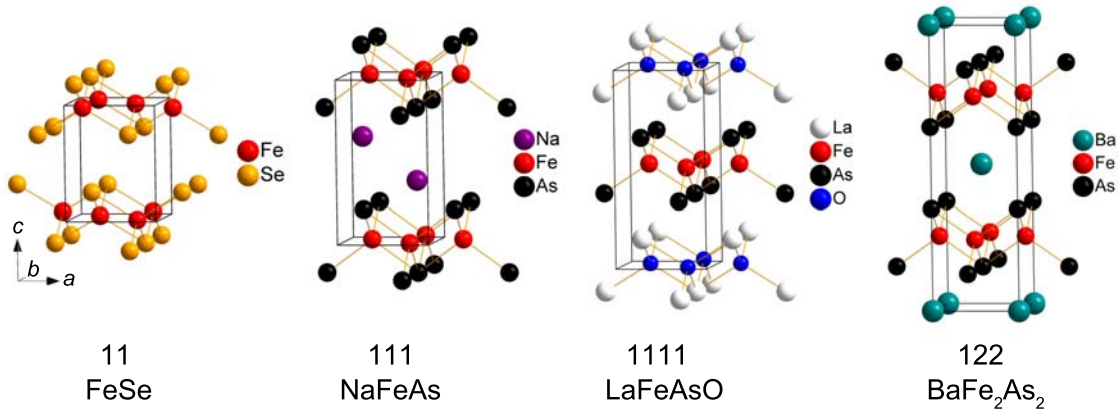


Figure 1.1 Crystal structures of some iron-based superconductors.

Recently, *Frankovsky* et al. reported a new method to synthesize high purity polycrystalline LaFeAsO and superconducting $\text{LaFeAsO}_{1-x}\text{F}_x$ ($0 \leq x \leq 0.15$) using a solid state metathesis reaction starting from LaOCl and NaFeAs as precursors. Partly replacement of iron by manganese in LaFeAsO changes the resistivity from metallic to semiconducting.^[10] In addition, *Frankovsky* et al. discovered short-range magnetic order in $\text{LaFe}_{1-x}\text{Mn}_x\text{AsO}$ and a suppression of magnetism by additional electron doping with fluorine, while superconductivity remains absent.^[11] In contrast, doping cobalt on the iron site in LaFeAsO can even induce superconductivity^[12], while full replacement of iron by other $3d$ transition metals leads to diverse and interesting properties.^[13] Among them, giant magnetoresistance in $RE\text{MnAsO}$ ^[14-17], itinerant ferromagnetism in $RE\text{CoAsO}$ ^[18-21] and low temperature superconductivity in $RE\text{NiAsO}$ ^[22-25].

Additional substitution of arsenic in $RETA_sO$ ($T =$ divalent transition metal) by selenium leads to compounds with the general molecular formula $RE_2TSe_2O_2$. These are relatively unusual materials which simultaneously contain oxide and selenide anions, as opposed to species such as selenates and selenites in which the chalcogen has a positive formal charge. Materials with mixed anions are interesting as they frequently contain transition metals in unusual chemical or electronic environments which can lead to compounds with unexpected and fascinating electronic, magnetic or optical properties. At the beginning of the present work, several compounds were known that retain a ZrCuSiAs-related structure with modulations in the transition-metal-selenide layers. Among them, $La_2CdSe_2O_2$ ^[26] contains layers with a checkerboard-like arrangement of corner-sharing cadmium-selenide tetrahedra, $Ce_2FeSe_2O_2$ ^[27] exhibits chains of edge-sharing iron-selenide tetrahedra, and $La_2ZnSe_2O_2$ ^[28], which has a mixture of both, edge- and corner-sharing zinc-selenide tetrahedra. A view on the ab -plane of these modulated $[TSe_2]^{2-}$ layers is shown in Figure 1.2. Moreover, *Ijjaali* et al. assumed randomly distributed vacancies in $Ce_2MnSe_2O_2$.^[29] Beside these compounds, numerous quaternary selenide oxides involving $4f$ elements and $3d$ transition-metals with various compositions have been identified and characterized in terms of their crystal structure and physical properties.

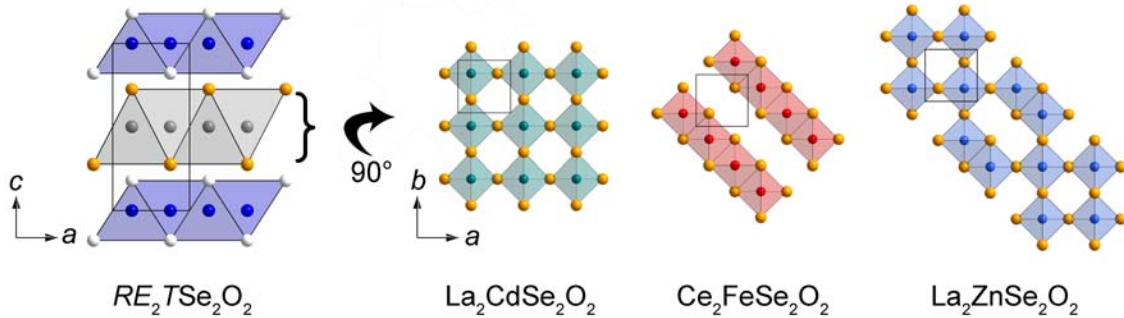


Figure 1.2 ZrCuSiAs-related crystal structure of $RE_2TSe_2O_2$ compounds and modulated $[TSe_2]^{2-}$ layers of $La_2CdSe_2O_2$, $Ce_2FeSe_2O_2$, and $La_2ZnSe_2O_2$. RE in white, O in dark blue, Se in yellow and T in the respective fourth colour.

The first part of the present thesis concentrates on the synthesis of compounds of the 1111 type of iron-based superconductors via the solid state metathesis reaction mentioned above. The limitations of the novel synthetic route were proved in Chapter 3.1 and 3.3, i.e. the solubility limit of fluorine in $LaFeAsO_{1-x}F_x$, as well as the synthesis of late rare-earth 1111 compounds ($RE = Tb, Dy$), which are solely accessible via high pressure synthesis

routes until now. In addition, the influence of structural parameters on superconductivity was examined by substitution of lanthanum in non-superconducting $\text{LaFeAsO}_{0.8}\text{F}_{0.2}$ by smaller rare-earth metals. Moreover, investigations on the critical current density of high- T_c $\text{SmFeAsO}_{0.85}\text{F}_{0.15}$ were made in cooperation with *Dr. A. Malagoli* (CNR-SPIN, Genova, Italy), which is presented in Chapter 3.2.

The second part of the thesis is based on advices of *Mazin*, who proposed a new set of guidelines taking into account new insights from recent high-temperature superconductors, which say: (1) Layered structures are good. (2) The carrier density should not be too high. (3) Transition metals of the fourth period (...) are good. (4) Magnetism is essential. (5) Proper Fermi surface geometry is essential. (6) Materials of interest are likely to be complex chemical compounds.^[4] Especially the third rule, which recommends the use of 3d transition metals, was heeded with regard to the search for new superconducting and related materials with interesting magnetic properties. Therefore, this part of the thesis presents the synthesis, as well as structural and physical characterization, of new transition-metal oxyselenides, i.e. *RE-T-Se-O* compounds with $T = \text{Ti, V, Cr and Mn}$. Discoveries here could also help to understand the pnictide systems.

In Chapter 4.1 the compounds $\text{La}_2\text{O}_2\text{MnSe}_2$ and $\text{Ce}_2\text{O}_2\text{MnSe}_2$ with modulated crystal structures are characterized in terms of magnetism and optical properties. The effect of substitution of lanthanum in $\text{La}_2\text{O}_2\text{MnSe}_2$ by smaller rare-earth metals on the modulated crystal structure is discussed in Chapter 4.2. Another high temperature polymorph of $\text{La}_2\text{O}_2\text{MnSe}_2$ and two new manganese-based compounds, $\text{La}_4\text{MnSe}_3\text{O}_4$ and $\text{La}_6\text{MnSe}_4\text{O}_6$, are presented in Chapter 4.3. The new materials, which can be summarized in the series $\text{La}_{2n+2}\text{MnSe}_{n+2}\text{O}_{2n+2}$ ($n = 0-2$), are analyzed with regard to their crystal structures and physical properties. Chapter 4.4 introduces four new quaternary chromium compounds $\text{RE}_2\text{CrSe}_2\text{O}_2$ ($\text{RE} = \text{La-Nd}$). Beside the structural characterization, magnetic properties are investigated for $\text{RE} = \text{La-Pr}$. Moreover, $\text{La}_2\text{CrSe}_2\text{O}_2$ is thoroughly analyzed in terms of magnetic ordering by neutron diffraction and μSR experiments. The first lanthanum vanadium oxyselenides are presented in Chapter 4.5, namely LaVSe_2O , $\text{La}_5\text{V}_3\text{Se}_6\text{O}_7$, $\text{La}_5\text{V}_3\text{Se}_7\text{O}_5$, $\text{La}_7\text{VSe}_5\text{O}_7$ and $\text{La}_{13}\text{V}_7\text{Se}_{16}\text{O}_{15}$. Three new structure types are discovered beside two compounds that crystallize in known structure types. Magnetic properties are discussed with the exception of those of LaVSe_2O . Two new La-Ti-Se-O compounds, $\text{La}_{12}\text{Ti}_{13}\text{Se}_9\text{O}_{32}$ and $\text{La}_{15}\text{Ti}_6\text{Se}_{10}\text{O}_{26-x}$ are introduced in

Chapter 4.6. Both crystal structures consist of structural building blocks that have not been reported in this quaternary system before.

1.1 References

- [1] H. K. Onnes, *Commun. Phys. Lab. Univ. Leiden* **1911**, *12*, 120.
- [2] B. T. Matthias, *Phys. Rev.* **1955**, *97*, 74.
- [3] B. T. Matthias, *Progress in Low Temperature Physics* **1957**, *2*, 138.
- [4] I. I. Mazin, *Nature* **2010**, *464*, 183.
- [5] P. Quebe, L. J. Terbüchte, W. Jeitschko, *J. Alloy. Compd.* **2000**, *302*, 70.
- [6] Y. Kamihara, T. Watanabe, M. Hirano, H. Hosono, *J. Am. Chem. Soc.* **2008**, *130*, 3296.
- [7] T. Nomura, S. W. Kim, Y. Kamihara, M. Hirano, P. V. Sushko, K. Kato, M. Takata, A. L. Shluger, H. Hosono, *Supercond. Sci. Technol.* **2008**, *21*, 125028.
- [8] F. Hummel, Y. Su, A. Senyshyn, D. Johrendt, *Phys. Rev. B* **2013**, *144517*, 88.
- [9] C. Löhnert, T. Sürzer, M. Tegel, R. Frankovsky, G. Friederichs, D. Johrendt, *Angew. Chem. Int. Ed.* **2011**, *9195*, 50.
- [10] D. Bérardan, L. Pinsard-Gaudart, N. Dragoë, *J. Alloy. Compd.* **2009**, *481*, 470.
- [11] R. Frankovsky, H. Luetkens, F. Tambornino, A. Marchuk, G. Pascua, A. Amato, H.-H. Klauss, D. Johrendt, *Phys. Rev. B* **2013**, *87*, 174515.
- [12] A. S. Sefat, A. Huq, M. A. McGuire, R. Jin, B. C. Sales, D. Mandrus, L. M. D. Cranswick, P. W. Stephens, K. H. Stone, *Phys. Rev. B* **2008**, *78*, 104505.
- [13] M. A. McGuire, *Phys. Rev. B* **2016**, *93*, 054404.
- [14] A. Marcinkova, T. C. Hansen, C. Curfs, S. Margadonna, J.-W. G. Bos, *Phys. Rev. B* **2010**, *82*, 174438.
- [15] N. Emery, E. J. Wildman, J. M. S. Skakle, G. Girit, R. I. Smith, A. C. McLaughlin, *Chem. Commun.* **2010**, *46*, 6777.
- [16] Y. Tsukamoto, Y. Okamoto, K. Matsuhira, M.-H. Whanbo, Z. Hiroi, *J. Phys. Soc. Jpn.* **2011**, *80*, 094708.

- [17] E. J. Wildman, J. M. S. Skakle, N. Emery, A. C. Mclaughlin, *J. Am. Chem. Soc.* **2012**, *134*, 8766.
- [18] H. Yanagi, R. Kawamura, T. Kamiya, Y. Kamihara, M. Hirano, T. Nakamura, H. Osawa, H. Hosono, *Phys. Rev. B* **2008**, *77*, 224431.
- [19] H. Ohta, K. Yoshimura, *Phys. Rev. B* **2009**, *80*, 184409.
- [20] M. A. McGuire, D. J. Gout, V. O. Garlea, A. S. Sefat, B. C. Sales, D. Mandrus, *Phys. Rev. B* **2010**, *81*, 104405.
- [21] A. Marcinkova, D. A. M. Grist, I. Margiolaki, T. C. Hansen, S. Margadonna, J.-W. G. Bos, *Phys. Rev. B* **2010**, *81*, 064511.
- [22] T. Watanabe, H. Yanagi, Y. Kamihara, T. Kamiya, M. Hirano, H. Hosono, *J. Solid State Chem.* **2008**, *181*, 2117.
- [23] Z. Li, G. Chen, J. Dong, G. Li, W. Hu, D. Wu, S. Su, P. Zheng, T. Xiang, N. Wang, J. Luo, *Phys. Rev. B* **2010**, *78*, 060504.
- [24] S. Matsuishi, A. Nakamura, Y. Muraba, H. Hosono, *Supercond. Sci. Technol.* **2012**, *25*, 084017.
- [25] Q. Luo, H. Han, H. Tan, X. Lin, Y. Li, S. Jiang, C. Feng, J. Dai, G. Cao, Z. Xu, S. Li, *J. Phys.: Condens. Matter* **2011**, *23*, 175701.
- [26] H. Hiramatsu, K. Ueda, T. Kamiya, H. Ohta, M. Hirano, H. Hosono, *J. Mater. Chem.* **2004**, *14*, 2946.
- [27] E. E. McCabe, D. G. Free, J. S. O. Evans, *Chem. Commun.* **2011**, *47*, 1261.
- [28] A. J. Tuxworth, E. E. McCabe, D. G. Free, S. J. Clark, J. S. O. Evans, *Inorg. Chem.* **2013**, *52*, 2078.
- [29] I. Ijjaali, K. Mitchell, C. L. Haynes, A. D. McFarland, R. Van Duyne, J. A. Ibers, *J. Solid State Chem.* **2003**, *176*, 170.

Chapter 2

Methods

2.1 Synthesis methods

2.1.1 Starting materials

The starting materials used in this work, including their purity, appearance and source of supply, are depicted in Table 2.1

Table 2.1 Starting materials used in this work.

material	purity (%)	appearance	supplier
As	99.999	pieces	ALFA AESAR
Ce	99.9	pieces	CHEMPUR
CeO ₂	99.99	pieces	ALFA AESAR
Cr	99.8	powder	ALFA AESAR
DyF ₃	99.9	powder	ALFA AESAR
Dy ₂ O ₃	99.99	powder	ALFA AESAR
Fe	99.90	powder	CHEMPUR
GdF ₃	99.99	powder	ABCR
Gd ₂ O ₃	99.9	powder	ALFA AESAR
KI	≥ 99.0	powder	SIGMA-ALDRICH
La	99.9	pieces	SMART ELEMENTS
LaF ₃	99.99	powder	ABCR
La ₂ O ₃	99.999	powder	CHEMPUR
Mn	99.99	pieces	ALFA AESAR
Na	99.8	block	ALFA AESAR
NaI	≥ 99.0	powder	SIGMA-ALDRICH
Nd	99.99	pieces	ALFA AESAR
NdF ₃	99.99	powder	ALFA AESAR

Continued on next page

Nd ₂ O ₃	99	powder	ALFA AESAR
NH ₄ Cl	99.9	powder	FLUKA
Pr	99.9	pieces	ALFA AESAR
PrF ₃	99.99	powder	SIGMA-ALDRICH
Pr ₂ O ₃	99.9	powder	SIGMA-ALDRICH
Se	99.999	pieces	CHEMPUR
SmF ₃	99.99	powder	ALFA AESAR
Sm ₂ O ₃	99.9	powder	ALFA AESAR
TbF ₃	99.99	powder	ABCR
Tb ₂ O ₃ /TbO ₂	99.9	powder	ABCR
Ti	99.5	powder	ALFA AESAR
TiO ₂	99.995	powder	ALFA AESAR
V	99.7	powder	ABCR

2.1.2 Equipment and conditions

If not stated otherwise all materials were weighed under argon atmosphere (99.999 %, AIR LIQUIDE) in a glove box (MBRAUN, MB150-GL with H₂O and O₂ < 1 ppm and UNILAB PLUS with H₂O and O₂ < 0.1 ppm). Alumina crucibles (FRIATEC), niobium ampoules (HOLDENRIEDER) and glassy carbon crucibles (HTW-HOCHTEMPERATUR-WERKSTOFFE GMBH) were used as reaction containers. The niobium tubes were welded under argon atmosphere using an electric arc melting apparatus. The containers were then transferred into pre-dried silica ampoules (VOGELBERGER, HSQ 300) and sealed under argon atmosphere. The reactions were performed in tubular resistance furnaces with Pt/PtRh or NiCr/Ni thermocouples and PID temperature controllers (EUROTHERM, model 2408).

2.1.3 Precursor synthesis

For the syntheses described in Chapter 3, NaFeAs and REOCl (*RE* = La, Pr, Nd, Sm, Gd, Tb, Dy) were used as precursors.

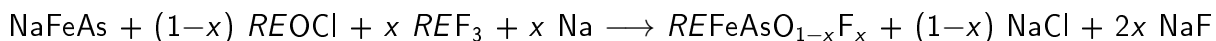
FeAs was obtained by heating stoichiometric mixtures of Fe and As up to 973 K, sealed in a silica ampoule, with a heating rate of 50 K/h, holding this temperature for 48 h and then turning off the furnace. The as-synthesized FeAs was heated with stoichiometric amounts of sodium to obtain NaFeAs. The mixture was heated to 1023 K in a niobium crucible sealed

in a silica ampoule with a heating rate of 50 K/h, holding this temperature for 48 h and then turning off the furnace.

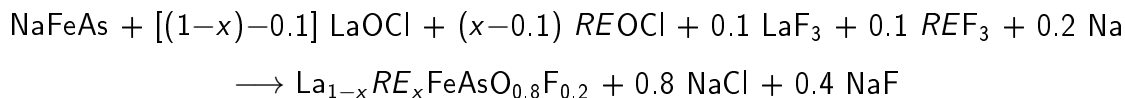
For the syntheses of $REOCl$ ($RE = La, Pr, Nd, Sm, Gd, Tb, Dy$), stoichiometric amounts of RE_2O_3 and NH_4Cl (with an excess of 0.15 eq.) were put on an alumina boat, which was placed inside a gas flow furnace. The product was synthesized in a dynamic atmosphere of argon at temperatures between 973–1173 K in a slightly modified version of Ref. [1].

2.1.4 Solid state metathesis reactions

The synthesis of the samples mentioned in Chapter 3 was performed by heating stoichiometric amounts of $NaFeAs$, $REOCl$, REF_3 , and Na ($RE = La, Pr, Nd, Sm, Gd, Tb, Dy$) according to the solid state metathesis reactions:



and



The precursors were mixed intimately, filled in alumina crucibles, welded in niobium ampoules enclosed by argon filled silica tubes. The reaction mixtures were heated to 1023 K for 48 h and 1223 K for 96 h, followed by cooling to room temperature. The coformed salts $NaCl$ and NaF were removed by washing the obtained mixture with water and ethanol, followed by drying the product in dynamic vacuum.^[2] The resulting products were black powders which are stable in air for months.

2.1.5 Flux-mediated reactions

The materials mentioned in Chapter 4 were prepared using a eutectic mixture of NaI/KI (mass ratio 0.6:0.4, dried in dynamic vacuum at 673 K) as flux. Therefore, the reactants were mixed intimately according to 0.2–0.3 g of the desired product and sandwiched in a glassy carbon or an alumina crucible between ≈ 1 g of the flux material. The crucibles were sealed in argon filled silica ampoules and heated to the respective reaction temperature with

a typical rate of 50 K/h. Finally, the ampoules were cooled down to 923–873 K with a rate of 5 K/h and quenched in air from this temperature. The resulting products were washed with water and ethanol and dried in dynamic vacuum.

2.2 Powder diffraction

2.2.1 X-ray powder diffraction

X-ray powder diffraction (XRD) patterns were recorded using the following diffractometers:

- HUBER G670 Guinier Imaging Plate diffractometer with Cu- $K_{\alpha 1}$ radiation ($\lambda = 0.15406$ nm), Ge(111) primary monochromator, silicon as external standard, and an oscillating sample holder, whereby the samples were held between two foils.

- HUBER G670 Guinier Imaging Plate diffractometer with Co- $K_{\alpha 1}$ radiation ($\lambda = 0.17890$ nm), Ge(111) primary monochromator, silicon as external standard, an oscillating sample holder, and additionally equipped with the low-temperature device 670.4 with a closed-cycle He cryostat (CTI-CRYOGENICS, model 22 CP) and a temperature controller (LAKESHORE, model 331) for temperature-dependent measurements in the range of 300 to 10 K. The samples were held between two foils.

2.2.2 Neutron powder diffraction

High-resolution neutron powder-diffraction measurements were performed at SPODI, FRM II, Garching, at temperatures at 300, 20 and 4 K with an incident wavelength of 0.1548 nm in cooperation with *Dr. A. Senyshyn* and *Dr. M. Mühlbauer*.

2.2.3 Rietveld refinements

Rietveld refinements were performed with the TOPAS program package.^[3] Reflection profiles were generated by the fundamental parameters approach. Spherical harmonics functions describe the preferred orientation of the crystallites. A modified approach of Le Bail and Jounnaux was used to describe small peak half width and shape anisotropy effects. Rietveld refinements of the modulated crystal structures in Chapter 4 were done with Jana2006^[4] and neutron diffraction data were refined with Fullprof^[5].

2.3 Magnetic measurements

Magnetic measurements were carried out (1.6–300 K, $-50 \rightarrow +50$ kOe) either at a QUANTUM DESIGN MPMS XL5 SQUID magnetometer with the MPMS MultiVu software^[6] or at a vibrating sample magnetometer (VSM, CRYOGENIC LIMITED).

Additionally, a differential dual-coil AC susceptometer was used in a temperature range of 3.5–300 K with an applied field of 3 Oe.^[7]

2.4 Energy-dispersive X-ray analysis

Energy dispersive X-ray (EDX) experiments were performed on a CARL ZEISS EVO-MA 10 with SE and BSE detectors, controlled by the SmartSEM^[8] software. The microscope was equipped with a BRUKER Nano EDS detector (X-Flash detector 410-M) for EDS investigations using the QUANTAX200^[9] software to collect and evaluate the spectra. The samples were measured using adhesive conducting carbon films to fix them on aluminium sample holders. Therefore, the elements Al and C were not included in the analyses.

2.5 Muon spin rotation

Muon spin rotation (μ SR) experiments were conducted at the GPS spectrometer at the Swiss Muon Source (PSI, Switzerland) in cooperation with *Dr. H. Luetkens* and *S. Holenstein*.

2.6 UV-VIS-spectroscopy

Diffuse reflectance spectra were measured with powder samples with an UV/Vis/NIR Varian Cary 500 spectrophotometer (200–800 nm). The spectra were converted to absorption spectra based on the Kubelka-Munk theory^[10] to determine the optical bandgap.

2.7 Single-crystal X-ray diffraction

Single-crystal X-ray diffraction data was collected in the range of 300 to 100 K with a BRUKER D8 QUEST (fixed- χ goniometer, Mo- K_{α} , $I\mu$ S with HE-LIOS multi-layer optics, PHOTON 100 detector, closed-cycle He cryostat) or with a Bruker D8 Venture (Mo- K_{α} , rotating anode,

Photon-II CPAD detector). Reflection intensity integrations, data reductions, and multi-scan absorption corrections were done with APEX2^[11] and SADABS^[12] or TWINABS^[13]. The structures were solved and refined with the Jana2006^[4,14] or Shelxl^[15] packages.

2.8 References

- [1] H. P. Beck, *J. Solid State Chem.* **1976**, *17*, 275.
- [2] R. Frankovsky, A. Marchuk, R. Pobel, D. Johrendt, *Solid State Chem.* **2012**, *152*, 632.
- [3] A. Coelho, *TOPAS-Academic*, Version 4.1, Coelho Software, Brisbane, Australia **2007**.
- [4] V. Petricek, M. Dusek, L. Palatinus, *Jana2006* (Version 26/09/2012), Institute of Physics, Praha, Czech Republic **2006**.
- [5] J. Rodriguez-Carvajal, *Physica B* **1993**, *192*, 55.
- [6] *MPMS MultiVu*, v. 1.56 Build 72, Quantum Design Inc., S. Diego, **2005**.
- [7] M. Tegel, Ph. D. thesis, LMU Munich (Germany), **2011**.
- [8] *SmartSEM*, v. Version 5.07 Beta, Carl Zeiss Microscopy Ltd., **2014**.
- [9] *Quantax 200*, v. Version 1.9.4.3448, Bruker Nano GmbH, **2013**.
- [10] P. Kubelka, F. Munk, *Z. Tech. Phys.* **1931**, *12*, 593.
- [11] *APEX2* (Version 2012.12-0), Bruker AXS Inc., Madison, WI, USA, **2007**.
- [12] G. M. Sheldrick, *SADABS* (Version 2012/1), Bruker AXS Inc., Madison, WI, USA, **2001**.
- [13] G. M. Sheldrick, *TWINABS* (Version 2012/1), Bruker AXS Inc., Madison, WI, USA, **2001**.
- [14] V. Petricek, M. Dusek, L. Palatinus, *Z. Kristallogr.* **2014**, *229*, 345.
- [15] G. M. Sheldrick, *Acta Crystallogr. Sect. A* **2008**, *64*, 112.

Chapter 3

Solid State Metathesis of $REFeAsO_{1-x}F_x$ Compounds

3.1 $LaFeAsO_{1-x}F_x$

S. Peschke, S. Vogel, and D. Johrendt

Parts published in: *Z. Anorg. Allg. Chem.* **2016**, *642*, 1063.

Copyright 2016, Wiley-VCH Verlag GmbH & Co. KGaA, Weinheim.

3.1.1 Introduction

The discovery of superconductivity at 26 K in $LaFeAsO_{1-x}F_x$ by *Kamihara* et al. in 2008 indicated that the field of layered oxypnictides is a promising new platform to realize high- T_c superconductors.^[1] The parent compound $LaFeAsO$ adopts the $ZrCuSiAs$ -type structure (space group $P4/nmm$) with two formula units per unit cell. Therefore, the structure can be described as alternating $[La_2O_2]^{2+}$ and $[Fe_2As_2]^{2-}$ layers with edge-sharing $OLa_{4/4}$ and $FeAs_{4/4}$ tetrahedra (Fig. 3.1).

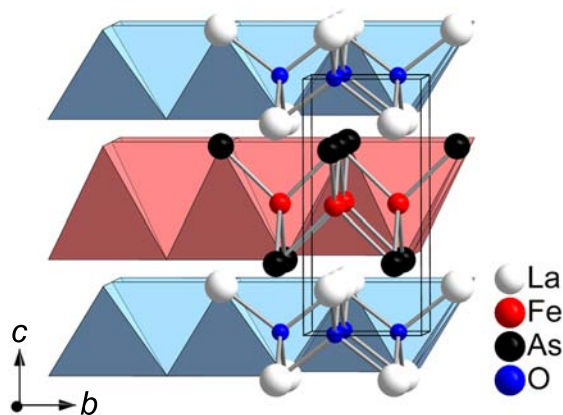


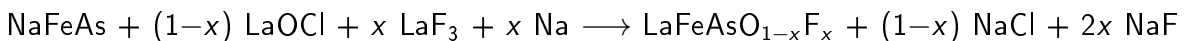
Figure 3.1 Crystal structure of $LaFeAsO$.

The compound is a paramagnetic metal at room temperature and undergoes a tetragonal-to-orthorhombic ($P4/nmm \rightarrow Cmme$) phase transition around 160 K accompanied by an antiferromagnetic transition at ≈ 140 K.^[2] In contrast to the insulating $[La_2O_2]^{2+}$ layer, the $[Fe_2As_2]^{2-}$ layer serves as a two-dimensionally confined carrier conduction path. The substitution of oxygen by fluorine or the formation of oxygen vacancies provides an extra positive charge in the insulating layer and a negative charge in the conduction layer. Superconductivity appears when both transitions are suppressed by exceeding a critical quantity of carrier doping, which is $\approx 5\%$ in $LaFeAsO_{1-x}F_x$. The suppression of the structural as well as the magnetic transition is ascribed to the interplay of geometric and electronic structural

changes due to doping. An antiferromagnetic spin fluctuation model resulting from Fermi surface nesting between hole and electron pockets as well as the suppression of the tendency to magnetism was proposed based on density functional theory calculations. These fluctuations turned out to be crucial to create a superconducting state with order parameters of opposite signs on the electron and hole pockets.^[3]

Conventional solid-state synthesis reactions were used to obtain new compounds in the REFeAsO_{1-x}F_x family ($RE = \text{Ce, Pr, Nd, Sm, Eu, Gd}$) with critical temperatures up to 58.1 K in SmFeAsO_{1-x}F_x.^[4-10] As the ionic radius of fluorine is distinctly smaller than that of oxygen, the resulting lattice mismatch between the [RE₂O_{2-x}F_x] layer and the [Fe₂As₂] layer leads to a solubility limit of fluorine of $x \approx 0.2$ in these compounds.^[11] However, samples with late rare-earth elements like Tb and Dy were either inaccessible or very impure due to the decreasing ionic radii of the rare-earth metal (lanthanide contraction) and the resulting large lattice mismatch between the two layers. High pressure and temperature synthesis routes were developed to overcome this problem, as it is known that pressure can stabilise many late rare-earth analogues of early rare-earth compounds.^[12] Moreover *Lu et al.* reported the high pressure synthesis of LaFeAsO_{0.4}F_{0.6} with $T_c = 41$ K, which indicates that also the solubility limit of fluorine at ambient pressure can be overcome by high pressure.^[13] In addition, high pressure syntheses were also successfully applied to partially substitute oxide by hydride in REFeAsO_{1-x}H_x ($RE = \text{La, Ce, Sm}$).^[11,14,15] These findings opened the way to study the physical properties of electron doped compounds over a wide x region as the solubility limit of hydride ($x \approx 0.8$) is considerable higher compared to fluoride.^[16] Beside substitutions on the oxygen position, there are also reports on the substitution of the rare-earth element by thorium in RE_{1-x}Th_xFeAsO ($RE = \text{La, Nd, Sm, Gd, Tb, Dy}$) with critical temperatures up to 56 K.^[17-22] The substitution of a trivalent rare-earth metal by a relatively large tetravalent ion represents an alternative route to introduce electrons in the structure.

Recently, *Frankovsky et al.* reported a solid state metathesis (SSM) reaction which is efficient to prepare very pure, polycrystalline LaFeAsO_{1-x}F_x ($0 \leq x \leq 0.15$).^[23] The synthesis of LaFeAsO was performed by heating stoichiometric amounts of NaFeAs and LaOCl according to the scheme in Figure 3.2. Additional substitution of oxygen by fluorine in LaFeAsO was enabled by the addition of LaF₃ and Na according to the following solid state metathesis reaction:



Temperature-dependent X-ray diffraction showed that the reaction pathway has actually no topotactic character but binary intermediates were identified. Superconducting samples were found for $x = 0.05$, 0.10 and 0.15 at critical temperatures of 11 K, 26 K and 9 K, respectively. Bulk superconductivity was confirmed for the $x = 0.10$ and 0.15 samples and only traces of superconductivity (superconducting volume fraction $< 4\%$) for $x = 0.05$.^[23] However, until now there is no information about samples with $x > 0.15$ and whether the solubility limit of fluorine can be shifted to higher x using this novel synthesis route.

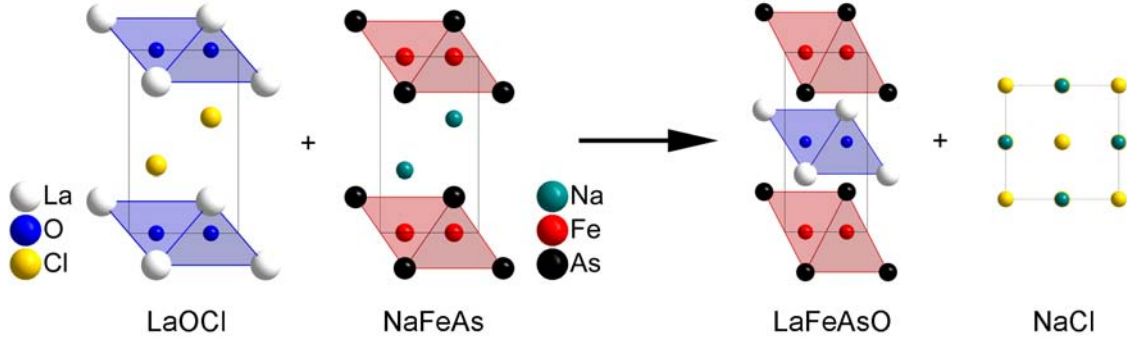


Figure 3.2 Scheme of the solid state metathesis reaction.

3.1.2 Results and Discussion

Solubility Limit via Metathesis

First, we made investigations to determine the solubility limit of fluorine in $LaFeAsO$ using the SSM route. Therefore, we prepared additional samples to Ref. [23] with $x = 0.20$ – 0.45 and analysed them in terms of purity and superconductivity by X-ray powder diffraction and magnetic susceptibility measurements. Figure 3.3 (A) displays the course of the cell volume (black dots) and the yield of the desired phase (striped bars) upon fluorine doping in $LaFeAsO_{1-x}F_x$. Further structural and physical details of the samples are depicted in Table 3.1. The lattice parameters and the cell volume decrease with increasing fluorine content until $x = 0.25$ and then remain almost constant, which indicates that there is a homogeneous fluorine doping up to $\approx 25\%$. The sudden drop of the yield from 93 to 70 wt% between $x = 0.20$ and 0.25 , together with almost unchanged lattice parameters for $x \geq 0.25$, supports the assumption that the solubility limit is in this region. The yield further decreases until we did not find any traces of the desired phase in the X-ray powder diffraction patterns for samples with $x > 0.4$. AC-susceptibility measurements (Fig. 3.3 B) confirmed

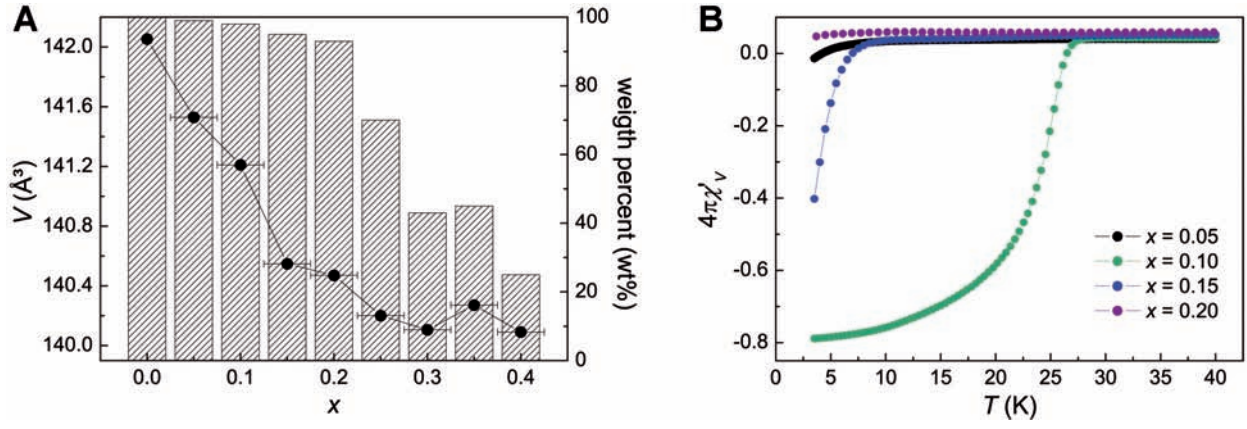


Figure 3.3 (A) Trend of the cell volume (black dots) and of the yield (striped bars) of $\text{LaFeAsO}_{1-x}\text{F}_x$ against the fluorine content x . (B) AC-susceptibility plots ($H = 3$ Oe) of $\text{LaFeAsO}_{1-x}\text{F}_x$ for $x = 0$ – 0.20 .

superconductivity in samples with $x = 0.05, 0.10$ and 0.15 , however samples with $x \geq 0.20$ are no longer superconducting. The rapid drop of T_c up to non-superconducting samples at $x \geq 0.2$ can be explained by over-doping with electrons to the filling level of the hole pockets. This is in line with neutron scattering studies, which revealed that the spin fluctuations are already highly suppressed in $\text{LaFeAsO}_{0.842}\text{F}_{0.158}$ due to a disturbed nesting condition upon electron over-doping.^[24]

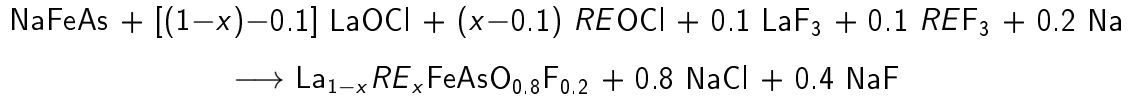
Table 3.1 Lattice parameters, cell volume, yield and critical temperatures of the series $\text{LaFeAsO}_{1-x}\text{F}_x$ ($0 \leq x \leq 0.4$).

x	0	0.05	0.10	0.15	0.20	0.25	0.30	0.35	0.40
a/pm	403.2	402.8	402.6	402.0	401.9	401.5	401.3	401.5	401.4
b/pm	873.8	872.3	871.2	869.7	869.7	869.9	870.0	870.1	869.9
$V/\text{\AA}^3$	142.1	141.5	141.2	140.5	140.5	140.2	140.1	140.3	140.1
LaFeAs(O,F)/wt%	100	99	98	95	93	70	43	45	25
T_c/K	-	11	26	9	-	-	-	-	-

Re-emergence of Superconductivity in $\text{La}_{1-x}\text{RE}_x\text{FeAsO}_{0.8}\text{F}_{0.2}$ ($RE = \text{Pr-Sm}$)

Although the SSM reaction provides no possibility to overcome the solubility limit of fluorine in the $\text{LaFeAsO}_{1-x}\text{F}_x$ system, it stays an easy and efficient method to prepare high purity polycrystalline samples. However, *Lu* et al. were able to prepare superconducting samples with even higher fluorine contents up to $\text{LaFeAsO}_{0.4}\text{F}_{0.6}$ (nominal composition) using a high pressure and temperature synthesis route. Remarkably, the highest T_c of those samples is

41.0 K for $x = 0.6$ in spite of constant electron doping. They attribute the increase of T_c to further shrinkage of the crystal structure, which causes stronger chemical pressure on the $[Fe_2As_2]$ layer.^[13] The observations of *Lu* et al. led us to the idea to compress the crystal structure without physical pressure but with chemical substitution of lanthanum by smaller rare-earth metals at constant fluorine content. This would provide an easy opportunity to investigate the physical properties of over-doped $LaFeAsO_{1-x}F_x$ upon further shrinkage of the cell volume at ambient pressure. Starting from non-superconducting $LaFeAsO_{0.8}F_{0.2}$, we extended the SSM reaction in order to get samples of $La_{1-x}RE_xFeAsO_{0.8}F_{0.2}$ ($RE = Pr-Sm$) using the following SSM reaction:



X-ray powder diffraction experiments of the worked-up samples revealed a purity of > 90 wt%. Figure 3.4 shows the Rietveld refinement of the X-ray powder diffraction pattern of $La_{0.8}Pr_{0.2}FeAsO_{0.8}F_{0.2}$ as an example. The course of the lattice parameters and the cell volume upon substitution are depicted in Figure 3.5.

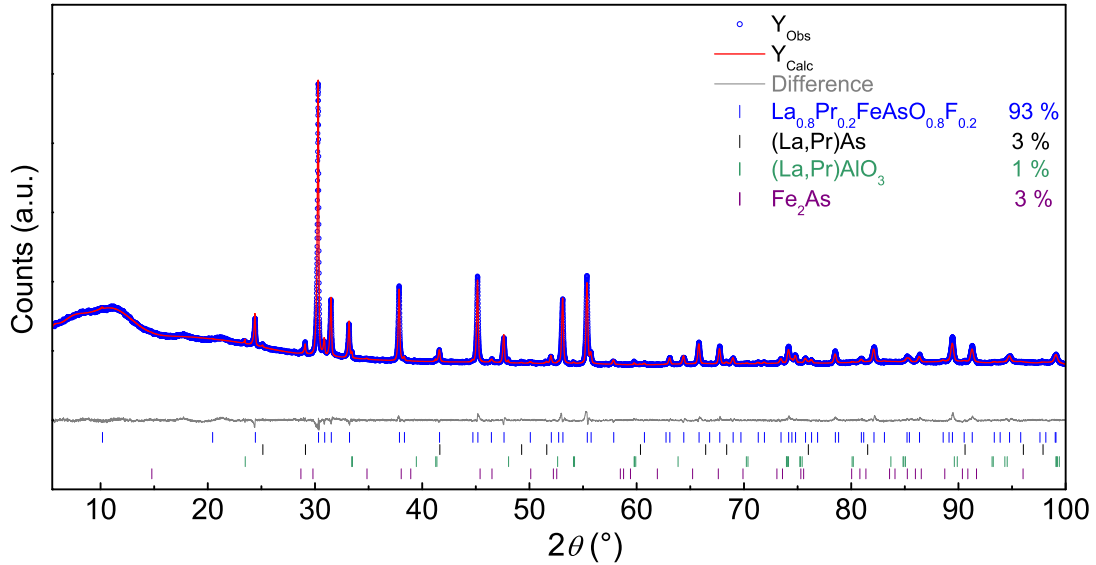


Figure 3.4 X-ray powder pattern (blue), Rietveld fit (red) and difference plot (gray) of $La_{0.8}Pr_{0.2}FeAsO_{0.8}F_{0.2}$.

The parameters a and c decrease linearly with increasingly smaller rare-earth content according to Vegard's law, which can be simply explained by the smaller radii of Pr, Nd and Sm compared to La ($r_{La} = 143.4$ pm, $r_{Pr} = 137.6$ pm, $r_{Nd} = 136.1$ pm, $r_{Sm} = 133.2$ pm)^[25].

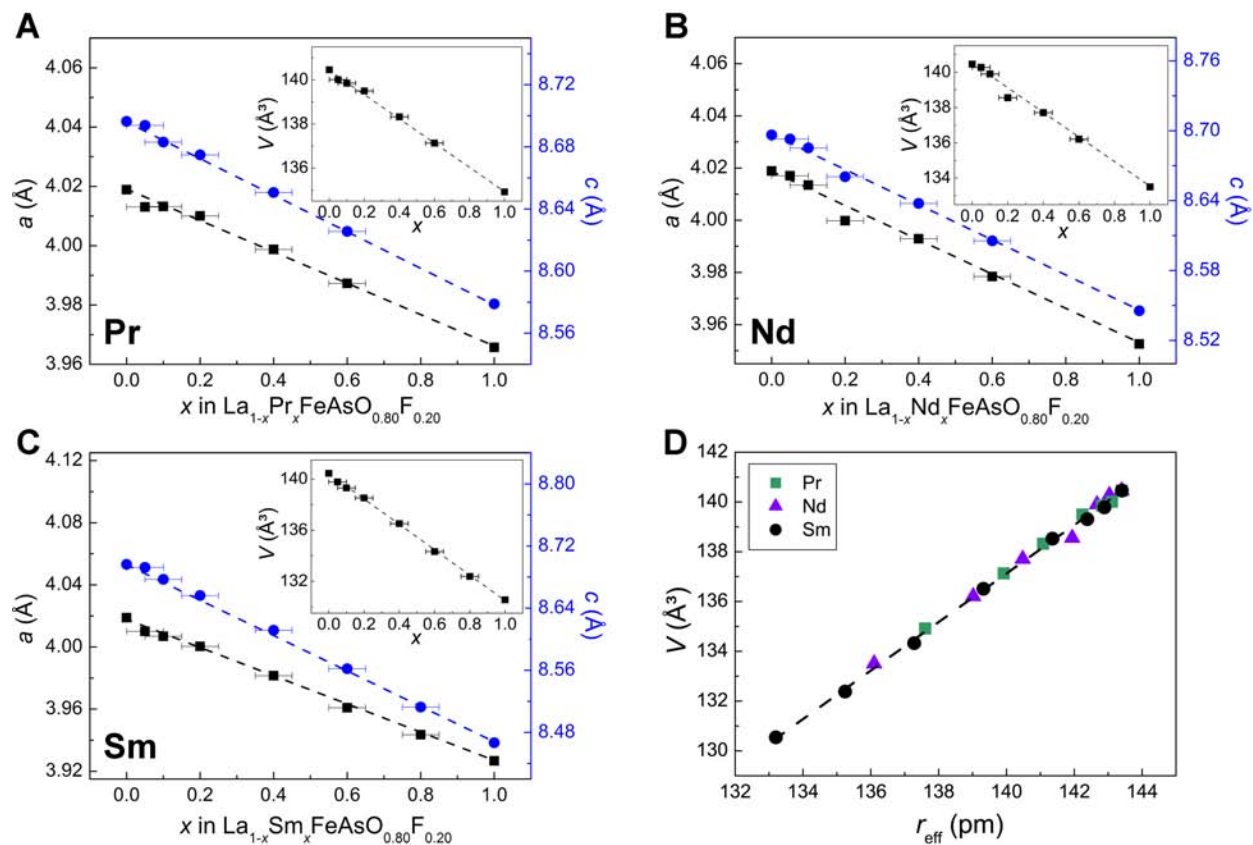


Figure 3.5 Lattice parameters a (black squares) and c (blue dots) and cell volume (inset) for the substitution of lanthanum in $La_{1-x}RE_xFeAsO_{0.8}F_{0.2}$ by (A) Pr, (B) Nd and (C) Sm. (D) Cell volume against the effective radii of the mixed rare-earth atoms. Dashed lines are guides to the eye.

Regarding the cell volume against the effective radii of the mixed rare-earth metals in their $ORE_{4/4}$ -tetrahedra ($r_{\text{eff}} = (1-x)r_{\text{La}} + xr_{\text{RE}}$), a linear trend is observed (Fig. 3.5 D), which points to a constant fluorine content of the samples, whereas the shrinking of the lattice parameters is solely controlled by the substitution of the rare-earth metals.

Magnetic susceptibility measurements between 3.5 and 65 K were used to study the physical properties and, if superconducting, to determine T_c and the superconducting volume fraction. The AC-susceptibility plots for the different substitutions (Fig. 3.6) reveal traces of superconductivity for $x = 0.1$ (superconducting volume fraction $< 15\%$) and bulk superconductivity for $x > 0.10$.

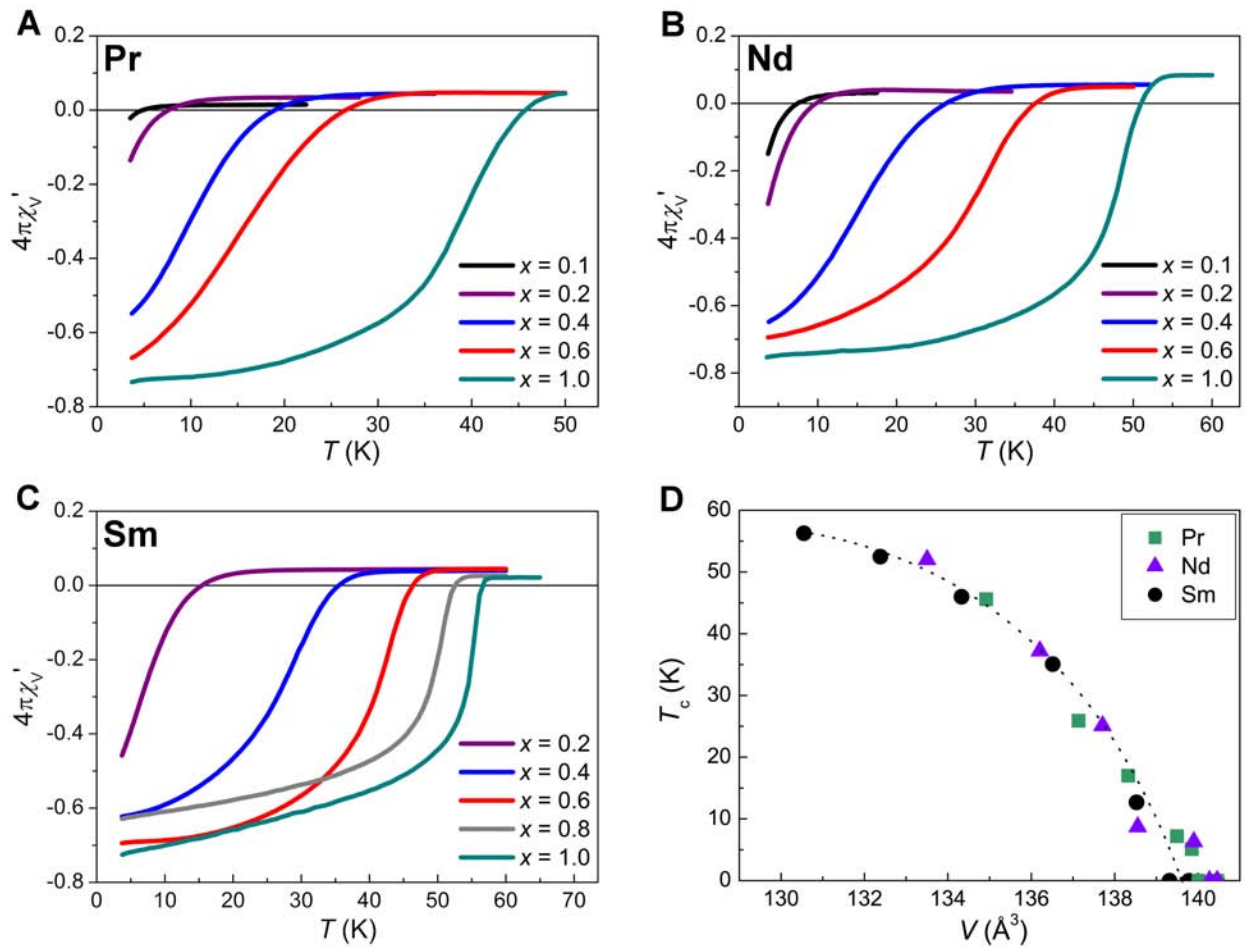


Figure 3.6 AC-susceptibility plots for the substitution of lanthanum by (A) Pr, (B) Nd and (C) Sm. (D) Critical temperature T_c of $\text{La}_{1-x}\text{RE}_x\text{FeAsO}_{0.8}\text{F}_{0.2}$ ($\text{RE} = \text{Pr, Nd, Sm}$; $0 \leq x \leq 1$) against the unit cell volume. Dashed lines are guides to the eye.

A little paramagnetic background is visible for temperatures $\geq T_c$, which can be attributed to a small amount of magnetic impurities (e.g. Fe₂As, REAs). Remarkably, superconductivity re-emerges in the solid solutions La_{1-x}RE_xFeAsO_{0.8}F_{0.2} at $x \geq 0.20$ in spite of constant electron over-doping. As shown in Figure 3.6 (D), the critical temperature increases power-law-like as soon as the unit cell volume decreases below $\approx 140 \text{ \AA}^3$, and reaches 56 K at $\approx 130 \text{ \AA}^3$. From this we infer that T_c cannot be controlled alone by the charge carrier density and suggest that structural parameters may play a decisive role.

3.2 SmFeAsO_{1-x}F_x

3.2.1 Introduction

Iron based superconductors have great potential for the use in high magnetic field applications. Among all compounds in the 1111-family, optimally doped SmFeAsO_{1-x}F_x with $x \approx 0.15$ exhibits the highest critical temperature up to 58 K.^[8] Due to their high T_c , large upper critical fields of $H_{c2} > 100$ T^[26] and relatively low anisotropy, these compounds are interesting in terms of application as conductors. Another parameter, the global critical current density (J_c^{global}), which represents the current flowing in the whole sample, has to be as high as possible even at high magnetic fields. A transport of J_c^{global} over 1×10^6 A/cm² at 5 K under 140 kOe has been reported in a SmFeAsO_{1-x}F_x single crystal, which is comparable to values of commercially used NbTi or Nb₃Sn wires.^[27] J_c^{global} is mainly dependent on the purity and the granularity of polycrystalline samples, thus it is important to prepare high purity bulk samples with a minimum of grain boundaries for the practical use of superconducting wires. Thereby, the performance of wires and tapes can be improved by cold and hot press^[28] or the addition of metals like Ag^[29]. Beside the global current, an intragrain current J_c^{intra} , which is dominated by vortex pinning, usually occurs within the small grains. *Dou et al.* showed that the intergranular and intragranular critical current densities can be determined quantitatively from measurements of a tape's remanent magnetic moment m_R as a function of the applied magnetic field H_a .^[30] During the last years, many efforts have been made to produce wires and tapes of SmFeAsO_{1-x}F_x and substantial progress has been made in 1111 tapes, where recently a transport J_c of 3.95×10^4 A/cm² has been reported as the highest value ever in the 1111 family.^[31] This value is still below the highest critical current densities of 122 tapes (1.2×10^5 A/cm² in (Sr,K)Fe₂As₂), which may be due to the higher anisotropy than in 122 samples.^[32] However, results from literature revealed that polycrystalline powder synthesis as well as fabrication conditions of wires and tapes have not been optimized yet.

As the SSM reaction provides a good opportunity to prepare high quality samples of SmFeAsO_{1-x}F_x, we used this background to investigate the behavior of J_c of those samples in cooperation with *Dr. A. Malagoli* (CNR-SPIN, Genova, Italy).

3.2.2 Results and Discussion

Synthesis and Characterization

Optimally doped $\text{SmFeAsO}_{0.85}\text{F}_{0.15}$ (≈ 600 mg) was prepared using the SSM reaction using NaFeAs , SmOCl , SmF_3 and Na as precursors. The sample was divided into eight parts of ≈ 70 mg and pressed to eight pellets (4 mm diameter, 600 MPa pressure). The as-prepared sample is called **S**. Two pellets were annealed at 1173, 1273 and 1373 K, respectively for 10 h in silica ampoules and are therefore called **A1**, **A2** and **A3**. One pellet of each sample (**S**, **A1**, **A2** and **A3**) were sent to *Dr. A. Malagoli* (CNR-SPIN, Genova, Italy) for SEM/EDX and magnetization measurements. The four remaining pellets were analyzed in terms of purity and superconductivity by powder X-ray diffraction and AC-susceptibility measurements, respectively. Rietveld refinement of the initial sample **S** revealed only small impurities (≈ 1.5 wt%) of SmAlO_3 and SmAs (Fig. 3.7). The presence of aluminium can be explained by the reaction of a small amount of the alumina crucible during the synthesis.

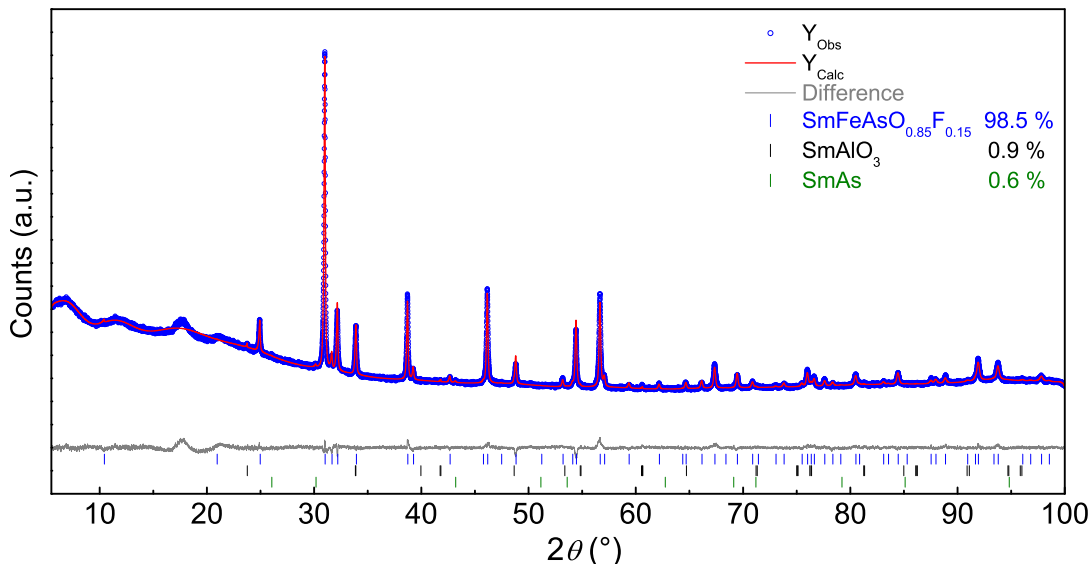


Figure 3.7 X-ray powder pattern (blue), Rietveld fit (red) and difference plot (gray) of as-prepared $\text{SmFeAsO}_{0.85}\text{F}_{0.15}$.

Unit cell parameters, cell volume and purity of the samples are summarized in Table 3.2. The lattice parameters and the cell volume of the samples **A1–A3** show only a slight decrease (< 0.25 %) after the sintering process. This indicates that the fluorine content stays almost unchanged during heat treatment. After grinding the pellets, Rietveld refinements of the XRD patterns of **A1–A3** revealed a decrease in terms of phase purity. The drop is quite

Table 3.2 Lattice parameters, cell volume and major and minor phases as determined by powder X-ray diffraction of the samples **S**, **A1**, **A2** and **A3**.

	S	A1	A2	A3
a/pm	392.8(1)	392.6(1)	392.5(1)	392.6(1)
b/pm	846.7(1)	846.1(1)	846.0(1)	846.0(1)
$V/\text{\AA}^3$	130.6(1)	130.4(1)	130.3(1)	130.4(1)
$\text{SmFeAsO}_{0.85}\text{F}_{0.15}/\text{wt}\%$	98.5	95.0	92.6	86.3
Impurities/wt%	0.9 SmAlO_3	1.7 FeAs	1.0 SmAs	2.7 SmAs
	0.6 SmAs	3.3 SmOF	1.6 FeAs	3.8 FeAs
			4.8 SmOF	7.2 SmOF

small for the samples **A1** and **A2**, which still contain 95.0 and 92.6 wt% of the desired phase. However, sintering at 1373 K degrades the purity to 86.3 wt%, while the amount of the impurity phases SmAs , FeAs and SmOF increases significantly.

Figure 3.8 shows high magnification scanning electron microscopy images of the untreated sample **S** (Fig. 3.8 A) and of the sintered samples **A1–A3** (Fig. 3.8 B–D). Simultaneous EDX measurements revealed that the samples contain multiple impurity phases (dark gray contrasts), which is consistent with the results from Rietveld refinements. However, the samples become significantly denser after sintering, increasing from $\approx 70\%$ in **S** to $\approx 90\%$ in **A1** and **A2**, and $\approx 80\%$ in **A3** (values of the density are visually estimated). Interestingly, the microstructure becomes less dense after sintering at 1373 K, which is consistent with the destruction of the desired phase and the highly increasing amount of impurity phases at this temperature.

The temperature dependences of resistivity of all samples are shown in Figure 3.9. Resistivity of **S** begins to drop at 54.0 K, however zero resistivity was not fully achieved down to 10.0 K, probably due to the weak connection between the grains and high grain boundary resistivity. In contrast, the samples **A1–A3** show immeasurable small resistivities at low temperatures and the onsets of T_c were determined to be 54.4, 54.8 and 53.8 K, respectively. Zero resistivity was reached at 51.2, 51.8 and 50.3 K for **A1–A3**, respectively. Further data of the resistivity measurements are compiled in Table 3.3.

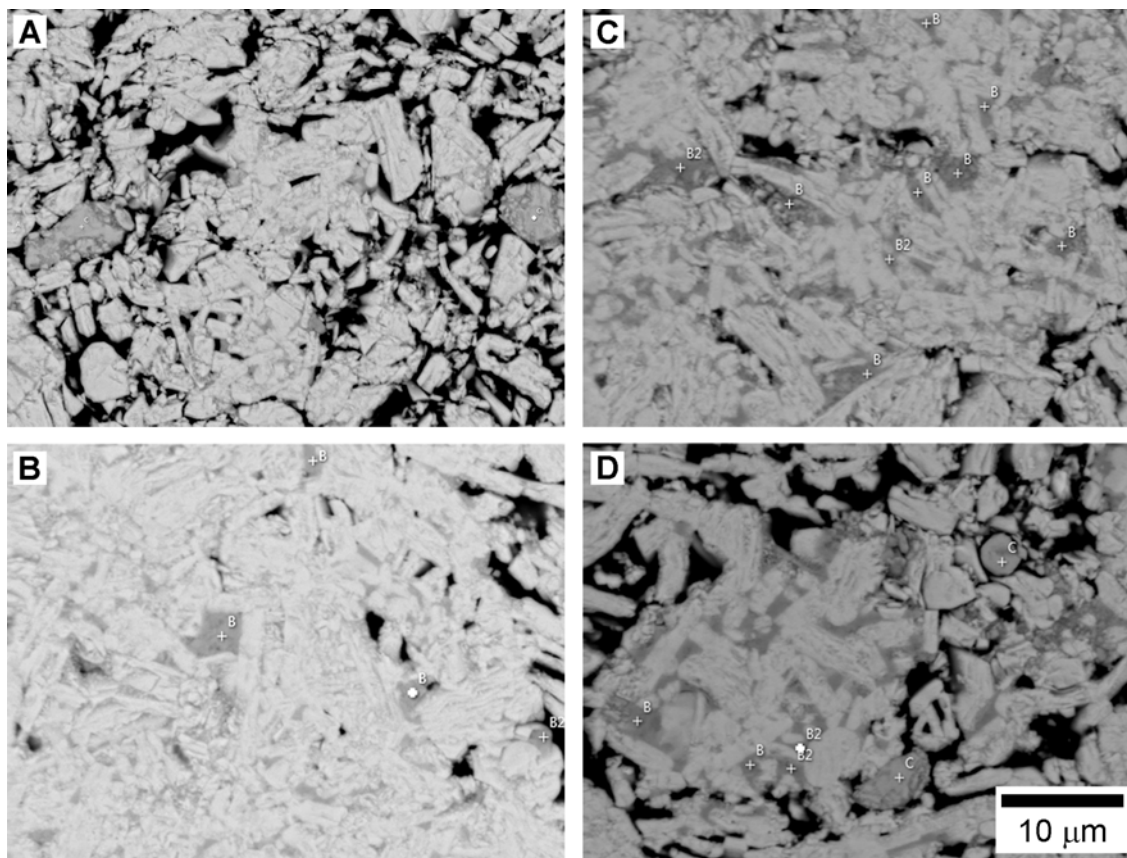


Figure 3.8 Scanning electron microscope images of the different $SmFeAsO_{0.85}F_{0.15}$ samples. (A) S, (B) A1, (C) A2 and (D) A3.

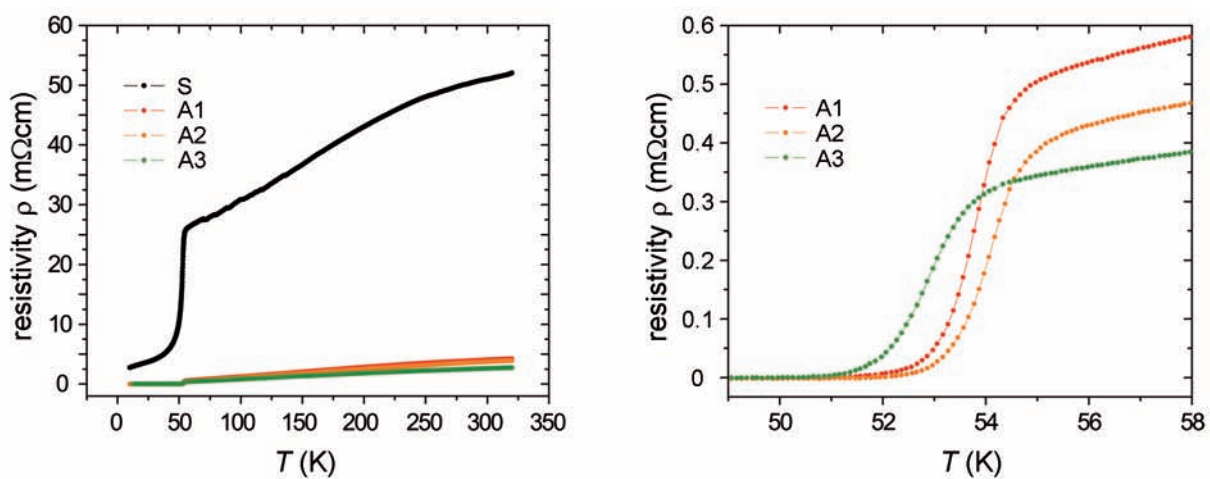


Figure 3.9 Plots of the electrical resistivity against temperature of the samples S and A1–A3 (left). Magnification of the plots for A1–A3 (right).

Table 3.3 Data of the resistivity measurements of the samples **S**, **A1**, **A2** and **A3**.

	S	A1	A2	A3
T_c/K	54.0	54.5	54.8	53.8
$\rho(300\text{ K})/\text{m}\Omega\times\text{cm}$	51.0	4.05	3.74	2.61
$\rho(55\text{ K})/\text{m}\Omega\times\text{cm}$	125.57	0.508	0.384	0.343
$\rho(300\text{ K})/\rho(55\text{ K})$	2.0	8.0	9.7	7.6

Magnetization Measurements

Plots of the AC-susceptibility measurements are displayed in Figure 3.10. The onset T_c was found to be 53.5 K for **S** and 54.0 K for **A1–A3**, which is in good agreement with the resistivity measurements. The continuous decrease of χ below T_c of the untreated sample **S** indicates inhomogeneity of the fluorine distribution in the sample, whereas sintering of the samples seems to improve the sample quality as χ saturates at low temperatures.

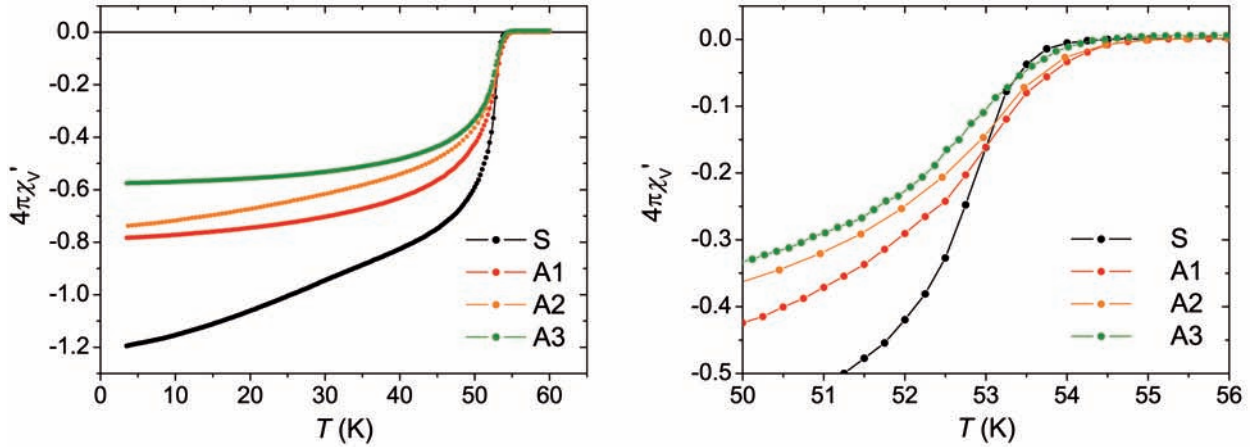

Figure 3.10 Left: AC-susceptibility plots of the samples **S**, **A1**, **A2** and **A3**. Right: Magnification of the plots near the superconducting transition temperature.

Figure 3.11 shows the field dependence of the magnetic hysteresis loop widths (ΔM) at 5 K. The loop widths of the samples **S** and **A3** are almost identical for small fields ($H < 5000$ Oe) but differ significantly at high fields. The widths of the samples **A1** and **A2** are 10–20 % larger compared to the other samples. The increase of the hysteresis loop width can be attributed to either a larger grain size or to an improved connectivity between the grains. As SEM images revealed no considerable difference between the grain size of the sample **S** compared to the samples **A1–A3** (Fig. 3.8), the increased hysteresis arises more probably from increased intergranular current flow. This is in line with the enhanced density

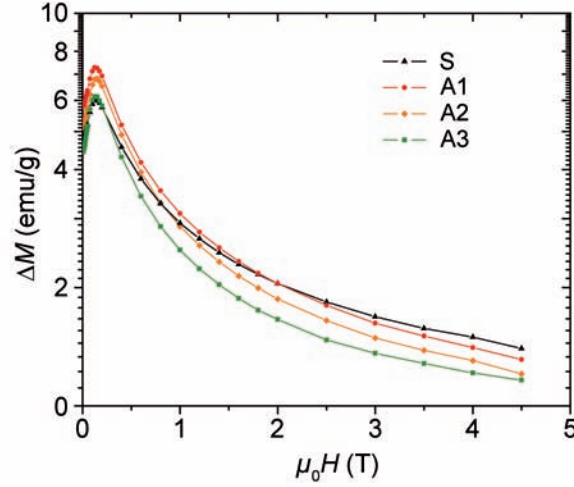


Figure 3.11 Magnetic hysteresis loop widths (ΔM) against the field at 5 K of the samples **S** and **A1–A3**. μ_0 is the vacuum permeability.

of the samples **A1** and **A2** compared to **S** and **A3**. The critical current density J_c can be derived from the hysteresis loop width based on the extended Bean model.^[33] However, the magnetization hysteresis convolutes contributions from both, intergranular and intragranular current flow and a distinction between both cannot be made here.

To distinguish the inter- and intragranular current flows in these samples, field dependent remanent magnetization (RM) measurements were performed. Therefore, the polycrystalline bulk samples were exposed to many cycles of ever increasing magnetic field H_a , followed by removal of the field and measurement of the remanent moment, m_R . It is known that flux starts to penetrate into a sample when $H_a/(1-D)$ first exceeds the lower critical field H_{c1} (D is the relevant demagnetizing factor).^[33,34] However, for polycrystalline samples with weak intergranular coupling due to impurities or a weak connection between the grains, flux penetration into grain boundaries occurs at lower fields than into the grains. As m_R is proportional to the product of critical current density and current loop size, the information about the size of current loops derived from m_R can be extracted from the dependence of m_R on the applied field H_a and the particle size.^[30,33–35]

Figure 3.12 (A) shows the remanent magnetization as a function of increasing applied field for all four samples. All samples exhibit one major transition at ≈ 100 mT. The sintered samples **A1–A3** have an additional minor transition at ≈ 1 mT, which indicates two distinctly different scales of current flow in those samples. This behavior is better visible in the derivative of m_R (H_a) shown in Figure 3.12 (B), in which two separated peaks exist

for **A1–A3** (≈ 1 mT and ≈ 100 – 150 mT) but only one for the sample **S** (≈ 100 mT). The single step transition of sample **S** proves that there is no intergranular current path probably due to a weak connection of the grains, which was already supposed on the basis of resistivity and SEM measurements. Therefore, the higher field transition can be attributed to an intragranular current which is present in all samples as at high applied magnetic fields, flux penetrates the grains and the induced grain pinning current contributes to m_R .

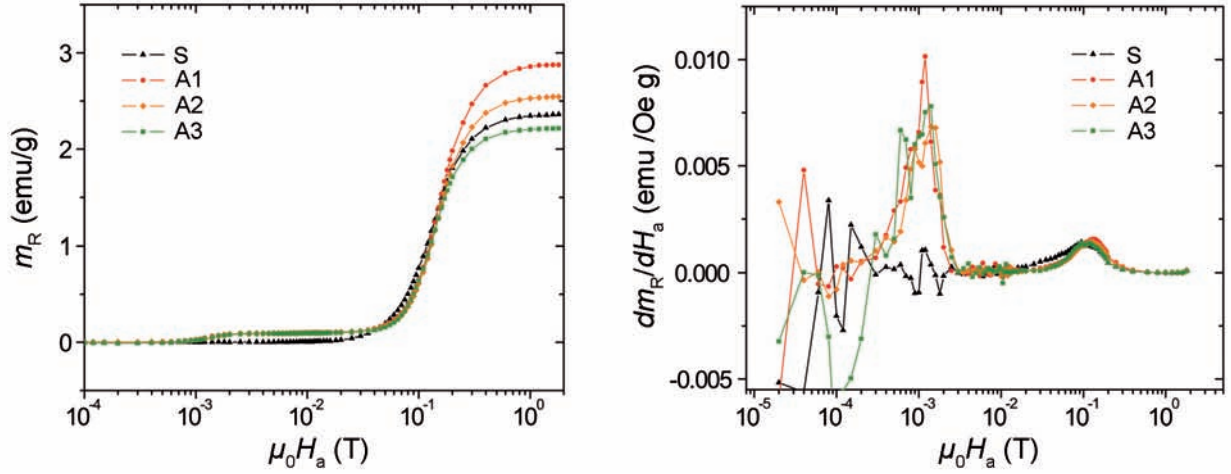


Figure 3.12 (A) Plot of the remanent magnetization (m_R) against the applied field (H_a) and (B) the derivative dm_R/dH_a against the applied field. μ_0 is the vacuum permeability.

The critical intragranular current density can be calculated by $J_c^{\text{intra}} = 2.81H_{\text{peak2}}/r$, where H_{peak2} is the higher field peak position and r is the effective grain size.^[35] We estimated grain sizes to be 5–10 μm from SEM images, which leads to intragranular critical current densities in the range of 10^6 – 10^7 A/cm² at 5 K.

The peak positions of the lower field transition of the three sintered samples are only slightly shifted to each other assuming that the current flows over the whole sample have similar values. According to the Bean model, the global critical current is given by $J_c^{\text{global}} = 2H_{\text{peak1}}/\omega$, where ω is the thickness of the whole bulk sample. The unknown demagnetization factor as well as the anisotropy of J_c is neglected in this simplified model. The values of J_c^{global} are ≈ 200 , 250 and 235 A/cm² for **A1–A3**, respectively. The sample **A2** exhibits the highest J_c^{global} although in the order of those of **A1** and **A3**. These values are comparable to those of samples in the literature, which were prepared by hot isostatic pressing (HIP).^[35]

The SSM reaction provides a good opportunity to prepare almost phase-pure samples of $SmFeAsO_{0.85}F_{0.15}$. Sintering of those samples at 1173–1373 K increases the density but continuously degrades the sample quality due to increased formation of impurity phases. This may be responsible for the low values of J_c^{global} as the global current is limited by the connection across grain boundaries.

3.3 $REFeAsO_{1-x}F_x$ ($RE = Gd-Dy$)

3.3.1 Introduction

Samples of $REFeAsO_{1-x}F_x$ with late rare-earth elements like Tb and Dy are solely accessible by high pressure synthesis due to the small ionic radii of the rare-earth metals and the resulting large lattice mismatch between the $[RE_2(O,F)_2]$ layer and the $[Fe_2As_2]$ layer. While there exist only a few reports about a conventional solid state reaction synthesis of $GdFeAsO_{1-x}F_x$ with critical temperatures up to 43.9 K, there are no such reports for compounds with heavier rare-earth metals.^[36-38] However, regarding the gadolinium compound, critical temperatures for samples produced via conventional synthesis are significantly lower compared to samples prepared by high pressure synthesis, where T_c can be increased to 54.0 K in $GdFeAsO_{0.85}$.^[39] The enhanced critical temperature can be referred to a further shrinking of the cell volume, which is not accessible using conventional solid state methods. Moreover, critical temperatures in the range of 45.0–52.6 K are reported for high pressure synthesized $REFeAsO_{1-\delta}$ and $REFeAsO_{1-x}F_x$ ($RE = Tb, Dy$).^[12,40] Just as for the light analogues, the compounds $REFeAsO$ with $RE = Gd-Dy$ show a structural transition and a stripe-type antiferromagnetic ordering of the Fe ions at $\approx 120-140$ K. Additionally, a second magnetic transition caused by the antiferromagnetic ordering of the magnetic moments of the rare-earth metals was observed at low temperatures between $\approx 4-9$ K.^[41,42] Magnetic susceptibility measurements of some samples revealed a paramagnetic background, which can be attributed to either impurity phases or to the magnetic moment of the rare-earth metal in $REFeAsO_{1-x}F_x$.^[36] Based on these findings, we investigated whether the SSM reaction is suitable as an alternative method to prepare superconducting late rare-earth 1111 compounds in sufficient purity.

3.3.2 Results and Discussion

Synthesis and Characterization

A series of the $REFeAsO_{1-x}F_x$ ($RE = Gd-Dy$, $x = 0-0.25$) samples was prepared using the SSM reaction mentioned above. In contrast to the reports in the literature using temperatures between 1373–1473 K to prepare $GdFeAsO_{1-x}F_x$ via conventional solid state reactions, a maximum temperature of 1223 K was applied regarding the SSM reaction used here. Fig-

Figure 3.13 displays the X-ray diffraction patterns of the $REFeAsO$ ($RE = \text{Gd-Dy}$) samples. The main phases were identified as the desired 1111 phases, however some minor impurities ($< 5 \text{ wt}\%$ from Rietveld refinements) are present, which could be identified as Gd_2O_3 , Dy_2O_3 (marked with asterisks) and Fe_2As (marked with circles).

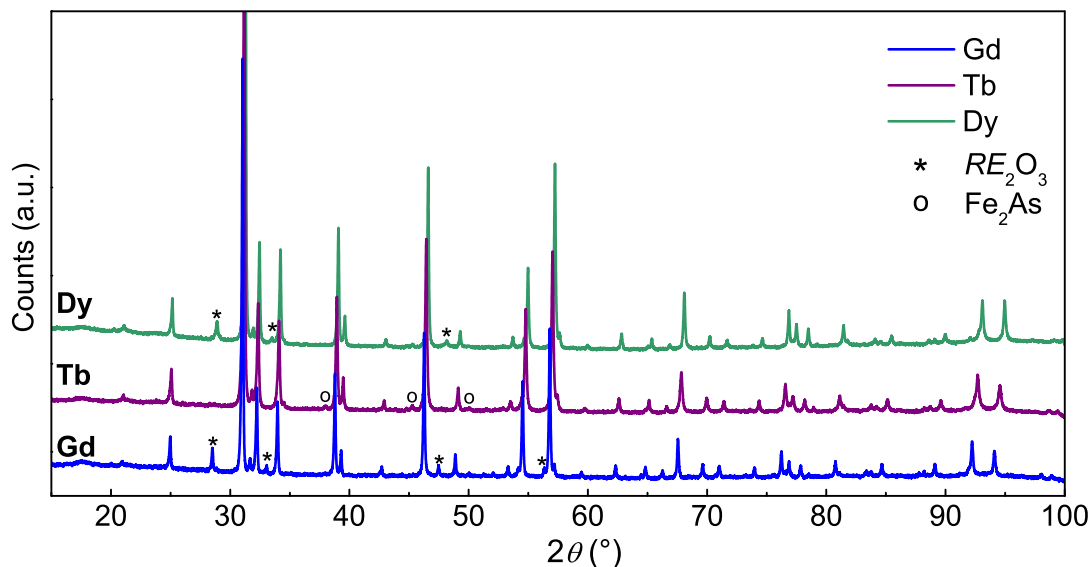


Figure 3.13 X-ray diffraction patterns of $REFeAsO$ ($RE = \text{Gd-Dy}$).

The lattice parameters a and c , as well as the unit cell volume, decrease with increasing atomic number, which is in line with the decreasing ionic radii of the rare-earth metals. The structural parameters from a consistent set of single-crystal data of $REFeAsO$ ($RE = \text{La, Ce, Pr, Nd, Sm, Gd, Tb}$) from the literature^[25] and the data obtained from Rietveld refinements of our samples are plotted against the rare-earth radii^[43] in Figure 3.14. Both, lattice parameters and the cell volume, shrink linearly with decreasing ionic radii. The values for $RE = \text{Gd}$ and Tb are in excellent agreement with single crystal data and those for Dy fit well in the series.

Rietveld refinements of samples with $x \geq 0.05$ revealed that impurity phases increase with increasing fluorine content. While samples with $x \leq 0.15$ for Gd and $x \leq 0.10$ for Tb and Dy include still more than $85 \text{ wt}\%$ of the 1111 compound, the amount of the desired phase significantly decreases after this point. The course of the lattice parameters as a function of x of these three series of samples is shown in Figure 3.15. The parameters a and c , as well as the cell volume, decrease linearly in the range $0 \leq x \leq 0.15$ for Gd and $0 \leq x \leq 0.10$ for Tb and Dy , and then remain almost constant. The a/c quotient increases very slightly with

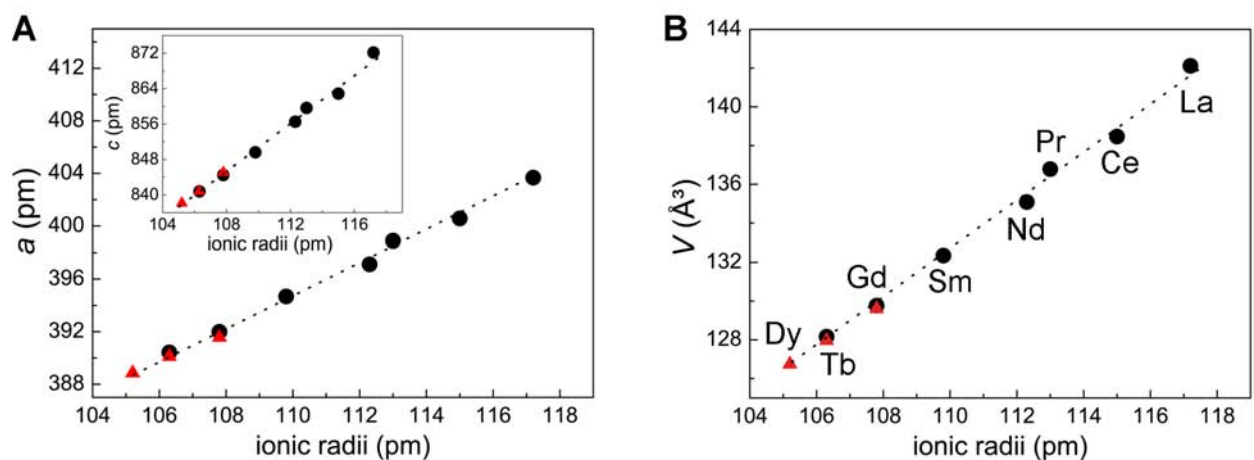


Figure 3.14 (A) Lattice parameters a and c (inset) and (B) cell volume V against the ionic radii of the rare-earth metals. Red triangles are data from the SSM reactions presented in this chapter. Black dots are data from the literature.^[25] Dotted lines are guides to the eye.

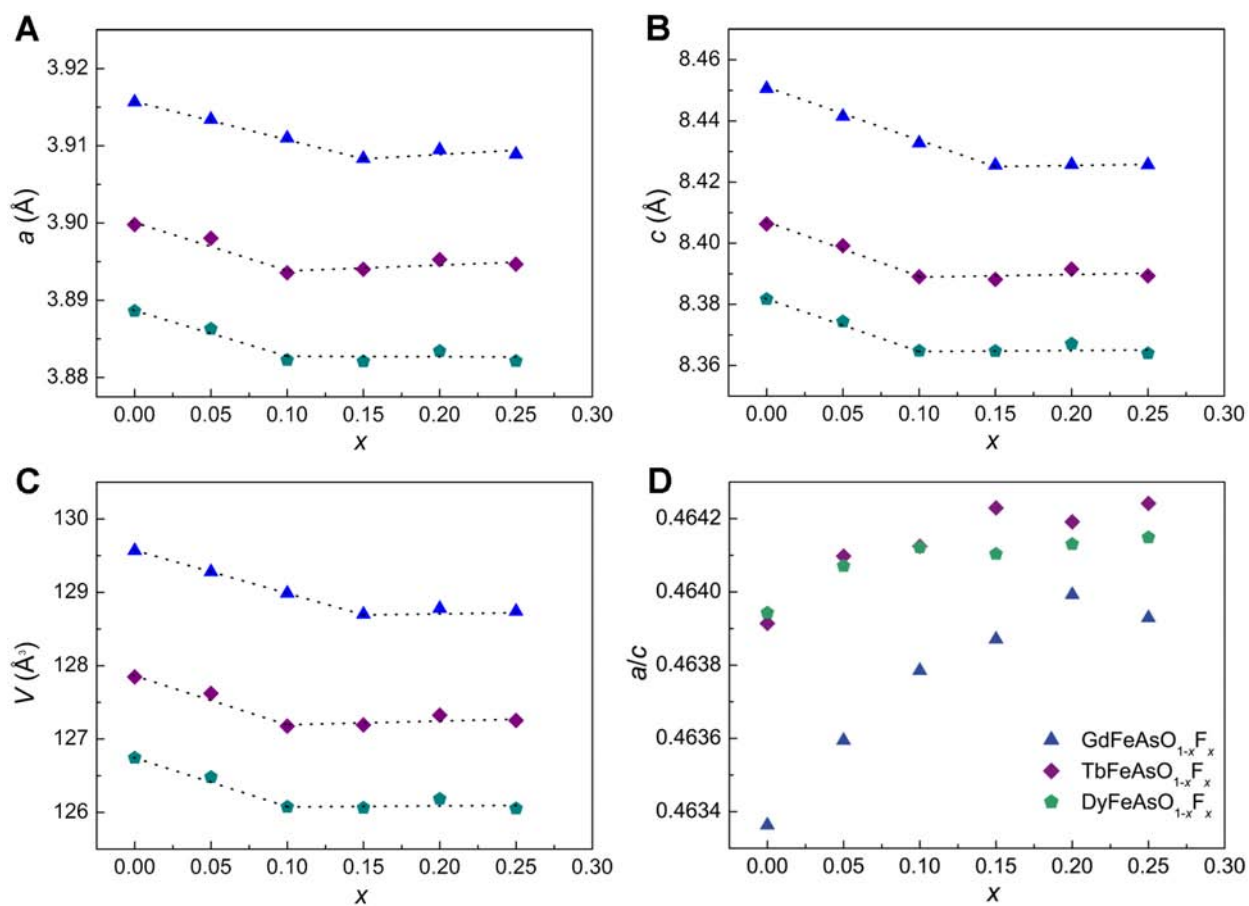


Figure 3.15 (A) Lattice parameter a , (B) lattice parameter c , (C) cell volume V and (D) quotient a/c against the fluorine content x of the series $REFeAsO_{1-x}F_x$ [$RE = \text{Gd}$ (blue), Tb (magenta), Dy (green)]. Dotted lines are guides to the eye.

increasing x , however the changes are smaller than 0.1 %. These findings indicate a saturation of the fluorine doping content which is in line with the increased formation of impurity phases when $x \geq 0.10$ – 0.15 . However, in case of the Gd series, we observe considerably smaller values of a , c and V compared to a reported series in the literature.^[38] A reason could be the use of significantly lower reaction temperatures (1223 vs 1393 K) accompanied with a reduced loss of fluorine in the samples, which enables a more effective introducing of fluorine into the system. As expected, in the case of $RE = \text{Tb}$ and Dy , our values for a , c and V are significantly higher (≈ 2 – 3 %) compared to values from high pressure syntheses reported in the literature.^[12,40]

Magnetization Measurements

Magnetic susceptibility measurements were performed to determine T_c and the superconducting volume fraction. AC-susceptibility data of $RE\text{FeAsO}_{1-x}\text{F}_x$ ($RE = \text{Gd}$ – Dy) are shown in Figure 3.16 (A–C). Similar to measurements from the literature^[36], a paramagnetic background is visible at temperatures $T > T_c$, which can be attributed to either impurity phases or to the magnetic moments of the rare-earth metal in $RE\text{FeAsO}_{1-x}\text{F}_x$. Bulk superconductivity of the Gd-samples is observed for $x \geq 0.10$. T_c increases with increasing fluorine content from 25.3 K for $x = 0.10$ to 50.3 K for $x = 0.25$. The high T_c is, to our best knowledge, the highest critical temperature observed for $\text{GdFeAsO}_{1-x}\text{F}_x$ samples synthesized under ambient pressure. This value is ≈ 6 K higher than the value from previous reports^[37] and only 4 K lower than for $\text{GdFeAsO}_{1-\delta}$ ^[39] synthesized under high pressure. Interestingly, T_c slightly increases in the range $0.15 \leq x \leq 0.25$, which indicates small but continuously electron doping in spite of almost unchanged values of the cell parameters. Data of $\text{TbFeAsO}_{1-x}\text{F}_x$ show bulk superconductivity at $T_c = 27.1$ K for $x = 0.15$ and traces of superconductivity with slightly higher T_c for $x = 0.20$ and 0.25 . Similar observations can be made for $RE = \text{Dy}$, where bulk superconductivity at 15.6 K is present for $x = 0.15$ and traces of superconductivity for $x = 0.10$, 0.20 and 0.25 . A significant kink arises at ≈ 6.6 K, which is probably due to magnetic ordering of the magnetic moments of Dy in $RE\text{FeAsO}_{1-x}\text{F}_x$ or in a Dy-containing impurity phase (e.g. DyOF, DyAs). The maximum values of T_c for samples with $RE = \text{Tb}$ and Dy are significantly lower than values from high pressure syntheses as shown in Figure 3.16 (D). Just as suggested for the solid solutions $\text{La}_{1-x}\text{RE}_x\text{FeAsO}_{0.80}\text{F}_{0.20}$, the results obtained for the late rare-earth compounds here lead to the conclusion that T_c

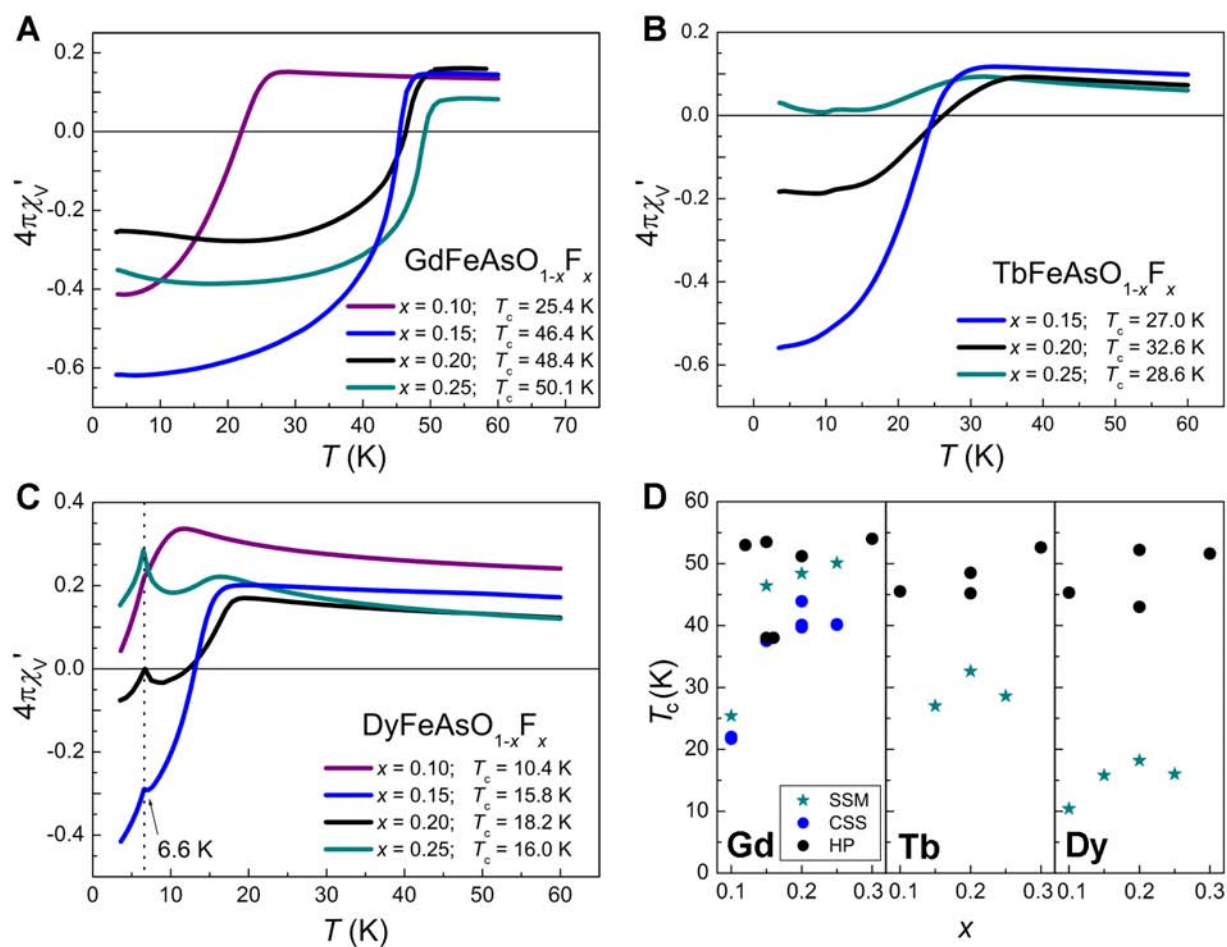


Figure 3.16 AC-susceptibility plots of $REFeAsO_{1-x}F_x$ with (A) Gd, (B) Tb and (C) Dy. (D) Comparison of T_c against the fluorine content x of samples synthesized by solid-state metathesis reactions (SSM), conventional solid state syntheses (CSS)^[36-38] and high pressure syntheses (HP)^[12,39,40].

cannot be controlled alone by the charge carrier density and that structural parameters may play a crucial role. Therefore, a reason for the low T_c in our samples with Tb and Dy could be found in the unit cell size. In contrast to conventional solid state synthesis methods at ambient pressure, a further shrinkage of the lattice parameters for $x > 0.10$ is possible by applying high pressures, which may also enable the introduction of more fluorine in the system. However, the presented results revealed bulk superconductivity of $TbFeAsO_{0.85}F_{0.15}$ and $DyFeAsO_{0.85}F_{0.15}$ synthesized via a conventional solid state metathesis reaction at ambient pressure for the first time.

3.4 Conclusion

Superconducting samples of $LaFeAsO_{1-x}F_x$ emerge in the range $0.05 \leq x \leq 0.15$, however samples with a higher fluorine content up to $x = 0.40$ were increasingly impure and non superconducting upon electron over-doping. Remarkably, superconductivity re-emerges in the solid solution $La_{1-x}RE_xFeAsO_{0.8}F_{0.2}$ ($RE = Pr, Nd, Sm$) at $x \geq 0.10$ in spite of constant electron doping. T_c is strongly dependent on the unit cell volume and raises with decreasing volume. Samples of $SmFeAsO_{0.85}F_{0.15}$ were prepared and sintered at different temperatures to investigate the magnitude of J_c . Global critical current densities were estimated from the Bean model to be 200–250 A/cm² and intragranular critical current densities in the range 10^6 – 10^7 A/cm² at 5 K. A series of the $REFeAsO_{1-x}F_x$ ($RE = Gd$ – Dy) samples have been prepared and bulk superconductivity up to 50.3 K was observed for $GdFeAsO_{1-x}F_x$, which is the highest value for Gd-1111 compounds without using high pressure synthesis methods. T_c of the samples with $RE = Tb$ and Dy are significantly lower than those of high pressure synthesized samples from the literature, whereat we found a large discrepancy in terms of lattice parameters to our samples. Therefore, we infer that T_c cannot be controlled alone by the charge carrier density and suggest that structural parameters may play a decisive role in the whole 1111-family.

3.5 References

- [1] Y. Kamihara, T. Watanabe, M. Hirano, H. Hosono, *J. Am. Chem. Soc.* **2008**, *130*, 3296.
- [2] T. Nomura, S. W. Kim, Y. Kamihara, M. Hirano, P. V. Sushko, K. Kato, M. Takata, A. L. Shluger, H. Hosono, *Supercond. Sci. Technol.* **2008**, *21*, 125028.
- [3] I. I. Mazin, D. J. Singh, M. D. Johannes, M. H. Du, *Phys. Rev. Lett.* **2008**, *101*, 057003.
- [4] G. F. Chen, Z. Li, D. Wu, G. Li, W. Z. Hu, J. Dong, P. Zheng, J. L. Luo, N.-L. Wang, *Phys. Rev. Lett.* **2008**, *100*, 247002.
- [5] Z.-A. Ren, J. Yang, W. Lu, W. Yi, G.-C. Che, L.-L. Sun, Z.-X. Zhao, *Mat. Res. Innov.* **2008**, *12*, 105.
- [6] Z.-A. Ren, J. Yang, W. Lu, X.-L. Shen, Z.-C. Li, G.-C. Che, X.-L. Dong, L.-L. Sun, F. Zhou, Z.-X. Zhao, *EPL* **2008**, *82*, 57002.
- [7] X. H. Chen, T. Wu, G. Wu, R. H. Liu, H. Chen, D. F. Fang, *Nature* **2008**, *453*, 761.
- [8] M. Fujioka, S. J. Denholme, T. Ozaki, K. Deguchi, S. Demura, H. Hara, T. Watanabe, H. Takeya, T. Yamaguchi, H. Kumakura, Y. Takano, *Supercond. Sci. Technol.* **2013**, *26*, 085023.
- [9] V. M. Dmitriev, I. E. Kostyleva, E. P. Khlybov, A. J. Zaleski, A. V. Terekhov, L. F. Rybaltchenko, E. V. Khristenko, L. A. Ishchenko, O. E. Omelyanovskiy, A. V. Sadakov, *Low. Temp. Phys.* **2009**, *35*, 517.
- [10] G.-F. Chen, L. Zheng, D. Wu, J. Dong, G. Li, W.-Z. Hu, P. Zheng, J.-L. Luo, N.-L. Wang, *Chin. Phys. Lett.* **2008**, *6*, 2235.
- [11] T. Hanna, Y. Muraba, S. Matsuishi, N. Igawa, K. Kodama, S.-i. Shamoto, H. Hosono, *Phys. Rev. B* **2011**, *84*, 024521.
- [12] J.-W. G. Bos, G. B. S. Penny, J. A. Rodgers, D. A. Sokolov, A. D. Huxley, J. P. Attfield, *Chem. Commun.* **2008**, *31*, 3634.
- [13] W. Lu, X.-L. Shen, J. Yang, Z.-C. Li, W. Yi, Z.-A. Ren, X.-L. Dong, G.-C. Che, L.-L. Sun, F. Zhou, Z.-Z. Zhao, *Solid State Commun.* **2008**, *148*, 168.
- [14] S. Iimura, S. Matsuishi, H. Sato, T. Hanna, Y. Muraba, S. W. Kim, J. E. Kim, M. Takata, H. Hosono, *Nat. Commun.* **2012**, *3*, 943.

- [15] S. Matsuishi, T. Hanna, Y. Muraba, S. W. Kim, J. E. Kim, M. Takata, S.-i. Shamoto, R. I. Smith, H. Hosono, *Phys. Rev. B* **2012**, *85*, 014514.
- [16] H. Hosono, *private communication* **2016**.
- [17] J. Prakash, S. J. Singh, S. Patnaik, A. K. Ganguli, *J. Phys.: Condens. Matter* **2009**, *21*, 175705.
- [18] M. Xu, F. Chen, C. He, H.-W. Ou, J.-F. Zhao, D.-L. Feng, *Chem. Mater.* **2008**, *20*, 7201.
- [19] Y.-k. Li, X. Lin, Q. Tao, H. Chen, C. Wang, L.-J. Li, Y.-K. Luo, M. He, Z.-W. Zhu, G.-H. Cao, Z.-A. Xu, *Chin. Phys. Lett.* **2009**, *26*, 017402.
- [20] C. Wang, L. Li, S. Chi, Z. Zhu, Z. Ren, Y. Li, Y. Wang, X. Lin, Y. Luo, S. Jiang, X. Xu, G. Cao, Z.-A. Xu, *EPL* **2008**, *83*, 67006.
- [21] L.-J. Li, Y.-K. Li, Z. Ren, Y.-K. Luo, X. Lin, M. He, Q. Tao, Z.-W. Zhu, G.-H. Cao, Z.-A. Xu, *Phys. Rev. B* **2008**, *78*, 132506.
- [22] Y. Luo, X. Lin, Y. Li, Q. Tao, L. Li, Z. Zhu, G. Cao, Z. A. Xu, *Int. J. Mod. Phys. B* **2010**, *26*, 1250207.
- [23] R. Frankovsky, A. Marchuk, R. Pobel, D. Johrendt, *Solid State Chem.* **2012**, *152*, 632.
- [24] S. Wakimoto, K. Kodama, M. Ishikado, M. Matsuda, R. Kajimoto, M. Arai, K. Kakurai, F. Esaka, A. Iyo, H. Kito, H. Eisaki, S.-i. Shamoto, *J. Phys. Soc. Jpn.* **2010**, *79*, 074715.
- [25] F. Nitsche, A. Jesche, E. Hieckmann, T. Doert, M. Ruck, *Phys. Rev. B* **2010**, *82*, 134514.
- [26] C. Senatore, R. Flükiger, M. Cantoni, G. Wu, R. H. Liu, X. H. Chen, *Phys. Rev. B* **2008**, *78*, 054514.
- [27] P. J. W. Moll, R. Puzniak, F. Balakirev, K. Rogacki, J. Karpinski, M. Zhigadlo, B. Batlogg, *Nature Mater.* **2010**, *9*, 628.
- [28] J. D. Weiss, C. Tarantini, J. Jiang, F. Kametani, A. A. Polyanskii, D. C. Larbalestier, E. E. Hellstrom, *Nature Mater.* **2012**, *11*, 682.
- [29] A. Malagoli, E. Wiesenmayer, S. Marchner, D. Johrendt, A. Genovese, M. Putti, *Supercond. Sci. Tech.* **2015**, *28*, 095015.
- [30] K.-H. Müller, C. Andrikidis, H. K. Lui, S. X. Dou, *Phys. Rev. B* **1994**, *50*, 10218.

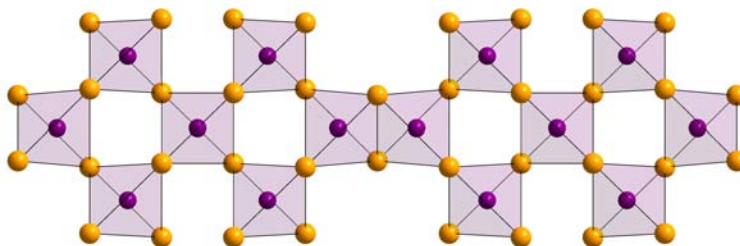
- [31] Q. Zhang, H. Lin, P. Yuan, X. Zhang, C. Yao, D. Wang, C. Dong, Y. Ma, S. Awaji, K. Watanabe, *Supercond. Sci. Technol.* **2015**, *28*, 105005.
- [32] H. Lin, C. Yao, X. Zhang, C. Dong, H. Zhang, D. Wang, Q. Zhang, Y. Ma, S. Awaji, K. Watanabe, H. Tian, J. Li, *Sci. Rep.* **2014**, *4*, 6944.
- [33] A. Yamamoto, A. A. Polyanskii, J. Jiang, F. Kametani, C. Tarantini, F. Hunte, J. Jaroszynski, E. E. Hellstrom, P. J. Lee, A. Gurevich, D. C. Larbalestier, Z. A. Ren, J. Yang, X. L. Dong, W. Lu, Z. X. Zhao, *Supercond. Sci. Technol.* **2008**, *21*, 095008.
- [34] A. Yamamoto, J. Jiang, C. Tarantini, N. Craig, A. A. Polyanskii, F. Kametani, F. Hunte, E. E. Jaroszynski, J. Hellstrom, D. C. Larbalestier, R. Jin, A. S. Sefat, M. A. McGuire, B. C. Sales, D. K. Christen, D. Mandrus, *Appl. Phys. Lett.* **2008**, *92*, 252501.
- [35] A. Yamamoto, J. Jiang, F. Kemtani, A. Polynaskii, E. Hellstrom, D. Larbalestier, A. Martinelli, A. Palenzona, M. Tropeano, M. Putti, *Supercond. Sci. Technol.* **2011**, *24*, 045010.
- [36] Y. J. Cui, Y. L. Chen, C. H. Cheng, Y. Yang, Y. Zhang, Y. Zhao, *J. Supercond. Nov. Magn.* **2010**, *23*, 625.
- [37] K. Kadowaki, T. Goya, T. Mochiji, S. V. Chong, *J. Phys. Conf. Ser.* **2008**, *150*, 052088.
- [38] Y. J. Cui, Y. L. Chen, C. H. Cheng, Y. Yang, Y. Z. Wang, Y. C. Li, Y. Zhao, *J. Phys. Chem. Solids* **2011**, *72*, 449.
- [39] K. Miyazawa, K. Kihou, P. M. Shirage, C.-H. Lee, H. Kito, H. Eisaki, A. Iyo, *J. Phys. Soc. Jpn.* **2009**, *78*, 034712.
- [40] J. Yang, X.-L. Shen, W. Lu, W. Yi, Z.-C. Li, Z.-A. Ren, G.-C. Che, X.-L. Dong, L.-L. Sun, F. Zhou, Z.-X. Zhao, *New J. Phys.* **2008**, *11*, 025005.
- [41] Y. Luo, Q. Tao, Y. Li, X. Lin, L. Li, G. Cao, Z.-a. Xu, Y. Xue, H. Kaneko, A. V. Savinkov, H. Suzuki, C. Fang, J. Hu, *Phys. Rev. B* **2009**, *80*, 224511.
- [42] Y. Luo, X. Lin, Y. Li, Q. Tao, L. Li, Z. Zhu, G. Cao, Z. A. Xu, *Int. J. Mod. Phys. B* **2012**, *26*, 1250207.
- [43] R. D. Shannon, *Acta Cryst.* **1976**, *32*, 751.

Chapter 4

Flux Mediated Synthesis of New Quaternary *RE-T-Se-O* Compounds

4.1 Flux Synthesis, Modulated Crystal Structures, and Physical Properties of $RE_2O_2MnSe_2$ ($RE = La, Ce$)

S. Peschke, F. Nitsche, and D. Johrendt



Parts published in: *Z. Anorg. Allg. Chem.* **2015**, *641*, 529–536.

Copyright 2015, Wiley-VCH Verlag GmbH & Co. KGaA, Weinheim.

4.1.1 Abstract

The selenide oxides $RE_2O_2MnSe_2$ ($RE = La, Ce$) were synthesized by heating RE_2O_3 , RE , Mn , and Se in a NaI/KI flux at 1073 K, and their modulated crystal structures determined by (low temperature) X-ray single crystal and powder diffraction $\{Cmme(\alpha 0 \frac{1}{2}) 0 s 0, Z = 2, La_2O_2MnSe_2: a = 573.7(1) \text{ pm}, b = 573.7(1) \text{ pm}, c = 915.0(1) \text{ pm}, \mathbf{q} = [\frac{1}{5}, 0, \frac{1}{2}]; Ce_2O_2MnSe_2: a = 568.6(1) \text{ pm}, b = 568.3(1) \text{ pm}, c = 910.9(1) \text{ pm}, \mathbf{q} = [0.1573(2), 0, \frac{1}{2}]\}$. The structures are related to the $ZrCuSiAs$ -type structure with ordered vacancies at the manganese sites. The resulting modulations of the checkerboard pattern in the $[MnSe_2]^{2-}$ layers can be approximated by $5\sqrt{2}a_{\text{subcell}} \times \sqrt{2}b_{\text{subcell}} \times 2c_{\text{subcell}}$ and $19\sqrt{2}a_{\text{subcell}} \times \sqrt{2}b_{\text{subcell}} \times 2c_{\text{subcell}}$ supercells in $La_2O_2MnSe_2$ and $Ce_2O_2MnSe_2$, respectively. Both compounds are insulators. The optical bandgap of $La_2O_2MnSe_2$ was determined to 2.13 eV from the Kubelka-Munk function. Magnetic measurements indicate antiferromagnetic ordering of the Mn^{2+} moments with Néel points well above room temperature, as known from related manganese compounds.

4.1.2 Introduction

The discovery of high- T_c superconductivity in iron pnictides and iron selenides with critical temperatures up to 56 K has revived the search for new superconducting materials with similar building blocks.^[1] Among the different structure types of iron arsenide families,

compounds with the tetragonal ZrCuSiAs-type structure such as $REOFeAs$ (RE = rare-earth metal) exhibit the highest critical temperatures. Substitution of arsenic in $REOTAs$ (T = divalent transition metal) by selenium leads to compounds $RE_2O_2TSe_2$ with vacancies at the transition metal sites. There are only few examples known so far which retain a ZrCuSiAs-related structure. Among them, $La_2O_2CdSe_2$ ^[2] exhibits $[CdSe_2]^{2-}$ layers with a checkerboard-like arrangement of corner-sharing $CdSe_4$ -tetrahedra, $RE_2O_2FeSe_2$ (RE = La, Ce)^[3,4] contains chains of edge-sharing $FeSe_4$ -tetrahedra, and $La_2O_2ZnSe_2$ ^[5] has a mixture of both, stripe-like and checkerboard-like motifs. Furthermore, *Ijjaali* et al. assumed randomly distributed vacancies in $Ce_2O_2MnSe_2$.^[6] Beside ZrCuSiAs-type variants, there are also compounds like β - $La_2O_2TSe_2$ (T = Mn, Fe), which crystallize in a different type with sheets of TSe_n polyhedra, separated by La_2O_2Se blocks.^[7] Recently, we found new polymorphs of $RE_2O_2FeSe_2$ (RE = La, Ce)^[3] which crystallize in the $Pb_2HgCl_2O_2$ -structure type^[8] at lower reaction temperatures. During our recent investigations into ZrCuSiAs-related compounds with magnetic transition metals, we obtained crystals and almost single phase polycrystalline samples of $La_2O_2MnSe_2$ and $Ce_2O_2MnSe_2$. Single-crystal and powder X-ray diffraction experiments revealed motifs of transition metal vacancy ordering with higher complexity. These are described as either commensurate or incommensurate modulations of the checkerboard pattern for $La_2O_2MnSe_2$ and $Ce_2O_2MnSe_2$, respectively.

4.1.3 Experimental Details

Single crystals of $La_2O_2MnSe_2$ were prepared by the reaction of La_2O_3 (99.999 %, CHEMPUR, heated to 673 K prior to use), La (99.9 %, SMART ELEMENTS), Mn (99.99 %, ALFA AESAR) and Se (99.999 %, CHEMPUR) in a 2:2:3:6 ratio. Crystals of $Ce_2O_2MnSe_2$ were obtained by the reaction of CeO_2 (99.9 %, ALFA-AESAR, heated to 673 K prior to use), Ce (99.9 %, CHEMPUR), Mn (99.99 %, ALFA AESAR) and Se (99.999 %, CHEMPUR) in a 1:1:1:2 ratio. The starting materials (0.25 g) were mixed intimately in an agate mortar and sandwiched in a glassy carbon crucible between 0.75 g of a eutectic NaI/KI mixture (mass ratio 0.6:0.4, dried in dynamic vacuum at 673 K) as flux. The crucibles were sealed in argon filled silica tubes and heated to 1073 K with a rate of 100 K h⁻¹, kept at this temperature for four days and slowly cooled down to 923 K with a cooling rate of 5 K h⁻¹. The crucibles were quenched in air from 923 K and the reaction mixture was washed with deionized water and dried in

air. The resulting crystals were bright red, transparent plates. Besides numerous single crystals, the NaI/KI flux method also leads to almost single phase polycrystalline samples of $\text{La}_2\text{O}_2\text{MnSe}_2$ (brick-red) and $\text{Ce}_2\text{O}_2\text{MnSe}_2$ (purple) (purity > 90 wt%). The compounds are stable in air for months. Single-crystal X-ray diffraction data was collected with a Bruker D8 QUEST (fixed- χ goniometer, Mo- K_α , $1\mu\text{S}$ with HE-LIOS multi-layer optics, PHOTON 100 detector, closed-cycle helium cryostat). Reflection intensity integrations, data reductions, and multi-scan absorption corrections were done with APEX2^[9] and SADABS^[10]. The structures were solved with Jana2006^[11]. X-ray powder diffraction patterns were recorded between 10 K and 300 K using a Huber G670 diffractometer with $\text{CuK}_{\alpha 1}$ or $\text{CoK}_{\alpha 1}$ radiation (Ge(111)-monochromator, closed-cycle helium cryostat). Rietveld refinements were done with TOPAS^[12] and with Jana2006^[11]. Susceptibility measurements were performed with a MPMS-XL SQUID magnetometer (Quantum Design Inc.). Diffuse reflectance spectra were measured with powder samples with a UV/Vis/NIR Varian Cary 500 spectrophotometer (200–800 nm). The spectra were converted to absorption spectra based on the Kubelka-Munk theory^[13] to determine the optical bandgap.

4.1.4 Results and Discussion

4.1.4.1 $\text{La}_2\text{O}_2\text{MnSe}_2$

Conventional high-temperature synthesis starting from rare-earth metal oxide, rare-earth metal, manganese, and selenium powder leads to mixtures of La_2SeO_2 , MnSe , together with a minor fraction (< 10 wt%) of the desired compound. In contrast, almost single phase samples (> 90 wt%) with well-shaped crystals are obtained by reacting the same starting materials in a NaI/KI flux (Fig. 4.1). Energy dispersive X-ray spectroscopy (EDX) of the single crystals (Fig. 4.2) revealed the averaged atomic percentages La 27.4(3) %, O 31.5(8) %, Mn 12.1(1) % and Se 29.0(6) %, which corresponds to $\text{La}_{2.0}\text{O}_{2.3(1)}\text{Mn}_{0.9(1)}\text{Se}_{2.1(1)}$ in agreement with the nominal composition (Table 4.1). Characteristic emission lines of neither potassium or sodium nor iodine were observed, thus inclusion or incorporation of the flux material can be excluded, as shown in Figure 4.2.

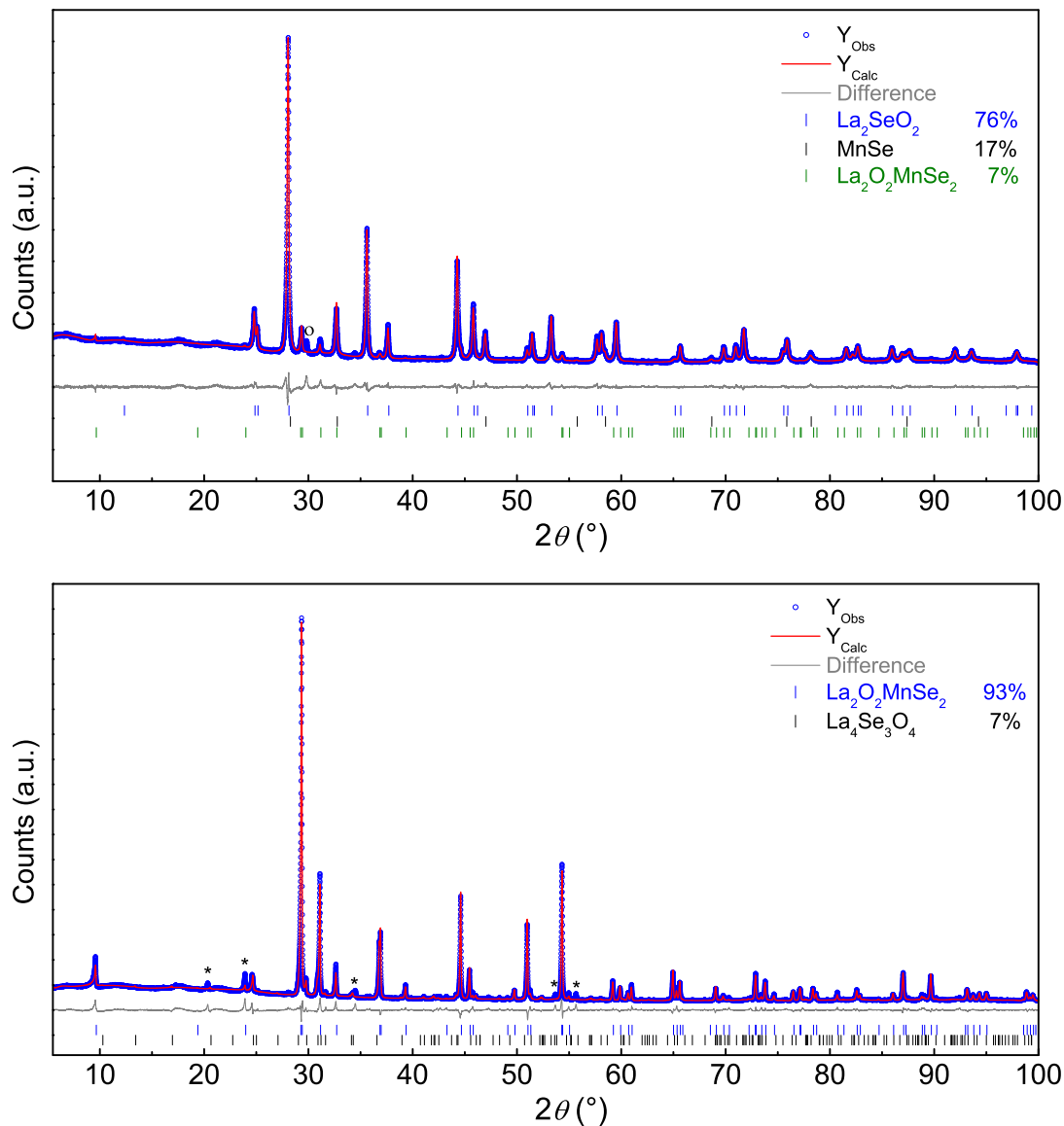


Figure 4.1 X-ray powder patterns (blue) and Rietveld fits (red) of La₂O₂MnSe₂ obtained by (top) conventional solid-state reaction and (bottom) NaI/KI-flux. The structure of La₂O₂MnSe₂ was refined in the tetragonal space group $P4/nmm$. Reflections marked with o (top) are of an unknown side phase. Those marked with asterisks (bottom) are superstructure reflections of La₂O₂MnSe₂.

Crystal Structure

For $\text{La}_2\text{O}_2\text{MnSe}_2$ one expects a defect ZrCuSiAs -type structure with slabs of edge-sharing OLa_4 -tetrahedra stacked alternating with slabs of MnSe_4 -tetrahedra, in which the Mn-site is half occupied. Refinements of X-ray powder data with this model ($P4/nmm$, $a \approx 405$ pm, $c \approx 914$ pm) resulted in good fits to the main peaks (Fig. 4.1), but additional reflections, marked with asterisks, remained unindexed. The intensities of these reflections relative to main peaks is constant in different samples, thus they do not belong to an impurity phase, but are superstructure reflections of $\text{La}_2\text{O}_2\text{MnSe}_2$.

Table 4.1 EDX data /at% of $\text{La}_2\text{O}_2\text{MnSe}_2$.

	La	Mn	Se	O
#1	27.38	11.98	29.64	31.00
#2	28.33	12.48	28.66	30.53
#3	26.88	12.13	30.02	30.97
#4	27.64	12.05	29.97	30.34
#5	26.70	11.71	26.88	34.71
Average	27.39	12.07	29.03	31.51
σ_{Average}	0.29	0.12	0.59	0.81

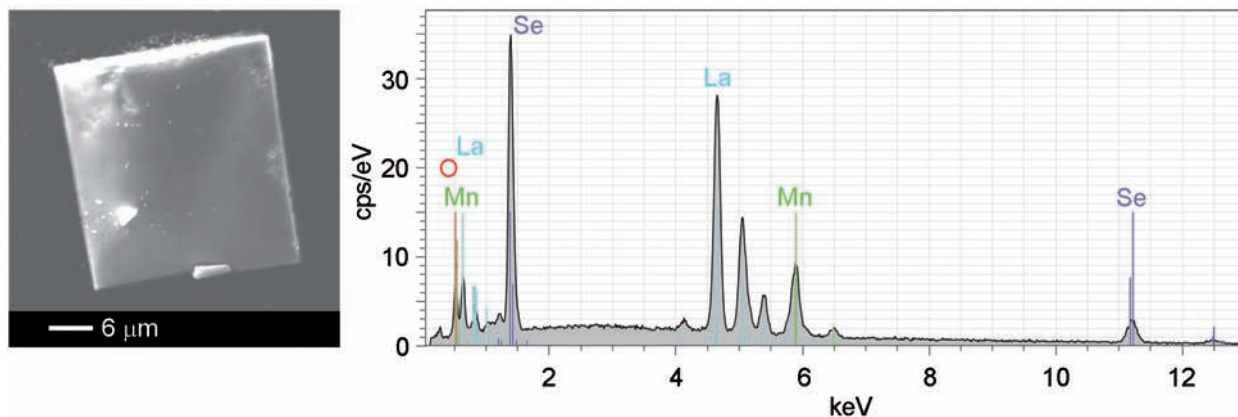


Figure 4.2 Typical plate-like single crystal (left) and EDX spectrum (right) of $\text{La}_2\text{MnSe}_2\text{O}_2$. Characteristic lines of the elements of the flux are not observed. The peak at ≈ 0.25 keV belongs to carbon from the adhesive conducting carbon film.

Single crystal X-ray diffraction experiments using a plate-like crystal (Fig. 4.2) confirmed the superstructure. As observed by *Ainsworth* et al. in selected area electron diffraction (SAED) images for similar compounds with Zn as transition metal, the tetragonal symmetry

($P4/nmm$) of the parent compound is lost and the substructure can be described in an orthorhombic cell with dimensions $\sqrt{2}a_{\text{subcell}} \times \sqrt{2}b_{\text{subcell}} \times c_{\text{subcell}}$.^[14] The superstructure can be described in the (3+1)D superspace group $Cmme(\alpha 0 \frac{1}{2})0s0$ with the modulation vector $\mathbf{q} = [\alpha a^* + 0b^* + \frac{1}{2}c^*]$. The inspection of the reciprocal space revealed additional satellite spots surrounding each Bragg position of the orthorhombic unit cell. These satellites, which also can be observed in the $hk\frac{1}{2}$ -layer (Fig. 4.3), were indexed as simple fractions of the reciprocal lattice vectors of the substructure ($\mathbf{q} = [\frac{1}{5}a^* + 0b^* + \frac{1}{2}c^*]$), which results in a commensurate supercell with the dimension $5\sqrt{2}a_{\text{subcell}} \times \sqrt{2}b_{\text{subcell}} \times 2c_{\text{subcell}}$. Indeed, refinement of α during the integration of the data gives a value close to $\frac{1}{5}$ [$\alpha = 0.196(1)$].

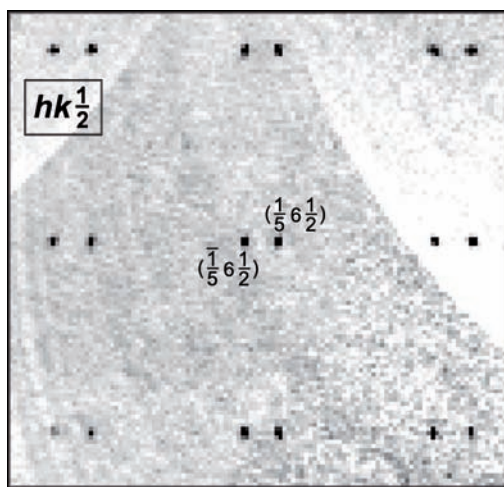


Figure 4.3 $hk\frac{1}{2}$ -layer with 1st order satellite reflections. The reflections can be described with $\mathbf{q} = [\frac{1}{5}, 0, \frac{1}{2}]$.

The structure of $\text{La}_2\text{O}_2\text{MnSe}_2$ was solved using the superspace group $Cmme(\alpha 0 \frac{1}{2})0s0$ with $\alpha = \frac{1}{5}$, $a = 573.7(1)$ pm, $b = 573.7(1)$ pm and $c = 915.0(1)$ pm. The modulation was described by first order harmonic functions for the positions of all atoms. Fourier maps (Fig. 4.4) show that the Mn site occupancy is strongly modulated, mainly along x_1 [x_i ($i = 1-4$) are the superspace axes]. Therefore, the occupancy parameter of manganese was modeled with a fixed crenel function with a length of 0.5 and the centre at 0.25, as arises from Figure 4.4. The Fourier maps of Figure 4.5 show that the positions of La, Se and O are mainly modulated along the x_2 direction. As refinement of the modulation vector gives a value close to $\frac{1}{5}$ within the standard deviation, the commensurate option was used to refine the structure. Transforming from (3+1)D superspace group to the 3D space group, there are three symmetry space groups along different t -sections: $I2cb$ (45), $Imcb$ (72) and $Ibca$ (73).

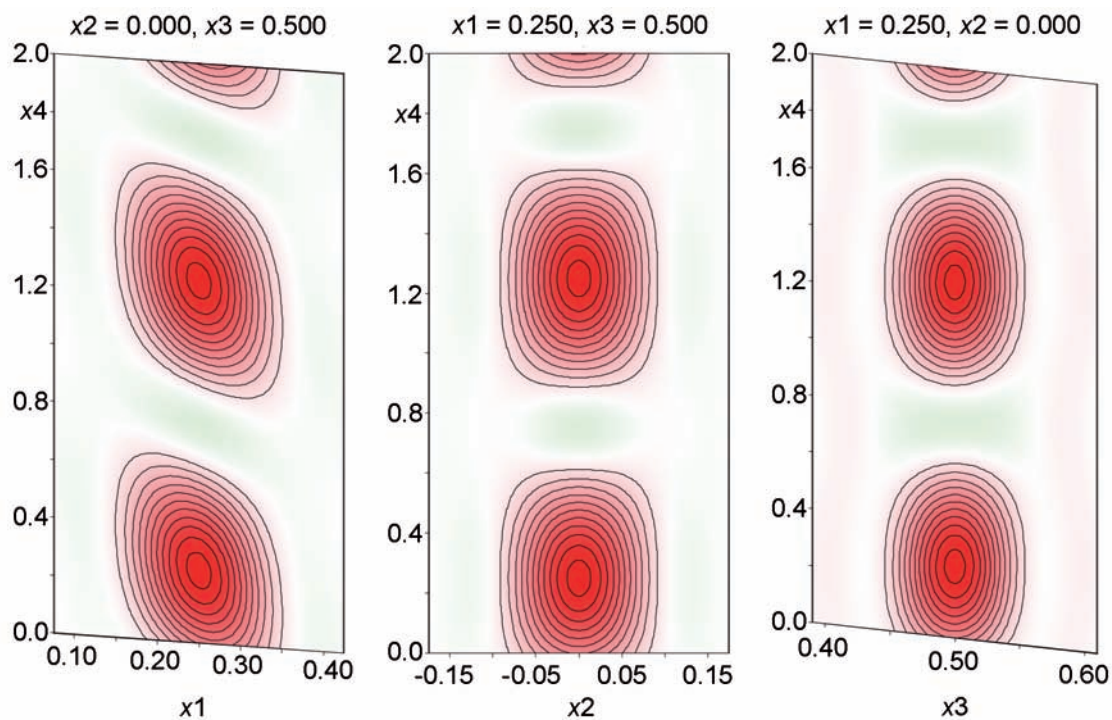


Figure 4.4 Fourier electron density maps of $\text{La}_2\text{O}_2\text{MnSe}_2$ from charge flipping. Center at Mn ($\frac{1}{4}, 0, \frac{1}{2}$).

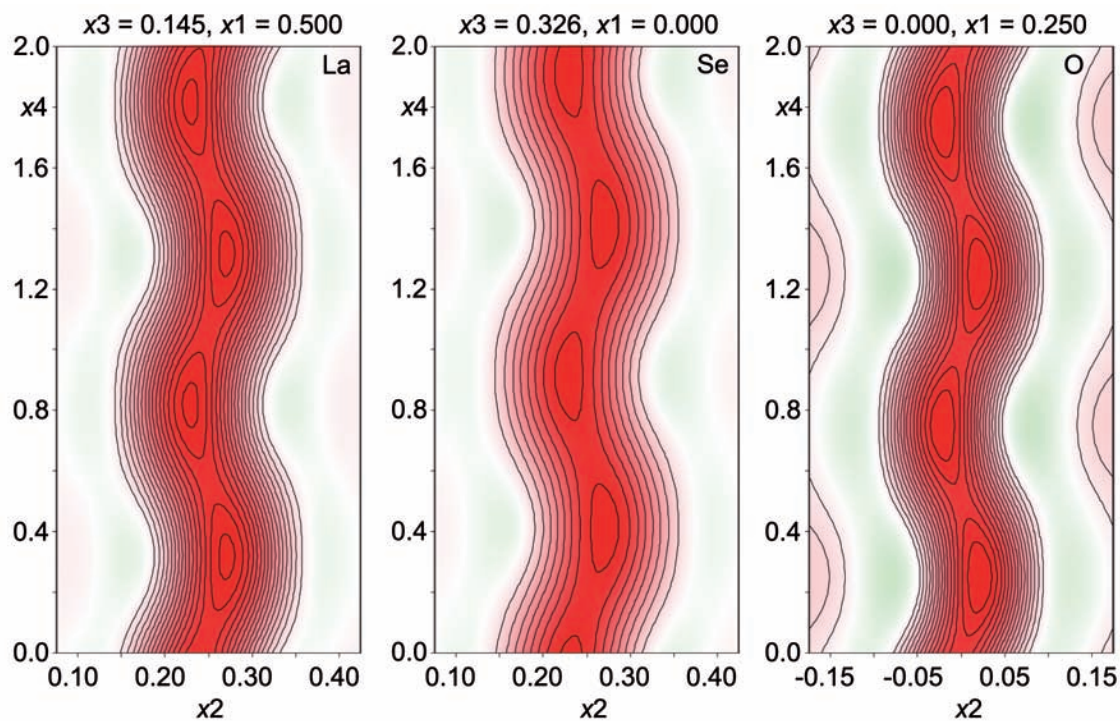


Figure 4.5 Fourier electron density maps of $\text{La}_2\text{O}_2\text{MnSe}_2$ from charge flipping. Center at La (left), Se (middle) and O (right).

Among these space groups, $Imcb$ ($t_0 = 0.05$) gives significantly better agreement with the experimental data than the others. Relevant crystallographic data are compiled in Table A.1. The modulated structure uncovers a so far unknown motif of ordered vacancies in the $[\text{MnSe}_2]^{2-}$ layer. The modulated $[\text{MnSe}_2]^{2-}$ layer consists of blocks of five corner-sharing $\text{MnSe}_{4/2}$ -tetrahedra which are separated by a pair of edge-sharing tetrahedra as shown in Figure 4.6 (B). The $[\text{MnSe}_2]^{2-}$ layers are stacked along the c axis in a way that tetrahedra of one layer fill the gaps of the layer above and vice versa. The distances between the manganese atoms (Fig. 4.7) in the edge-shared [311.9(1) pm] and corner-shared [400.2(1)–402.3(1) pm] tetrahedra are significantly longer than the bonds in manganese metal (273.4 pm). Mn-Se bond lengths vary from 255.8(1)–258.4(1) pm and La-O from 236.5(1)–238.1(1) pm.

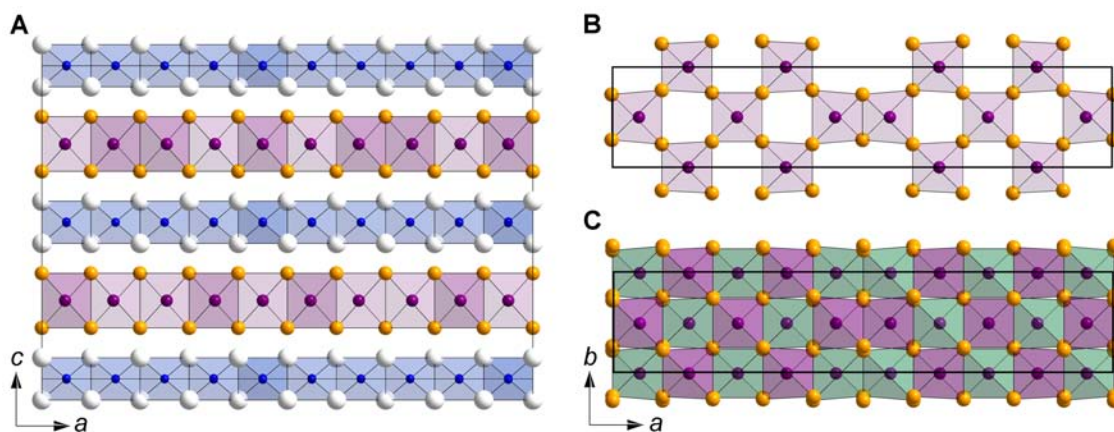


Figure 4.6 (A) Alternating layers of $\text{OLa}_{4/4}^-$ (blue) and $\text{MnSe}_{4/2}^-$ (purple) tetrahedra. Lanthanum in white, manganese in purple, selenium in orange and oxygen in blue. (B) $[\text{MnSe}_2]^{2-}$ layer of $\text{La}_2\text{O}_2\text{MnSe}_2$ along c . (C) Stacking of two $[\text{MnSe}_2]^{2-}$ layers. The second layer is coloured in green for clarity.

The $[\text{La}_2\text{O}_2]^{2+}$ layer is substantially smaller than the $[\text{MnSe}_2]^{2-}$ layer as can be roughly estimated from the effective ionic radii, which results in a size mismatch between the layers. One or both layers have to distort in order to reduce the strain in the ab -plane, which also gives rise to the observed modulation. Regarding the respective bond angles along t in Figure 4.8, the Se-Mn-Se bond angles vary from $102.9(1)$ – $119.4(1)^\circ$ and the La-O-La from $105.2(1)$ – $119.8(1)^\circ$. Se(1)-Mn-Se(4) and Se(2)-Mn-Se(3) bond angles are around 103° which is significantly smaller than the ideal tetrahedral angle of 109.5° . In contrast, Se(1)-Mn-Se(2) and Se(3)-Mn-Se(4) angles are considerable larger ($\approx 113^\circ$). This distortion leads to an elongation of the MnSe_4 -tetrahedra along c and to a compression in the ab -plane. The bond

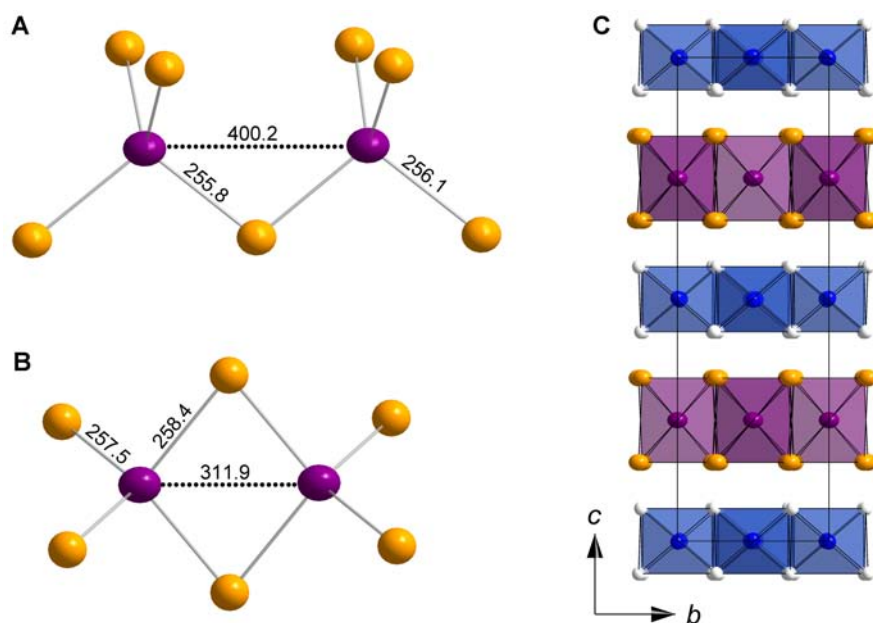


Figure 4.7 Selected distances (pm) in the (A) corner- and (B) edge-sharing tetrahedra. (C) Alternating $[\text{La}_2\text{O}_2]^{2+}$ and $[\text{MnSe}_2]^{2-}$ layers along a . Ellipsoids represent 99 % probability.

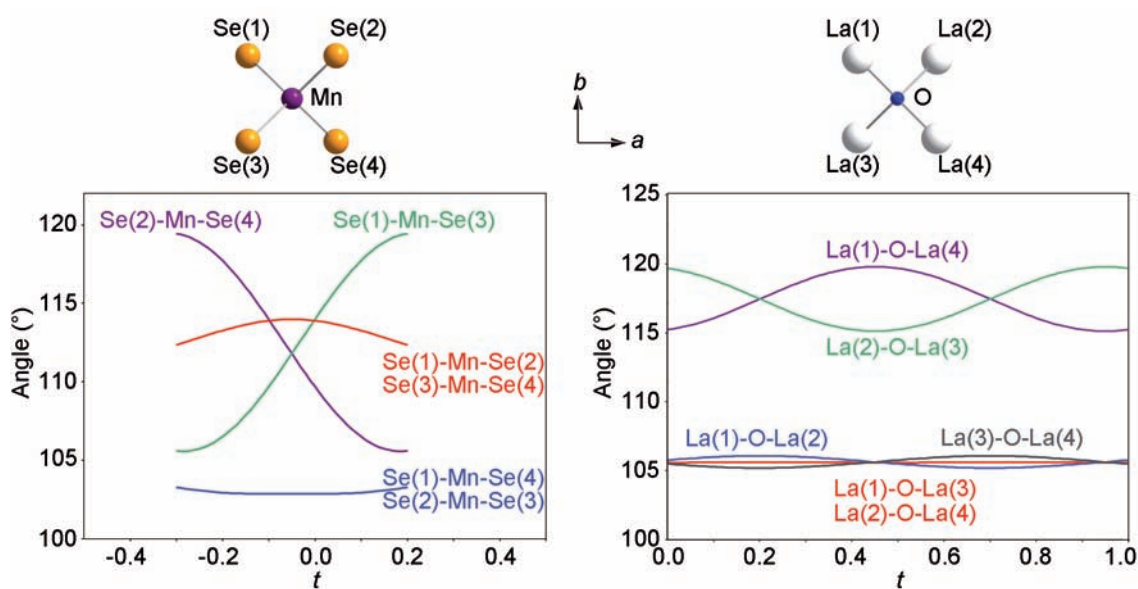


Figure 4.8 Se-Mn-Se and La-O-La bond angles in $\text{La}_2\text{O}_2\text{MnSe}_2$.

angles Se(1)-Mn-Se(3) and Se(2)-Mn-Se(4) are strongly modulated due to the displacement modulation of Mn in the ab plane and vary in a wide range from ≈ 106 – 119° . In contrast to the $[\text{MnSe}_2]^{2-}$ layer, the $[\text{La}_2\text{O}_2]^{2+}$ layer seems to be more rigid as the tetrahedral bond angle modulation is smaller. However, the La(1)-O-La(4) and La(2)-O-La(3) bond angles are around 115 – 120° and the La(1)-O-La(2) and La(3)-O-La(4) bond angles are around 105° , which is the other way around as in the MnSe_4 -tetrahedra. The contrary behaviour of these angles in the $[\text{La}_2\text{O}_2]^{2+}$ layer expands the OLa_4 -tetrahedra in the ab -plane and reduces, together with the compression of the MnSe_4 -tetrahedra, the strain between the two layers. The distortion of the two layers is visible by viewing the unit cell along a for instance, which is depicted in Figure 4.7 (C).

Subsequent refinements against X-ray powder data using the superspace group $Cmme(\alpha 0 \frac{1}{2})0s0$ resulted in good fits of both, the main (black) and superstructure reflections (green), as shown in Figure 4.9. The modulation vector component α was determined to be $\alpha = 0.200(2)$ at 300 K, which is in agreement with the data from single crystal experiments. To investigate the behaviour of α at low temperatures, a powder diffraction experiment at 10 K was recorded and analyzed (Fig. 4.10). The modulation vector of $\mathbf{q} = [0.201(5)a^* + 0b^* + \frac{1}{2}c^*]$ remains almost unchanged within the standard deviation. We made similar observations for low-temperature single crystal X-ray experiments at 100 K. Refinement of α during the integration of the data resulted in $\alpha = 0.196(1)$, which is close to $\frac{1}{5}$ and also in excellent agreement with the value of the room temperature measurement. Relevant crystallographic data of the measurement at 100 K are compiled in Table A.2.

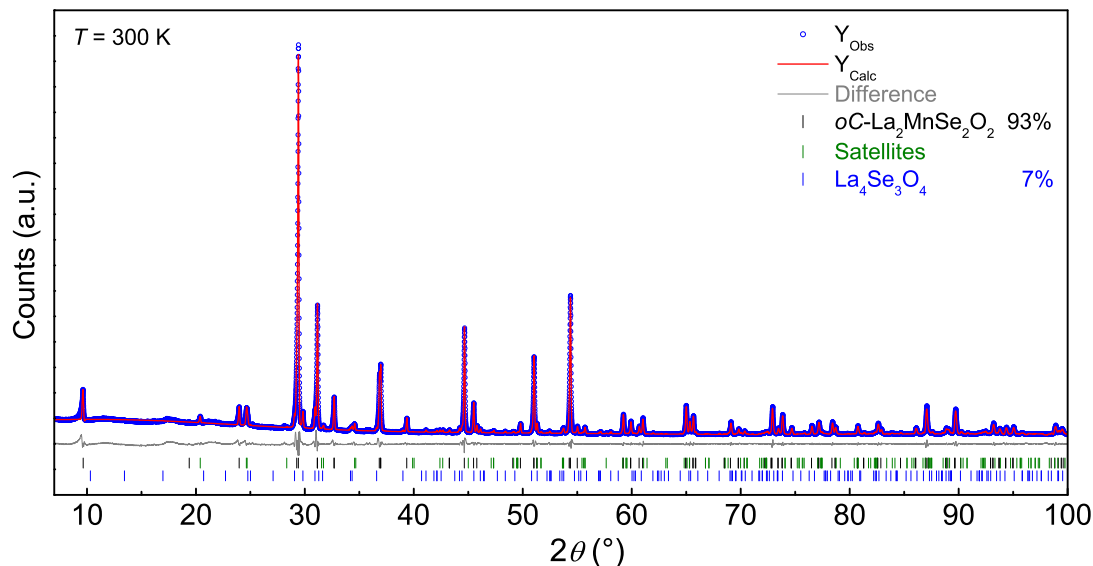


Figure 4.9 X-ray powder diffraction pattern of $\text{La}_2\text{O}_2\text{MnSe}_2$ (blue) at $T = 300$ K, with Rietveld fit (red) and difference curve (gray) using the modulated structure model with the superspace group $Cmme(\alpha 0 \frac{1}{2}) 0 s 0$ ($\mathbf{q} = [\frac{1}{5}, 0, \frac{1}{2}]$).

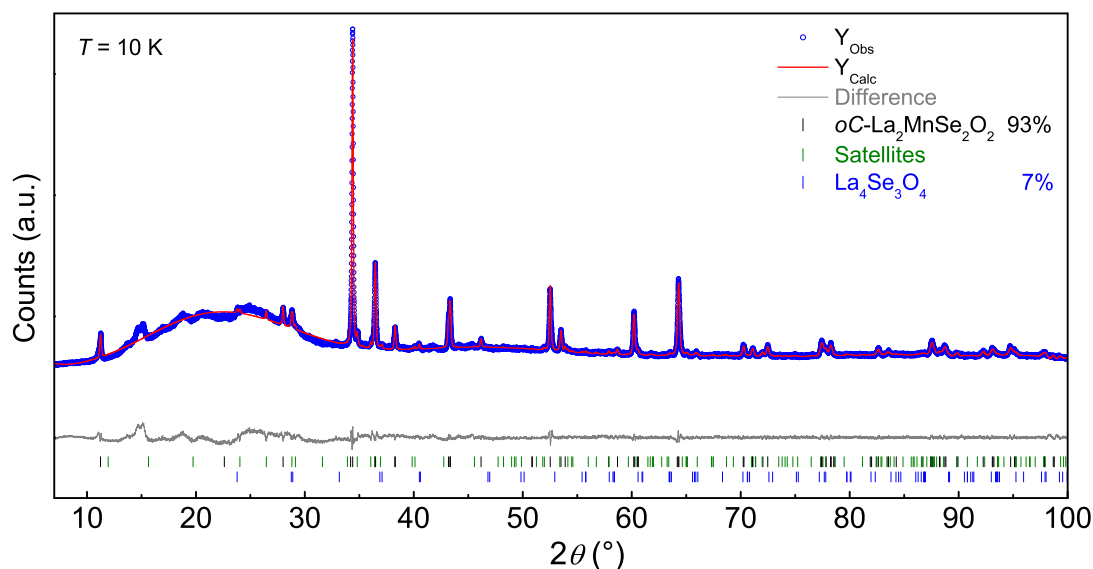


Figure 4.10 X-ray powder diffraction pattern of $\text{La}_2\text{O}_2\text{MnSe}_2$ (blue) at $T = 10$ K, with Rietveld fit (red) and difference curve (gray) using the modulated structure model with the superspace group $Cmme(\alpha 0 \frac{1}{2}) 0 s 0$ ($\mathbf{q} = [\frac{1}{5}, 0, \frac{1}{2}]$). The signals at $2\theta \approx 15^\circ$ and the increased background arise from frozen grease.

Magnetism

The magnetic susceptibility of $\text{La}_2\text{O}_2\text{MnSe}_2$ is weakly temperature dependent and shows no Curie-Weiss behavior between 300 and 1.8 K (Fig. 4.11 A). An increase below 40 K during the field cooled cycle may indicate ferromagnetic ordering. As the values of χ_{mol} are small, the anomaly is presumably not an effect of $\text{La}_2\text{O}_2\text{MnSe}_2$, but arises from traces of an unknown ferromagnetic impurity. Indeed magnetization isotherms at 300 and 1.8 K (Fig. 4.11 B) reveal no ferromagnetic ordering, and are consistent either with paramagnetism or with an antiferromagnetically ordered state. The small and weakly temperature dependent susceptibility suggests antiferromagnetic ordering of the Mn^{2+} moments already at room temperature, as it is known from related manganese compounds with ZrCuSiAs and ThCr_2Si_2 -type structures. However, given the complex crystal structure, the magnetic ordering pattern may also be much more complicated than the typical G- or C-types of the simple tetragonal compounds.

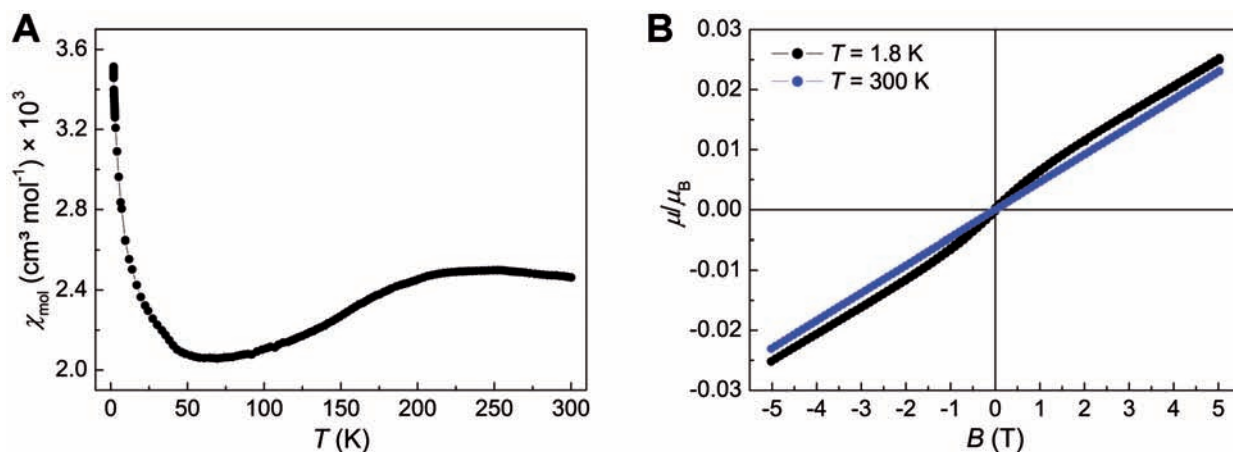


Figure 4.11 (A) Field-cooled magnetic susceptibility measurement ($B = 1$ T) and (B) isothermal magnetization at 300 and 1.8 K of $\text{La}_2\text{O}_2\text{MnSe}_2$.

Optical Properties

Optical reflection measurements with a $\text{La}_2\text{O}_2\text{MnSe}_2$ powder sample (Fig. 4.12 A) were performed with an UV/Vis/NIR spectrophotometer ($\lambda = 490\text{--}800$ nm). Reflectance spectra in absorbance units cannot be compared directly to true absorption spectra due to the fact that weak signals in absorbance spectra are enhanced in reflected spectra. On the other hand, reflectance spectra can be analyzed using the Kubelka-Munk function, which make them similar to absorbance spectra and allows the determination of the bandgap energy E_g .^[13]

$$F(R_\infty) = \frac{(1 - R_\infty)^2}{2R_\infty} = \frac{K(\lambda)}{s(\lambda)} \propto \alpha = \frac{(h\nu - E_g)^n}{h\nu} \quad (4.1)$$

R_∞ is the diffuse reflectance of an infinitely thick sample, $K(\lambda)$ is the absorption coefficient and $s(\lambda)$ is the scattering coefficient. The direct bandgap energy is determined by extrapolating the linear portion of the plot of $[F(R_\infty)h\nu]^2$ against $h\nu$ (*Tauc* plot for a direct bandgap with $n = 1/2$). The estimated bandgap energy is about 2.13 eV (Fig. 4.12 B), which is consistent with the brick-red color of $\text{La}_2\text{O}_2\text{MnSe}_2$ as seen in the inset of Figure 4.12 (B). The bandgap energy is slightly higher than that of $\text{Ce}_2\text{O}_2\text{MnSe}_2$ (2.01 eV) reported in the literature.^[6]

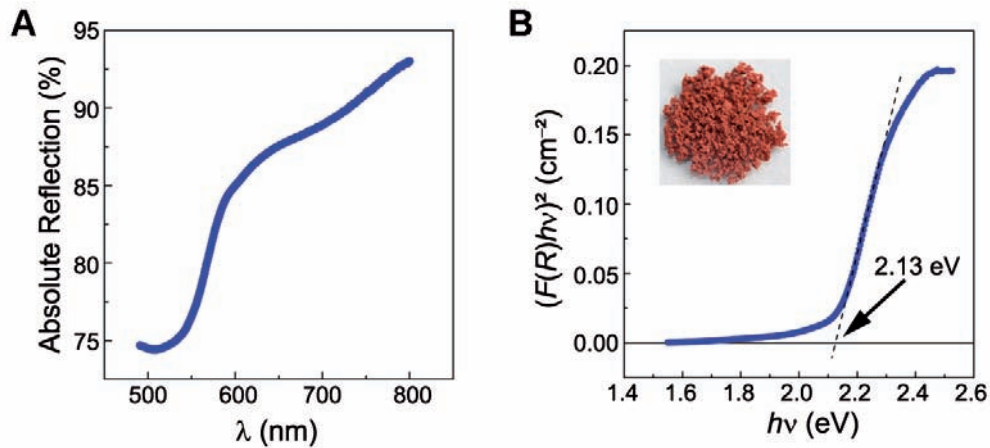


Figure 4.12 (A) Reflectance spectrum of $\text{La}_2\text{O}_2\text{MnSe}_2$. (B) Band gap calculation using the Kubelka-Munk function. Inset: Polycrystalline sample of $\text{La}_2\text{O}_2\text{MnSe}_2$.

4.1.4.2 $\text{Ce}_2\text{O}_2\text{MnSe}_2$

Single crystals of $\text{Ce}_2\text{O}_2\text{MnSe}_2$ were reported by *Ijjaali et al.* in 2003.^[6] However, the yield was very low ($< 5\%$) and the sample quantity did not allow magnetic or other measurements. As for the lanthanum compound, we obtained almost phase pure polycrystalline samples and single crystals of $\text{Ce}_2\text{O}_2\text{MnSe}_2$ using a NaI/KI flux. Energy dispersive X-ray spectroscopy of the single crystals (Fig. 4.13) revealed the averaged atomic percentages Ce 25.7 %, Mn 15.3 %, Se 27.3 % and O 31.6 %, which corresponds to $\text{Ce}_{2.0}\text{O}_{2.5(2)}\text{Mn}_{1.2(1)}\text{Se}_{2.1(1)}$ in agreement with the nominal composition (Table 4.2). Moreover, the EDX spectrum (Fig. 4.13) shows no hints for incorporation or inclusion of the elements of the flux material.

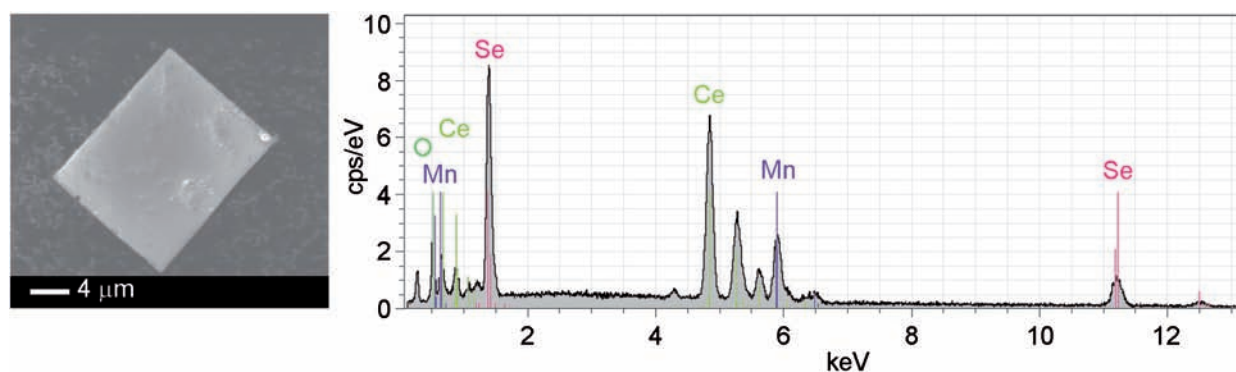


Figure 4.13 Typical plate-like single crystal (left) and EDX spectrum (right) of $\text{Ce}_2\text{MnSe}_2\text{O}_2$. Characteristic lines of the elements of the flux are not observed. The peak at ≈ 0.25 keV belongs to carbon from the adhesive conducting carbon film.

Table 4.2 EDX data /at% of $\text{Ce}_2\text{O}_2\text{MnSe}_2$.

	Ce	Mn	Se	O
#1	25.12	14.53	28.61	31.74
#2	27.22	15.41	28.90	28.48
#3	25.70	15.42	29.56	29.33
#4	25.83	15.95	25.24	32.98
#5	24.64	15.39	24.38	35.59
Average	25.70	15.34	27.34	31.62
σ_{Average}	0.44	0.23	1.05	1.27

Crystal Structure

Refinement of the X-ray powder diffraction data using the defect ZrCuSiAs-type structure (space group $P4/nmm$) fits the main peaks in the diffraction pattern (Fig. 4.14) while, similar to $\text{La}_2\text{O}_2\text{MnSe}_2$, some minor peaks, marked with asterisks, remained unindexed. The lattice parameters $a \approx 402$ pm and $c \approx 911$ pm are slightly smaller than those of $\text{La}_2\text{O}_2\text{MnSe}_2$ due to the smaller effective radii of the cerium atom [$r(\text{La}^{3+}) = 143.4$ pm, $r(\text{Ce}^{3+}) = 139.3$ pm].^[15]

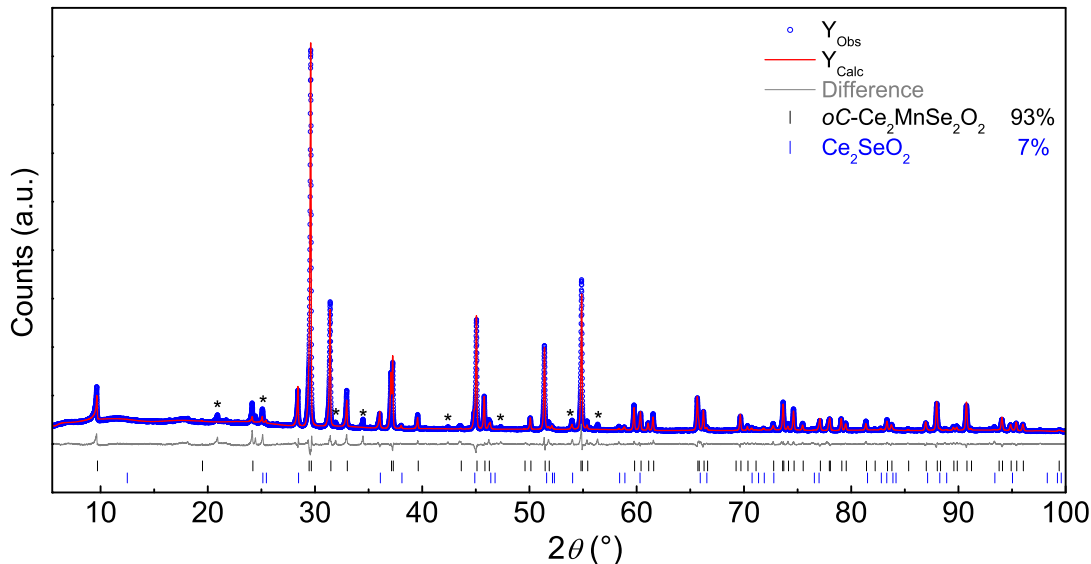


Figure 4.14 X-ray powder pattern (blue), Rietveld fit (red) and difference curve (gray) of $\text{Ce}_2\text{O}_2\text{MnSe}_2$. The structure of $\text{Ce}_2\text{O}_2\text{MnSe}_2$ was refined in the tetragonal space group $P4/nmm$. Reflections marked with asterisks are superstructure reflections of $\text{Ce}_2\text{O}_2\text{MnSe}_2$.

Single-crystal X-ray diffraction revealed satellite spots (Fig. 4.15) in agreement with superstructure reflections in the powder pattern (Fig. 4.14). The satellites occur at positions that do not exactly represent simple fractions of the reciprocal lattice vectors, and suggested a modulation vector $\mathbf{q} = [0.1573(2), 0, \frac{1}{2}]$. In contrast to the lanthanum compound, it is not clear whether the modulation in $\text{Ce}_2\text{O}_2\text{MnSe}_2$ is commensurate or not. The best approximant for the modulation vector is $\mathbf{q} = [\frac{3}{19}, 0, \frac{1}{2}]$ which would give a large supercell with the dimension $19\sqrt{2}a_{\text{subcell}} \times \sqrt{2}b_{\text{subcell}} \times 2c_{\text{subcell}}$. Since there is no further evidence of a commensurate modulation, the structure was solved as incommensurate using the superspace group $Cmme(\alpha 0 \frac{1}{2})0s0$ with $\alpha = 0.1573(2)$.

The Fourier maps of Figure 4.16 show that the Mn site occupancy is strongly modulated, mainly along x_1 and those of Figure 4.17 show that the positions of Ce, Se and O are mainly

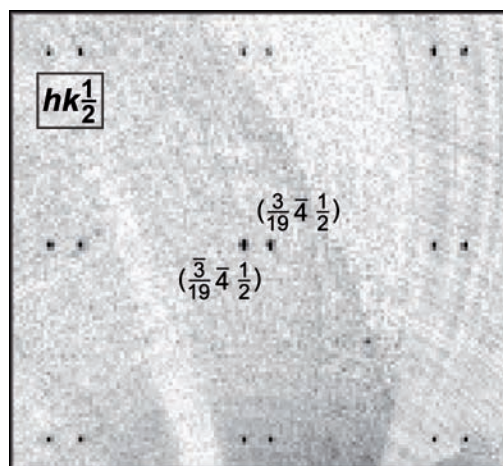


Figure 4.15 $hk\frac{1}{2}$ -layer with 1st order satellite reflections. The reflections can be approximated with $\mathbf{q} = [\frac{3}{19}, 0, \frac{1}{2}]$.

modulated along the x_2 direction. Therefore first order harmonic functions were used for the positional parameters of all atoms and a fixed Crenel function (with a length of 0.5 and the centre at 0.75) was used to model the occupancy variation of manganese. Crystal and refinement data are given in Table A.3.

The commensurate option ($\alpha = \frac{3}{19}$) was chosen in order to visualise the Mn occupancy modulation. Transforming from (3+1)D superspace group to the 3D space group, there are three symmetry space groups along different t -sections: $I2cb$ (45), $Imcb$ (72) and $Ibca$ (73). Among these space groups, $Imcb$ ($t_0 = \frac{1}{76} + \frac{n}{38}$) gives significantly better agreement with the experimental data than the others. An approximation of a $[\text{MnSe}_2]^{2-}$ layer ($19\sqrt{2}a_{\text{subcell}} \times \sqrt{2}b_{\text{subcell}}$ supercell) is shown in Figure 4.18 (B). The following discussion is based on the average atomic distances and angles in this supercell.

The structure is similar to $\text{La}_2\text{O}_2\text{MnSe}_2$ with an even more complicated vacancy ordering pattern. $\text{Ce}_2\text{O}_2\text{MnSe}_2$ can be described as blocks of six or seven corner-sharing $\text{MnSe}_{4/2}$ -tetrahedra, which are separated by a pair of edge-sharing tetrahedra. The repetitive sequence of blocks of corner-sharing tetrahedra along a is "6-6-7". Thus there are twice as many blocks with six as blocks with seven corner-sharing tetrahedra in the modulated structure. Similar to $\text{La}_2\text{O}_2\text{MnSe}_2$, the $[\text{MnSe}_2]^{2-}$ layers are stacked along the c axis in a way that tetrahedra of one layer fill the gaps of the layer above and vice versa (Fig. 4.18 C). The distance between the manganese atoms in the corner-shared tetrahedra [397.2(1)–400.9(1) pm] is significantly longer than in edge-shared tetrahedra [307.7(1)–308.3(1) pm], however both are smaller than those in $\text{La}_2\text{O}_2\text{MnSe}_2$. Mn-Se bond lengths vary from 255.3(1)–258.2(1) pm, which is com-

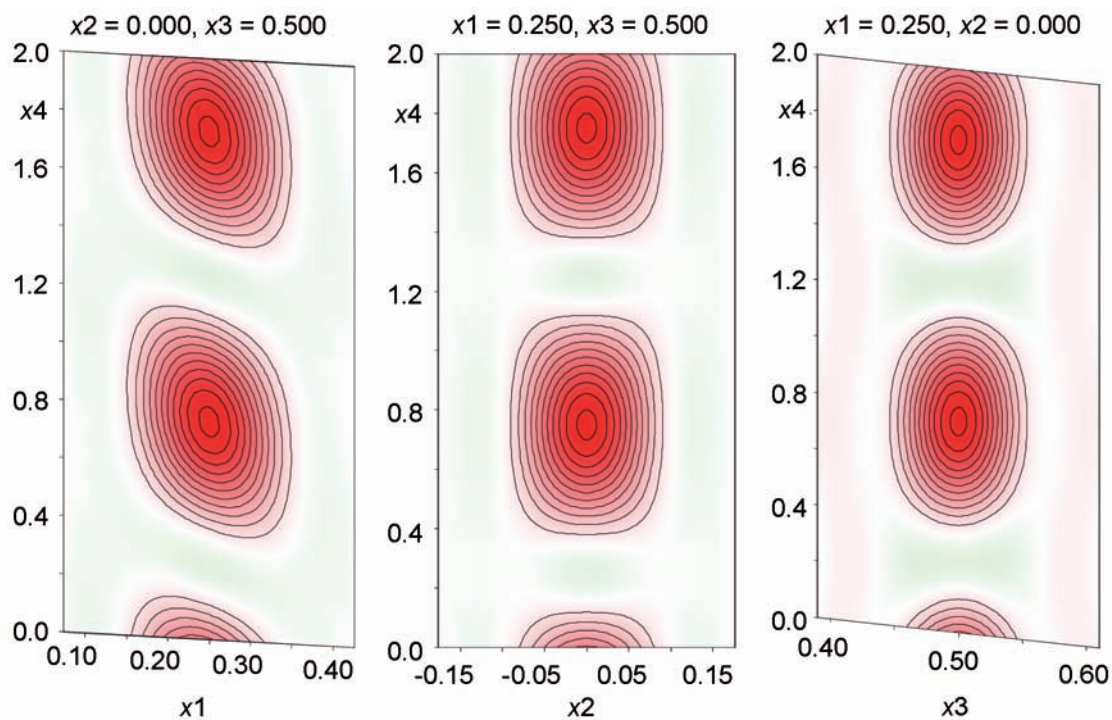


Figure 4.16 Fourier electron density maps of $\text{Ce}_2\text{O}_2\text{MnSe}_2$ from charge flipping. Center at Mn ($\frac{1}{4}, 0, \frac{1}{2}$).

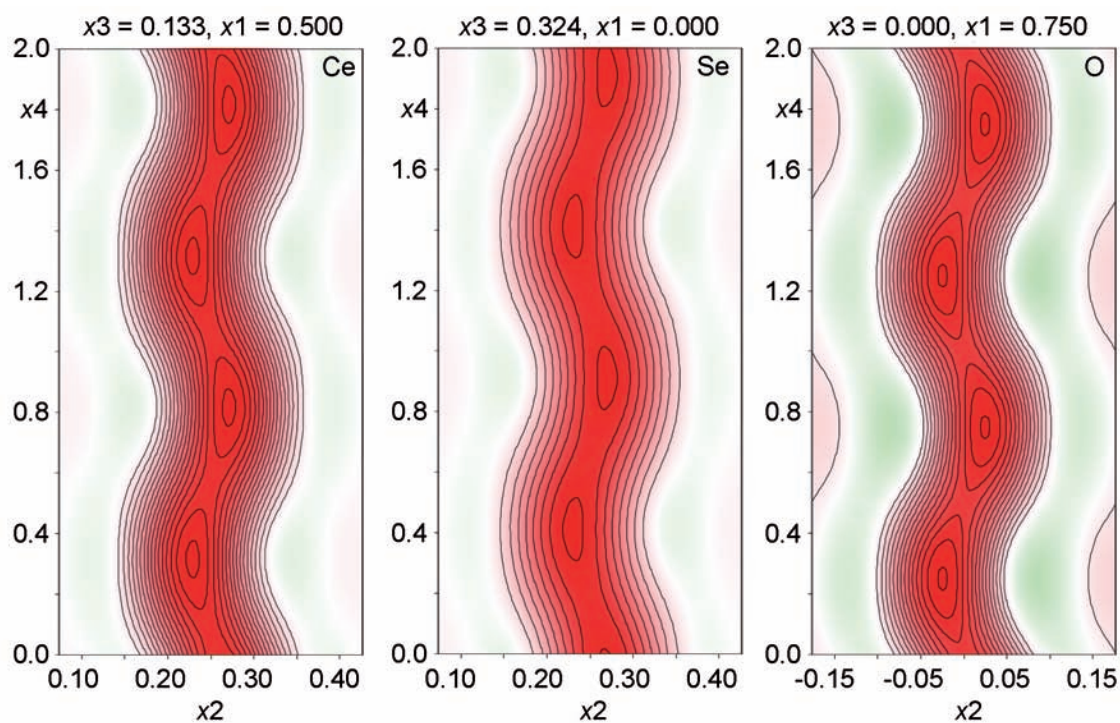


Figure 4.17 Fourier electron density maps of $\text{Ce}_2\text{O}_2\text{MnSe}_2$ from charge flipping. Center at Ce (left), Se (middle) and O (right).

parable to those in the lanthanum compound, and Ce-O vary from 233.8(1)–236.1(1) pm, which is significantly smaller than La-O bond lengths in $\text{La}_2\text{O}_2\text{MnSe}_2$.

In terms of the average structure of $\text{Ce}_2\text{O}_2\text{MnSe}_2$ the inspection of the changes of the Se-Mn-Se and Ce-O-Ce bond angles along t reveals an almost identical behaviour as for $\text{La}_2\text{O}_2\text{MnSe}_2$, solely the absolute values are different. The Ce-O-Ce bond angles vary from 105.1(1)–119.6(1)°, which is comparable to the values of the lanthanum compound. In contrast, the Se-Mn-Se bond angles vary in a broader range from 102.1(1)–119.6(1)°. These observations confirm the assumption of a flexible $[\text{MnSe}_2]^{2-}$ layer, whereas the rare-earth oxide layer stays more rigid.

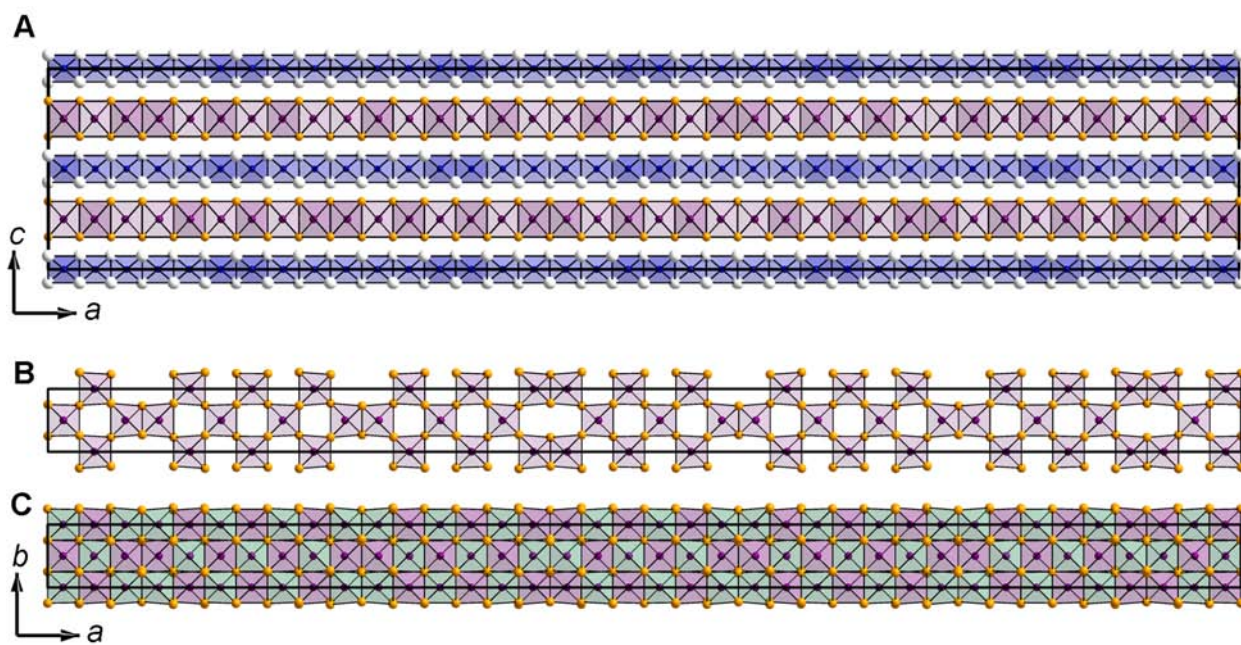


Figure 4.18 (A) Alternating layers of $\text{OCe}_{4/4-}$ (blue) and $\text{MnSe}_{4/2-}$ (purple) tetrahedra. Cerium in white, manganese in purple, selenium in orange and oxygen in blue. (B) $[\text{MnSe}_2]^{2-}$ layer of $\text{Ce}_2\text{O}_2\text{MnSe}_2$ approximated by a commensurate $19\sqrt{2}a_{\text{subcell}} \times \sqrt{2}b_{\text{subcell}}$ supercell. (C) Stacking of two $[\text{MnSe}_2]^{2-}$ layers. The second layer is coloured in green for clarity.

In summary both layers, the $[\text{RE}_2\text{O}_2]^{2+}$ as well as the $[\text{MnSe}_2]^{2-}$, distort in order to achieve a structural balance between them. The inherent size mismatch and the resulting strain between the layers is reduced by both, compression of the $[\text{MnSe}_2]^{2-}$ layer and expansion of the $[\text{RE}_2\text{Se}_2]^{2+}$ layer in the ab -plane, as well as by mixing corner- and edge-sharing $\text{MnSe}_{4/2}$ -tetrahedra in an appropriate way leading to the observed patterns of ordered vacancies. The lattice mismatch may also be an explanation why we were not able to prepare

samples with smaller rare earth metals (e.g. $\text{Pr}_2\text{O}_2\text{MnSe}_2$, $\text{Nd}_2\text{O}_2\text{MnSe}_2$) via the flux method. However, it is remarkable that $\text{La}_2\text{O}_2\text{MnSe}_2$ and $\text{Ce}_2\text{O}_2\text{MnSe}_2$ try to minimize the layer mismatch by the formation of relatively complicated and unexpected modulated structures while no other binary or ternary compounds are energetically favorable.

Figure 4.19 displays the Rietveld refinement of $\text{Ce}_2\text{O}_2\text{MnSe}_2$. Main reflections (black) as well as the superstructure reflections (green) are satisfactorily described.

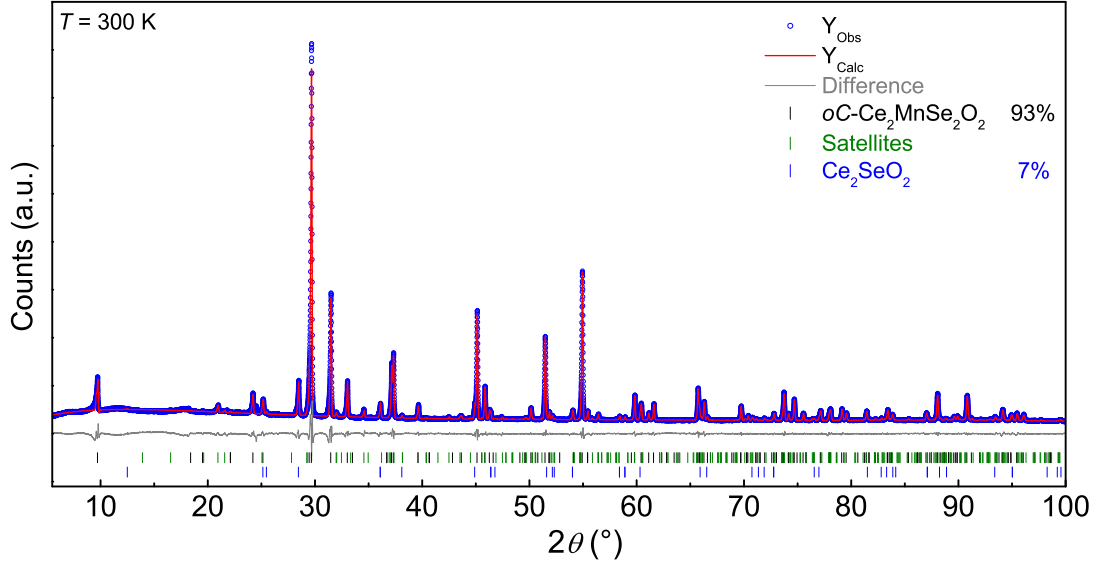


Figure 4.19 X-ray powder diffraction pattern of $\text{Ce}_2\text{O}_2\text{MnSe}_2$ (blue) at $T = 300\text{ K}$, with Rietveld fit (red) and difference curve (gray) using the modulated structure model with the superspace group $Cmme(\alpha 0 \frac{1}{2})0s0$ ($\mathbf{q} = [0.1573(2), 0, \frac{1}{2}]$).

Low temperature measurements on powder and single crystal samples uncovered a small effect on the \mathbf{q} vector. Powder diffraction measurements at 10 K (Fig. 4.20) as well as single crystal diffraction measurements at 100 K (Table A.4) revealed a change of α from 0.1573(2) at room temperature to 0.160(4) and 0.1603(1) at 10 and 100 K, respectively. The alteration of approximately 1.7 % has an effect on the modulation. The best approximant for the modulation vector at low temperatures is $\mathbf{q} = [\frac{4}{25}, 0, \frac{1}{2}]$ which gives a supercell with the dimension $25\sqrt{2}a_{\text{subcell}} \times \sqrt{2}b_{\text{subcell}} \times 2c_{\text{subcell}}$. We then transformed again from (3+1)D superspace group to the 3D space group in order to visualise the Mn occupancy modulation. There are three symmetry space groups along different t -sections: $C2ce$ (48), $Cmce$ (64) and $Ccce$ (68). Among these space groups, $C2ce$ and $Ccce$ give significantly better agreement with the experimental data than $Cmce$. As $Ccce$ is higher symmetric, we used this space

group to plot the unit cell. An approximation of a $[\text{MnSe}_2]^{2-}$ layer is shown in Figure 4.21. The effect on the modulation is an increased content of blocks of six corner-sharing $\text{MnSe}_{4/2}$ -tetrahedra compared to those with seven tetrahedra. The repetitive sequence changes from "6-6-7" at room temperature to "6-6-7-6-6-7-6-6", which means a ratio of 3:1.

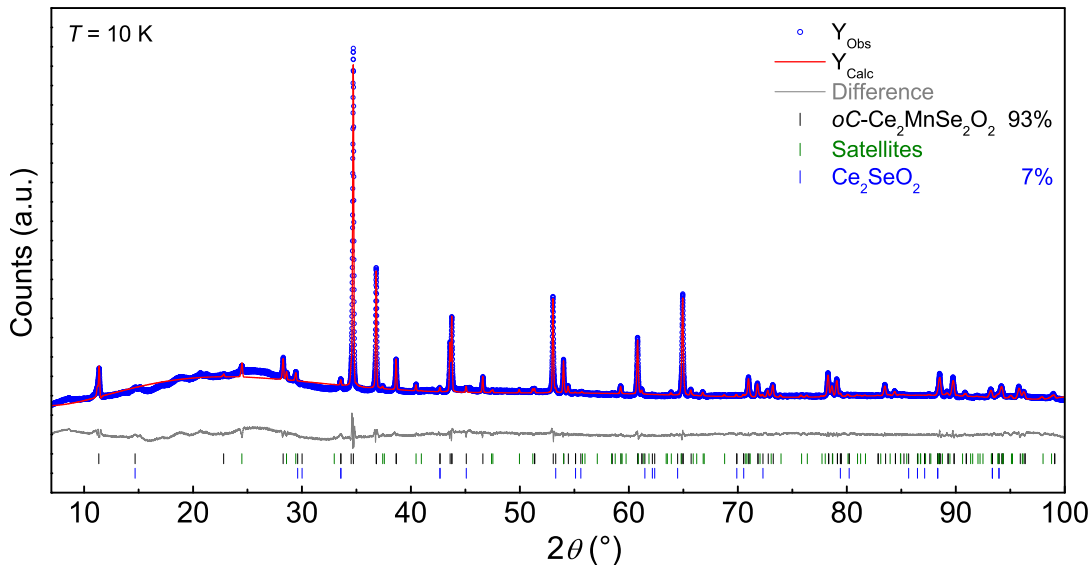


Figure 4.20 X-ray powder diffraction pattern of $\text{Ce}_2\text{O}_2\text{MnSe}_2$ (blue) at $T = 10$ K, with Rietveld fit (red) and difference curve (gray) using the modulated structure model with the superspace group $Cmme(\alpha 0 \frac{1}{2})0s0$ ($\mathbf{q} = [0.160(4), 0, \frac{1}{2}]$).

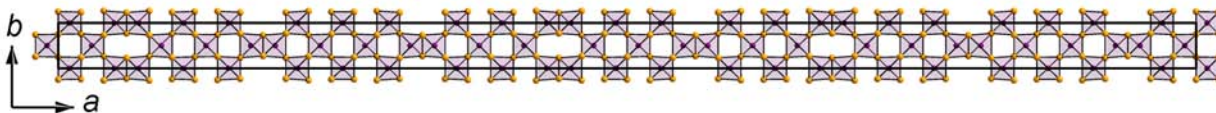


Figure 4.21 $[\text{MnSe}_2]^{2-}$ layer of $\text{Ce}_2\text{O}_2\text{MnSe}_2$ at 100 K approximated by a commensurate $25\sqrt{2}a_{\text{subcell}} \times \sqrt{2}b_{\text{subcell}}$ supercell.

Magnetism

The magnetic susceptibility ($B = 1$ T) of $\text{Ce}_2\text{O}_2\text{MnSe}_2$ shows relatively high values for χ_{mol} (Fig. 4.22 A) and a paramagnetic curve shape. Similar to $\text{La}_2\text{O}_2\text{MnSe}_2$, we assume antiferromagnetic ordering of the Mn^{2+} ions already at room temperature while the $4f$ electron of Ce^{3+} is paramagnetic. Thus we observe no Curie-Weiss behavior and cannot estimate the cerium moment. This is in line with the magnetization isotherms shown in Figure 4.22 (B), which suggest antiferromagnetism with small deviations at low temperatures.

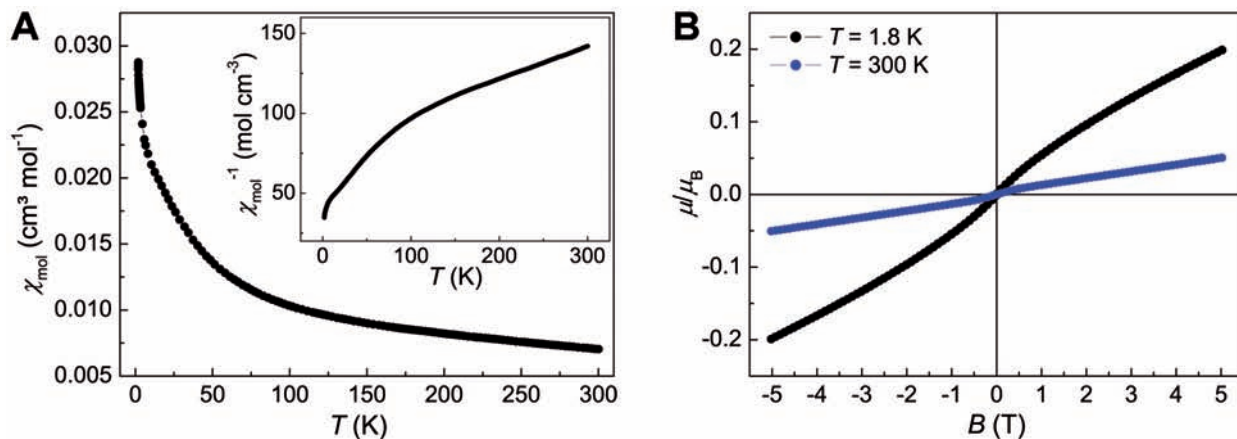


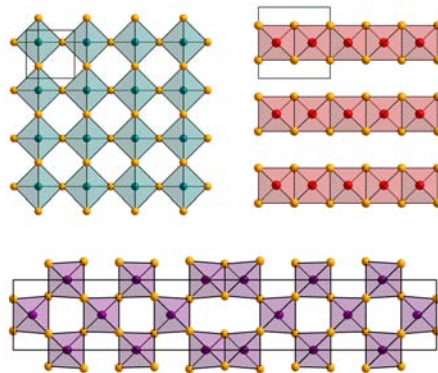
Figure 4.22 (A) Magnetic susceptibility measurement at $B = 1$ T and inverse susceptibility (inset). (B) Isothermal magnetization of $\text{Ce}_2\text{O}_2\text{MnSe}_2$ at 300 and 1.8 K.

4.1.5 Conclusion

$\text{RE}_2\text{O}_2\text{MnSe}_2$ ($\text{RE} = \text{La}, \text{Ce}$) were obtained by heating La_2O_3 , CeO_2 , RE , Mn , and Se in a NaI/KI flux. The crystal structures are related to the ZrCuSiAs -type structure with ordered vacancies at the manganese sites. Modulated structure models were refined against X-ray single crystal and powder data using the superspace group $Cmme(\alpha 0 \frac{1}{2})0s0$ with $\alpha = \frac{1}{5}$ and $0.1573(2)$, respectively. The resulting modulations of the checkerboard pattern of $[\text{MnSe}_2]^{2-}$ layers can be approximated by $5\sqrt{2}a_{\text{subcell}} \times \sqrt{2}b_{\text{subcell}} \times 2c_{\text{subcell}}$ and $19\sqrt{2}a_{\text{subcell}} \times \sqrt{2}b_{\text{subcell}} \times 2c_{\text{subcell}}$ supercells in $\text{La}_2\text{O}_2\text{MnSe}_2$ and $\text{Ce}_2\text{O}_2\text{MnSe}_2$, respectively. Low temperature diffraction experiments revealed no change of the modulation in $\text{La}_2\text{O}_2\text{MnSe}_2$ but a small increase of α for $\text{Ce}_2\text{O}_2\text{MnSe}_2$ at 100 and 10 K. Both compounds are insulators. The optical bandgap of $\text{La}_2\text{O}_2\text{MnSe}_2$ was determined to 2.13 eV from the Kubelka-Munk function. Magnetic measurements indicate antiferromagnetic ordering of the Mn^{2+} moments with Néel points well above room temperature, as known from related manganese compounds.

4.2 The Modulated Structures of $\text{La}_{2-x}\text{Pr}_x\text{O}_2\text{MnSe}_2$ and $\text{La}_{2-x}\text{Nd}_x\text{O}_2\text{MnSe}_2$

S. Peschke and D. Johrendt



Parts published in: *Z. Kristallogr.* **2016**, *231(2)*, 89–95.

De Gruyter The Modulated Structures of $\text{La}_{2-x}\text{Pr}_x\text{O}_2\text{MnSe}_2$ and $\text{La}_{2-x}\text{Nd}_x\text{O}_2\text{MnSe}_2$, Walter De Gruyter GmbH Berlin Boston, 2016. Copyright and all rights reserved. Material from this publication has been used with the permission of Walter De Gruyter GmbH.

4.2.1 Abstract

The solid solutions $\text{La}_{2-x}\text{Pr}_x\text{O}_2\text{MnSe}_2$ ($0 \leq x \leq 1$) and $\text{La}_{2-x}\text{Nd}_x\text{O}_2\text{MnSe}_2$ ($0 \leq x \leq 0.6$) were synthesized in a NaI/KI flux between 1073 and 1173 K. The selenide oxides adopt a ZrCuSiAs-related structure with modulated $[\text{MnSe}_2]^{2-}$ layers which consist of a mixture of edge- and corner-sharing $\text{MnSe}_{4/2}$ -tetrahedra. The crystal structures are described with a (3+1)D model in superspace group $Cmme(\alpha 0 \frac{1}{2})0s0$. The modulation vector \mathbf{q} can be controlled by partial substitution of La^{3+} for Pr^{3+} and Nd^{3+} via the unit cell volume leading to, amongst others, $(\text{La}_{0.55}\text{Pr}_{0.45})_2\text{O}_2\text{MnSe}_2$ with $\alpha = \frac{1}{6}$, which allows the projection onto 3D space by using a simple sixfold a axis.

4.2.2 Introduction

After the discovery of superconductivity in the iron pnictides $RE\text{FeAsO}$ (RE = rare-earth metal), the ZrCuSiAs-type structure leads to enormous interest in this family of superconducting materials. The structure consists of slabs of edge-sharing $\text{FeAs}_{4/4}$ -

tetrahedra in anti-PbO-type structure, stacked alternating with slabs of rare-earth oxide tetrahedra with PbO-type structure. Substitution of arsenic in $RETA_sO$ ($T =$ divalent transition-metal) by selenium leads to compounds $RET_{0.5}SeO$ ($= RE_2TSe_2O_2$) with vacancies at the transition metal site. These days, several compounds are known that retain a ZrCuSiAs-related structure with modulations in the transition-metal-selenide layers. Among them, $La_2O_2MnSe_2$ ^[16], $Ce_2O_2MnSe_2$ ^[16,17], $La_2O_2FeSe_2$ ^[3], $Ce_2O_2FeSe_2$ ^[4], $La_2O_2ZnSe_2$ ^[5], $Ce_2O_2ZnSe_2$ ^[14], $La_2O_2CdSe_2$ ^[2], and $Ce_2O_2CdSe_2$ ^[18]. The $[TSe_2]^{2-}$ layers of those structures that can be described as commensurate modulated are shown in Figure 4.23.

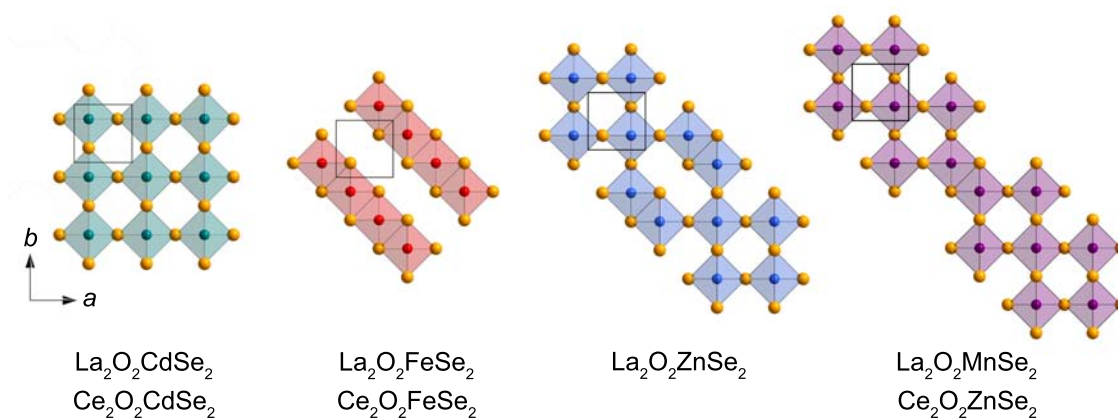


Figure 4.23 Schematic presentation of ZrCuSiAs-related modulated $[TSe_2]^{2-}$ layers of $RE_2O_2TSe_2$ ($RE = La, Ce; T = Mn, Fe, Zn, Cd$). The shown unit cell is for the tetragonal parent phase ($P4/nmm$).

The difference in their structures is the ratio of edge- to corner-sharing $TSe_{4/2}$ -tetrahedra which reaches a maximum in $La_2O_2FeSe_2$ and $Ce_2O_2FeSe_2$ (stripe like arrangement) and a minimum in $La_2O_2CdSe_2$ and $Ce_2O_2CdSe_2$ (checkerboard arrangement). In contrast, compounds with $T = Mn$ and Zn show a mixture of edge- and corner sharing tetrahedra whereby the ratio is 3:1 for $La_2O_2ZnSe_2$, and 4:1 for $La_2O_2MnSe_2$ and $Ce_2O_2ZnSe_2$. Among all mentioned materials, $Ce_2O_2MnSe_2$ is the only compound that reveals an incommensurate modulated structure with a ratio of edge- to corner-sharing tetrahedra which is larger than 5:1. Recently, we reported the modulated crystal structures of $La_2O_2MnSe_2$ and $Ce_2O_2MnSe_2$ in the monoclinic superspace group $P 1 1 2/n (\alpha\beta\frac{1}{2})0s$.^[16] After that, *Ainsworth* et al. found that all mentioned compounds above can be described in the higher symmetric superspace group $Cmme(\alpha 0\frac{1}{2})0s0$, with modulation vector $\mathbf{q} = [\alpha, 0, \frac{1}{2}]$. These authors lately

discovered further modulated compounds in this family by either mixing the rare-earth elements in $\text{La}_{2-x}\text{Ce}_x\text{O}_2\text{TSe}_2$ ($T = \text{Mn, Fe, Zn, Cd}$) or mixing the transition metals in $\text{RE}_2\text{O}_2\text{Fe}_{1-x}\text{Zn}_x\text{Se}_2$, $\text{RE}_2\text{O}_2\text{Zn}_{1-x}\text{Mn}_x\text{Se}_2$ and $\text{RE}_2\text{O}_2\text{Mn}_{1-x}\text{Cd}_x\text{Se}_2$ ($\text{RE} = \text{La, Ce}$), which leads to a huge amount of mostly incommensurate modulated compounds in this family.^[18] In order to increase this continuously growing family, we prepared high purity powder samples of the solid solutions $\text{La}_{2-x}\text{RE}_x\text{O}_2\text{MnSe}_2$ [$\text{RE} = \text{Pr}$ ($0 \leq x \leq 1$), Nd ($0 \leq x \leq 0.6$)].

4.2.3 Experimental Details

Powder samples and single crystals of the solid solutions $\text{La}_{2-x}\text{RE}_x\text{O}_2\text{MnSe}_2$ ($\text{RE} = \text{Pr, Nd}$) were prepared by the reaction of appropriate amounts of La_2O_3 , Pr_2O_3 , La , Mn , and Se (purity $\geq 99.9\%$). The rare-earth oxides were heated to 673 K prior to use. The starting materials (0.25 g) were mixed intimately and sandwiched in a glassy carbon crucible between 0.75 g of a eutectic NaI/KI mixture (mass ratio 0.6:0.4, dried in dynamic vacuum at 673 K) as flux. The crucibles were sealed in argon filled silica tubes and heated to 1073 or 1173 K with a rate of 100 K/h, kept at this temperature for 3–5 days and slowly cooled to 923 K with a cooling rate of 5 K/h. The crucibles were quenched in air from 923 K and the reaction mixture was washed with deionized water and ethanol and dried in vacuum. The resulting samples were red powder (purity $> 95\text{ wt}\%$) and bright red, transparent single crystals. The compounds are stable in air for months. Single crystal X-ray diffraction data was collected with a Bruker D8 QUEST (fixed- χ goniometer, $\text{Mo-K}\alpha$, $1\mu\text{S}$ with HE-LIOS multilayer optics, PHOTON 100 detector). Reflection intensity integration, data reduction, and multi-scan absorption correction were done with APEX2^[9] and SADABS^[10]. The structure was solved with Jana2006^[11]. Further details of the crystal structure investigation may be obtained from the Fachinformationszentrum Karlsruhe, 76344 Eggenstein- Leopoldshafen, Germany (Fax: +49-7247-808-666; E-mail: crysdata@fiz-karlsruhe.de, <http://www.fiz-karlsruhe.de>) on quoting the depository number CSD-429957 for $(\text{La}_{0.55}\text{Pr}_{0.45})_2\text{O}_2\text{MnSe}_2$. X-ray powder diffraction patterns were measured with a Huber G670 diffractometer ($\text{Cu-K}\alpha_1$ radiation, Ge-monochromator). Rietveld refinements were done with Jana2006^[11].

4.2.4 Results and Discussion

La_{2-x}Pr_xO₂MnSe₂

The solid solution La_{2-x}Pr_xO₂MnSe₂ could be prepared for $0 \leq x \leq 1$ in a NaI/KI flux at 1073–1173 K. Samples which appeared inhomogeneous because of relatively broad or asymmetric reflections in the X-ray diffraction pattern were ground and heated again with the same flux conditions as described in the experimental part. Almost single phase samples (> 95 wt%) with well-shaped crystals are obtained for $0 \leq x \leq 0.9$ which turned out to be the solubility limit of praseodymium. La_{2-x}Pr_xSeO₂, La_{4-x}Pr_xSe₃O₄ and MnSe are possible minor impurity phases. Samples with higher praseodymium content ($x > 0.9$) contain significant amounts of impurity phases (> 10 wt%). The powder samples appeared brick red whereas the single crystals are bright red and translucent. Energy dispersive X-ray spectroscopy (EDX) of some crystals of each sample revealed a homogeneous distribution of lanthanum and praseodymium and confirmed the nominal compositions (± 3 at%).

As observed by *Ainsworth* et al. in selected area electron diffraction (SAED) images, the tetragonal symmetry ($P4/nmm$) of the parent compound is lost and the substructure can be described in an orthorhombic cell with dimensions $\sqrt{2}a_{\text{subcell}} \times \sqrt{2}b_{\text{subcell}} \times c_{\text{subcell}}$.^[18] The superstructure can be described in the (3+1)D superspace group $Cmme(\alpha 0 \frac{1}{2})0s0$ with the modulation vector $\mathbf{q} = [\alpha a^* + 0b^* + \frac{1}{2}c^*]$. According to the respective \mathbf{q} vector, all known commensurately ordered RE₂O₂TSe₂ compounds can be described with a supercell with dimensions $n\sqrt{2}a_{\text{subcell}} \times \sqrt{2}b_{\text{subcell}} \times 2c_{\text{subcell}}$. In the case when α is an irrational number, the modulation is incommensurate. X-ray powder data of all samples were refined with Jana2006^[11] using the superspace group mentioned above to determine the cell parameters and the modulation vector component α . The occupancy variation of manganese was modeled with a fixed Crenel function. Figure 4.24 shows the Rietveld refinement of the X-ray powder pattern of La_{1.4}Pr_{0.6}O₂MnSe₂ as an example.

Figure 4.25 shows the course of lattice parameters and cell volume upon praseodymium doping. The solubility limit ($x = 0.9$) is marked with a dotted line. The parameters a , b and c decrease linearly with the praseodymium content $0 \leq x \leq 0.9$ according to Vegard's law. The decrease can be explained by the smaller effective radius of praseodymium compared to lanthanum ($r_{\text{La}} = 143.4$ pm, $r_{\text{Pr}} = 137.6$ pm).^[15] Once the solubility limit is passed ($x > 0.9$), the parameters remain almost constant and the amount of impurities raises which

indicates that the nominal compositions do not fit anymore with the actual compositions of the samples.

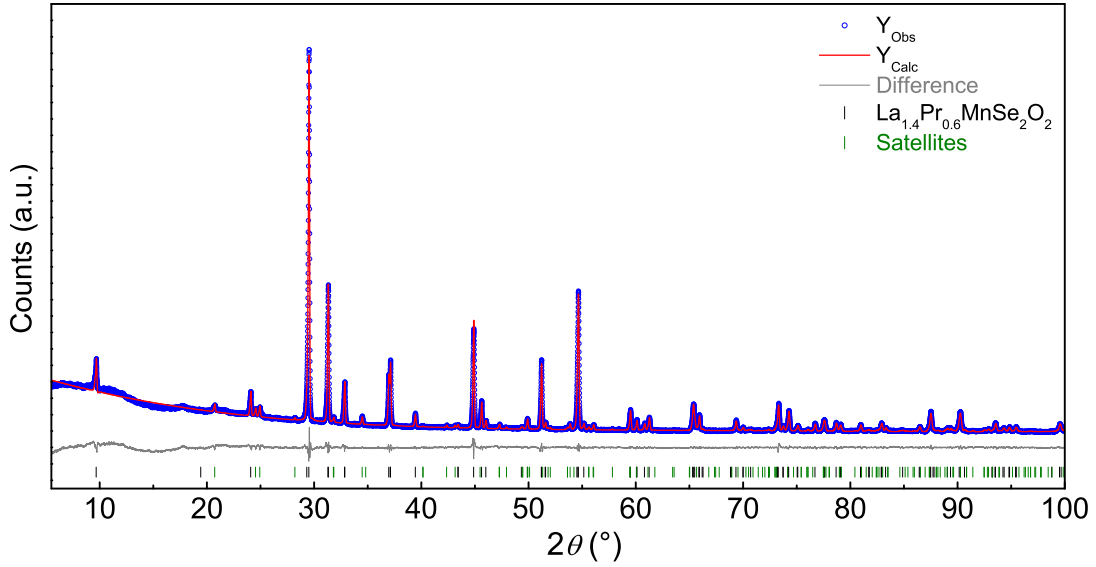


Figure 4.24 X-ray powder pattern (blue), Rietveld fit (red) and difference plot (gray) of $\text{La}_{1.4}\text{Pr}_{0.6}\text{O}_2\text{MnSe}_2$ using the modulated structure model with the superspace group $Cmme(\alpha 0 \frac{1}{2}) 0s0$. Peak positions in green are those of the satellites.

The modulation vector component α has a maximum in $\text{La}_2\text{O}_2\text{MnSe}_2$ ($x = 0$, $\alpha = 0.2$) and can be controlled by partial substitution of La^{3+} by smaller Pr^{3+} (Fig. 4.26 A). In contrast to the lattice parameters, α drops rapidly in the range $0 \leq x < 0.2$ and then shows an almost linear decrease in the range $0.2 \leq x \leq 0.9$. For $x = 0.9$, α adopts, within experimental errors, a value close to $\alpha = \frac{1}{6}$ (dashed line). Regarding the effective radii of the mixed rare-earth metals in their $ORE_{4/4}$ -tetrahedra, which are calculated as shown in equation 4.2, an analogous behavior for α is observed in Figure 4.26 (B).

$$r(\text{eff}) = \frac{2-x}{2}r(\text{La}) + \frac{x}{2}r(\text{Pr}) \quad (4.2)$$

In addition, the variation of the cell volume upon doping has a similar effect on α as depicted in the inset of Figure 4.26 (B). However, plotting the cell volume against the effective radii gives a linear trend. This shows that the evolution of α in the range $0 \leq x < 0.2$ is not an effect of the structural changes due to Pr^{3+} doping but is an intrinsic effect of the solid solution. As the modulation of $(\text{La}_{0.55}\text{Pr}_{0.45})_2\text{O}_2\text{MnSe}_2$ can be approximated by

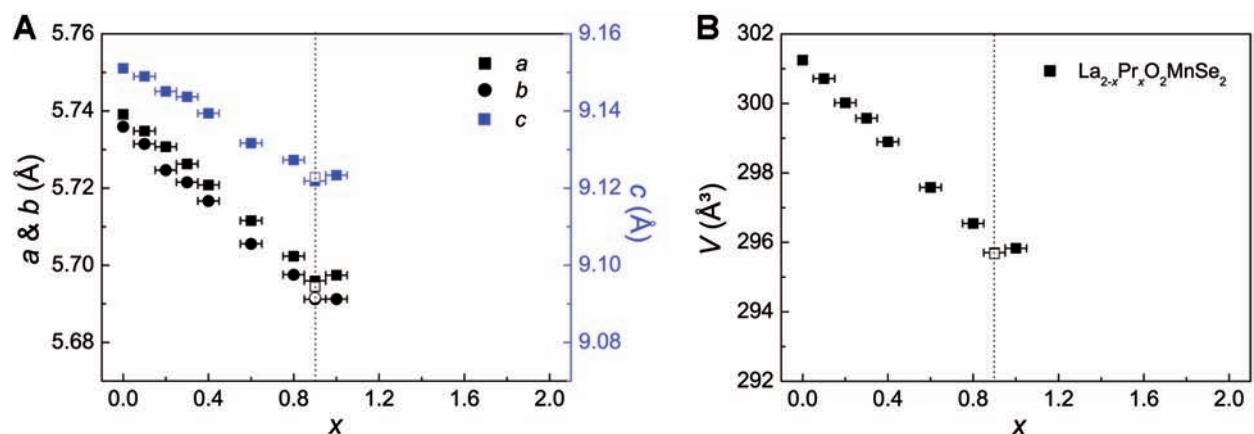


Figure 4.25 (A) Lattice parameters a (black squares), b (black dots) and c (blue squares) and (B) the cell volume of the orthorhombic unit cell versus x . Unfilled symbols are from single-crystal data. The dotted line symbolizes the solubility limit.

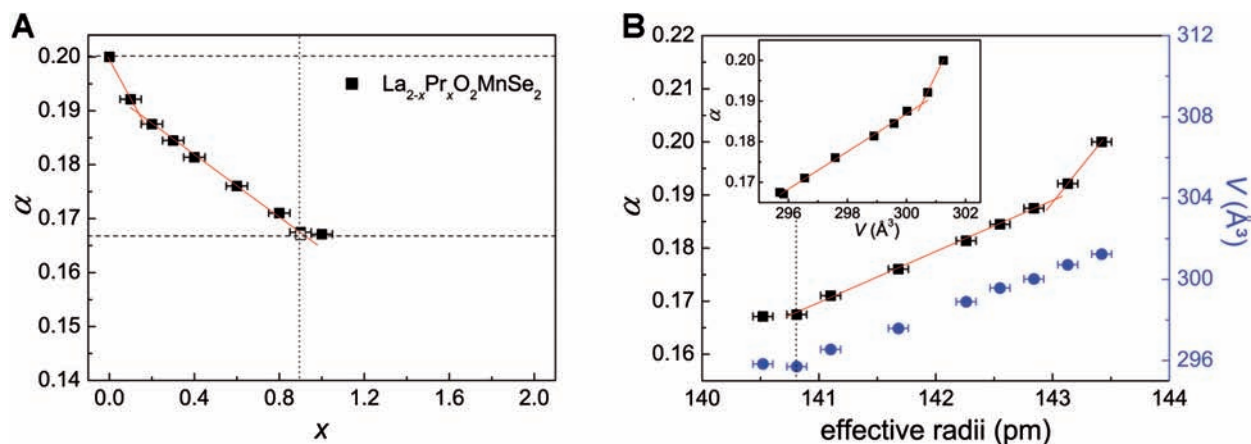


Figure 4.26 (A) Modulation vector component α of $\text{La}_{2-x}\text{Pr}_x\text{O}_2\text{MnSe}_2$ against x . The dashed lines represent the cases for $\alpha = \frac{1}{5}$ and $\frac{1}{6}$. (B) Modulation vector component α (black squares) and unit cell volume (blue dots) against the effective radii of the rare-earth metal in $\text{La}_{2-x}\text{Pr}_x\text{O}_2\text{MnSe}_2$. Dotted lines symbolize the solubility limit. Red lines are guides to the eye. Inset: Modulation vector component α against the cell volume.

using a simple sixfold a axis ($\alpha = \frac{1}{6}$), the superstructure was determined by single crystal X-ray diffraction experiments using a small plate-like single crystal (Figure 4.27). EDX experiments determined the content of rare-earth metals in this crystal to be 13.1(4) at% La and 11.0(2) at% Pr. These values correspond to $(\text{La}_{0.54(2)}\text{Pr}_{0.46(2)})_2\text{O}_2\text{MnSe}_2$ which is in good agreement with the nominal composition. The inspection of the $hk0$ layer of the diffraction image revealed additional satellite spots (blue arrows) surrounding each Bragg position of the orthorhombic unit cell (Fig. 4.28 A) which could be indexed as integer fractions of the reciprocal lattice vectors of the substructure with $\mathbf{q} = [\frac{1}{3}a^* + 0b^* + \frac{1}{2}c^*]$. In contrast to the $hk0$ layer, the strong satellite reflections in the $hk\frac{1}{2}$ layer (Fig. 4.28 B) can be indexed using the modulation vector $\mathbf{q} = [\frac{1}{6}a^* + 0b^* + \frac{1}{2}c^*]$. This indicates that 2nd order satellite reflections are predominant in the $hk0$ layer, whereas only 1st order satellite reflections can be observed in the $hk\frac{1}{2}$ layer.

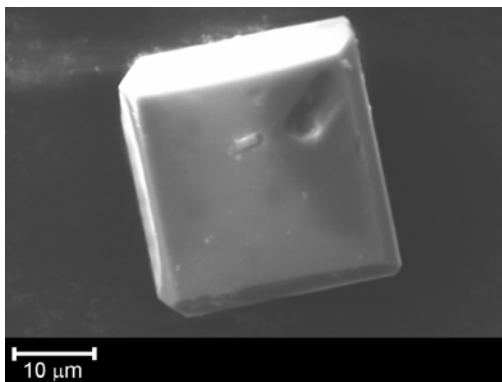


Figure 4.27 Typical plate-like single crystal of $(\text{La}_{0.55}\text{Pr}_{0.45})_2\text{O}_2\text{MnSe}_2$ obtained from the NaI/KI flux.

In addition, the section of the $hk\frac{1}{2}$ layer indicates twinning by partial pseudo-merohedry with a 90° rotation along $[0\ 0\ 1]$. The two twin domains are marked with either black or blue arrows of selected reflections in Figure 4.28 (B). Regarding the pseudo-tetragonal subcell, this kind of modulation gives a commensurate supercell with the dimension $6\sqrt{2}a_{\text{subcell}} \times \sqrt{2}b_{\text{subcell}} \times 2c_{\text{subcell}}$. The crystal structure was refined using the superspace group $Cmme(\alpha 0 \frac{1}{2})0s0$ and the commensurate option. The modulation was described by first order harmonic functions for the positions of all atoms. The occupancy parameters of manganese was modeled with a fixed crenel function. The refinement of the modulation vector during the integration gives an almost commensurate value of $\frac{1}{6}$ within the standard deviation. Only 1st order satellite reflections were considered for the refinement as the refinement was unstable

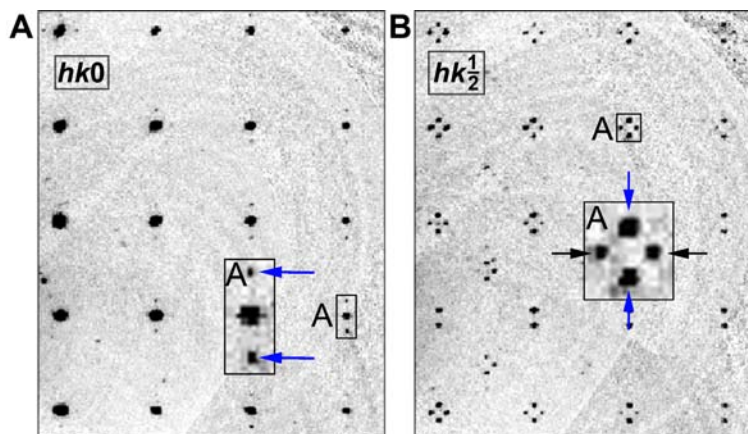


Figure 4.28 (A) $hk0$ -layer of $(\text{La}_{0.55}\text{Pr}_{0.45})_2\text{O}_2\text{MnSe}_2$ with main reflections and 2nd order satellite spots (blue arrows) at $\mathbf{q} = [\frac{1}{3}, 0, \frac{1}{2}]$. (B) $hk\frac{1}{2}$ layer with two twin domains and 1st order satellite reflections (black and blue arrows) at $\mathbf{q} = [\frac{1}{6}, 0, \frac{1}{2}]$.

when including 2nd order satellite reflections. Transforming from (3+1)D superspace group to the 3D space group, there are three symmetry space groups along different t -sections: $B2eb$ (41), $Bbeb$ (68) and $Bmcb$ (64). Among these space groups, $Bmcb$ gives significantly better agreement with the experimental data than the others. Relevant crystallographic data are compiled in Table A.5. The modulated $[\text{MnSe}_2]^{2-}$ layer consists of blocks of six corner-sharing $\text{MnSe}_{4/2}$ -tetrahedra which are separated by a pair of edge-sharing tetrahedra as shown in Figure 4.29. This motif is already known from the compound $(\text{Ce}_{0.78}\text{La}_{0.22})_2\text{O}_2\text{MnSe}_2$ in the solid solution $\text{Ce}_{2-x}\text{La}_x\text{O}_2\text{MnSe}_2$ ($0 \leq x \leq 1.4$).^[17]

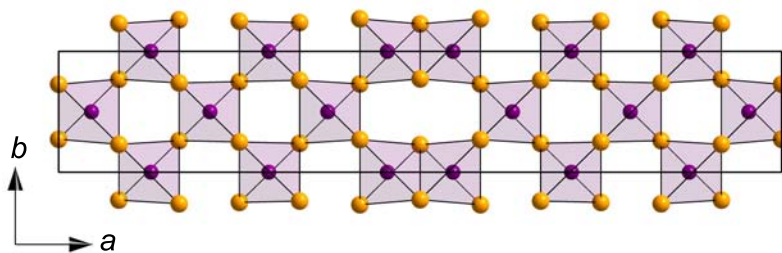


Figure 4.29 $[\text{MnSe}_2]^{2-}$ layer of $(\text{La}_{0.55}\text{Pr}_{0.45})_2\text{O}_2\text{MnSe}_2$. Approximant $a = 6a(\text{sub})$. Space group $Bmcb$ ($t_0 = 0$).

$\text{La}_{2-x}\text{Nd}_x\text{O}_2\text{MnSe}_2$

We were also successful to partially substitute La^{3+} by the even smaller Nd^{3+} ($r_{\text{La}} = 143.4$ pm, $r_{\text{Nd}} = 136.1$ pm)^[15] in the solid solution $\text{La}_{2-x}\text{Nd}_x\text{O}_2\text{MnSe}_2$ ($0 \leq x \leq 0.6$). The lattice

parameters, the cell volume and the modulation vector component α across the series are plotted in Figure 4.30. The solubility limit is beyond $x = 0.5$. In this range, the cell parameters decrease linearly whereas the modulation vector component α shows a similar behavior as for the substitution with praseodymium. However, also the sample with $x = 0.6$ beyond the solubility limit shows reasonable lattice parameters as well as values for the cell volume and α which are in line with the others. This indicates that the actual composition fits with the nominal composition although the increasing formation of impurities. EDX analysis confirmed these observations. However, we were not able to prepare samples with an even higher neodymium content.

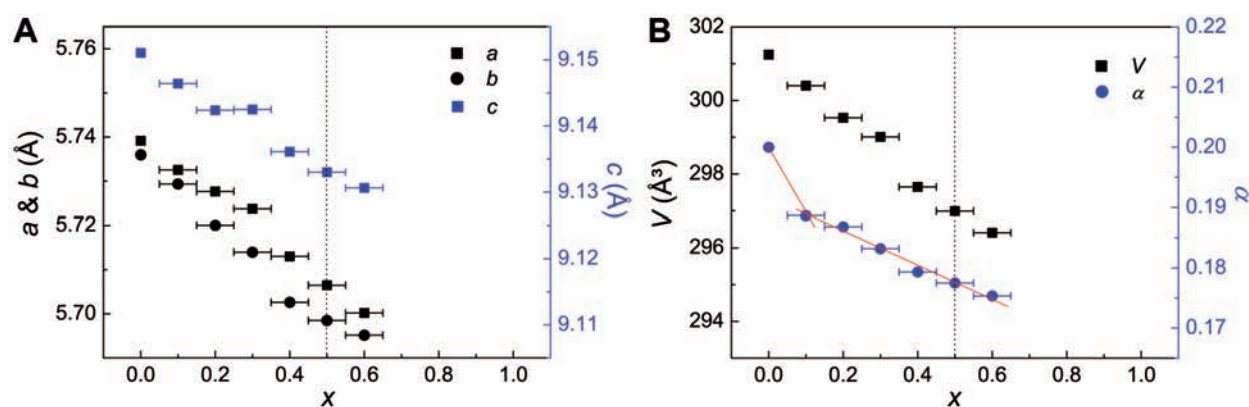


Figure 4.30 (A) Lattice parameters a (black squares), b (black dots) and c (blue squares) and (B) the cell volume of the orthorhombic unit cell (black squares) and the modulation vector component α (blue dots) versus x . Dotted lines symbolize the solubility limit. Red lines are guides to the eye.

Comparison of the Solid Solutions $\text{La}_{2-x}\text{RE}_x\text{O}_2\text{MnSe}_2$ ($\text{RE} = \text{Ce-Nd}$)

The structural relationship between all known $\text{RE}_2\text{O}_2\text{TSe}_2$ compounds which retain a ZrCu-SiAs-related structure can be found in their ratio of edge- to corner-sharing $\text{TSe}_{4/2}$ -tetrahedra. The compounds $\text{La}_2\text{O}_2\text{CdSe}_2$ and $\text{Ce}_2\text{O}_2\text{CdSe}_2$ ($\alpha = 0$) adopt a checkerboard arrangement of the transition metal vacancies with only corner-sharing tetrahedra. On the other side, $\text{La}_2\text{O}_2\text{FeSe}_2$ and $\text{Ce}_2\text{O}_2\text{FeSe}_2$ ($\alpha = 1$) show a contrary behavior as they build strands of only edge-sharing tetrahedra. $\text{La}_2\text{O}_2\text{MnSe}_2$ ($\alpha = \frac{1}{5}$), which we discovered recently, and $(\text{La}_{0.55}\text{Pr}_{0.45})_2\text{O}_2\text{MnSe}_2$, which we present in this paper ($\alpha = \frac{1}{6}$), can be seen as intermediates (Figure 4.31). They adopt both features, on the one hand, domains with a checkerboard arrangement which are five or six corner-sharing tetrahedra broad, respectively. On the other hand, these domains are separated by pairs of edge-sharing tetrahedra.

Figure 4.32 shows the plot of the modulation vector component α against the relative effective radii $r_{\text{eff,rel}}$ which is defined as follows:

$$r(\text{eff,rel}) = \frac{\frac{2-x}{2}r(\text{La}) + \frac{x}{2}r(\text{RE})}{r(\text{La})} \quad (4.3)$$

with $\text{RE} = \text{Ce, Pr, Nd}$.

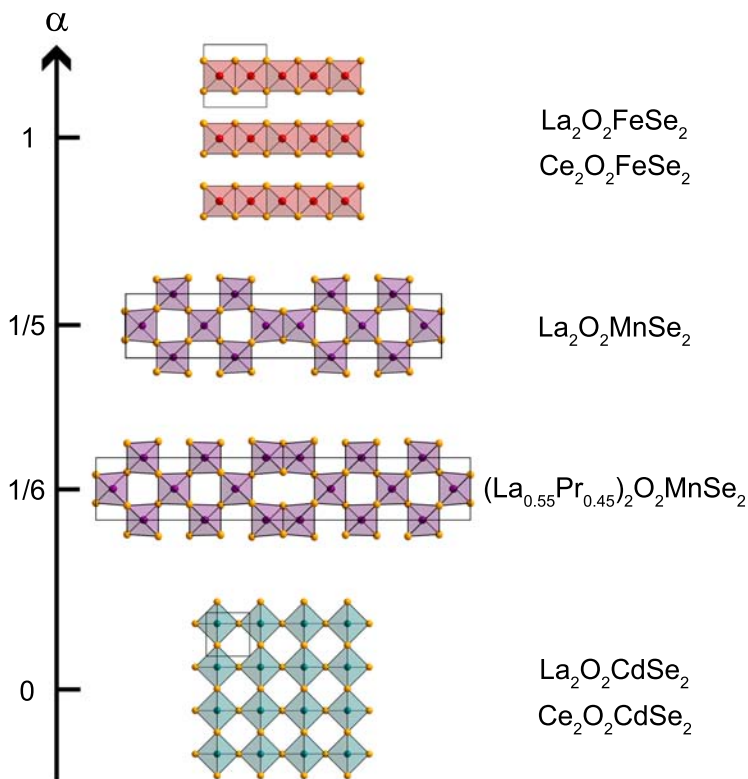


Figure 4.31 Schematic presentation of the influence of the modulation vector component α on the ratio of edge- and corner-sharing tetrahedra in the modulated structures.

Comparison of the data of the solid solutions $\text{La}_{2-x}\text{RE}_x\text{O}_2\text{MnSe}_2$ ($\text{RE} = \text{Ce-Nd}$) shows an almost linear trend in the range $0.2 \leq x \leq 2$ (dotted and dashed lines). This finding enhances the conclusion that the modulation in the $[\text{TSe}_2]^{2-}$ layers of these compounds is controlled by the effective radius of the rare-earth metal in the $[\text{La}_{2-x}\text{RE}_x\text{O}_2]^{2+}$ layer in the same degree in this range. However, the solid solutions show a divergent behavior in the range $0 \leq x < 0.2$ as α increases stronger than expected until the end compound ($x = 0$) is reached. For $\text{RE} = \text{Ce}$, there is no data available for the range $0 < x < 0.3$. However, the approximation to the end compound $\text{La}_2\text{O}_2\text{MnSe}_2$ leads to the conclusion that a linear trend is also unlikely.

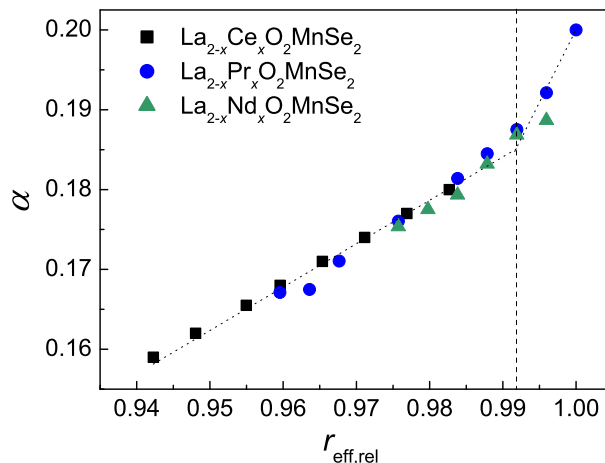


Figure 4.32 Modulation vector component α versus the relative effective radius of the particular (mixed) rare-earth metal in tetrahedral environment. The dashed line symbolizes $x = 0.2$ and the dotted lines are guides to the eye. Data points of $\text{La}_{2-x}\text{Ce}_x\text{O}_2\text{MnSe}_2$ are taken from the literature.^[17]

4.2.5 Conclusion

The solid solutions of the layered oxychalcogenides $\text{La}_{2-x}\text{Pr}_x\text{O}_2\text{MnSe}_2$ ($0 \leq x \leq 1$) and $\text{La}_{2-x}\text{Nd}_x\text{O}_2\text{MnSe}_2$ ($0 \leq x \leq 0.6$) have been prepared by a solid state flux synthesis. The solubility limit of praseodymium was determined to be $x \approx 0.9$ and that of neodymium $x \approx 0.5$. The crystal structures were determined using powder X-ray diffraction and single crystal X-ray data and can be described with a (3+1)D superspace model in superspace group $Cmme(\alpha 0 \frac{1}{2})0s0$. The modulation vector component α decreases with increasing praseodymium or neodymium content leading to mostly incommensurate values for α . $(\text{La}_{0.55}\text{Pr}_{0.45})_2\text{O}_2\text{MnSe}_2$ represents in this solid solution the unique case where α adopts a value of $\alpha = \frac{1}{6}$. This allows to approximate the projection onto 3D space by using a simple sixfold a -axis. Comparing the solid solutions $\text{La}_{2-x}\text{RE}_x\text{O}_2\text{MnSe}_2$ ($\text{RE} = \text{Ce}^{[17]}, \text{Pr}, \text{Nd}$) leads to the conclusion that α is affected equally in a wide range with respect to the effective relative radii of the rare-earth metals. However, α decreases stronger than expected in the range $0 \leq x < 0.2$ which is not an effect of the structural changes but an intrinsic effect of the solid solutions.

4.3 Flux Synthesis, Crystal Structures, and Magnetism of the Series $\text{La}_{2n+2}\text{MnSe}_{n+2}\text{O}_{2n+2}$ ($n = 0-2$)

S. Peschke and D. Johrendt

Parts published in: *Inorganics* **2017**, 5, 9.

4.3.1 Abstract

Three members of the homologous series of manganese oxyselenides with the general formula $\text{La}_{2n+2}\text{MnSe}_{n+2}\text{O}_{2n+2}$ ($n = 0-2$) have been synthesized in a NaI/KI flux and characterized by single-crystal X-ray diffraction, powder X-ray diffraction and magnetic measurements. The structures consist of chains of edge-sharing MnSe_4O_2 -octahedra along the b -axis which are linked together along the a -axis by edge-sharing OLa_4 - and/or OLa_3Mn -tetrahedra forming infinite ribbons of increasing width. mC - $\text{La}_2\text{MnSe}_2\text{O}_2$ ($\text{Pb}_2\text{HgCl}_2\text{O}_2$ -type, $C2/m$, $a = 11.6621(5)$ Å, $b = 3.9719(1)$ Å, $c = 7.2049(3)$ Å, $\beta = 121.655(2)^\circ$) represents a new polymorph of this compound. $\text{La}_4\text{MnSe}_3\text{O}_4$ ($P2/m$, $a = 9.0055(4)$ Å, $b = 4.0186(1)$ Å, $c = 7.1946(3)$ Å, $\beta = 109.715(2)^\circ$) and $\text{La}_6\text{MnSe}_4\text{O}_6$ ($C2/m$, $a = 24.760(2)$ Å, $b = 4.0359(3)$ Å, $c = 7.1850(6)$ Å, $\beta = 104.162(3)^\circ$) exhibit new structure types. Magnetic measurements suggest antiferromagnetic order of the moments below about 15 K with effective magnetic moments of 5.53(1), 5.99(1) and 6.01(1) μ_B per formula unit for $n = 1, 2$ and 3, respectively.

4.3.2 Introduction

The research into structural chemistry and physical properties of transition-metal oxyselenides has been very fruitful during the last years. Numerous new compounds with the general formula $\text{RE}_2\text{TSe}_2\text{O}_2$ ($\text{RE} = \text{La}, \text{Ce}$; $\text{T} = \text{Cd}, \text{Fe}, \text{Mn}, \text{Zn}$)^[2-5,7,14,16-18] have been discovered and their structures and magnetism have been studied. Among the particular families, different polymorphs may exist which makes the diversity even bigger. In order to distinguish the different polymorphs mentioned in this paper, we extended the formulas by the *Pearson* letters. Recently, we found new polymorphs in the $\text{RE}_2\text{FeSe}_2\text{O}_2$ -family ($\text{RE} = \text{La}, \text{Ce}$).^[3] mC - $\text{La}_2\text{FeSe}_2\text{O}_2$ and mC - $\text{Ce}_2\text{FeSe}_2\text{O}_2$ crystallize in the $\text{Pb}_2\text{HgCl}_2\text{O}_2$ -structure type with edge-sharing, distorted FeSe_4O_2 -octahedra linked together by edge-sharing OLa_3Fe -tetrahedra forming infinite ribbons which are two tetrahedra in width, which is shown

in Figure 4.33 (D). Similar building blocks with an analogous connectivity between the TSe_4O_2 -octahedra and the ORE_3T -tetrahedra have already been observed in the compounds $RE_{3,67}Ti_2Se_6O_3$ ($RE = Ce, Nd, Sm$), $La_4Ti_2Se_5O_4$, $La_6Ti_3Se_9O_5$ and $CeCrSe_2O$.^[19–21] Beside the mentioned iron compounds, there are two polymorphs known in the analogous manganese family, $oC-La_2MnSe_2O_2$ ^[16] and $oA-La_2MnSe_2O_2$ ^[7] (Fig. 4.33 A and B). $oC-La_2MnSe_2O_2$ has a defect ZrCuSiAs-type structure with slabs of edge-sharing OLa_4 -tetrahedra stacked alternating with slabs of $MnSe_4$ -tetrahedra. The structure of $oA-La_2MnSe_2O_2$ (Fig. 4.33 B) consists of $MnSe_4$ -tetrahedra and edge-sharing $MnSe_4O_2$ -octahedra which are connected by infinite ribbons of edge-sharing OLa_4 - and OLa_3Mn -tetrahedra four units wide.

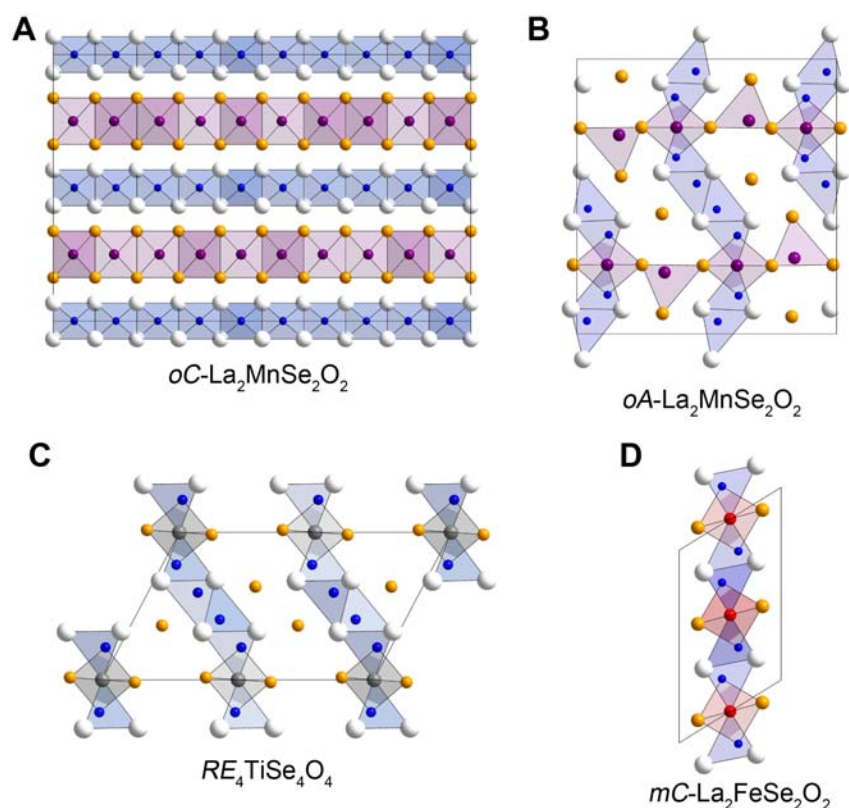


Figure 4.33 Illustration of the crystal structures of (A) $oC-La_2MnSe_2O_2$, (B) $oA-La_2MnSe_2O_2$, (C) $RE_4TiSe_4O_4$ and (D) $mC-La_2FeSe_2O_2$. ORE_4 - and OLa_3T -tetrahedra in blue, $MnSe_4O_2$ -octahedra and $MnSe_4$ -tetrahedra in violet, $TiSe_4O_2$ -octahedra in gray, and $FeSe_4O_2$ -octahedra in red. Rare-earth in white, manganese in violet, titanium in gray, iron in red, selenium in orange and oxygen in blue.

Beside oxyselenides with the general chemical composition mentioned above, numerous other rare-earth oxyselenides are known, for example $RE_4TiSe_4O_4$ ($RE = Sm, Gd-Er, Y$)^[22,23] and $RE_4O_4Se[Se_2]$ ($RE = La-Nd, Sm$)^[24]. $RE_4TiSe_4O_4$ can be regarded as a defect

variant of *oA*-La₂MnSe₂O₂ with the same building blocks but without TiSe₄-tetrahedra as depicted in Figure 4.33 (C). In contrast, RE₄O₄Se[Se₂] compounds contain Se²⁻ anions, as well as [Se–Se]²⁻ dumbbells, which are separated by layers of distorted [ORE₄]¹⁰⁺ tetrahedra. Their magnetism originates from the 4*f*-electrons of the particular rare-earth metal, and spin frustration is observed in the rare-earth-oxide tetrahedra of these compounds.^[24] Formally, it should be possible to insert divalent transition-metals in this structure by breaking up the diselenide units leading to the formula RE₄TSe₃O₄.

In this paper, we present La₄MnSe₃O₄ as the first example of such compounds with only Se²⁻ anions in a new structure related to the RE₄TiSe₄O₄-type. La₄MnSe₃O₄ can formally be obtained by adding one La₂SeO₂-unit to La₂MnSe₂O₂. We were also successful to add a second La₂SeO₂-unit in order to obtain the compound La₆MnSe₄O₆, which represents the third member of the homologous series La_{2n+2}MnSe_{n+2}O_{2n+2}. Additionally we have found *mC*-La₂MnSe₂O₂ as a new polymorph to the manganese-family and present magnetic susceptibility data of all compounds.

4.3.3 Experimental Details

All starting materials (purity $\geq 99.9\%$) were handled in an argon-filled glove box (M. Braun, $p(\text{O}_2) \leq 1$ ppm, $p(\text{H}_2\text{O}) \leq 1$ ppm). Powder samples and single crystals of *mC*-La₂MnSe₂O₂ were prepared in a NaI/KI-flux synthesis starting from *oC*-La₂MnSe₂O₂, which was prepared as described in Ref. [16]. *oC*-La₂MnSe₂O₂ (0.10 g) was sandwiched with 0.30 g of a eutectic mixture of NaI/KI (mass ratio 0.6:0.4, dried in dynamic vacuum at 673 K) in an alumina crucible. The crucible was sealed in an argon filled silica tube and heated to 1273 K at a rate of 100 K/h, kept at this temperature for 50 h and cooled to room temperature at a cooling rate of 100 K/h. Powder samples and single crystals of La₄MnSe₃O₄ and La₆MnSe₄O₆ were prepared in a two step reaction of appropriate amounts of La₂O₃, La₂Se₃ and MnSe. The rare-earth oxide was heated to 1273 K prior to use. La₂Se₃ was prepared by the reaction of freshly filed rare-earth metal and selenium powder at 573 K for 12 h. MnSe was prepared by the reaction of manganese and selenium powder at 1023 K for 24 hours. The starting materials (0.20 g) were mixed intimately, filled in an alumina crucible, sealed in an argon filled silica tube and heated to 873 K at a rate of 25 K/h, kept at this temperature for 10 h and slowly cooled to room temperature at a cooling rate of 50 K/h. In a second step, the reaction

mixture was ground in an agate mortar and sandwiched between 0.50 g of an eutectic mixture of NaI/KI. The crucibles were sealed in argon filled silica tubes and heated to 1073 K at a rate of 50 K/h, then to 1273–1373 K at a rate of 25 K/h, kept at this temperature for 40 h and cooled to room temperature at a cooling rate of 100 K/h. The reaction mixtures were then washed with deionized water and ethanol and dried in vacuum. The resulting samples were yellow-brown powders (purity > 95 wt%) and bright brown, transparent single crystals. The compounds are stable in air for months. Single-crystal X-ray diffraction data was collected with a Bruker D8 QUEST (fixed- χ goniometer, Mo- K_{α} , $I\mu\text{S}$ with HE-LIOS multi-layer optics, PHOTON 100 detector). Reflection intensity integrations, data reductions, and multi-scan absorption corrections were done with APEX2^[9] and SADABS^[10]. The structures were solved with Jana2006^[11]. X-ray powder diffraction patterns were recorded at 300 K using a Huber G670 diffractometer with $\text{CuK}_{\alpha 1}$ radiation (Ge(111)-monochromator). Rietveld refinements were done with TOPAS^[12]. Magnetisation isotherms and susceptibility measurements were performed with a MPMS-XL SQUID magnetometer (Quantum Design Inc.).

4.3.4 Results

Since conventional solid state synthesis did not lead to satisfying results, a flux synthesis was developed in order to get high purity samples (> 95 wt%). $mC\text{-La}_2\text{MnSe}_2\text{O}_2$ was synthesized in a NaI/KI-flux at 1273 K starting from the low temperature polymorph $oC\text{-La}_2\text{MnSe}_2\text{O}_2$. The other two members of the homologous series were synthesized starting from the binary compounds La_2O_3 , La_2Se_3 and MnSe , which were pre-reacted at 873 K, homogenized and then heated in a NaI/KI-flux at 1273–1373 K. After washing the reaction mixture to remove the flux, a large amount of bright brown, transparent rod-like crystals, as well as polycrystalline yellow-brown powders were obtained.

The crystal structures were determined by single-crystal X-ray diffraction. A comparison of the obtained data is given in Table 4.3. $mC\text{-La}_2\text{MnSe}_2\text{O}_2$ and $\text{La}_6\text{MnSe}_4\text{O}_6$ adopt monoclinic $C2/m$ (No. 12) symmetry, whereas $\text{La}_4\text{MnSe}_3\text{O}_4$ crystallizes in space group $P2/m$ (No. 10). It is noticeable, that the lattice parameter b increases ($\approx 1.6\%$) and c decreases ($\approx 0.3\%$) slightly with increasing n . In contrast, the monoclinic angle β decreases strongly ($\approx 14\%$) with increasing n . Further relevant crystallographic data are compiled in Tables A.6–A.8. Rietveld refinements of the X-ray powder patterns (Fig. 4.34) of $mC\text{-}$

$\text{La}_2\text{MnSe}_2\text{O}_2$ and $\text{La}_6\text{MnSe}_4\text{O}_6$ revealed small fractions of impurity phases of $\approx 1\%$ MnSe or $\approx 4\%$ La_2SeO_2 , respectively. The $\text{La}_4\text{MnSe}_3\text{O}_4$ sample contained a minor impurity phase (peak at $2\theta \approx 31^\circ$) which has not been identified.

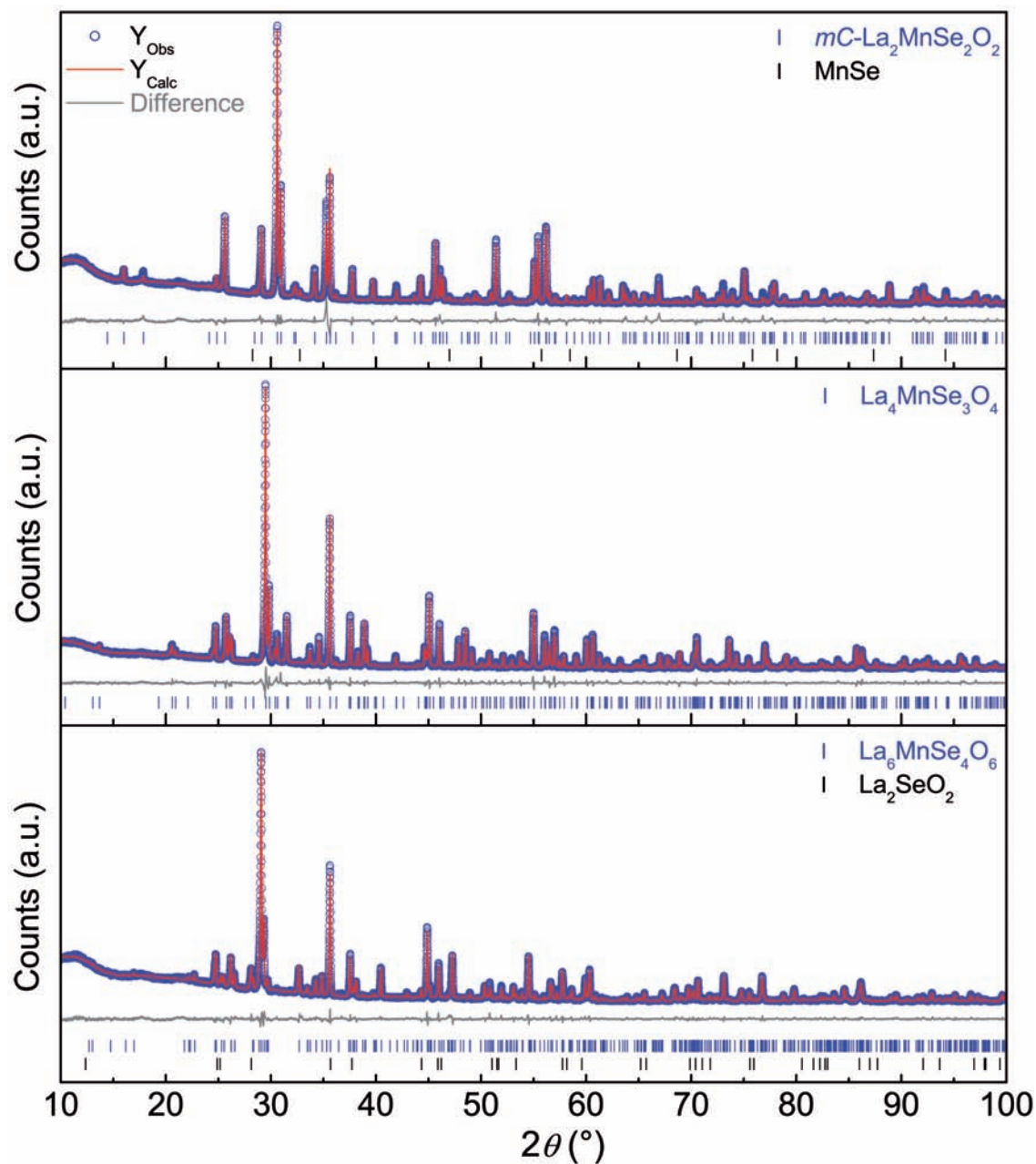


Figure 4.34 X-ray powder patterns (blue), Rietveld fits (red) and difference plots (gray) of $mC\text{-La}_2\text{MnSe}_2\text{O}_2$ (top), $\text{La}_4\text{MnSe}_3\text{O}_4$ (middle) and $\text{La}_6\text{MnSe}_4\text{O}_6$ (bottom).

Table 4.3 Crystal data and structure refinement data of $\text{La}_{2n+2}\text{MnSe}_{n+2}\text{O}_{2n+2}$ ($n = 0-2$). Atom positions can be found in Tables A.6, A.7 and A.8

	$mC\text{-La}_2\text{MnSe}_2\text{O}_2$	$\text{La}_4\text{MnSe}_3\text{O}_4$	$\text{La}_6\text{MnSe}_4\text{O}_6$
n	0	1	2
Space group	$C2/m$	$P2/m$	$C2/m$
a /Å	11.6621(5)	9.0055(4)	24.760(2)
b /Å	3.9719(1)	4.0186(1)	4.0359(3)
c /Å	7.2049(3)	7.1946(3)	7.1850(6)
β /°	121.655(2)	109.715(2)	104.162(3)
V /Å ³	284.08(2)	245.11(2)	696.16(10)
Z	2	1	2
$R_{\text{int}}, R_{\sigma}$	2.38, 3.16	2.75, 2.09	5.25, 4.83
θ_{max} /°	53.88	34.98	35.10
$R_1(\text{obs/all})$	0.024/0.036	0.023/0.032	0.023/0.049
$wR_2(\text{obs/all})$	0.048/0.051	0.050/0.056	0.041/0.049
$GooF$	1.20	1.51	1.00
$\Delta\rho_{\text{max}}, \Delta\rho_{\text{min}}/\text{e}\text{Å}^{-3}$	+1.9/-2.5	+3.9/-1.7	+1.7/-1.7

$mC\text{-La}_2\text{MnSe}_2\text{O}_2$

$mC\text{-La}_2\text{MnSe}_2\text{O}_2$ crystallizes isotypic with $mC\text{-La}_2\text{FeSe}_2\text{O}_2$ and $mC\text{-Ce}_2\text{FeSe}_2\text{O}_2$ in the $\text{Pb}_2\text{HgCl}_2\text{O}_2$ -type structure.^[3] The iron compounds are low-temperature polymorphs in the $RE_2\text{FeSe}_2\text{O}_2$ family (dwelling temperature = 1073 K), while $mC\text{-La}_2\text{MnSe}_2\text{O}_2$ is observed at high temperatures (≥ 1273 K). The structure of $mC\text{-La}_2\text{MnSe}_2\text{O}_2$ consists of chains of distorted, edge-sharing MnSe_4O_2 -octahedra along the b -axis which are linked together along the a -axis by edge-sharing OLa_3Mn -tetrahedra forming infinite ribbons parallel to b (Fig. 4.35). The La^{3+} ion has a distorted LaSe_5O_3 square antiprismatic coordination environment (Fig. 4.36), which was already observed in $RE_4\text{TiSe}_4\text{O}_4$ compounds^[22,23]. Similar to all $RE_2\text{FeSe}_2\text{O}_2$ polymorphs, the displacement ellipsoid of the manganese atom in $mC\text{-La}_2\text{MnSe}_2\text{O}_2$ exhibits an oblate spheroid shape in direction of the selenium atoms which is a consequence of the distorted MnSe_4O_2 -octahedra. The distance between two manganese atoms in the MnSe_4O_2 chains (d_{intra}) is 397.2(1) pm, whereas the distance between the chains (d_{inter}) is 583.1(1) pm. Mn-O and Mn-Se bond lengths are 205.4(1) and 284.1(1) pm, respectively, which shows that MnSe_4O_2 -octahedra are strongly compressed towards the oxygen atoms. The O-Mn-Se and Se-Mn-Se bond angles within the MnSe_4O_2 -octahedra are nearly

regular ($88.7(1)$ – $91.3(1)^\circ$), while the La-O-La and La-O-Mn bond angles in the OLa_3Mn -tetrahedra are $105.1(1)$ – $115.8(1)^\circ$, and thus differ significantly from a perfect tetrahedral shape (109.5°).

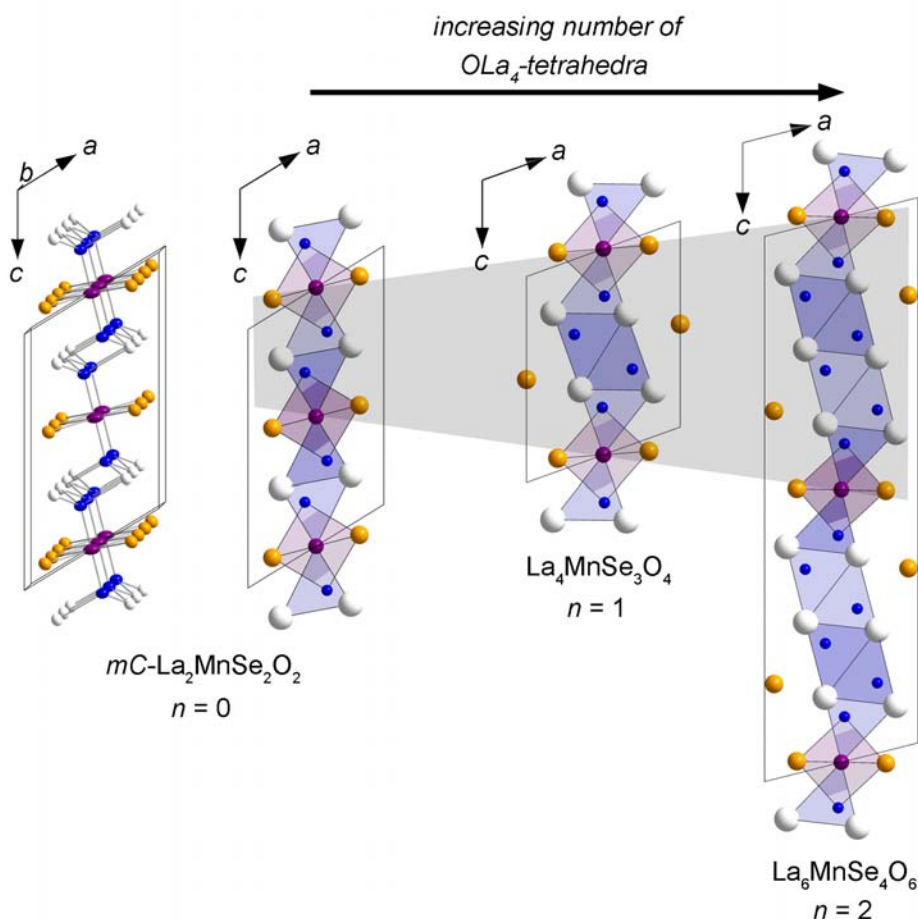


Figure 4.35 Crystal structures of $\text{La}_{2n+2}\text{MnSe}_{n+2}\text{O}_{2n+2}$ ($n = 0$ – 2). OLa_4 - and OLa_3Mn -tetrahedra in blue, MnSe_4O_2 -octahedra in violet. Rare-earth in white, manganese in violet, selenium in orange and oxygen in blue.

$\text{La}_4\text{MnSe}_3\text{O}_4$ and $\text{La}_6\text{MnSe}_4\text{O}_6$

$\text{La}_4\text{MnSe}_3\text{O}_4$ and $\text{La}_6\text{MnSe}_4\text{O}_6$ crystallize in new structure types which contain two or three crystallographically independent La atoms with two different coordination environments, respectively. The crystal structures are closely related to that of $mC\text{-La}_2\text{MnSe}_2\text{O}_2$ (Fig. 4.35). They also consist of chains of edge-sharing MnSe_4O_2 -octahedra along the b -axis. However, these octahedra are connected by two edge-sharing OLa_3Mn - as well as either two or four additional OLa_4 -tetrahedra along the a -axis, respectively. The framework of four units wide, edge-sharing tetrahedra forming infinite ribbons was already observed in $\text{RE}_4\text{TiSe}_4\text{O}_4$ ^[22,23]

and *oP/oA*-La₂TSe₂O₂ (T = Fe, Mn)^[7]. Frameworks with six units wide tetrahedra are, to our best knowledge, unknown so far. La₄MnSe₃O₄ has two crystallographically independent La³⁺ ions which have either a La(1)Se₅O₃ square antiprismatic or a La(2)Se₃O₄ monocapped trigonal antiprismatic coordination environment. La₆MnSe₄O₆ contains a third independent La³⁺ ion which shows also a monocapped trigonal antiprismatic coordination. A comparison of the coordination environments of the different lanthanum ions is depicted in Figure 4.36. The coordination polyhedra of La(1) and La(2) as well as La(2) and La(3) are connected via common Se-O edges. Compared to *mC*-La₂MnSe₂O₂, d_{intra} is slightly and d_{inter} is significantly longer in La₄MnSe₃O₄ and La₆MnSe₄O₆ as depicted in Table 4.4.

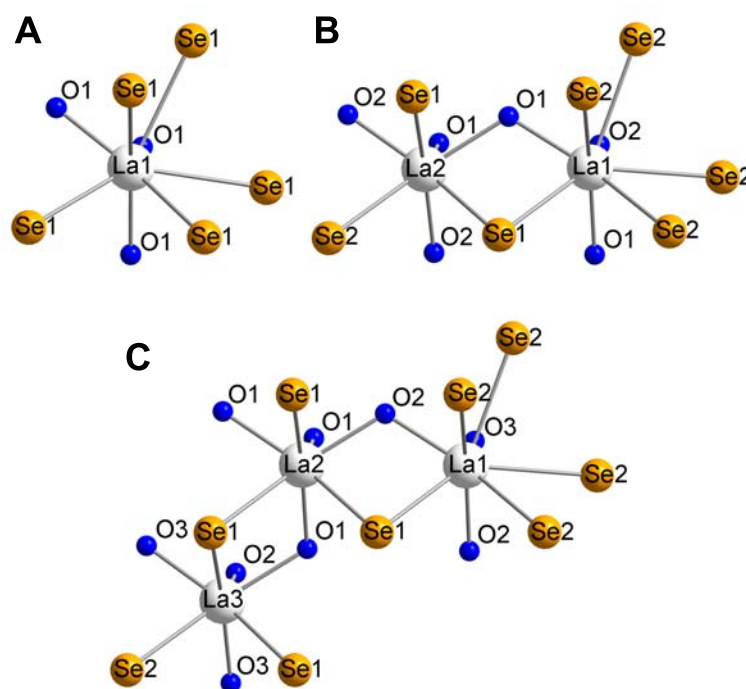


Figure 4.36 Coordination environments of the lanthanum ions in (A) *mC*-La₂MnSe₂O₂, (B) La₄MnSe₃O₄ and (C) La₆MnSe₄O₆, showing the connectivity between the distorted square and the monocapped trigonal antiprisms.

Selected bond lengths of the three members of the homologous series are depicted in Table 4.4. The Mn-O, Mn-Se and La-O bond lengths of La₄MnSe₃O₄ and La₆MnSe₄O₆ are very similar leading to strongly compressed MnSe₄O₂-octahedra analog to those in *mC*-La₂MnSe₂O₂. As observed in *mC*-La₂MnSe₂O₂, the octahedra in La₄MnSe₃O₄ and La₆MnSe₄O₆ are more regular than the tetrahedra with respect to the bond angles listed in Table 4.5.

Table 4.4 Distances between the manganese atoms in (d_{intra}) and between (d_{inter}) the MnSe_4O_2 -octahedra chains and selected bond lengths (/pm) of $mC\text{-La}_2\text{MnSe}_2\text{O}_2$ ($n = 0$), $\text{La}_4\text{MnSe}_3\text{O}_4$ ($n = 1$) and $\text{La}_6\text{MnSe}_4\text{O}_6$ ($n = 2$).

n	d_{intra}	d_{inter}	$d(\text{Mn-O})$	$d(\text{Mn-Se})$	$d(\text{La-O})$	$d(\text{La-Se})$
0	397.2(1)	616.0(2)	205.4(1)	284.1(1)	234.4(1)–240.8(1)	315.9(1)–337.1(1)
1	401.9(1)	900.6(1)	207.0(1)	284.8(1)	236.4(1)–246.5(1)	313.0(1)–333.8(1)
2	403.6(1)	1247.8(2)	207.7(1)	284.8(1)	236.2(1)–245.2(1)	309.4(1)–333.3(1)

Table 4.5 Selected bond angles ($^\circ$) of $mC\text{-La}_2\text{MnSe}_2\text{O}_2$ ($n = 0$), $\text{La}_4\text{MnSe}_3\text{O}_4$ ($n = 1$) and $\text{La}_6\text{MnSe}_4\text{O}_6$ ($n = 2$).

n	$\angle(\text{La-O-La})$	$\angle(\text{La-O-Mn})$	$\angle(\text{Se-Mn-Se})$	$\angle(\text{Se-Mn-O})$
0	105.1(1)–115.8(1)	106.4(1)–111.7(1)	88.7(1)–91.3(1)	89.5(1)–90.5(1)
1	102.8(1)–116.4(1)	106.9(1)–109.8(1)	89.8(1)–90.2(1)	87.8(1)–92.2(1)
2	102.8(1)–117.3(1)	106.0(1)–109.9(1)	89.8(1)–90.2(1)	88.0(1)–92.0(1)

Magnetism

The magnetic susceptibilities of $mC\text{-La}_2\text{MnSe}_2\text{O}_2$, $\text{La}_4\text{MnSe}_3\text{O}_4$ and $\text{La}_6\text{MnSe}_4\text{O}_6$ (Fig. 4.37) obey the Curie-Weiss rule and indicate antiferromagnetic ordering of the moments near 15 K, similar to the Néel temperature of $mC\text{-La}_2\text{FeSe}_2\text{O}_2$ ($T_N = 20$ K). In case of $mC\text{-La}_2\text{MnSe}_2\text{O}_2$ and $\text{La}_4\text{MnSe}_3\text{O}_4$, χ_{mol} decreases clearly below this temperature, whereas the effect is more distinctive for $mC\text{-La}_2\text{MnSe}_2\text{O}_2$. In contrast, the susceptibility of $\text{La}_6\text{MnSe}_4\text{O}_6$ shows no decrease in χ_{mol} but a clear turning point of the curve at this temperature.

Isothermal magnetization plots (Fig. A.1) at 300 K are linear with field. $mC\text{-La}_2\text{MnSe}_2\text{O}_2$ exhibits a tiny hysteresis at 1.8 K, which can be due to small impurities, while those of $\text{La}_4\text{MnSe}_3\text{O}_4$ and $\text{La}_6\text{MnSe}_4\text{O}_6$ are nearly linear at 1.8 K. Plots of the inverse susceptibilities versus temperature (insets in Fig. 4.37) allow Curie-Weiss fits. The resulting effective magnetic moments (μ_{eff}) are 5.53(1), 5.98(1) and 6.01(1) μ_B per formula unit for $n = 1, 2$ and 3, respectively. Only the value for $mC\text{-La}_2\text{MnSe}_2\text{O}_2$ is slightly smaller than the theoretical moment of Mn^{2+} (5.92 μ_B). Negative values of the Weiss constant θ (Table 4.6) support antiferromagnetic ordering in all compounds.

The detailed magnetic structure is not ascertainable from susceptibility data. We have recently determined the spin structure of $\text{La}_2\text{CrSe}_2\text{O}_2$ which is isotypic to $mC\text{-La}_2\text{MnSe}_2\text{O}_2$. Neutron powder diffraction^[25] experiments revealed a three-dimensional (G-type) ordering,

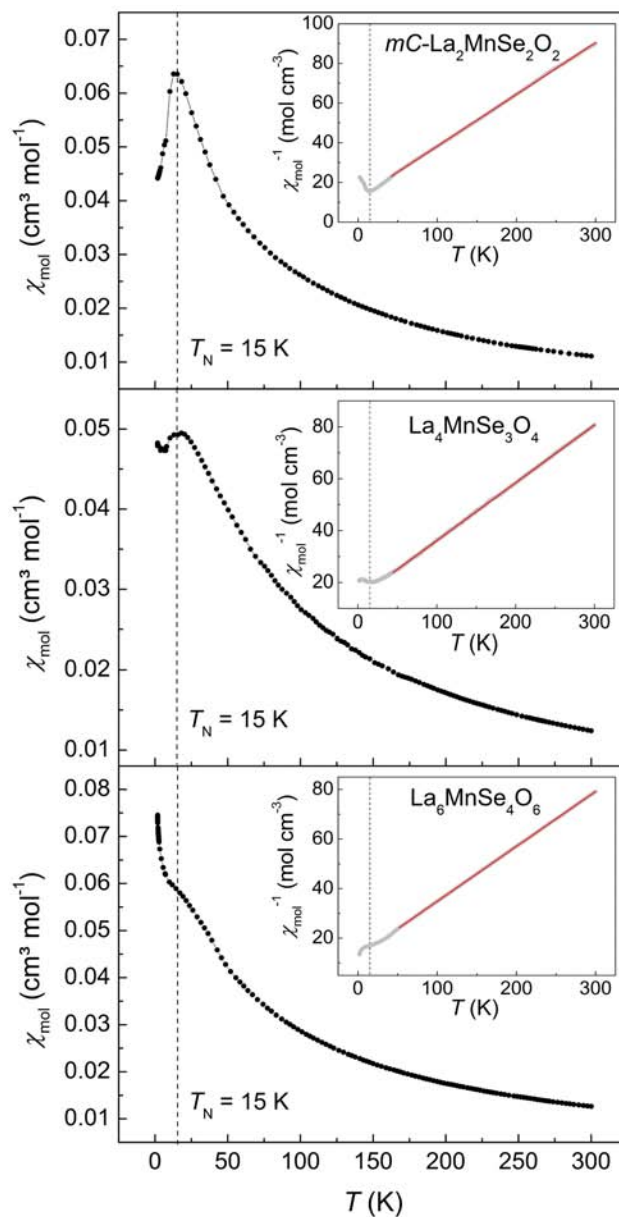


Figure 4.37 Magnetic susceptibilities (black, $B = 1$ T) and inverse susceptibilities (inset) of mC - $\text{La}_2\text{MnSe}_2\text{O}_2$ (top), $\text{La}_4\text{MnSe}_3\text{O}_4$ (middle) and $\text{La}_6\text{MnSe}_4\text{O}_6$ (bottom) with Curie-Weiss fit (red). Parameters obtained from the fits are given in Table 4.6. Dashed lines represent $T_N = 15$ K.

Table 4.6 Magnetic data of mC - $\text{La}_2\text{MnSe}_2\text{O}_2$, $\text{La}_4\text{MnSe}_3\text{O}_4$ and $\text{La}_6\text{MnSe}_4\text{O}_6$.

Compound	μ_{eff} (μ_B)	θ (K)	C ($\text{cm}^3 \text{K mol}^{-1}$)
mC - $\text{La}_2\text{MnSe}_2\text{O}_2$	5.53(1)	-46.5(1)	3.82(1)
$\text{La}_4\text{MnSe}_3\text{O}_4$	5.99(1)	-62.1(1)	4.48(1)
$\text{La}_6\text{MnSe}_4\text{O}_6$	6.01(1)	-57.4(1)	4.51(1)

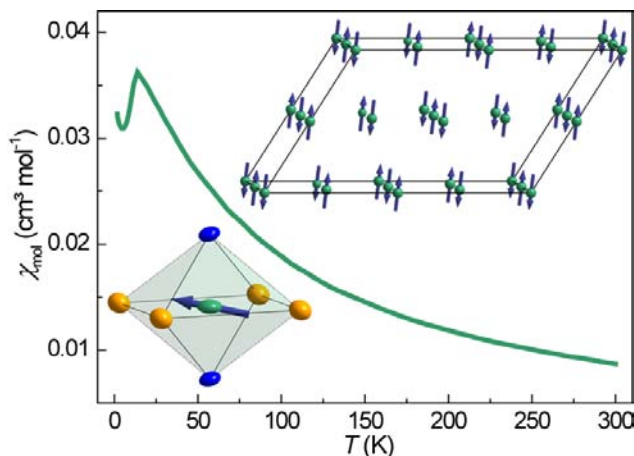
tantamount to antiferromagnetic order within and between the chains of CrSe_4O_2 -octahedra. mC - $\text{La}_2\text{MnSe}_2\text{O}_2$ has presumably the same magnetic structure, and the almost identical Néel temperatures suggest at least similar magnetic ordering patterns in $\text{La}_4\text{MnSe}_3\text{O}_4$ and $\text{La}_6\text{MnSe}_4\text{O}_6$.

4.3.5 Conclusion

We have reported the synthesis, structural characterization and magnetic properties of three new oxyselenides, which are members of the homologous series $\text{La}_{2n+2}\text{MnSe}_{n+2}\text{O}_{2n+2}$ ($n = 0-2$). The compounds are accessible using a flux synthesis at high temperatures (1273–1373 K). The crystal structures contain edge-sharing, distorted MnSe_4O_2 -octahedra along the b -axis as common building block. These are linked together along the a -axis by edge-sharing OLa_3Mn - and/or OLa_4 -tetrahedra forming ribbons of increasing width. The lattice parameters b and c vary only slightly whereas the monoclinic angle decreases strongly with increasing n . The magnetic susceptibilities obey the Curie-Weiss rule with effective magnetic moments compatible to Mn^{2+} and indicate antiferromagnetic ordering below 15 K.

4.4 Flux Synthesis, Crystal Structures, and Magnetic Ordering of the Rare-Earth Chromium(II) Oxyse-lenides $RE_2CrSe_2O_2$ ($RE = La-Nd$)

S. Peschke, V. Weippert, A. Senyshyn, M. Mühlbauer, O. Janka, R. Pöttgen, S. Holenstein, H. Luetkens, and D. Johrendt



published in: *Inorg. Chem.* **2017**, *56*, 2241–2247.

Copyright 2017, American Physical Society.

4.4.1 Abstract

The rare-earth chromium(II) oxyse-lenides $RE_2CrSe_2O_2$ ($RE = La-Nd$) were synthesized in eutectic NaI/KI fluxes, and their crystal structures were determined by single crystal and powder X-ray diffraction ($Pb_2HgCl_2O_2$ -type, $C2/m$, $Z = 2$). The magnetic structure of $La_2CrSe_2O_2$ was solved and refined from neutron powder diffraction data. Main building blocks are chains of edge-sharing $CrSe_4O_2$ -octahedra linked together by two edge-sharing ORE_3Cr -tetrahedra forming infinite ribbons. The Jahn-Teller instability of divalent Cr^{2+} (d^4) leads to structural phase transitions at 200 K and 130 K in $La_2CrSe_2O_2$ and $Ce_2CrSe_2O_2$, respectively. $RE_2CrSe_2O_2$ are Curie-Weiss paramagnetic above $T_N \approx 14-17$ K. Neutron powder diffraction reveals antiferromagnetic ordering of the Cr^{2+} moments in $La_2CrSe_2O_2$ below $T_N = 12.7(3)$ K with an average ordered moment of $3.40(4) \mu_B/Cr^{2+}$ at 4 K, which was confirmed by muon spin rotation experiments.

4.4.2 Introduction

Since the discovery of superconductivity in rare-earth oxide iron pnictides and iron chalcogenides during the past decade, there is ongoing interest in uncovering new rare-earth oxide transition-metal selenides. Recently, the series $RE_2TSe_2O_2$ ($RE = La, Ce$; $T = Cd, Fe, Mn, Zn$)^[2-5,7,14,16-18,26] has been reported, and their structures and physical properties have been studied. These compounds adopt a layered, ZrCuSiAs-related structure with modulated transition-metal selenide layers with a (3+1)-dimensional structure in the super-space group $Cmme(\alpha 0\frac{1}{2})0s0$.^[18] Further polymorphs exist with $T = Mn$ and Fe , respectively. To distinguish the polymorphs, we extended the formulas by the *Pearson* letters. Beside the modulated compound $oC-La_2MnSe_2O_2$ ^[16,26], there exist $oA-La_2MnSe_2O_2$ ^[7] and $mC-La_2MnSe_2O_2$ ^[27]. $oA-La_2MnSe_2O_2$ consists of disordered $MnSe_4$ -tetrahedra and edge-sharing $MnSe_4O_2$ -octahedra, which are connected by infinite ribbons of edge-sharing OLa_4 - and OLa_3Mn -tetrahedra four tetrahedral units in width. Ordering of the manganese cations is observed at low temperature, leading to a primitive structure with space group $Pna2_1$ ($oP-La_2MnSe_2O_2$). $mC-La_2MnSe_2O_2$ crystallizes in the $Pb_2HgCl_2O_2$ structure type with edge-sharing, distorted $MnSe_4O_2$ -octahedra, linked together by two edge-sharing OLa_3Mn -tetrahedra. Beside $oC-RE_2FeSe_2O_2$ ($RE = La, Ce$)^[3,4] in the iron family, there exist $mC-RE_2FeSe_2O_2$ ($RE = La, Ce$)^[3], which are isostructural to the monoclinic manganese compound, as well as $oP-La_2FeSe_2O_2$ ^[7] and $oA-Ce_2FeSe_2O_2$ ^[3], which adopt the low temperature and room temperature structure of the analogous manganese compound, respectively. Magnetic measurements of $mC-La_2MnSe_2O_2$, $mC-La_2FeSe_2O_2$ and $oA-La_2MnSe_2O_2$ indicate anti-ferromagnetic ordering of the transition metal moments at Néel temperatures of $\approx 15, 20$ and 27 K, respectively.^[3,4,27] Surprisingly only few rare-earth chromium oxyselenide compounds are known to date, namely $RECrSe_2O$ ($RE = La$ ^[28], Ce ^[21]) with trivalent Cr^{3+} . $LaCrSe_2O$ is isostructural to orthorhombic $LaCrS_2O$. The structure consists of edge-sharing $CrSe_5O$ -octahedra interconnected by two edge-sharing OLa_3Cr -tetrahedra forming infinite ribbons. Magnetic measurements revealed long range ferromagnetic exchange interactions. $CeCrSe_2O$ crystallizes in the monoclinic $CeCrS_2O$ structure type, space group $C2/m$. The structure resembles this of $mC-RE_2TSe_2O_2$ ($RE = La, Ce$; $T = Fe, Mn$) with the same building blocks but additional edge-sharing $CrSe_6$ -octahedra, which connect the $CrSe_4O_2$ -octahedra. In this paper, we present the crystallographic and magnetic structures of $La_2CrSe_2O_2$ with

chromium in the less common oxidation state Cr^{2+} together with isomorphous compounds $\text{RE}_2\text{CrSe}_2\text{O}_2$ ($\text{RE} = \text{Ce-Nd}$).

4.4.3 Experimental Details

All starting materials (purity $\geq 99.8\%$) were handled in an argon-filled glove box (M. Braun, $p(\text{O}_2) \leq 1$ ppm, $p(\text{H}_2\text{O}) \leq 1$ ppm). Polycrystalline powder samples and single crystals of mC - $\text{RE}_2\text{CrSe}_2\text{O}_2$ ($\text{RE} = \text{La-Nd}$) were prepared in the same way by the reaction of appropriate amounts of rare-earth oxide, freshly filed rare-earth metal, Cr and Se. The rare-earth oxides were heated to 1273 K prior to use. The starting materials (0.20 g) were mixed intimately and sandwiched in alumina crucibles between 0.50 g of a eutectic mixture of NaI/KI (mass ratio 0.6:0.4, dried in dynamic vacuum at 673 K). In addition, a polycrystalline sample (3×1 g) of $\text{La}_2\text{CrSe}_2\text{O}_2$ was synthesized for neutron diffraction experiments. The crucibles were sealed in argon filled silica tubes and heated to 1173 K with a 50 h dwell time, followed by slow cooling to 873 K. The crucibles were quenched in air from 873 K. The reaction mixtures were then washed with deionized water and ethanol and dried in vacuum. The procedure (heating with flux material and washing) was repeated once to increase the purity of the samples. The resulting samples were black powder (purity > 95 wt% according to Rietveld refinements) and black, rod-like single crystals.

Single crystal X-ray diffraction data was collected at 300 K with a Bruker D8 QUEST (fixed- χ goniometer, Mo- $\text{K}\alpha$, $1\mu\text{S}$ with HE-LIOS multi-layer optics, PHOTON 100 detector). Reflection intensity integration, data reduction, and multi-scan absorption correction were done with APEX2^[9] and SADABS^[10]. The structures were solved with Jana2006^[11].

X-ray powder diffraction patterns were recorded between 10 and 300 K with a Huber G670 diffractometer (Cu- $\text{K}\alpha_1$ or Co- $\text{K}\alpha_1$ radiation, Ge-monochromator, closed-cycle helium cryostat). For Rietveld refinements of the data the TOPAS^[12] package was used with spherical harmonic functions to describe the preferred orientation of the crystallites. Therefore the phase fractions from Rietveld refinements using X-ray powder diffraction data could be falsified. Thus, the purity of $\text{La}_2\text{CrSe}_2\text{O}_2$ was double-checked from refinements using neutron powder diffraction data.

Neutron powder diffraction measurements of $\text{La}_2\text{CrSe}_2\text{O}_2$ at 4, 20 and 300 K were performed at SPODI (FRM II, Garching)^[29] with a wavelength of 0.1548 nm. Rietveld refine-

ments of the neutron data was done with FullProf^[30].

Magnetization isotherms and susceptibility measurements were performed with a MPMS-XL SQUID magnetometer (Quantum Design Inc.). Magnetization isotherms at higher fields ($B = \pm 9$ T) were measured with a Vibrating Sample Magnetometer unit (VSM) in a Quantum Design Physical-Property-Measurement-System (PPMS).

The μ SR measurements were performed using the GPS spectrometer located at the π M3 beamline of the Swiss Muon Source at the Paul Scherrer Institut, Switzerland in a temperature range from 1.6 K to 40 K using a He flow cryostat. Transverse field μ SR data were taken in a field of 50 Oe applied perpendicular to the initial muon spin. The data were analyzed using the free MUSRFIT package^[31].

4.4.4 Results and Discussion

Synthesis and Crystal Structure

Single crystals of $\text{La}_2\text{CrSe}_2\text{O}_2$ were first obtained by the attempt to prepare a potential $\text{La}_3\text{CrSe}_3\text{O}_3$. However, energy dispersive X-ray spectroscopy revealed the formation of a mixture of LaCrSe_2O and $\text{La}_2\text{CrSe}_2\text{O}_2$, which both crystallize as black needles. Almost phase pure samples of $\text{La}_2\text{CrSe}_2\text{O}_2$ were obtained from the reaction of appropriate amounts of La_2O_3 , La, Cr and Se in a NaI/KI-flux synthesis. In addition, polycrystalline samples of $\text{RE}_2\text{CrSe}_2\text{O}_2$ ($\text{RE} = \text{Ce-Nd}$) have been prepared in the same way as for $\text{La}_2\text{CrSe}_2\text{O}_2$. Single-crystal X-ray diffraction experiments of $\text{La}_2\text{CrSe}_2\text{O}_2$ and powder X-ray diffraction experiments of $\text{RE}_2\text{CrSe}_2\text{O}_2$ ($\text{RE} = \text{La-Nd}$) revealed that the new compounds crystallize in the $\text{Pb}_2\text{HgCl}_2\text{O}_2$ structure type in space group $C2/m$ (No. 12), equal to $mC\text{-RE}_2\text{TSe}_2\text{O}_2$ ($\text{RE} = \text{La, Ce}$; $T = \text{Mn, Fe}$)^[3,27]. Relevant crystallographic data of $\text{La}_2\text{CrSe}_2\text{O}_2$ are compiled in Table A.9. Further structural discussion is based on powder X-ray and neutron diffraction data of the isostructural compounds $\text{RE}_2\text{CrSe}_2\text{O}_2$ ($\text{RE} = \text{La-Nd}$). Rietveld refinements of $\text{La}_2\text{CrSe}_2\text{O}_2$ (Fig. 4.38), $\text{Ce}_2\text{CrSe}_2\text{O}_2$ and $\text{Pr}_2\text{CrSe}_2\text{O}_2$ (Fig. A.2, A.3) revealed a small impurity of $\approx 1\text{-}4\%$ RE_2SeO_2 ($\text{RE} = \text{La-Pr}$), respectively. In contrast, only $\approx 10\%$ of the desired product was obtained for $\text{Nd}_2\text{CrSe}_2\text{O}_2$, while large amounts of NdCrSe_2O and Nd_2SeO_2 were formed. We could not prepare heavier rare-earth analogues under these conditions.

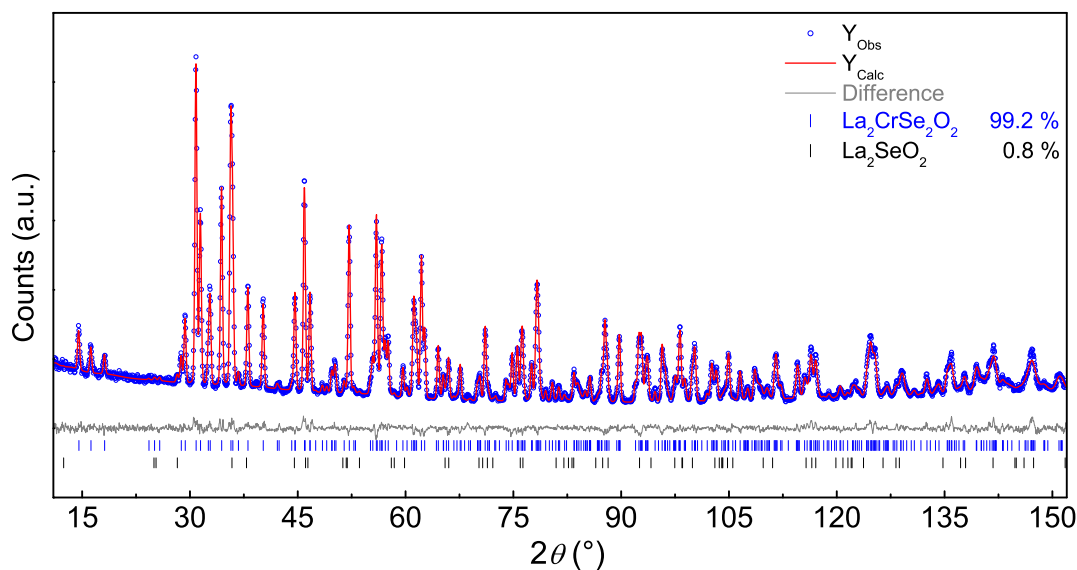


Figure 4.38 Neutron powder diffraction pattern of $\text{La}_2\text{CrSe}_2\text{O}_2$ (blue) with Rietveld fit (red) and difference plot (gray) at 300 K.

The crystal structure of the new compounds is closely related to that of CeCrSe_2O as can be seen in Figure 4.39. It consists of chains of edge-sharing, distorted CrSe_4O_2 -octahedra parallel to the b -axis, linked together by two edge-sharing ORE_3Cr -tetrahedra forming infinite ribbons along b . The rare-earth metal is in a bicapped trigonal prism of five selenium and three oxygen atoms. These building blocks can be found again in CeCrSe_2O , but additional chains of edge-sharing CrSe_6 -octahedra exist along b , which interconnect the CrSe_4O_2 -octahedra and extend the rare-earth metal coordination sphere to a tricapped trigonal prism with one additional selenium atom. Single crystal X-ray data of $\text{La}_2\text{CrSe}_2\text{O}_2$ revealed that the displacement ellipsoid of the chromium atom exhibits the same oblate spheroid shape in direction of the selenium atoms that was already observed for the transition metal sites in $mC\text{-La}_2\text{FeSe}_2\text{O}_2$ ^[3], $mC\text{-La}_2\text{MnSe}_2\text{O}_2$ ^[27] and $\text{RE}_4\text{TiSe}_4\text{O}_4$ ($\text{RE} = \text{Sm-Er, Y}$)^[23]. This may indicate a dynamic displacement of the Cr^{2+} atoms in the distorted CrSe_4O_2 -octahedra. A comparison of the structural parameters obtained from X-ray powder data of $\text{RE}_2\text{CrSe}_2\text{O}_2$ ($\text{RE} = \text{La-Nd}$) is given in Table 4.7.

The unit cell parameters a , b , and c decrease with the effective radii of the rare-earth metal ions, while the monoclinic angle β varies only slightly and shows a maximum for Ce (Fig. A.6). As a consequence, the cell volume also decreases with smaller effective rare-earth radii. Comparing the compounds $mC\text{-La}_2\text{TSe}_2\text{O}_2$ ($T = \text{Cr, Fe, Mn}$) in Figure 4.40, the cell

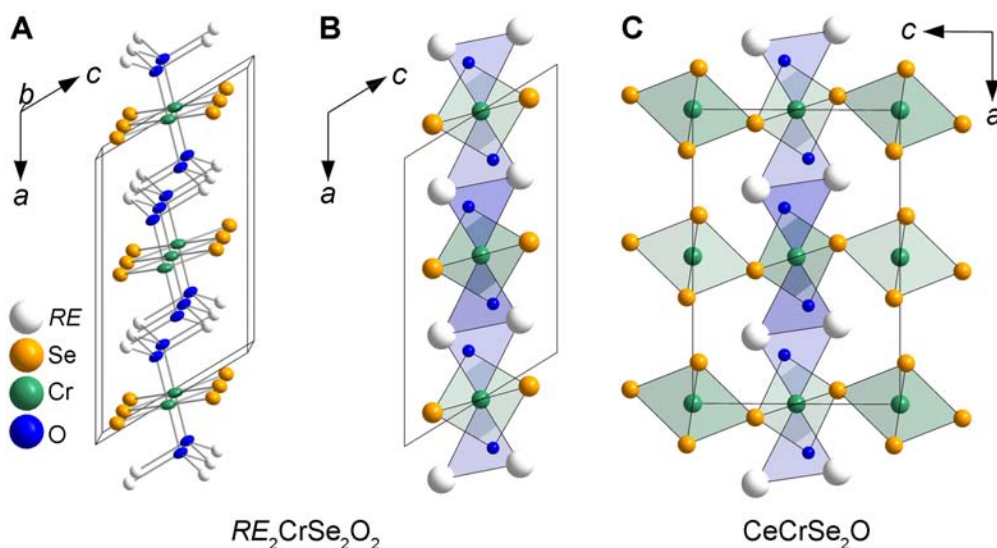


Figure 4.39 Illustration of the crystal structures of (A+B) $RE_2CrSe_2O_2$ ($RE = La-Nd$) and (C) $CeCrSe_2O$ along b . Chains of edge-sharing $CrSe_4O_2$ - and $CrSe_6$ -octahedra in green, ORE_3Cr edge-sharing tetrahedral ribbons in blue. Ellipsoids in (A) represent 99 % probability.

Table 4.7 Overview over the Rietveld refinement data of $RE_2CrSe_2O_2$ ($RE = La-Nd$) in space group $C2/m$.

	$La_2CrSe_2O_2$	$Ce_2CrSe_2O_2$	$Pr_2CrSe_2O_2$	$Nd_2CrSe_2O_2$
$a / \text{\AA}$	11.536(1)	11.436(1)	11.41481)	11.372(1)
$b / \text{\AA}$	3.9682(1)	3.3914(1)	3.9101(1)	3.8782(1)
$c / \text{\AA}$	7.1800(2)	7.1193(1)	7.0949(1)	7.0630(1)
$\beta / ^\circ$	121.617(1)	121.856(1)	121.800(1)	121.639(5)
Volume / \AA^3	279.905(9)	271.864(3)	269.117(7)	265.21(4)
R_{exp}	1.6	1.8	1.7	1.6
R_{wp}	3.1	2.2	1.9	4.2
$Goof$	1.9	1.3	1.2	2.6
Phase fraction	99 %	96 %	99 %	11 %
Side phase(s)	1 % La_2SeO_2	4 % Ce_2SeO_2	1 % Pr_2SeO_2	64 % Nd_2CrSe_2O 25 % Nd_2SeO_2

volume of $\text{La}_2\text{CrSe}_2\text{O}_2$ is in between these of $mC\text{-La}_2\text{MnSe}_2\text{O}_2$ and $mC\text{-La}_2\text{FeSe}_2\text{O}_2$, which is consistent with the trend of the ionic radii of the transition-metals. Furthermore, it is noticeable that in case of the manganese and iron compounds, it is not possible to prepare compounds with smaller rare-earth metals as lanthanum or cerium, respectively, whereas $\text{Pr}_2\text{CrSe}_2\text{O}_2$ and $\text{Nd}_2\text{CrSe}_2\text{O}_2$ are accessible via the synthesis route described here. In contrast to the manganese and iron compounds, we found no other polymorphs of $\text{RE}_2\text{CrSe}_2\text{O}_2$ by scanning different reaction temperatures from 1073–1373 K.

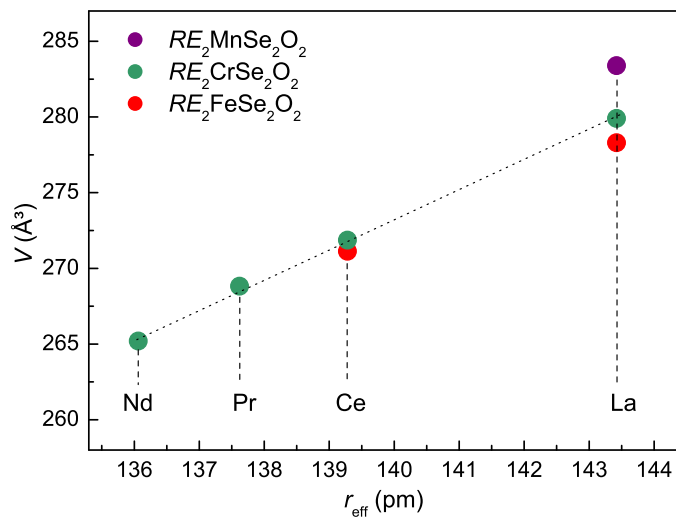


Figure 4.40 Unit cell volumes versus the effective radii^[15] of the respective rare-earth metal of $mC\text{-La}_2\text{MnSe}_2\text{O}_2$, $mC\text{-RE}_2\text{FeSe}_2\text{O}_2$ ($\text{RE} = \text{La}, \text{Ce}$) and $\text{RE}_2\text{CrSe}_2\text{O}_2$ ($\text{RE} = \text{La-Nd}$). Data points of the iron compounds are taken from the literature.^[3]

Low Temperature Structural Phase Transition

X-ray and neutron powder diffraction patterns of $\text{La}_2\text{CrSe}_2\text{O}_2$ reveal peak splitting below ≈ 200 K, exemplarily shown on the (111) reflection in Figure 4.41 (A). Generally, the reflections of the monoclinic phase $(hkl)_m$ gradually split into two reflection types that can be indexed as $(hkl)_t$ and $(h\bar{k}l)_t$ reflections of a triclinic phase. Rietveld refinement using space group $P\bar{1}$ is shown exemplarily for $T = 20$ K in Figure A.4 and gives excellent fit to the experimental data. Subsequent low temperature X-ray and neutron diffraction experiments between 300 and 4 K revealed continuously decreasing cell parameters a , b , c and shrinking unit cell volumes by 0.95 %, 0.23 %, 0.21 %, and 0.51 %, respectively (Fig. A.10). The

distortion of the unit cell, which affects primarily the unit cell angle α , is obvious below $T_{\text{tr}} = 200$ K, as depicted in Figure 4.41 (B). While the unit cell angles β and γ decrease slightly upon cooling (0.03 % and 0.15 %), there is a significant change of 1.00 % for α , which finally requires the symmetry reduction to $P\bar{1}$. The transition is reversible and non hysteretic upon heating the sample to room temperature again.

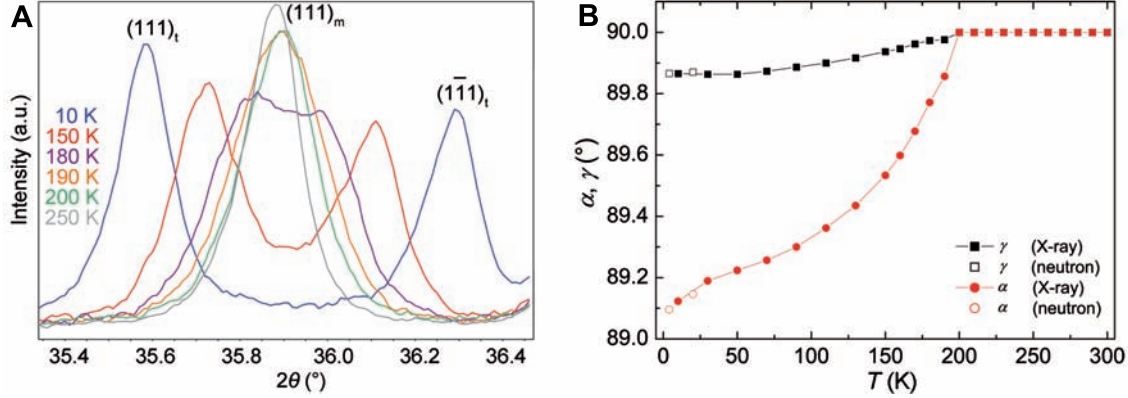


Figure 4.41 (A) Peak splitting of the (111) reflection of the monoclinic phase of $\text{La}_2\text{CrSe}_2\text{O}_2$ into (111) and $(\bar{1}\bar{1}\bar{1})$ reflections of the triclinic phase at different temperatures. (B) Evolution of the unit cell angles α and γ upon cooling including data from powder X-ray and neutron diffraction experiments. Error bars are smaller than the data points.

The Cr-O bond lengths in the CrSe_4O_2 -octahedra of $\text{La}_2\text{CrSe}_2\text{O}_2$ remain almost constant upon cooling, whereas the Cr-Se bond lengths split from $4 \times 281.9(1)$ pm into two shorter (272.4(1) or 274.5(1) pm) and two longer (288.1(1) or 291.3(1) pm) ones for Cr1 and Cr2, respectively. This distortion of the CrSe_4 -plane from square to rhombic is depicted in Figure 4.42. All Se-Cr-Se bond angles remain within $90 \pm 0.5^\circ$, while the O-Cr-Se bond angles deform from $89.2(1)$ – $90.8(1)^\circ$ to $87.6(1)$ – $92.4(1)^\circ$ at low temperatures. The d^4 high-spin configuration of Cr^{2+} is a typical *Jahn-Teller* case, which drives a distortion stabilizing the x^2-y^2 or z^2 orbital. In the $C2/m$ phase the occupied x^2-y^2 is already below the empty z^2 because of the closer apical oxygen ligands. Nevertheless the rhombic distortion of the square of selenium atoms reduces the overlap of the x^2-y^2 orbital and further reduces its energy ($\Delta E_2 > \Delta E_1$ in Fig. 4.42). Since we do not come from a degenerate state in the $C2/m$ phase, we refer this to a second order *Jahn-Teller* distortion.

We observed this effect in $\text{Ce}_2\text{CrSe}_2\text{O}_2$ at a significantly lower transition temperature of $T_{\text{tr}} = 130$ K (Fig. 4.43). The trend of the unit cell parameters of $\text{Ce}_2\text{CrSe}_2\text{O}_2$ upon cooling is depicted in Figure A.11. In contrast, $\text{Pr}_2\text{CrSe}_2\text{O}_2$ does not show any phase transition down

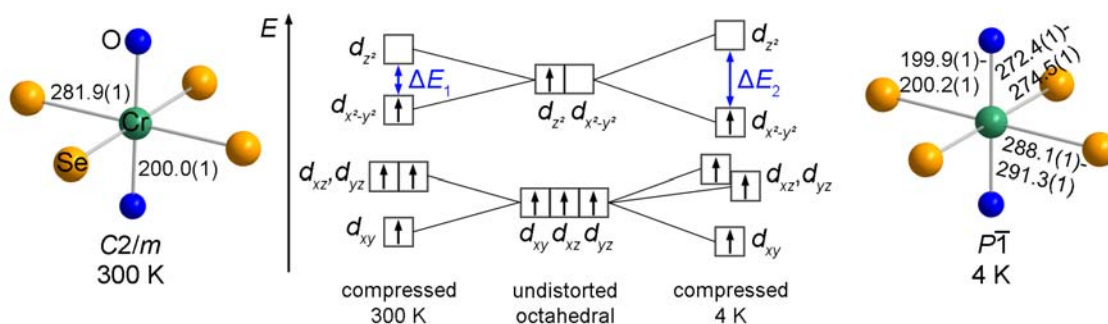


Figure 4.42 Selected bond lengths in the CrSe_4O_2 -octahedra obtained from Rietveld fits of neutron diffraction data at 300 K (left) and 4 K (right). Schematic crystal field splittings (middle) for an undistorted octahedral as well as for compressed octahedral (at 300 and 4 K) geometries of the $\text{Cr}^{2+}\text{Se}_4\text{O}_2$ polyhedron.

to 10 K. Similar observations were made by *Tuxworth* et al. for $\text{RE}_4\text{TiSe}_4\text{O}_4$ ($\text{RE} = \text{Sm}-\text{Er}, \text{Y}$) compounds. The materials with the largest rare-earth ions, $\text{Sm}_4\text{TiSe}_4\text{O}_4$ and $\text{Gd}_4\text{TiSe}_4\text{O}_4$, show a phase transition at low temperatures which could be an order-disorder transition of the displaced titanium atoms in the distorted TiSe_4O_2 -octahedra.^[23]

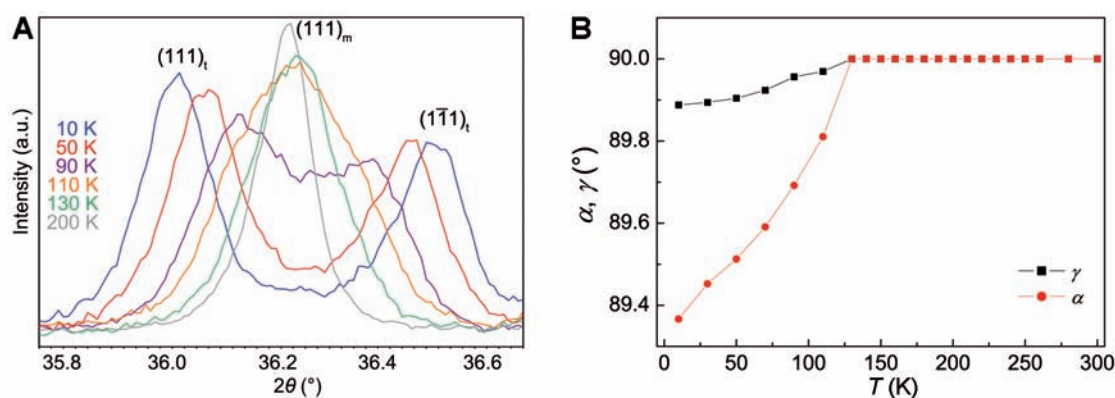


Figure 4.43 (A) Peak splitting of the (111) reflection of the monoclinic phase of $\text{Ce}_2\text{CrSe}_2\text{O}_2$ into (111) and $(1\bar{1}1)$ reflections of the triclinic phase at different temperatures. (B) Evolution of the unit cell angles α and γ upon cooling including data from powder X-ray experiments. Error bars are smaller than the data points.

Magnetic Properties

Magnetic measurements of $RE_2CrSe_2O_2$ ($RE = \text{La-Pr}$) reveal Curie-Weiss behavior down to ≈ 20 K (Fig. 4.44) with effective moments of 5.01(1) [4.90], 6.06(3) [6.08] and 7.24(1) [7.05] μ_B per formula unit for $RE = \text{La, Ce, and Pr}$, respectively (theoretical values in square brackets).

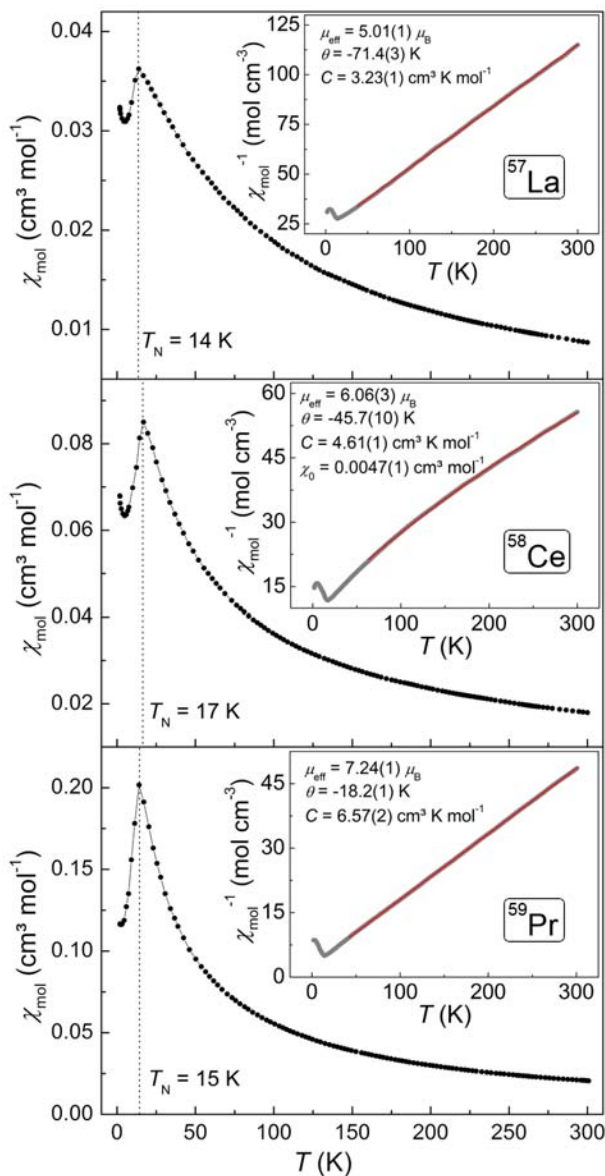


Figure 4.44 Magnetic susceptibilities (black) and inverse susceptibilities (inset) of $\text{La}_2\text{CrSe}_2\text{O}_2$ (top), $\text{Ce}_2\text{CrSe}_2\text{O}_2$ (middle) and $\text{Pr}_2\text{CrSe}_2\text{O}_2$ (bottom). $B = 1$ T. Curie-Weiss fits in red. Parameters obtained from the fits are given in the inset. Measurements were performed on free and randomly oriented powders.

The theoretical effective moments are calculated by taking the square root of the sum of the squares of the theoretical moments (μ_{th}) of the contributing magnetic cations, that is, $\mu_{\text{eff}}(\text{RE}_2\text{CrSe}_2\text{O}_2) = [2\mu_{\text{th}}(\text{RE}^{3+})^2 + \mu_{\text{th}}(\text{Cr}^{2+})^2]^{1/2}$, with $\mu_{\text{th}}(\text{Ce}^{3+}) = 2.53 \mu_{\text{B}}$, $\mu_{\text{th}}(\text{Pr}^{3+}) = 3.58 \mu_{\text{B}}$ and $\mu_{\text{th}}(\text{Cr}^{2+}) = 4.90 \mu_{\text{B}}$. Abruptly decreasing susceptibilities below 14–17 K indicate antiferromagnetic ordering similar to *mC*- $\text{La}_2\text{FeSe}_2\text{O}_2$ ($T_{\text{N}} = 20$ K) and *mC*- $\text{La}_2\text{MnSe}_2\text{O}_2$ ($T_{\text{N}} = 15$ K).^[3,27]

Isothermal magnetizations of $\text{La}_2\text{CrSe}_2\text{O}_2$ and $\text{Ce}_2\text{CrSe}_2\text{O}_2$ at 300 and 1.8 K are linear as expected (Fig. A.7, A.8). $\text{Pr}_2\text{CrSe}_2\text{O}_2$ shows a remarkable upturn of the magnetization at higher fields > 5 T at 3 K (Fig. 4.45) and > 3 T at 1.8 K (Fig. A.9). Figure 4.45 displays the magnetization isotherms of $\text{Pr}_2\text{CrSe}_2\text{O}_2$ measured at 3, 10, 20, and 50 K. The isotherms measured at 3 (red) and 10 K (blue), both below the Néel temperature, display a slight curvature at a critical field of $H_{\text{Cr}} \approx 50$ kOe. This indicates an antiferromagnetic-to-ferromagnetic spin-reorientation, also referred to as metamagnetic transition. Furthermore the 3 K isotherm exhibits a weak but well resolved hysteresis between 50 and 90 kOe in the increasing / decreasing field curves. Such features are rarely observed; one example is $\text{Pr}_2\text{Pd}_2\text{Mg}$ ^[32]. Magnetic moments of 1.77(1) μ_{B} per formula unit at 3 and 10 K and 90 kOe were found, substantially reduced when compared with the theoretical value of 3.20 μ_{B} per praseodymium atom. We assume that the Cr^{2+} contribution is small as found in $\text{La}_2\text{CrSe}_2\text{O}_2$. The isotherms at 20 and 50 K show the typical linear temperature dependence of the magnetization as expected for a paramagnetic material (above the Néel temperature).

Muon Spin Rotation and Relaxation

Zero field (ZF) and weak transverse field (wTF) muon spin rotation and relaxation (μSR)^[33] measurements have been performed on a powder sample of $\text{La}_2\text{CrSe}_2\text{O}_2$ to obtain further insight into the magnetic ordering of this compound. In Figure 4.46 (A), representative ZF- μSR spectra are shown for various temperatures. Above T_{N} , the muon spin polarization $P(t)$ is only weakly exponentially damped which is typical for a paramagnetic specimen with fast fluctuating electronic spins and randomly oriented and partly diluted nuclear moments. Below T_{N} , spontaneous muon spin precession is observed indicating the development of static internal magnetic fields B_i at the interstitial muon stopping sites within the lattice. The Fourier transform of the data which is depicted in Figure 4.46 (B) reveals the presence of two distinct precession frequencies $f_i = \frac{\gamma}{2\pi} B_i$ due to two magnetically inequivalent muon

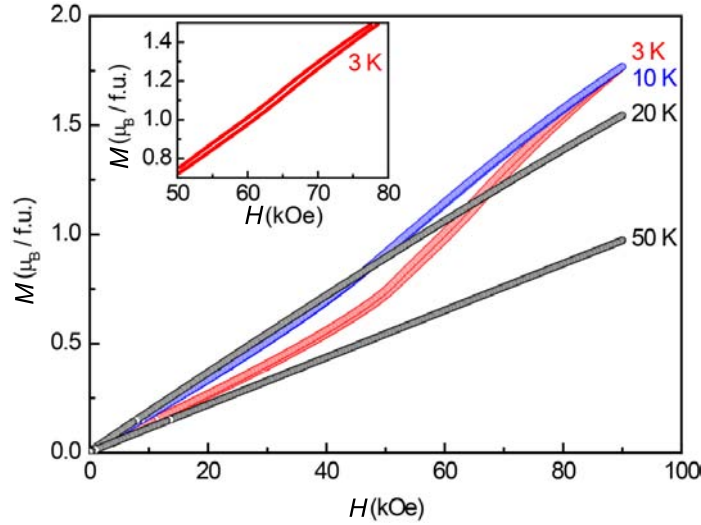


Figure 4.45 Magnetization isotherms of $\text{Pr}_2\text{CrSe}_2\text{O}_2$ at 3, 10, 20, and 50 K. The isotherms at 3 and 10 K, below the ordering temperature, exhibit a spin reorientation at $H_{\text{Cr}} \approx 50$ kOe, in addition the 3 K isotherm shows a hysteresis (enlarged in the inset) between 50 and 90 kOe.

sites (with the gyromagnetic ratio of the muon $\gamma = 2\pi 135.5$ MHz/T). Such well-defined fields at the muon sites prove the long range commensurate character of the magnetic ordering, because incommensurate magnetic order would lead to a broad distribution of internal fields.

The quantitative analysis of the ZF- μ SR data reveals that besides the two oscillating components two further non-oscillating contributions have to be taken into account to fully describe the low temperature spectra. Therefore the following polarization function has been used for the analysis of the ZF- μ SR data.

$$P(t) = \frac{2}{3} \sum_{i=1}^4 a_i e^{-\lambda_i t} \cos(2\pi f_i t) + \frac{1}{3} e^{-\lambda_L t} \quad (4.4)$$

The sum of a $\frac{2}{3}$ and a $\frac{1}{3}$ fraction of the signal originates from the powder average of the internal fields with respect to the initial muon spin direction in our polycrystalline sample. The $\frac{2}{3}$ transverse signal represents the muon spin components that are perpendicular to the internal fields while the $\frac{1}{3}$ signal fraction stems from the muon spin components which are parallel to the internal fields. The a_i are the amplitudes of the different signals which were determined at low temperatures and then kept fix for the higher temperature data ($a_1 = 0.19$, $a_2 = 0.06$, $a_3 = 0.38$, $a_4 = 0.37$, $f_3 = f_4 = 0$). The transverse relaxation rates λ_i are a measure for the width of the probed field distribution while the longitudinal or spin-lattice relaxation rate λ_L is solely related to the dynamics of the magnetic system under investigation.

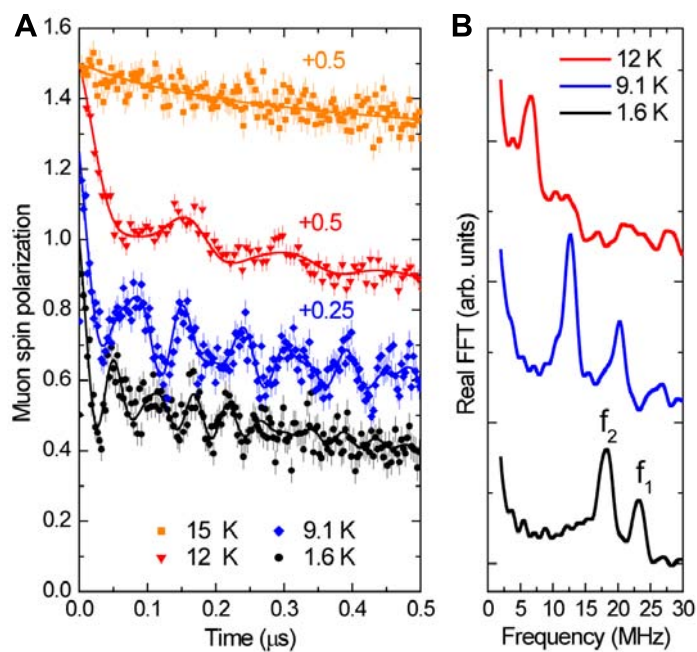


Figure 4.46 (A) Representative ZF- μ SR spectra of $\text{La}_2\text{CrSe}_2\text{O}_2$ showing muon spin precession due to the presence of static internal magnetic fields below T_N . Offset of the data is +0.25 (blue) and +0.5 (red and orange), respectively. (B) The Fourier transform of the raw data reveals that several magnetic inequivalent muon sites exist within the magnetic structure and that the magnetic structure is commensurate with the lattice.

In Figure 4.47 the extracted fit parameters are depicted. A gradual decrease of the frequencies $f_i(T)$, i.e. internal magnetic fields, is observed towards the Néel temperature of about 13 K (Fig. 4.47 A). Additionally, a peak is observed in the spin-lattice relaxation rate

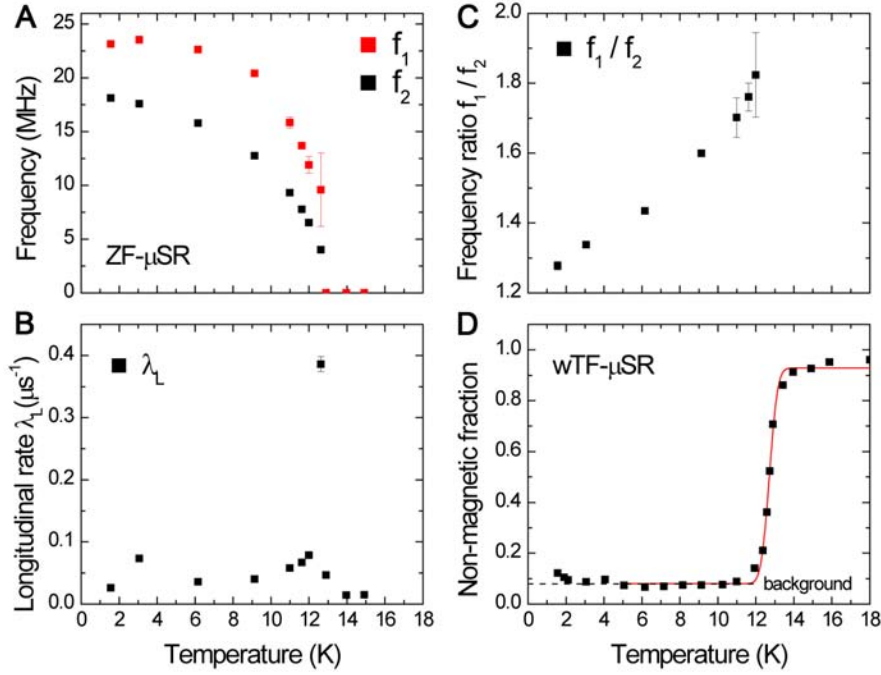


Figure 4.47 Results of the analysis of μSR measurements on $\text{La}_2\text{CrSe}_2\text{O}_2$. Temperature dependence of the spontaneous precession frequencies (A) and the longitudinal relaxation rate λ_L (B) from ZF- μSR . (C) Ratio of the frequencies. (D) Temperature dependence of the non-magnetic volume fraction determined by wTF- μSR showing a sharp transition of essentially the full sample volume at $T_N = 12.7(3)$ K.

λ_L at T_N (Fig. 4.47 B). Both these features are characteristic for a second order magnetic phase transition. Results of the wTF- μSR measurements which are able to determine the non-magnetic volume fraction of the sample are shown in Figure 4.47 (D). From these results it is obvious that through a sharp transition essentially the full sample volume orders magnetically at $T_N^{50\%} = 12.7(3)$ K. An unusual feature of our measurements is reported in Figure 4.47 (C). The ratio f_1/f_2 of the two frequencies changes dramatically as a function of temperature. In a rigid magnetic structure where only the magnetic order parameter increases as a function of decreasing temperature such a ratio is expected to be constant and both frequencies are an equivalent measure of the size of the ordered magnetic moment. The fact that f_1/f_2 is not constant as a function of temperature could therefore originate from a continuous change of the magnetic structure on lowering the temperature e.g. in the form of a changing canting

angle of the AFM structure. Since μ SR is a local probe technique, this conclusion is only rather indirect and awaits further experimental verification, for example, by temperature-dependent neutron scattering experiments well below the Néel temperatures.

Neutron Diffraction - Low Temperature Magnetic Structure of $\text{La}_2\text{CrSe}_2\text{O}_2$

Powder neutron diffraction experiments at low temperature were performed to characterize the magnetic ordering of $\text{La}_2\text{CrSe}_2\text{O}_2$ exemplarily for the $mC\text{-RE}_2\text{TSe}_2\text{O}_2$ compounds ($RE = \text{La-Nd}$; $T = \text{Cr-Fe}$) with similar magnetic susceptibility curves. The neutron powder diffraction pattern at 4 K, well below T_N , is plotted in Figure 4.48. Several strong magnetic reflections appear at $2\theta \approx 12.9, 15.2, 16.2, 21.9, 22.9,$ and 24.7° (labeled as m1–m6). The magnetic structure cannot be described within the crystallographic unit cell but requires a commensurate propagation vector $\mathbf{k} = (\frac{1}{2}, \frac{1}{2}, \frac{1}{2})$, which means doubling of the nuclear unit cell in all three dimensions. Refinements of the magnetic structure were performed in space group $P\bar{1}$ using the program FullProf^[30]. Assuming antiferromagnetic ordering with magnetic moments of Cr(1) and Cr(2) constrained to have the same magnitude gives excellent fits to the experimental data as can be seen in the Rietveld profile in Figure 4.48.

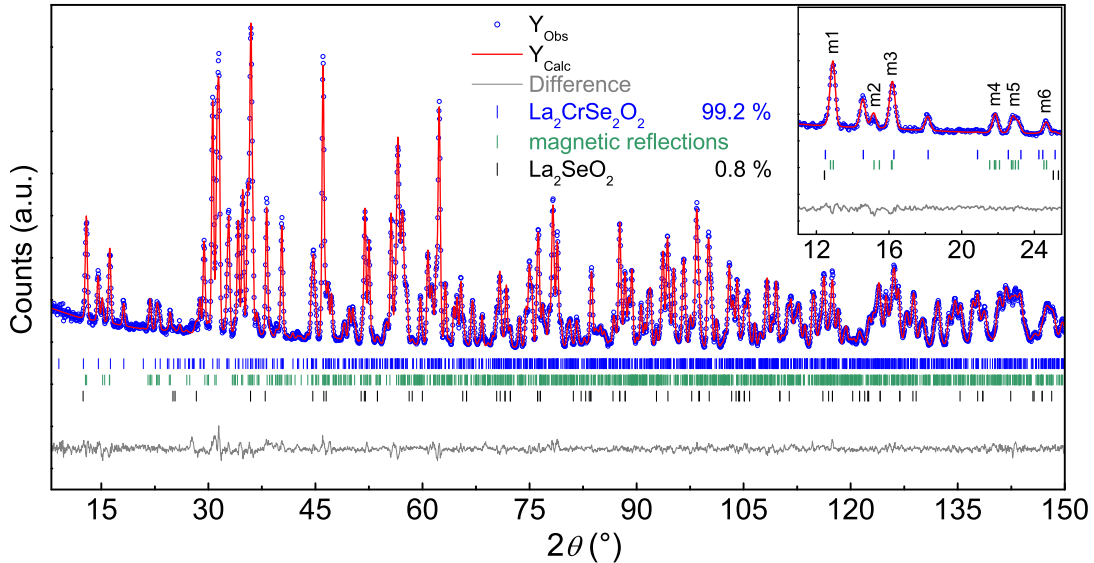


Figure 4.48 Neutron powder diffraction pattern of $\text{La}_2\text{CrSe}_2\text{O}_2$ (blue) with Rietveld fit (red) and difference plot (gray) at 4 K. Inset: Magnification of the pattern between $11^\circ \leq 2\theta \leq 25.5^\circ$. Peaks marked with m_i ($i = 1\text{--}6$) are magnetic Bragg reflections.

The magnetic cell has the dimensions $\approx 23.0 \text{ \AA} \times 7.9 \text{ \AA} \times 14.3 \text{ \AA}$. Figure 4.49 shows the magnetic structure of $\text{La}_2\text{CrSe}_2\text{O}_2$ with absolute values of the magnetization vectors along

the non orthogonal unit cell axes $(M_a, M_b, M_c) = (1.07(14) \mu_B, 1.46(11) \mu_B, 3.47(8) \mu_B)$ and an ordered magnetic moment of $3.40(4) \mu_B$ per Cr^{2+} atom at 4 K. The spin arrangement is G-type antiferromagnetic. Crystallographic data of $\text{La}_2\text{CrSe}_2\text{O}_2$ at 4 and 20 K can be found in Table A.10.

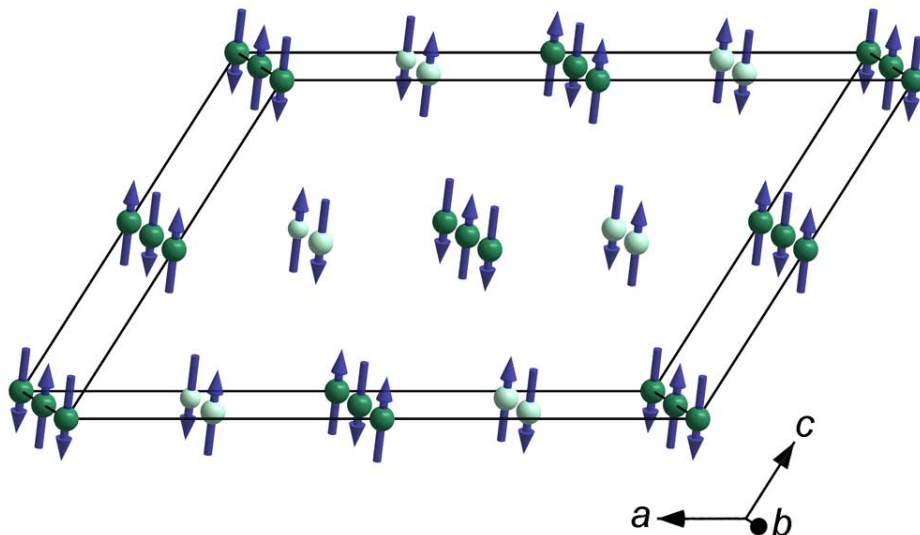


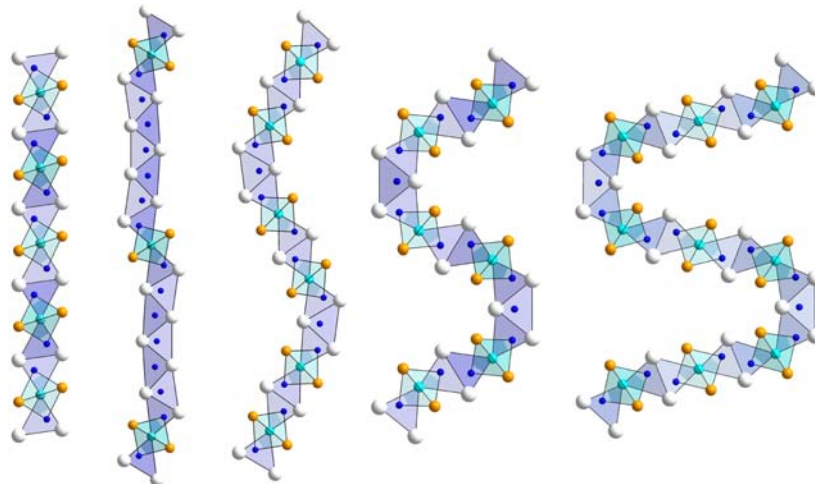
Figure 4.49 Magnetic ordering pattern of Cr^{2+} (green) in $\text{La}_2\text{CrSe}_2\text{O}_2$ at 4 K. The magnetic cell is doubled in all three directions in comparison to the nuclear cell (propagation vector $\mathbf{k} = (\frac{1}{2}, \frac{1}{2}, \frac{1}{2})$. Cr1 is dark green, Cr2 lime.

4.4.5 Conclusion

Crystals of the new members of $\text{RE}_2\text{CrSe}_2\text{O}_2$ ($\text{RE} = \text{La-Nd}$) compounds were grown in a NaI/KI flux. Single crystal X-ray diffraction identified the $\text{Pb}_2\text{HgCl}_2\text{O}_2$ structure type in space group $C2/m$. $\text{La}_2\text{CrSe}_2\text{O}_2$ and $\text{Ce}_2\text{CrSe}_2\text{O}_2$ undergo structural phase transitions to triclinic $P\bar{1}$ symmetry at ≈ 200 and 130 K, respectively, which are probably driven by the second order *Jahn-Teller* effect of the Cr^{2+} ions. Magnetometry revealed Curie-Weiss paramagnetism and indicated antiferromagnetic order below $T_N \approx 14\text{--}17$ K. $\text{Pr}_2\text{CrSe}_2\text{O}_2$ shows an antiferromagnetic-to-ferromagnetic spin reorientation (metamagnetism) at higher magnetic fields. Muon spin rotation experiments with $\text{La}_2\text{CrSe}_2\text{O}_2$ confirm a second order transition into a commensurate magnetic structure, which is proved by 4 K neutron powder diffraction data. The magnetic structure is G-type antiferromagnetic with an ordered Cr^{2+} moment of $3.40(4) \mu_B$ at 4 K.

4.5 Flux Synthesis, Crystal Structures, and Physical Properties of New Lanthanum Vanadium Oxyselenides

S. Peschke, L. Gamperl, V. Weippert, and D. Johrendt



published in: *Dalton Trans.* **2017**, *accepted*.

Copyright 2017, Royal Society of Chemistry.

4.5.1 Abstract

The new lanthanum vanadium oxyselenides LaVSe_2O , $\text{La}_5\text{V}_3\text{Se}_6\text{O}_7$, $\text{La}_5\text{V}_3\text{Se}_7\text{O}_5$, $\text{La}_7\text{VSe}_5\text{O}_7$, and $\text{La}_{13}\text{V}_7\text{Se}_{16}\text{O}_{15}$ were synthesized in eutectic NaI/KI fluxes, and their crystal structures were determined by single-crystal and powder X-ray diffraction. LaVSe_2O and $\text{La}_5\text{V}_3\text{Se}_6\text{O}_7$ adopt known structure types, whereas $\text{La}_5\text{V}_3\text{Se}_7\text{O}_5$, $\text{La}_7\text{VSe}_5\text{O}_7$, and $\text{La}_{13}\text{V}_7\text{Se}_{16}\text{O}_{15}$ crystallize in so far unknown structures. Main building blocks of these compounds are chains of edge-sharing VSe_6 , VSe_5O , and/or VSe_4O_2 octahedra, linked together by edge-sharing OLa_4 and/or OLa_3V tetrahedra forming fluorite-like ribbons. LaVSe_2O , $\text{La}_5\text{V}_3\text{Se}_7\text{O}_5$, and $\text{La}_7\text{VSe}_5\text{O}_7$ contain only V(III) ions, whereby $\text{La}_5\text{V}_3\text{Se}_6\text{O}_7$ and $\text{La}_{13}\text{V}_7\text{Se}_{16}\text{O}_{15}$ contain mixtures of either V(III)/V(IV) or V(III)/V(V) cations. Magnetic measurements indicate Curie-Weiss paramagnetism and magnetic ordering of the vanadium moments at low temperatures. More precisely, we observe antiferromagnetism for $\text{La}_5\text{V}_3\text{Se}_6\text{O}_7$, metamagnetism for $\text{La}_5\text{V}_3\text{Se}_7\text{O}_5$, ferromagnetism for $\text{La}_7\text{VSe}_5\text{O}_7$ and a complex magnetic structure for $\text{La}_{13}\text{V}_7\text{Se}_{16}\text{O}_{15}$.

4.5.2 Introduction

Recently, several rare-earth transition-metal oxyselenides with the general formula $RE_2TSe_2O_2$ ($RE = \text{La-Nd}$; $T = \text{Cr, Mn, Fe, Zn, Cd}$) have been characterized, which reveal interesting structural motifs and physical properties.^[2-7,14,16-18,25,27] Beside these compounds, there exist other quaternary oxyselenides containing 3d transition-metals with different compositions, among them $RECuSeO$ ($RE = \text{La, Sm, Gd, Y}$), $RECrSe_2O$ ($RE = \text{La, Ce}$), $La_4MnSe_3O_4$, $La_6MnSe_4O_6$, $La_2T_2Se_2O_3$ ($T = \text{Mn, Fe}$), La_4TSe_6O ($T = \text{Mn, Fe}$), $La_4Ti_2Se_5O_4$, $La_6Ti_3Se_9O_5$, $RE_{3,67}Ti_2Se_6O_3$ ($RE = \text{Ce, Nd, Sm}$), $RE_3Ti_3Se_2O_8$ ($RE = \text{Nd, Sm}$), and $RE_4TiSe_4O_4$ ($RE = \text{Sm, Gd-Er, Y}$).^[19-23,27,28,34-36] However, related quaternary compounds with vanadium as transition-metal are rare. Literature review revealed that there exists - to our best knowledge - only one compound in the systems RE-V-Se-O, namely $RE_7VSe_8O_4$ ($RE = \text{Nd, Sm, Gd}$)^[37], and another compound in the RE-V-S-O systems, which is $RE_5V_3S_6O_7$ ($RE = \text{La-Nd}$)^[38]. Quaternary rare-earth vanadium oxyselenides containing lanthanum are entirely unknown. The crystal structure of $RE_7VSe_8O_4$ consists of chains of edge-sharing VSe_4O_2 - and distorted $LaSe_6$ -octahedra. The VSe_4O_2 -octahedra are connected to neighboring OLa_3V - and OLa_4 -tetrahedra, which form infinite fluorite-like ribbons. Magnetic susceptibility measurements indicate that $Gd_7VSe_8O_4$ is paramagnetic down to 5 K. The structure of the sulfides $RE_5V_3S_6O_7$ also consists of chains of edge-sharing VS_4O_2 -octahedra, linked by edge-sharing OLa_3V - and OLa_4 -tetrahedra in an even more complex pattern than in the $RE_7VSe_8O_4$ compounds. Magnetic measurements of $La_5V_3S_6O_7$ revealed paramagnetism between 30 and 800 K with an effective magnetic moment of $4.0 \mu_B$. Due to a lack of La-V-Se-O compounds, we made investigations on this quaternary system, using a NaI/KI flux synthesis in order to promote crystal growth. In this paper, we present the crystal structures and magnetic properties of the first five quaternary lanthanum vanadium oxyselenides.

4.5.3 Experimental Details

All starting materials were handled in an argon-filled glove box (M. Braun, $p(O_2) \leq 1$ ppm, $p(H_2O) \leq 1$ ppm). Polycrystalline samples and single crystals of all materials were prepared by the reaction of appropriate amounts of La_2O_3 , freshly filed lanthanum metal, V or VSe_2 , and Se. La_2O_3 was heated to 1273 K prior to use. VSe_2 was prepared from the reaction of the elements at 1073 K for 15 h. The starting materials (0.20–0.30 g) were mixed intimately

and sandwiched in alumina crucibles between 1 g of a eutectic mixture of NaI/KI (mass ratio 0.6:0.4, dried in dynamic vacuum at 673 K). The crucibles were sealed in argon filled silica tubes and heated to the desired temperature (stated in the respective sections) with a 50 h dwell time, followed by slow cooling to 873 K. The crucibles were quenched in air from 873 K. The reaction mixtures were then washed with deionized water and ethanol and dried in vacuum. The procedure (heating with flux material and washing) was repeated once to increase the purity of the samples. The compounds are stable in moist air for months.

Single crystal X-ray diffraction data was collected at 300 K with a Bruker D8 QUEST (fixed- χ goniometer, Mo- K_{α} , $I\mu$ S with HE-LIOS multi-layer optics, PHOTON 100 detector, Bruker, Karlsruhe, Germany) or with a Bruker D8 Venture (Mo- K_{α} , rotating anode, Photon-II CPAD detector). Reflection intensity integration, data reduction, and multi-scan absorption correction were done with APEX2^[9] and SADABS^[10]. The structures were solved and refined with the Jana2006^[11,39] or Shelxl^[40] packages. Further details of the crystal structure data may be obtained from the Cambridge Crystallographic Database on quoting the CCDC Numbers 1535833 (LaVSe₂O), 1535834 (La₅V₃Se₇O₅), 1535837 (La₅V₃Se₆O₇), 1535836 (La₇VSe₅O₇), and 1535835 (La₁₃V₇Se₁₆O₁₅).

X-ray powder diffraction patterns were recorded with a Huber G670 diffractometer (Cu- $K_{\alpha 1}$ radiation, Ge-monochromator). For Rietveld refinements of the data the TOPAS^[12] package was used with spherical harmonic functions to describe the preferred orientation of the crystallites.

Energy dispersive X-ray (EDX) experiments were performed on a CARL ZEISS EVO-MA 10 with SE and BSE detectors, controlled by the SmartSEM^[41] software. The microscope was equipped with a BRUKER Nano EDS detector (X-Flash detector 410-M) for EDS investigations using the QUANTAX200^[42] software to collect and evaluate the spectra. The samples were fixed on aluminium sample holders using adhesive conducting carbon. Therefore, the elements Al and C were not included in the analyses.

Magnetization isotherms and susceptibility data were measured with either a MPMS-XL SQUID magnetometer (Quantum Design Inc., San Diego, CA, USA) or with a Vibrating Sample Magnetometer (Cryogenic, London, United Kingdom).

4.5.4 Results and Discussion

4.5.4.1 LaVSe₂O

A few black, needle-like single crystals (Fig. 4.50) could be isolated by the attempt to prepare La₃VSe₃O₃. Data from EDX measurements of the single crystals revealed the averaged atomic percentages La 20.5(2) %, V 19.7(3) %, Se 40.9(3) %, and O 18.8(8) %, which corresponds to La_{1.0}V_{0.9(1)}Se_{2.0(1)}O_{0.9(1)}. No emission lines of potassium, sodium or iodine were detected,

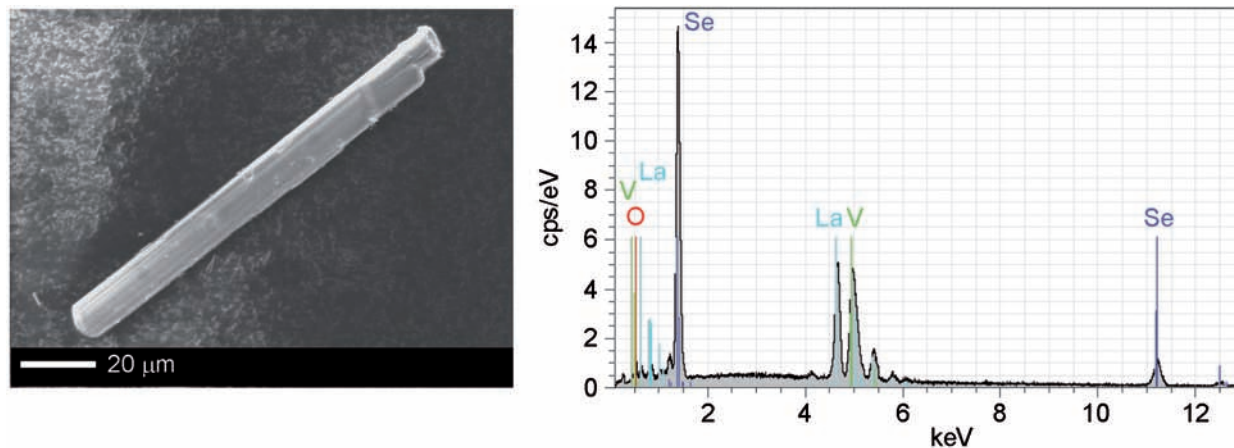


Figure 4.50 Typical needle-like single crystal (left) and EDX spectrum (right) of LaVSe₂O. Characteristic lines of the elements of the flux are not observed. The small peak at ≈ 0.25 keV belongs to carbon from the adhesive conducting carbon film.

thus substantial inclusion or incorporation of the flux material can be excluded. Single crystal X-ray diffraction experiments were used to solve the crystal structure. The molecular formula was determined to be LaVSe₂O, which is in line with the data from EDX measurements. The compound crystallizes in the CeCrSe₂O structure type in space group $C2/m$ (No. 12) with $a = 11.7(1)$ Å, $b = 3.89(1)$ Å, $c = 8.44(1)$ Å, $\beta = 90.19(1)^\circ$, and $Z = 4$. The crystal structure, which is shown in Figure 4.51, consists of strands of edge-sharing VSe₄O₂-octahedra along b , which are linked to each other along a via two edge-sharing OLa₃V-tetrahedra.

The OLa₃V-tetrahedra and the VSe₄O₂-octahedra form infinite layers in the ab plane. The layers are connected to each other along c via the axial selenium atoms of strands of edge-sharing VSe₆-octahedra. Thus, the coordination environments of the two crystallographically unique vanadium atoms are VSe₄O₂- and VSe₆-octahedra. The coordination environment of the lanthanum atom is a tricapped trigonal prism with four selenium, two oxygen, two capping selenium and one capping oxygen atoms. Relevant crystallographic data are given

in Table A.11. The different strands appearing in the crystal structure are shown separately in Figure 4.52.

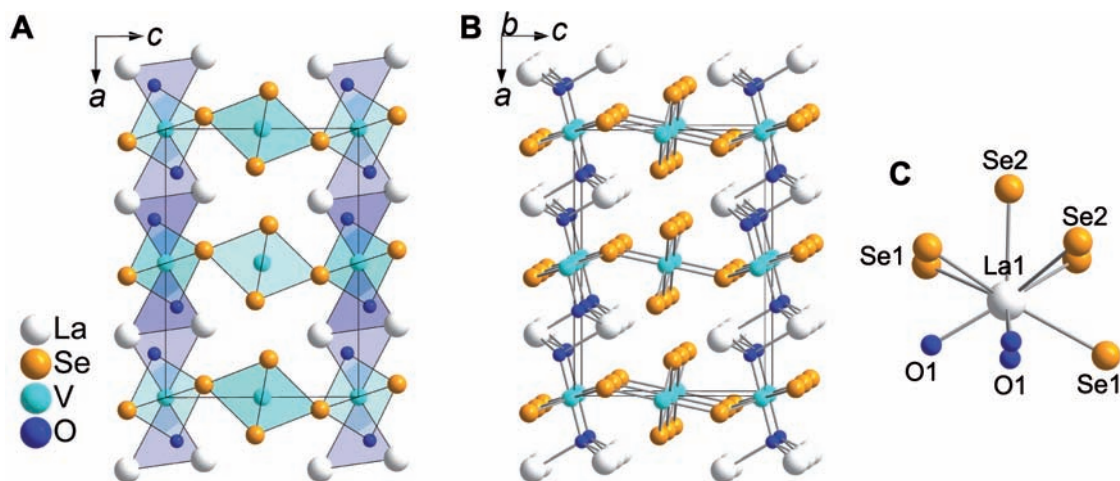


Figure 4.51 (A) and (B) Structure of LaVSe₂O with OLa₃V-tetrahedra in blue, and VSe₆- and VSe₄O₂-octahedra in cyan. (C) The environment around the lanthanum cation as a tricapped trigonal prism.

The V-O and V-Se bond lengths of the VSe₄O₂-octahedra are 196.8(1) and 262.9(1) pm, respectively, whereas the V-Se bond lengths in the VSe₆-octahedra vary from 256.5(1)–259.3(1) pm. This shows that VSe₄O₂-octahedra are strongly compressed along the O-V-O direction, whereas VSe₆-octahedra are more regular regarding the bond lengths within the polyhedron. The V-O bond length is similar to that in V₂O₃ (196.1(4) pm)^[43], which confirms the oxidation state of V^{III}. However, V-Se bond lengths are significantly longer than in V₂Se₃ (242.2–246.7 pm)^[44] but similar to bond lengths found in VSe (260.3 pm)^[45]. The La-O-La and La-O-V bond angles in the tetrahedra vary between 105.0(1)–116.0(1)°, and thus differ significantly from an ideal shape. O-V-Se and Se-V-Se bond angles in the VSe₄O₂-octahedra vary from 84.7(1)–95.3(1)° and Se-V-Se bond angles in the VSe₆-octahedra between 81.5(1)–98.5(1)°, which shows that VSe₆-octahedra are more distorted than the mixed VSe₄O₂-octahedra regarding the bond angles. The shortest distance between two equivalent vanadium atoms (= *b*-axis) is 388.6(1) pm. The distance between V(1) and V(2) of 464.4(1) pm is significantly longer.

The crystal structure of LaVSe₂O is closely related to those of La₂TSe₂O₂ (*T* = Cr, Mn, Fe)^[3,25,27], which also crystallize in the monoclinic spacegroup *C2/m* with larger values of β between 121.5(1)–121.7(1)°. The isostructural compounds consist of the same structural

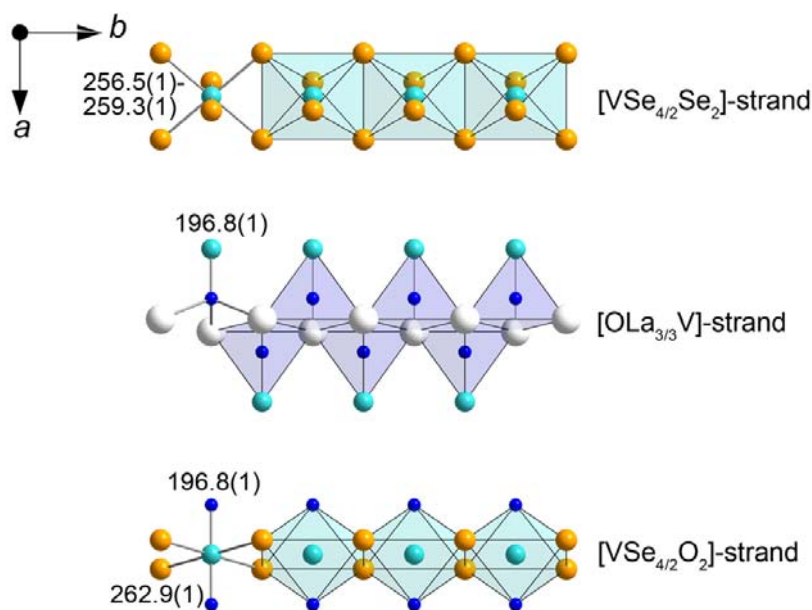


Figure 4.52 Illustration of the $[\text{VSe}_{4/2}\text{Se}_2]$ -, $[\text{OLa}_{3/3}\text{V}]$ - and $[\text{VSe}_{4/2}\text{O}_2]$ - strands, and selected bond lengths.

building blocks as LaVSe_2O but without the joining $T\text{Se}_6$ -octahedra between the ribbons. Unfortunately, different synthesis approaches to prepare pure samples of LaVSe_2O always resulted in mixtures of the desired phase and different binary and ternary compounds. Therefore, the magnetic properties of LaVSe_2O remain still unknown.

4.5.4.2 $\text{La}_5\text{V}_3\text{Se}_6\text{O}_7$

Synthesis and Characterization

We came across single crystals of $\text{La}_5\text{V}_3\text{Se}_6\text{O}_7$ likewise during attempts to prepare $\text{La}_3\text{VSe}_3\text{O}_3$. Samples with higher purity (≈ 90 wt%) were prepared from the reaction of appropriate amounts of La_2O_3 , freshly filed lanthanum metal, V and Se at 1373 K. The resulting black needles are depicted in Figure 4.53.

The crystal structure obtained from single-crystal X-ray diffraction is compatible with the X-ray powder pattern (Fig. 4.54). EDX experiments revealed the ratio of the elements to be $\text{La}_{5.0}\text{V}_{2.7(2)}\text{Se}_{5.7(3)}\text{O}_{6.3(4)}$, which is in good agreement with the molecular formula determined from single crystal X-ray data. No hints of incorporation or inclusion of the flux material were found in the EDX spectrum (Fig. 4.53). Rietveld refinement revealed the presence of small amounts of LaVO_3 and LaSe_2 .

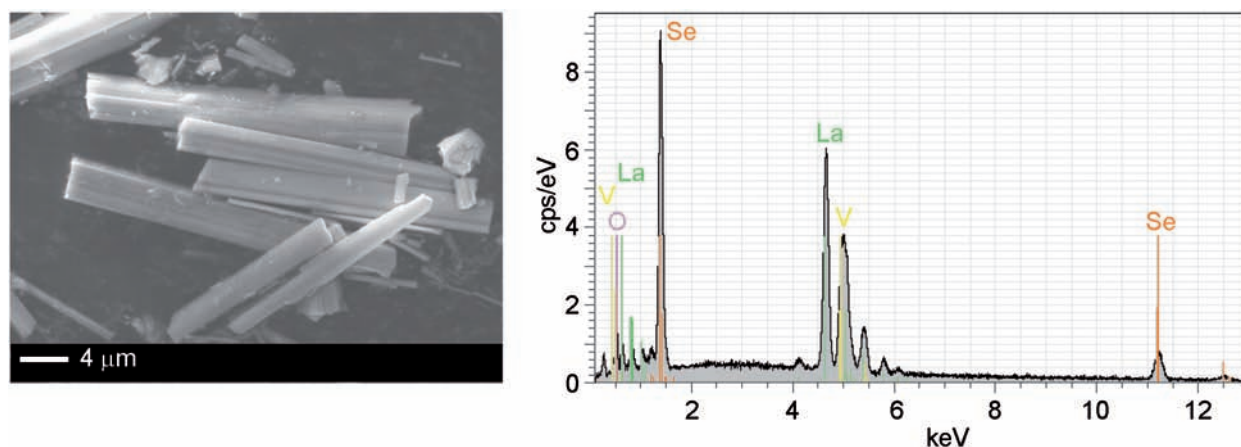


Figure 4.53 Typical needle-like single crystals (left) and EDX spectrum (right) of $\text{La}_5\text{V}_3\text{Se}_6\text{O}_7$. Characteristic lines of the elements of the flux are not observed. The small peak at ≈ 0.25 keV belongs to carbon from the adhesive conducting carbon film.

The compound crystallizes isostructural to the sulfur-analogue ($\text{La}_5\text{V}_3\text{S}_6\text{O}_7$ -type structure)^[38] in the orthorhombic space group $Pm\bar{m}n$ (No. 59) with $a = 18.2(1)$ Å, $b = 3.91(1)$ Å, $c = 10.5(1)$ Å, and $Z = 2$. Details of the data collection and refinement results of the structure determination are listed in Table A.12. There are similar building blocks as found in the crystal structure of LaVSe_2O , namely VSe_4O_2 -octahedra, OLa_3V -, and additionally OLa_4 -tetrahedra. Using these building blocks, the crystal structure can be described as follows. Two types of edge-sharing VSe_4O_2 -octahedra (cyan in Fig. 4.55) form infinite strands along b . These octahedra are linked together in the ac -plane by edge-sharing OLa_4 - and OLa_3V -tetrahedra (blue). The tetrahedra form infinite ribbons along b , in which they are connected to each other via common edges and corners.

The three crystallographically unique lanthanum atoms show two different environments. $\text{La}(1)$ and $\text{La}(2)$ are in trigonal prisms of four selenium, two oxygen, two capping oxygen atoms and one capping selenium atom. $\text{La}(3)$ is in a trigonal prism of two selenium and four oxygen atoms with two capping selenium atoms and one capping oxygen atom. The polyhedra of $\text{La}(1)$ and $\text{La}(2)$ are linked to each other via a common $\text{O}(2)$ - $\text{O}(3)$ -edge, whereas $\text{La}(2)$ and $\text{La}(3)$ share a triangular plane of one $\text{Se}(2)$ and two $\text{Se}(3)$ atoms (Fig. 4.55 C).

The shortest V-V-distances, $\text{V}(1)$ - $\text{V}(1)$ and $\text{V}(2)$ - $\text{V}(2)$, are 391.1(1) pm. Further V-V distances in the ab -plane vary from 560.6(1)–611.2(1) pm. The V-O bond length within the VSe_4O_2 -octahedra is 181.6(1) pm for $\text{V}(1)$ and varies from 186.0(1)–192.0(1) pm for $\text{V}(2)$. The V-Se bond lengths are 254.4(1)–265.7(1) pm, resulting in strongly compressed octahedra

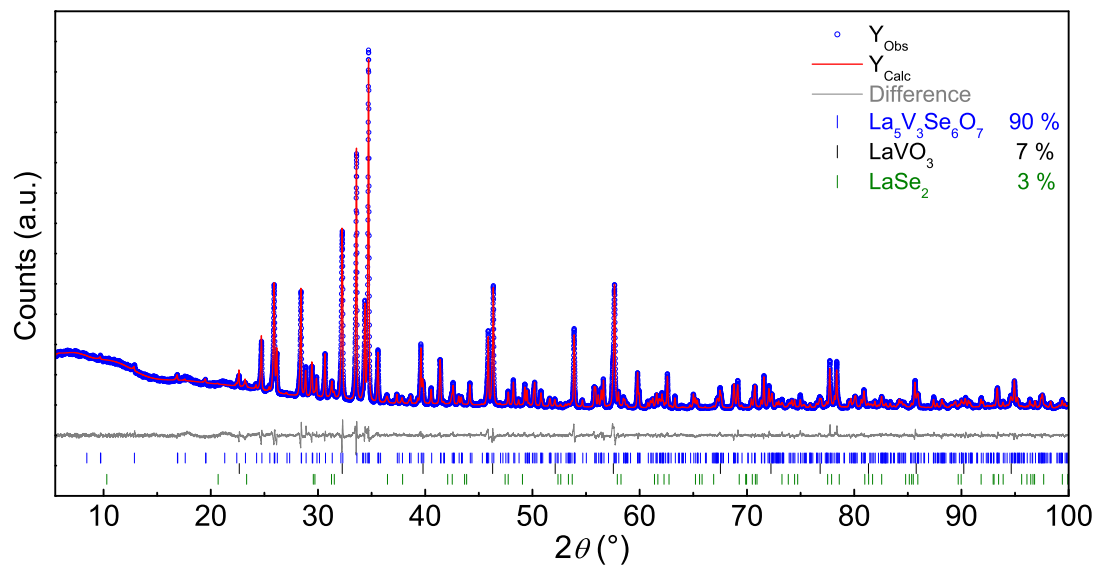


Figure 4.54 X-ray powder pattern (blue), Rietveld fit (red) and difference plot (gray) of $\text{La}_5\text{V}_3\text{Se}_6\text{O}_7$.

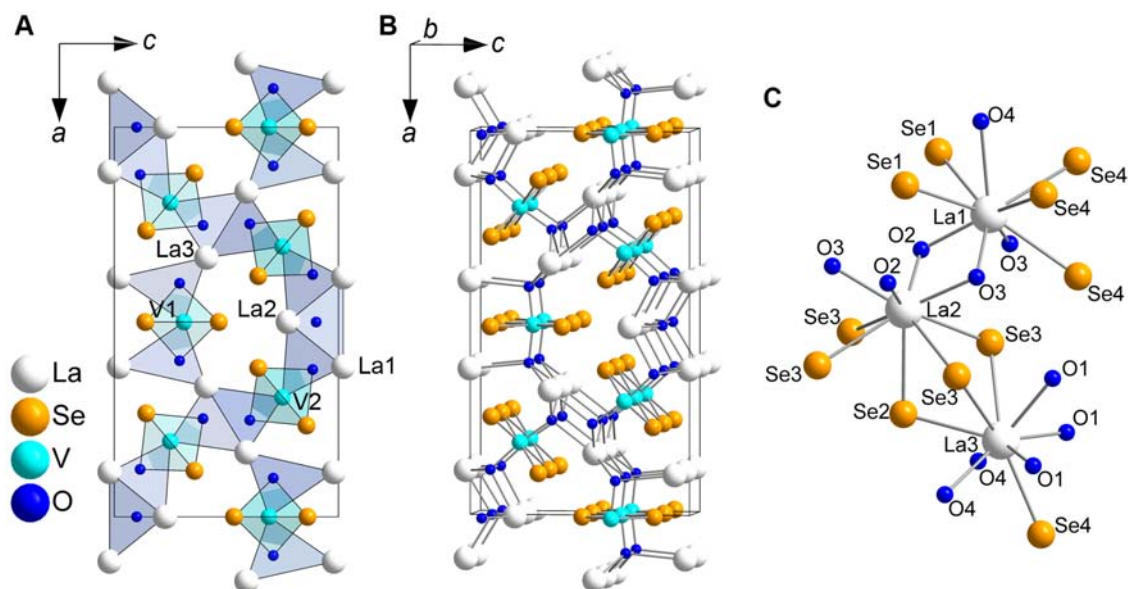


Figure 4.55 (A) and (B) Structure of $\text{La}_5\text{V}_3\text{Se}_6\text{O}_7$ with OLa_4^- and OLa_3V -tetrahedra in blue, and VSe_4O_2 -octahedra in cyan. (C) Coordination environments around the three lanthanum atoms.

along the oxygen positions similar to those in LaVSe_2O . Se-V-Se and O-V-Se bond angles vary from $82.4(1)$ – $100.5(1)^\circ$, which shows that the VSe_4O_2 -octahedra differ significantly from an ideal shape and are more irregular than in LaVSe_2O . La-O-La and La-O-V bond angles vary from $97.0(1)$ – $117.9(1)^\circ$, indicating strongly distorted tetrahedra.

As there are no Se–Se bonds, the formal oxidation states of La/Se/O are +III/–II/–II. The average oxidation state of vanadium is +3.67, which may be explained by the multiplicities of the two vanadium positions. As V(1) is on a $2a$ and V(2) is on a $4f$ *Wyckoff*-position, there are two possibilities to assign oxidation numbers to the vanadium atoms in order to get an average of +3.67. The two options are listed in Table 4.8.

Table 4.8 Possibilities for the oxidation states of V(1) and V(2).

Site	<i>Wyckoff</i> position	1 st option	2 nd option
V(1)	$2a$	V^{V}	V^{III}
V(2)	$4f$	V^{III}	V^{IV}

As the bond length of V(1)-O is smaller than V(2)-O, the oxidation number of V(1) should be higher than that of V(2), which argues for option 1. However, there are no examples in the literature of compounds with a mixture of $\text{V}^{\text{III}}/\text{V}^{\text{V}}$. In contrast, a mixture of $\text{V}^{\text{III}}/\text{V}^{\text{IV}}$ is well known from the Magnéli phases^[46,47] $\text{V}_n\text{O}_{2n-1}$, which supports option 2. Therefore, V-O bond lengths can not clarify this problem but option 2 seems to be more probable.

Magnetization Measurements

Magnetic susceptibility measurements show paramagnetism and an increase of χ_{mol} below 15 K (Fig. 4.56 A). A Curie-Weiss fit of the linear part of the inverse susceptibility between 150 and 300 K (inset) reveals an effective paramagnetic moment of $\mu_{\text{eff}} = 4.60(1) \mu_{\text{B}}$ per formula unit, which is higher than the theoretical values of 3.74 or $4.00 \mu_{\text{B}}$. This may be caused by the magnetic impurity phase LaVO_3 . The negative Weiss constant ($\theta = -100.1(2)$ K) indicates antiferromagnetic ordering of the moments. Isothermal magnetization plots at 300 and 1.8 K (Fig. 4.56 B) display low values of μ/μ_{B} and are in line with either paramagnetism or an antiferromagnetically ordered state. The tiny hysteresis at 1.8 K, as well as the increase of χ_{mol} below 15 K, may be caused by the magnetic impurity phase LaVO_3 , which undergoes a paramagnetic to antiferromagnetic transition at ≈ 140 K and shows weak ferromagnetism at low temperatures.^[48] However, given the complex crystal structure with two unique vana-

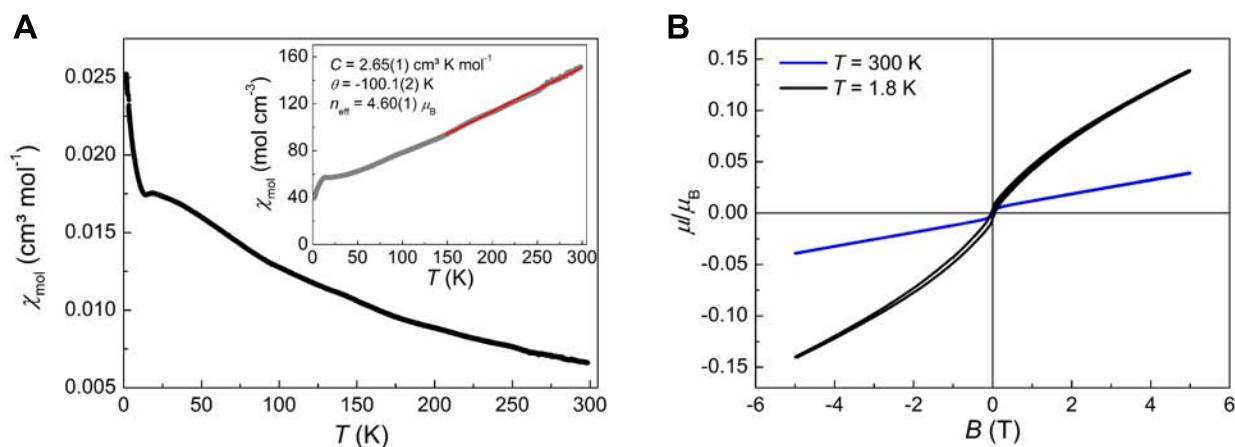


Figure 4.56 (A) Magnetic susceptibility measurement at $B = 1 \text{ T}$ and inverse susceptibility (inset) with Curie-Weiss fit (red). (B) Isothermal magnetization of $\text{La}_5\text{V}_3\text{Se}_6\text{O}_7$ at 300 and 1.8 K.

dium positions, the magnetic ordering pattern may be complex and not determinable from susceptibility data alone.

4.5.4.3 $\text{La}_5\text{V}_3\text{Se}_7\text{O}_5$

Synthesis and Characterization

The $\text{La}_5\text{V}_3\text{Se}_7\text{O}_5$ phase was first obtained as a side product in the attempt to prepare $\text{La}_4\text{VSe}_6\text{O}$. Energy dispersive X-ray spectroscopy of the small, black needles revealed the characteristic lines of lanthanum, vanadium, selenium and oxygen but none of the flux material, as shown in Figure 4.57. The averaged atomic percentages are La 23.1(7) %, V 16.6(5) %, Se 31.3(14) %, and O 29.0(2) %, which corresponds to $\text{La}_{5.0}\text{V}_{3.6(2)}\text{Se}_{6.8(7)}\text{O}_{6.3(2)}$.

The crystal structure of the new compound was solved using single crystal X-ray diffraction leading to the molecular formula $\text{La}_5\text{V}_3\text{Se}_7\text{O}_5$. Subsequently, samples with higher purity were prepared from the reaction of appropriate amounts of La_2O_3 , freshly filed lanthanum metal, V and Se at 1273 K. Small traces ($\leq 5 \text{ wt}\%$) of LaVO_3 and $\text{La}_{2.67}\text{Se}_4$ are identified as impurities from the Rietveld fit (Fig. 4.58).

$\text{La}_5\text{V}_3\text{Se}_7\text{O}_5$ crystallizes in a new structure type in space group $Pnma$ (No. 62) with $a = 16.5(1) \text{ \AA}$, $b = 3.90(1) \text{ \AA}$, $c = 24.8(1) \text{ \AA}$, and $Z = 4$. Relevant crystallographic data are compiled in Table A.13. The crystal structure, which is shown in Figure 4.59, can be described using the structural building blocks found in LaVSe_2O and $\text{La}_5\text{V}_3\text{Se}_6\text{O}_7$. There exist three independent vanadium positions, of which V(1) and V(2) form chains of edge-sharing VSe_4O_2 -octahedra along b . These octahedra are linked together along the c -axis by

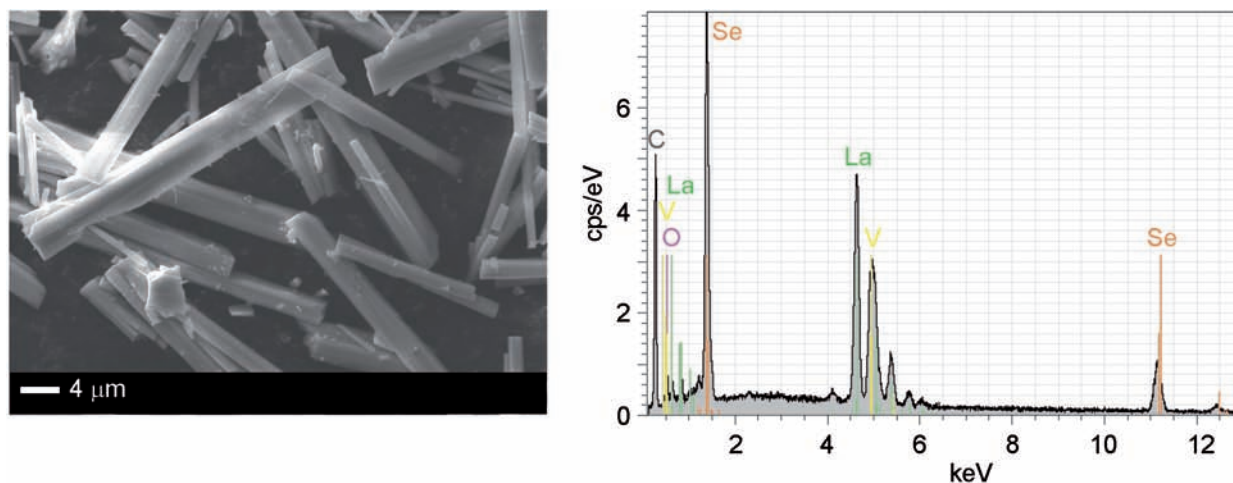


Figure 4.57 Typical needle-like single crystals (left) and EDX spectrum (right) of $\text{La}_5\text{V}_3\text{Se}_7\text{O}_5$. Characteristic lines of the elements of the flux are not observed. The peak at ≈ 0.25 keV belongs to carbon from the adhesive conducting carbon film.

alternating two or three edge-sharing OLa_4 - and/or OLa_3V -tetrahedra forming meandering strands along c . These tetrahedra are connected to each other forming infinite fluorite-like ribbons parallel to b . Furthermore, each VSe_4O_2 -octahedra is connected to the VSe_4O_2 -octahedra of a neighboring, meandering strand along a via the axial selenium atoms of a distorted $\text{V}(3)\text{Se}_6$ -octahedra. Thus, the coordinations of the three crystallographically unique vanadium atoms are twice a VSe_4O_2 -octahedra and once a VSe_6 -octahedra.

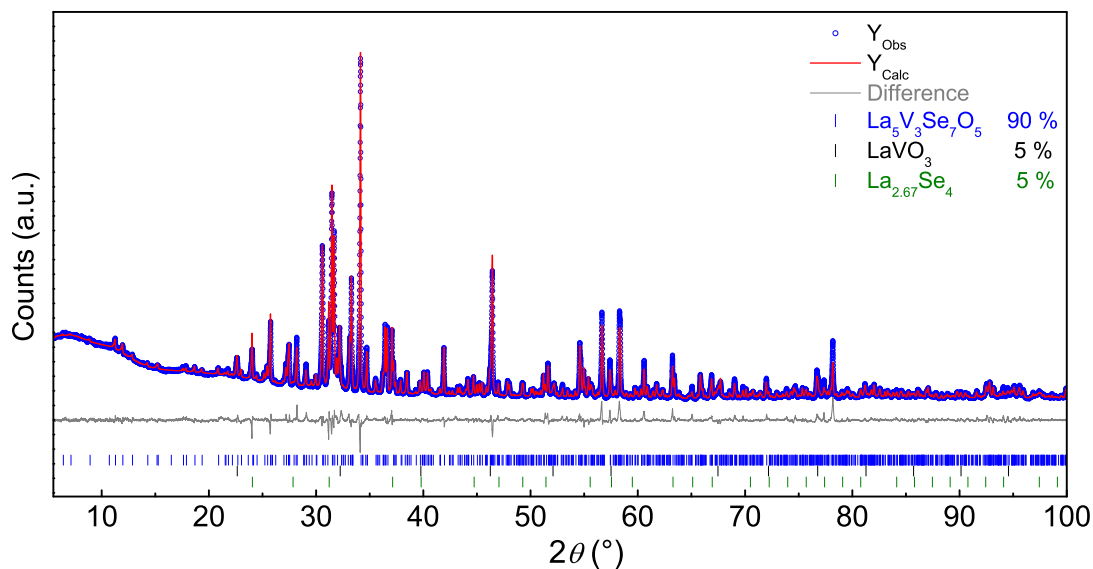


Figure 4.58 X-ray powder pattern (blue), Rietveld fit (red) and difference plot (gray) of $\text{La}_5\text{V}_3\text{Se}_7\text{O}_5$.

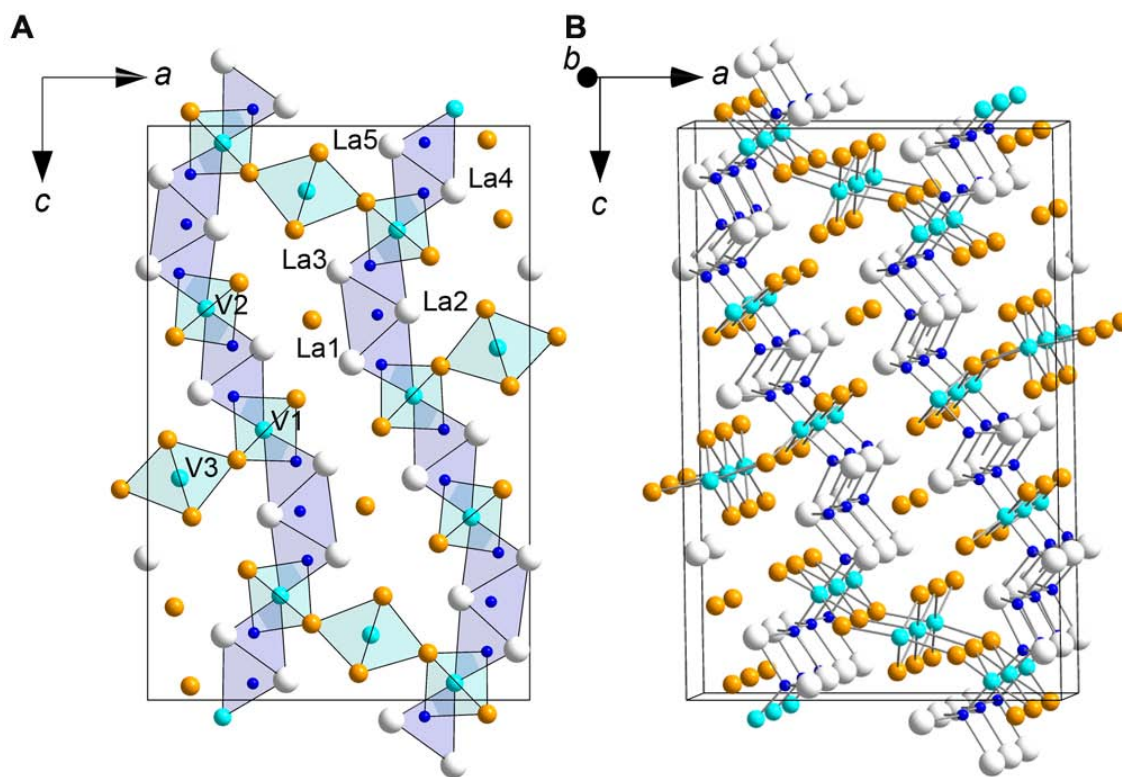


Figure 4.59 Structure of $\text{La}_5\text{V}_3\text{Se}_7\text{O}_5$ with OLa_4 - and OLa_3V -tetrahedra in blue, and VSe_6 - and VSe_4O_2 -octahedra in cyan.

V-O bond lengths within the compressed VSe_4O_2 -octahedra vary from 192.0(1)–194.8(1) pm, which is similar to the bond lengths in V_2O_3 (196.1(4) pm)^[43] and LaVSe_2O , and is therefore in line with vanadium in the oxidation state +III. However, V-Se bond lengths of 259.4(1)–262.1(1) pm are significantly longer than in V_2Se_3 (242.2–246.7 pm)^[44] but similar to values found in LaVSe_2O and $\text{La}_5\text{V}_3\text{Se}_6\text{O}_7$ in the previous sections. O-V-Se and Se-V-Se bond angles in the VSe_4O_2 -octahedra vary from 86.2(1)–97.0(1)° and those in the VSe_6 -octahedra from 83.6(1)–96.6(1)°. Moreover, tetrahedral angles within the OLa_4 - and OLa_3V -tetrahedra (101.9(1)–116.3(1)°) significantly deviate from the ideal value of $\approx 109.5^\circ$.

There exist five crystallographically unique La atoms. The atoms La(1), La(3) and La(4) are in trigonal prisms of four Se atoms and two O atoms with one capping Se atom and one capping O atom. La(2) is in a square antiprism of four Se and four O atoms and one capping Se atom. La(5) is in a trigonal prism of four Se and two O atoms and two capping Se atoms and one capping O atom. The connection between the different polyhedra around the lanthanum cations is shown in Figure 4.60.

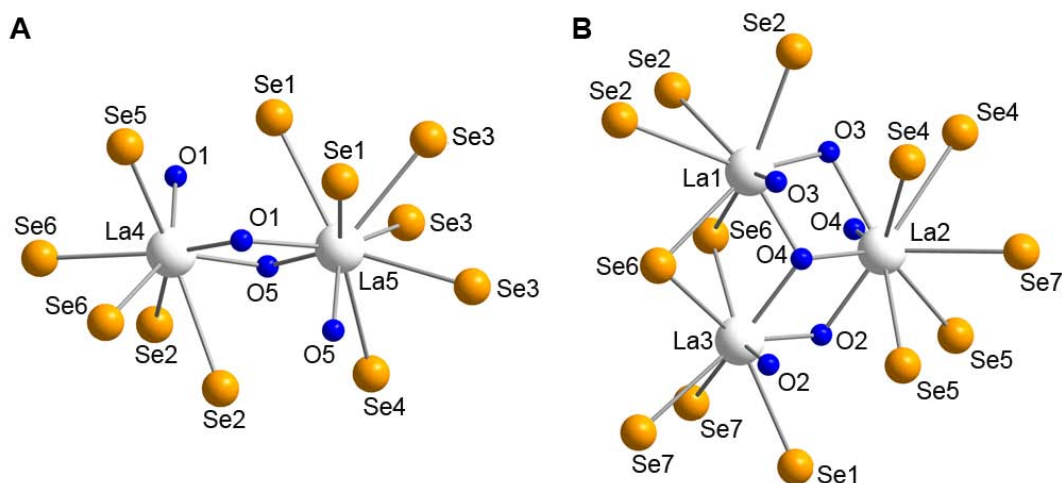


Figure 4.60 Connection between the coordination environments of (A) La(4) and La(5) and (B) La(1), La(2) and La(3) in $\text{La}_5\text{V}_3\text{Se}_7\text{O}_5$.

The coordination environments of La(4) and La(5) are edge-shared via the common oxygen atoms O(1) and O(5). A similar connectivity is found for La(1) and La(2), as well as for La(2) and La(3). Simply the polyhedra of La(1) and La(3) are linked to each other via a common Se_2O -plane. The V(1)-V(1) and V(2)-V(2) distances (= *b*-axis) within the octahedral VSe_4O_2 -chains is 390.1(1) pm and is therefore equal to the V(3)-V(3) distance in the VSe_6 -chains. However, distances between different vanadium positions are significantly longer. The V(1)-V(3) distance is in the range of 460.9(1)–468.3(1) pm and the V(1)-V(2) distance varies between 611.6(1)–718.9(1) pm.

Magnetization Measurements

The magnetic susceptibility reveals paramagnetism between 16 and 300 K, and a drop in the susceptibility at ≈ 16 K (Fig. 4.61 A). A fit of χ^{-1} according to a modified Curie-Weiss expression was applied in the almost linear part of the curve between 180 and 300 K. The measurement range below 180 K was excluded from the fit as the graph significantly deviates from a linear behaviour and as the impurity phase LaVO_3 shows a magnetic transition at ≈ 140 K.^[48] The fit delivered a paramagnetic Weiss temperature of $-8.5(8)$ K, a temperature independent contribution of $4.7(4) \times 10^{-3} \text{ cm}^3/\text{mol}$, and an experimental paramagnetic moment of $\mu_{\text{eff}} = 4.72(2) \mu_{\text{B}}$ per formula unit, which is compatible with the theoretically expected value of $4.90 \mu_{\text{B}}$ for V^{III} . The negative Weiss constant together with the drop in χ_{mol} indicate antiferromagnetic ordering of the moments below $T_{\text{N}} \approx 16$ K. Figure 4.61 (B)

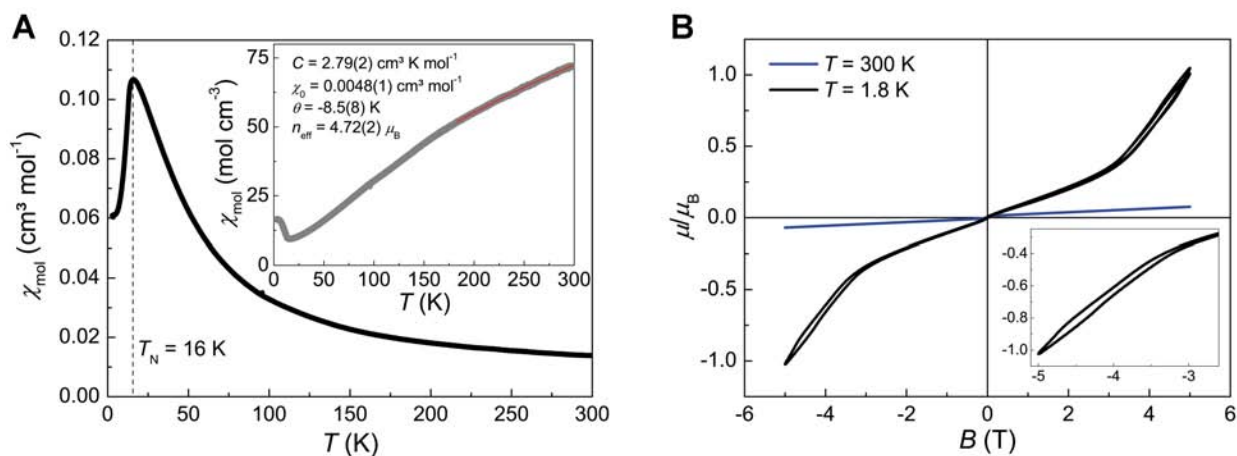


Figure 4.61 (A) Magnetic susceptibility measurement at $B = 1$ T and inverse susceptibility (inset) with extended Curie-Weiss fit (red). (B) Isothermal magnetization of $\text{La}_5\text{V}_3\text{Se}_7\text{O}_5$ at 300 and 1.8 K.

displays the magnetization isotherms of $\text{La}_5\text{V}_3\text{Se}_7\text{O}_5$ at 1.8 and 300 K. The isotherm measured at 300 K is linear with the applied field with tiny deviations at low fields. At 1.8 K, well below the Néel temperature, the behaviour is linear in the range $-3 \text{ T} \rightarrow +3 \text{ T}$, and the absolute value of the magnetization increases drastically at a critical field of $B_{\text{Cr}} \approx \pm 3 \text{ T}$. This upturn can be associated with a spin reorientation, also known as metamagnetic step (antiparallel to parallel spin alignment). Furthermore, the 1.8 K isotherm exhibits a weak but well resolved hysteresis between $|B| \approx 3\text{--}5 \text{ T}$ in the increasing / decreasing field curves (inset in Fig. 4.61). The magnetization of $\text{La}_5\text{V}_3\text{Se}_7\text{O}_5$ at 1.8 K does not saturate and reaches $\approx 1 \mu_B$ per formula unit at the highest obtainable field of 5 T.

4.5.4.4 $\text{La}_7\text{VSe}_5\text{O}_7$

Synthesis and Characterization

Analogously to the previous compound, $\text{La}_7\text{VSe}_5\text{O}_7$ was first observed by the attempt to prepare $\text{La}_4\text{VSe}_6\text{O}$. Single crystals, which appear as thin red needles (Fig. 4.62), and polycrystalline samples of $\text{La}_7\text{VSe}_5\text{O}_7$ were obtained from the reaction of appropriate amounts of La_2O_3 , freshly filed lanthanum metal, VSe_2 and Se at 1323 K.

Energy dispersive X-ray spectroscopy of the single crystals revealed the average atomic percentages La 36.8(3) %, V 4.4(7) %, Se 25.3(2) %, and O 33.4(6) %, which corresponds to $\text{La}_{7.0}\text{V}_{0.8(2)}\text{Se}_{4.8(1)}\text{O}_{6.4(2)}$. No traces of the elements of the flux material were found in the EDX spectrum, as shown in Figure 4.62. Single-crystal X-ray diffraction (details of the refinement

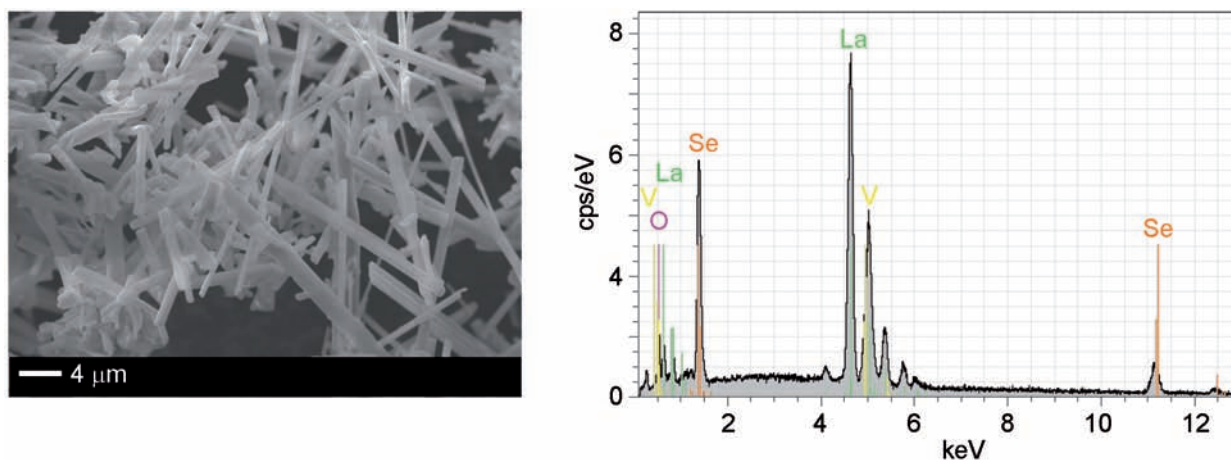


Figure 4.62 Typical needle-like single crystals (left) and EDX spectrum (right) of $\text{La}_7\text{VSe}_5\text{O}_7$. Characteristic lines of the elements of the flux are not observed. The peak at ≈ 0.25 keV belongs to carbon from the adhesive conducting carbon film.

can be found in Table A.14) was used to determine the structure of the new compound. The purity of the samples were checked by X-ray powder diffraction (Fig. 4.63), which uncovered a small amount of La_2SeO_2 as impurity phase.

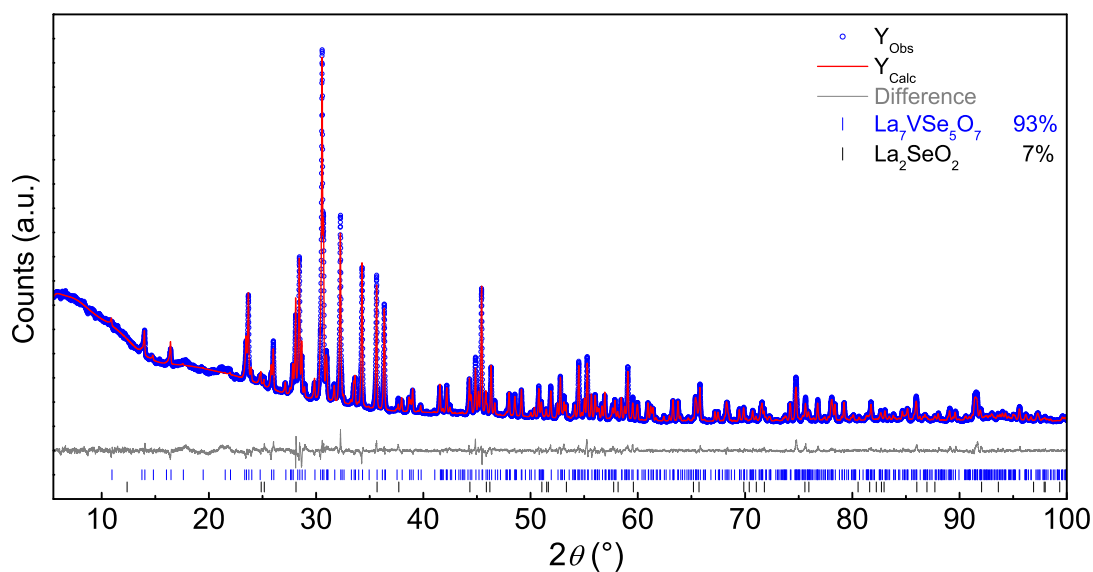


Figure 4.63 X-ray powder pattern (blue), Rietveld fit (red) and difference plot (gray) of $\text{La}_7\text{VSe}_5\text{O}_7$.

$\text{La}_7\text{VSe}_5\text{O}_7$ crystallizes in a new structure type in space group $Cmcm$ (No. 63) with $a = 3.99(1)$ Å, $b = 12.9(1)$ Å, $c = 32.3(1)$ Å, and $Z = 2$. Oxygen atoms were refined isotropically. The structure (Fig. 4.64) consists of chains of edge-sharing VSe_4O_2 -octahedra along a , which are linked along the c -axis by strands of seven edge-sharing $\text{OLa}_3\text{V}/\text{OLa}_4$ -tetrahedra. These

edge-sharing tetrahedra build infinite fluorite-like ribbons along a . The structure is closely related to that of $\text{La}_6\text{MnSe}_4\text{O}_6$.^[27] Apparently, the structures only differ in the width of the $\text{OLa}_3\text{T}/\text{OLa}_4$ -tetrahedra framework, which is six in $\text{La}_6\text{MnSe}_4\text{O}_6$ and seven in $\text{La}_7\text{VSe}_5\text{O}_7$.

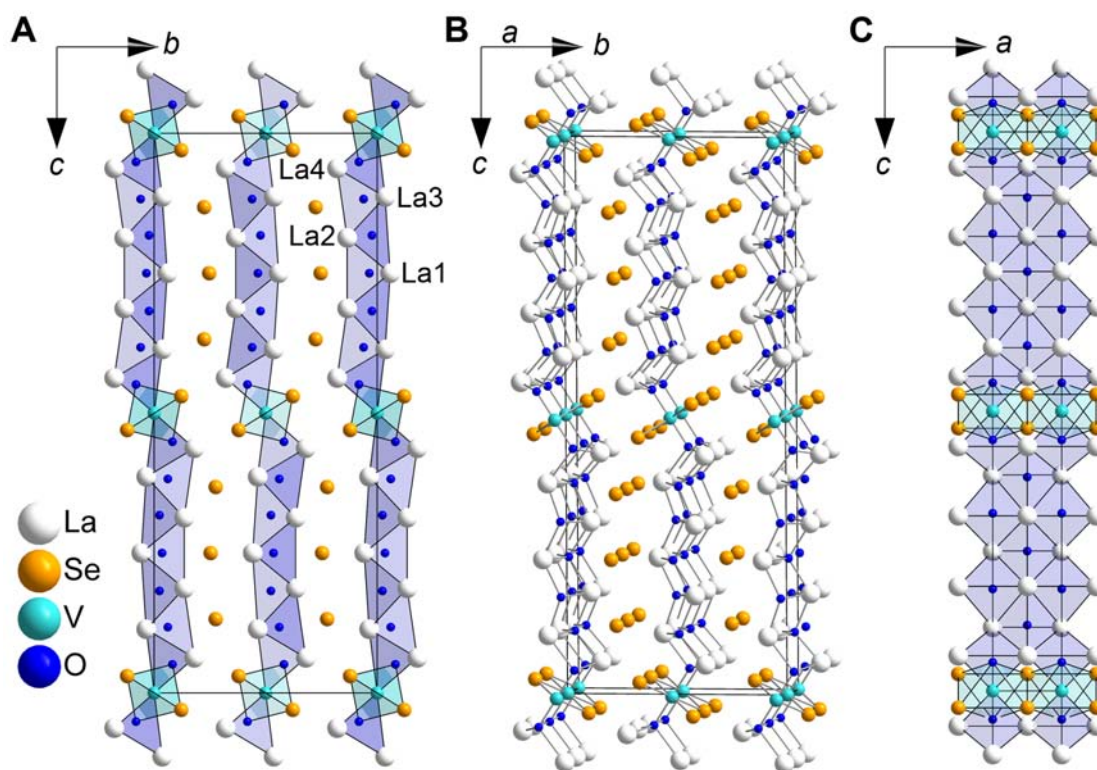


Figure 4.64 (A) and (B) Structure of $\text{La}_7\text{VSe}_5\text{O}_7$ along a with OLa_4 - and OLa_3V -tetrahedra in blue and VSe_4O_2 -octahedra in cyan. (C) Structure of $\text{La}_7\text{VSe}_5\text{O}_7$ along b with chains of edge-sharing VSe_4O_2 -octahedra and fluorite-like ribbons of La_4 - and OLa_3V -tetrahedra.

The coordinations of the four crystallographically unique La atoms in $\text{La}_7\text{VSe}_5\text{O}_7$ are shown in Figure 4.65. Atom La(1) is in a tetrahedra of two Se atoms and two O atoms with two capping O atoms. La(2) is in a square antiprism of four Se and four O atoms. Atoms La(3) and La(4) are in distorted square antiprisms of five Se and three O atoms or four Se and four O atoms, respectively. Similar to $\text{La}_5\text{V}_3\text{Se}_7\text{O}_5$, the coordination environments of La(1)/La(2), La(2)/La(4) and La(3)/La(4) are linked via two common oxygen atoms (edge-sharing), respectively. The polyhedra of La(1) and La(4) share one oxygen atom and are therefore corner-sharing, whereas La(2) and La(3) are linked via a common Se_2O plane. V-O and V-Se bond lengths in the VSe_4O_2 octahedra are 195.8(1) and 271.2(1) pm, which is similar to previous described bond lengths of compounds with V^{III} (LaVSe_2O and $\text{La}_5\text{V}_3\text{Se}_7\text{O}_5$). O-V-Se and Se-V-Se bond angles vary from 85.4(1)–94.6(1)°, and La-O-La/La-O-V from

100.9(1)–135.4(1)°, thus tetrahedra are significantly more distorted than octahedra regarding the bond angles. As there are no Se-Se or Se-O bonds, the oxidation states of La/V/Se/O are +III/+III/−II/−II. The V-V distance within the octahedra chains (= *a*-axis) is 398.6(1) pm, whereas the V-V distances of 673.3(1) and 1614.5(1) pm along *b* and *c* are significantly larger.

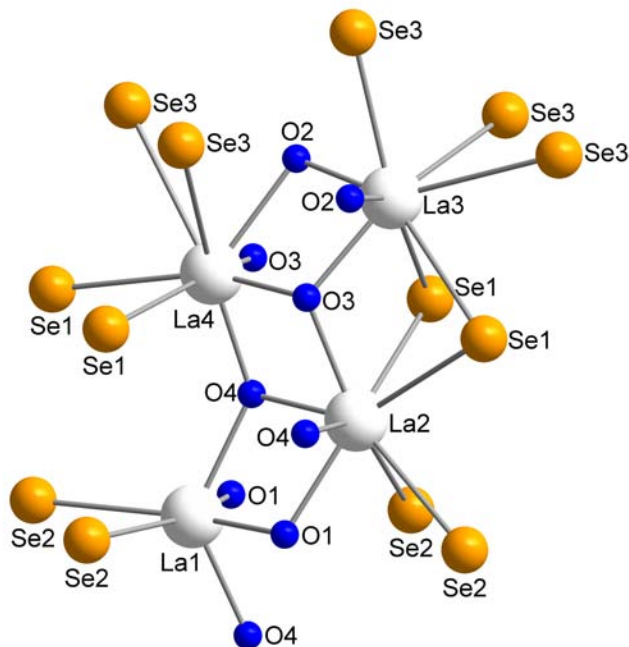


Figure 4.65 Connection between the coordination environments of the lanthanum atoms in $\text{La}_7\text{VSe}_5\text{O}_7$.

Magnetization Measurements

The magnetic susceptibility of $\text{La}_7\text{VSe}_5\text{O}_7$ obeys the Curie-Weiss rule and indicates two types of magnetic ordering. On the one hand, ferromagnetic ordering below 12 K as χ_{mol} significantly increases below this temperature and on the other hand, antiferromagnetic ordering at even lower temperatures (< 7 K) as the curve flattens. The effective paramagnetic moment of 3.20(1) μ_{B} per formula unit was calculated from a Curie-Weiss fit of the inverse molar susceptibility (inset of Figure 4.66 A). The obtained value of 3.20 μ_{B} is slightly larger than the theoretical spin-only value of 2.83 μ_{B} for V^{III} . Although the negative Weiss temperature of $\theta = -66.2(3)$ K argues for antiferromagnetism, measurements of the isothermal magnetization confirm ferromagnetic ordering of the moments at very low temperature (Fig. 4.66 B). The magnetization over applied field curve at 1.6 K shows a broad hysteresis loop with a saturation magnetization of $\approx 0.35 \mu_{\text{B}}$ per formula unit. Isotherms at 5 and 10 K also show

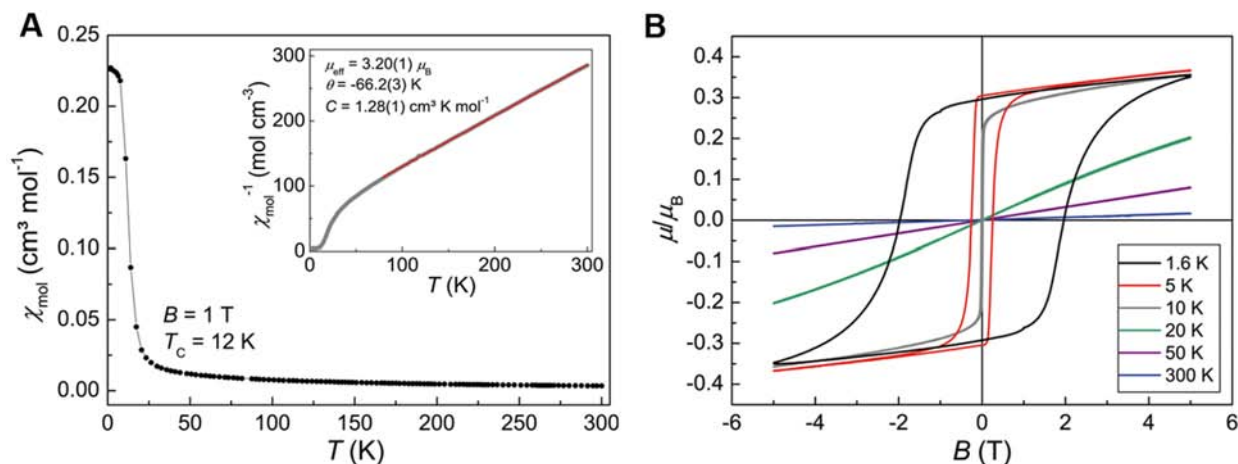


Figure 4.66 (A) Magnetic susceptibility (black) and inverse susceptibility (inset) of $\text{La}_7\text{VSe}_5\text{O}_7$. Curie-Weiss fit in red. Parameters obtained from the fit are given in the inset. (B) Magnetization isotherms of $\text{La}_7\text{VSe}_5\text{O}_7$ at 1.6, 5, 10, 20, 50, and 300 K.

hysteresis loops with smaller loop widths compared to that at 1.6 K, but with the same saturation magnetization. For temperatures > 20 K, the isothermal magnetization curves are linear with field. Based on these observations, we suggest ferromagnetic ordering of the V^{III} 3d-electrons along the VSe_4O_2 -octahedral chains and partial antiferromagnetic ordering between the strands, which is in line with the low saturation magnetization at 1.6 K. These findings are in strong contrast to magnetic measurements of compounds with similar building blocks, as for example the series $\text{La}_{2n+2}\text{MnSe}_{n+2}\text{O}_{2n+2}$ ($n = 0-2$), which indicate solely antiferromagnetic ordering of the manganese atoms below 15 K.^[27]

4.5.4.5 $\text{La}_{13}\text{V}_7\text{Se}_{16}\text{O}_{15}$

Synthesis and Characterization

Thin black plates (Fig. 4.67) were found beside black needles by the attempt to prepare $\text{La}_5\text{V}_3\text{Se}_7\text{O}_5$. EDX measurements revealed that the needles are $\text{La}_5\text{V}_3\text{Se}_7\text{O}_5$, whereas the plates have a different ratio of the elements. The composition of these crystals were La:V:Se:O $\approx 2:1:2:2$ within the EDX accuracy. The inclusion or incorporation of the flux material can be excluded as the characteristic emission lines of neither potassium and sodium nor iodine were observed, as can be seen in Figure 4.67. Single crystal X-ray diffraction experiments uncovered a new compound with the formula $\text{La}_{13}\text{V}_7\text{Se}_{16}\text{O}_{15}$, which crystallizes in a new structure type. Powder X-ray diffraction experiments (Fig. 4.68) revealed a phase pure sample of this compound from the reaction of appropriate amounts of La_2O_3 , freshly filed

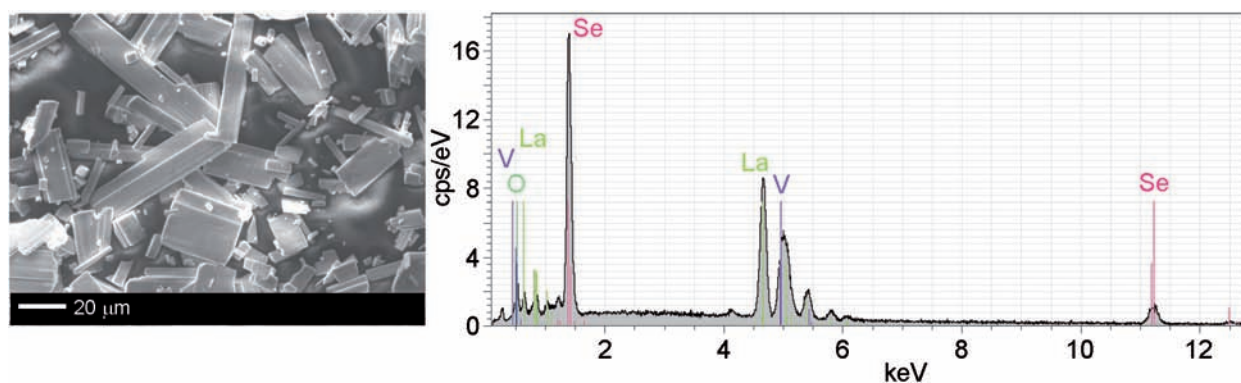


Figure 4.67 Single crystals (left) and EDX spectrum (right) of $\text{La}_{13}\text{V}_7\text{Se}_{16}\text{O}_{15}$. Characteristic lines of the elements of the flux are not observed. The small peak at ≈ 0.25 keV belongs to carbon from the adhesive conducting carbon film.

lanthanum metal, vanadium (5 wt% excess) and selenium at 1303 K.

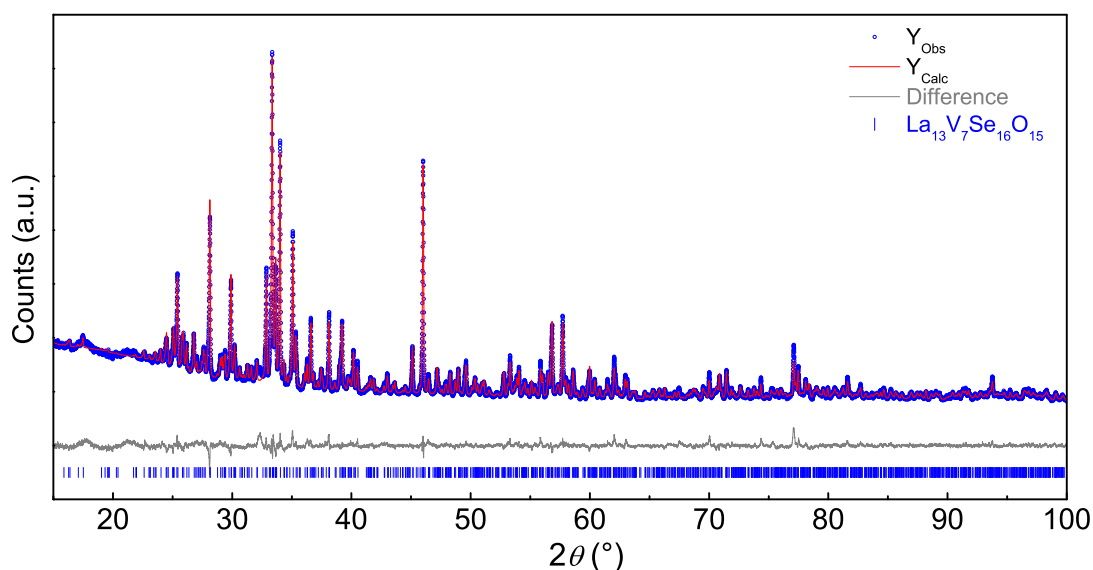


Figure 4.68 X-ray powder pattern (blue), Rietveld fit (red) and difference plot (gray) of $\text{La}_{13}\text{V}_7\text{Se}_{16}\text{O}_{15}$.

The crystal structure can be described as a stacked combination of the $\text{La}_5\text{V}_3\text{S}_6\text{O}_7$ and the $\text{La}_4\text{Ti}_2\text{Se}_5\text{O}_4$ structure types. The compounds $\text{La}_5\text{V}_3\text{S}_6\text{O}_7$ and $\text{La}_4\text{Ti}_2\text{Se}_5\text{O}_4$ have been characterized by *Dugué et al.*^[38] and *Tougait et al.*^[20], respectively. We were able to prepare the analogous selenium compound $\text{La}_5\text{V}_3\text{Se}_6\text{O}_7$ (Section 4.5.4.2). However, we were not successful to prepare $\text{La}_4\text{V}_2\text{Se}_5\text{O}_4$. Nevertheless, the formal combination of one formula unit of $\text{La}_5\text{V}_3\text{Se}_6\text{O}_7$ and two formula units of the hypothetical $\text{La}_4\text{V}_2\text{Se}_5\text{O}_4$ gives the molecular formula of the new material $\text{La}_{13}\text{V}_7\text{Se}_{16}\text{O}_{15}$. *Tougait et al.* observed that one Se atom in

La₄Ti₂Se₅O₄ is split over two positions with an occupancy ration of $\approx 0.5:0.5$ (Fig. 4.69). In contrast, we found an ordering of the equivalent split position in the La₄V₂Se₅O₄ substructure of our compound, which will be discussed later.

La₁₃V₇Se₁₆O₁₅ crystallizes in space group *Cmc*2₁ (No. 36) with $a = 3.94(1)$ Å, $b = 54.0(1)$ Å, $c = 18.3(1)$ Å, and $Z = 4$. Oxygen atoms were refined isotropically. Relevant crystallographic data are listed in Table A.15. The lattice parameters a and c are similar to the equivalent lattice parameters of the two compounds La₅V₃Se₆O₇ and La₄Ti₂Se₅O₄ (Table 4.9), which is in line with the description of a simple stacking of both structure types.

Table 4.9 Overview over the space group, Z and lattice parameters of the three oxyselenides La₅V₃Se₆O₇, La₄Ti₂Se₅O₄^[20] and La₁₃V₇Se₁₆O₁₅.

	La ₅ V ₃ Se ₆ O ₇	La ₄ Ti ₂ Se ₅ O ₄	La ₁₃ V ₇ Se ₁₆ O ₁₅
Space group, Z	<i>Pmnm</i> , 2	<i>Cmcm</i> , 8	<i>Cmc</i> 2 ₁ , 4
$a/\text{Å}$	18.2(1)	3.97(1)	3.94(1)
$b/\text{Å}$	3.91(1)	33.1(1)	54.0(1)
$c/\text{Å}$	10.5(1)	18.6(1)	18.3(1)

We initially used space group *Cmcm* to solve the crystal structure. The result can be described as a combination of the two substructures La₅V₃Se₆O₇ (La₅V₃Se₆O₇-type structure) and La₄V₂Se₅O₄ (La₄Ti₂Se₅O₄-type structure), which is illustrated in Figure 4.69. The La₅V₃Se₆O₇ substructure is coloured in green, the La₄V₂Se₅O₄ substructure in blue.

However, by choosing the space group *Cmcm*, the displacement ellipsoids for one Se position and one O position in the VSe₅O-octahedra were unusually high. Similar to the observations of *Tougait et al.*^[20] in La₄Ti₂Se₅O₄, two residual peaks approximately 50 % of the height of a Se atom were located close to the initial position of the Se atom in question. A third residual peak about 50 % of the height of an oxygen atom was located near the O atom in question. In consequence, the initial Se position was split into two approximately half Se positions and the initial O position, which was on a $4c$ *Wyckoff* site, was changed to an approximately half oxygen position on an $8f$ *Wyckoff* site.^[20] Subsequent refinements showed better R -values (Table 4.10) and more reasonable displacement ellipsoids with occupancies of ≈ 0.5 for these three atoms. However, especially the residual electron density ($-6.51/+4.73$) was still very high. Having a closer look at the ellipsoids of the vanadium atom and the axial selenium atom of the VSe₅O_{2/2}-octahedra in Figure 4.70, one can recognize that these are significantly elongated along c . Together with the unusual split position of the equato-

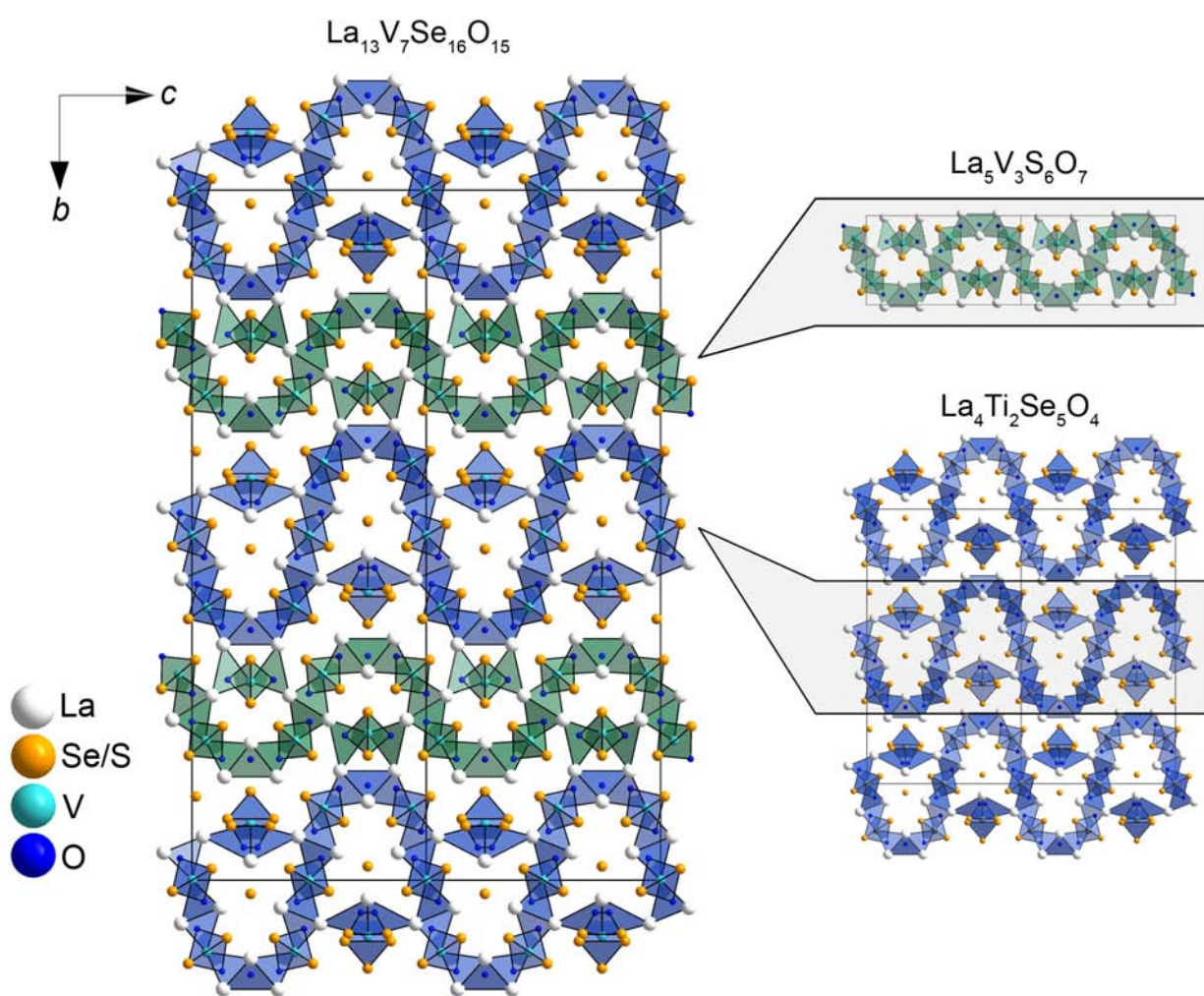


Figure 4.69 Illustration of the crystal structure of $\text{La}_{13}\text{V}_7\text{Se}_{16}\text{O}_{15}$ (space group $Cmcm$) composed of the $\text{La}_5\text{V}_3\text{S}_6\text{O}_7$ and $\text{La}_4\text{Ti}_2\text{Se}_5\text{O}_4$ structure types.

rial selenium atoms and the half occupied oxygen position, one may assume two different overlapping, distorted VSe_5O -octahedra, marked in black and red in Figure 4.70 (B).

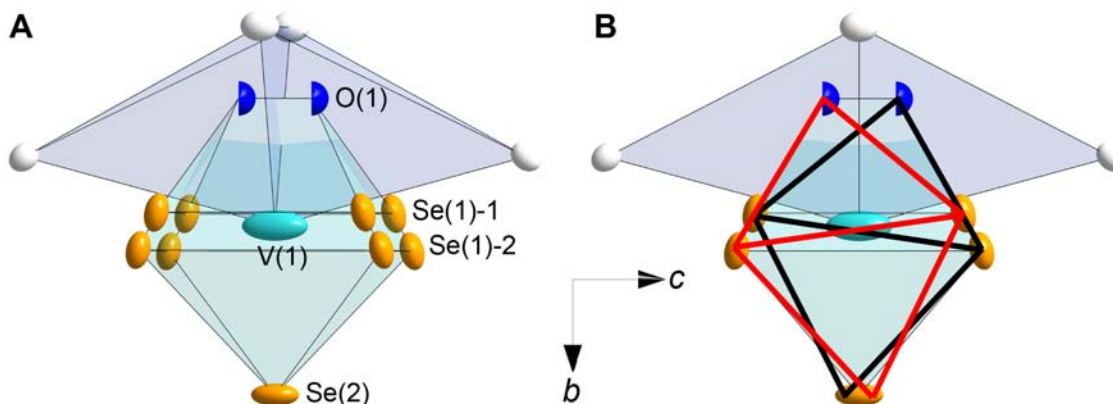


Figure 4.70 (A) Illustration of the splitting of the equatorial selenium atoms in the $VSe_5O_{2/2}$ -octahedra using space group $Cmcm$. (B) Overlapping of two separate VSe_5O -octahedra in black and red. Ellipsoids represent 90 % probability.

The mirror plane perpendicular to c has to be removed in order to check whether an ordering upon distinction of these octahedra occurs. Symmetry reduction leads to the subgroup $Cmc2_1$. The Flack-parameter was determined to be 0.506(1), thus the structure was subsequently refined as an inversion twin. As shown in Table 4.10, the R -values are strongly improved by choosing this space group, which indicates that the splitting of the selenium position in space group $Cmcm$ arised from twinning. The twin fractions were determined to be 0.506(1):0.494(1).

Table 4.10 Overview over the agreement indices of the refinement of the crystal structure of $La_{13}V_7Se_{16}O_{15}$ using space groups $Cmcm$ and $Cmc2_1$.

Space group	$Cmcm$	$Cmc2_1$
R_{int}, R_{σ}	0.053, 0.025	0.052, 0.036
No. data with $I > 3\sigma(I)$	3015	5694
No. parameters	146	263
R_1 (obs/all)	0.046/0.051	0.017/0.023
ωR_2 (obs/all)	0.120/0.120	0.036/0.038
$Goof$ (obs/all)	3.72/3.58	1.00/0.99
$\Delta\rho_{min}, \Delta\rho_{max}$ [$e/\text{\AA}^3$]	-6.51, 4.73	-1.12, 0.81
Flack-parameter	-	0.506(1)

The crystal structure in the space group $Cmc2_1$ is depicted in Figure 4.71. The $La_5V_3Se_6O_7$ -unit (green) consists of strands of edge-sharing VSe_4O_2 -octahedra along a with three crystallographically unique vanadium atoms. The $V(1)Se_4O_2$ - and $V(2)Se_4O_2$ -octahedra are alternately linked to each other by two or three edge-sharing OLa_4/OLa_3V -tetrahedra forming a meandering strand along c . These blocks of two or three tetrahedra form infinite fluorite-like ribbons along a . The $V(3)Se_4O_2$ -octahedra are connected to two OLa_3V -tetrahedra, which are embedded in the loop of the meandering strand.

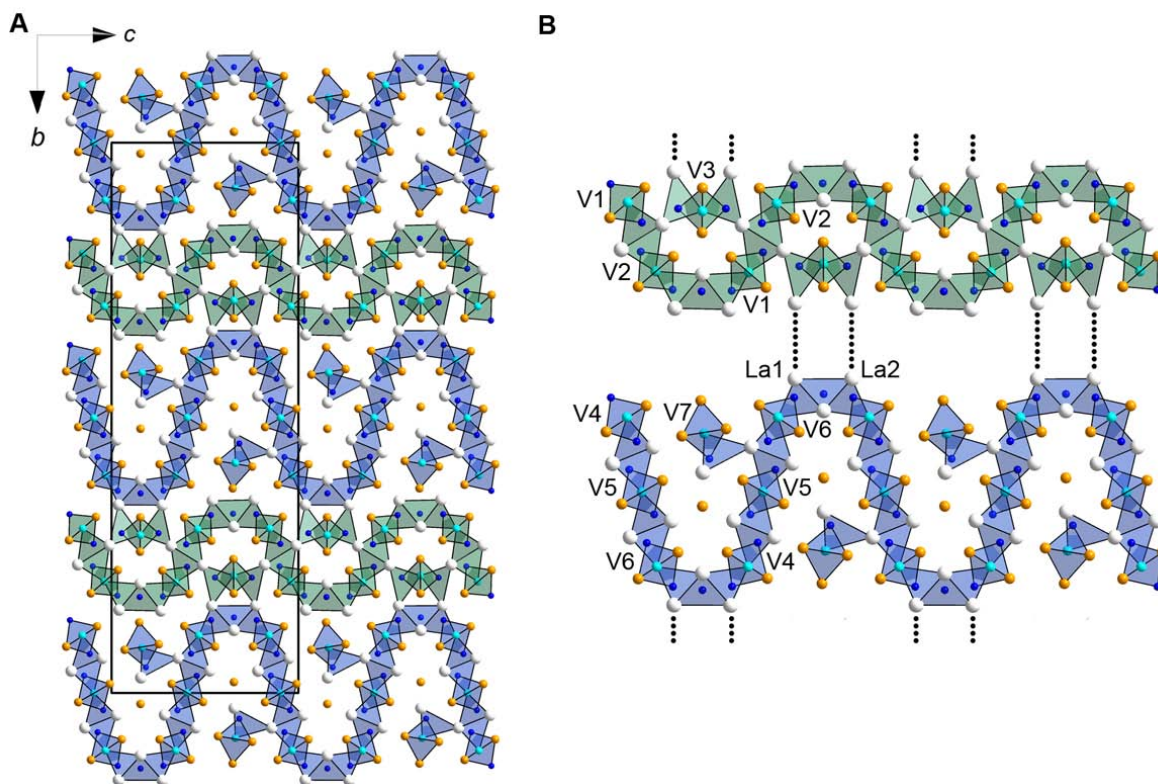


Figure 4.71 (A) Illustration of the crystal structure of $La_{13}V_7Se_{16}O_{15}$ using space group $Cmc2_1$ (B) Connectivity of the two substructures via common lanthanum atoms.

The $La_4V_2Se_5O_4$ building block (blue) has similarities to the $La_5V_3Se_6O_7$ unit (green) discussed above. It also consists of edge-sharing VSe_4O_2 -octahedra with additional VSe_5O -octahedra along a and has four crystallographically unique vanadium atoms. The $V(5)Se_4O_2$ -octahedra are connected to the $V(4)Se_4O_2$ - as well as to the $V(6)Se_4O_2$ -octahedra via two edge-sharing OLa_3V -tetrahedra. The $V(4)Se_4O_2$ - and the $V(6)Se_4O_2$ -octahedra are linked to each other by three edge-sharing $OLa_3V/OLa_4/OLa_3V$ -tetrahedra, which also results in a meandering strand along c . The tetrahedral units extend to infinite fluorite-like ribbons along a . The difference to the first building block is an additional VSe_4O_2 -unit connected to

two OLa_3V -tetrahedra, which broadens the meandering strand of the $\text{La}_4\text{V}_2\text{Se}_5\text{O}_4$ building block along b . Additionally, there exist strongly distorted $\text{V}(7)\text{Se}_5\text{O}$ -octahedra, which are connected to one single OLa_3V -tetrahedron and are embedded in the loop of the meandering strand similar to the first substructure.

Both building blocks stack alternately via common lanthanum atoms, $\text{La}(1)$ and $\text{La}(2)$, along b (Fig. 4.71 B). The coordinations of the 13 crystallographically independent lanthanum atoms are square antiprisms, monocapped square antiprisms, bicapped and tricapped trigonal prisms and bicapped trigonal antiprisms. The shortest V-V bond length between two equivalent vanadium atoms is 393.8(1) (= a -axis). There are several V-V distances in the bc -plane, which are significantly longer as depicted in Table 4.11. The oxidation states of the different vanadium atoms can be estimated from the V-O bond lengths which are also listed in Table 4.11.

Table 4.11 Overview of the V-O and V-V distances in $\text{La}_{13}\text{V}_7\text{Se}_{16}\text{O}_{15}$.

n	$d[\text{V}(n)\text{-O}] / \text{pm}$	$n\text{-}m$	$d[\text{V}(n)\text{-V}(m)] / \text{pm}$
1	185.1(1)–191.7(1)	1-2	594.5(1)
2	185.9(1)–190.3(1)	1-3	568.6(1)
3	178.9(1)–184.8(1)	2-3	565.1(1)
4	191.9(1)–197.8(1)	4-5	611.5(1)
5	191.3(1)–196.2(1)	4-6	690.8(1)
6	193.9(1)–195.5(1)	4-7	630.5(1)
7	194.2(1)	5-7	626.1(1)
		5-6	607.4(1)
		6-7	604.4(1)

The $\text{La}_4\text{V}_2\text{Se}_5\text{O}_4$ building block formally consists of V^{III} , which is in line with V-O bond lengths of 191.3(1)–197.8(1) pm. Similar V-O distances for V^{III} have been observed in the literature for $\text{RE}_7\text{VSe}_8\text{O}_4$ ^[37] (194 pm) and in previous sections for the compounds LaVSe_2O (196.8(1) pm), $\text{La}_5\text{V}_3\text{Se}_7\text{O}_5$ (192.0(1)–194.8(1) pm) and $\text{La}_7\text{VSe}_5\text{O}_7$ (195.8(1) pm). In contrast, the three crystallographically independent vanadium atoms in the $\text{La}_5\text{V}_3\text{Se}_6\text{O}_7$ substructure can not be described with vanadium in the single oxidation state +III as described in section 4.5.4.2. In fact, vanadium exhibits a mixed valence state of either $2 \times +\text{III}$ and $1 \times +\text{V}$ or $2 \times +\text{IV}$ and $1 \times +\text{III}$. Regarding the V-O bond lengths in Table 4.11, the first option seems to be more reasonable with $\text{V}(1)$ and $\text{V}(2)$ in oxidation state +III and $\text{V}(3)$ with +V, although $\text{V}^{\text{III}}/\text{V}^{\text{V}}$ compounds are not described in the literature. In contrast, mixed

valent compounds with V^{III}/V^{IV} are well known, e.g. in the series V_nO_{2n-1} .^[46,47] A further hint to discuss this question can be found in the magnetic measurements.

Magnetization Measurements

The theoretical effective paramagnetic moment μ_{eff} can be calculated with regard to the different oxidation numbers of vanadium in the two substructures. As there are two options for the three unique vanadium atoms in the $\text{La}_5\text{V}_3\text{Se}_6\text{O}_7$ substructure, the effective paramagnetic moment has to be calculated for each option as shown in Table 4.12. Unfortunately the theoretical magnetic moments of 6.93 and 6.78 μ_B for option 1 and 2 differ only very slightly.

Table 4.12 Calculation of theoretical μ_{eff} of $\text{La}_{13}\text{V}_7\text{Se}_{16}\text{O}_{15}$.

	Oxidation number			theoretical μ_{eff} / μ_B
	+III	+ IV	+V	
Option 1	6×	0×	1×	6.93
Option 2	5×	2×	0×	6.78

The magnetic susceptibility reveals paramagnetism between ≈ 17 and 290 K, a drop of χ_{mol} below 17 K followed by an increase at ≈ 12 K (Fig. 4.72). A Curie Weiss fit of the linear part of the inverse susceptibility results an effective paramagnetic moment of $\mu_{\text{eff}} = 6.79(1) \mu_B$ per formula unit. This is in excellent agreement with the theoretically expected value of 6.78 μ_B for option 2. The negative Weiss constant $\theta = -22.2(1)$ K, together with

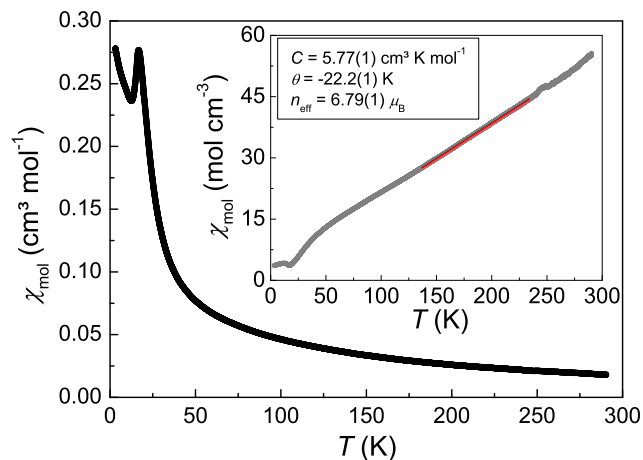


Figure 4.72 Magnetic susceptibility of $\text{La}_{13}\text{V}_7\text{Se}_{16}\text{O}_{15}$ measured at $B = 1$ T and inverse magnetic susceptibility (inset) with Curie-Weiss fit (red).

the drop of χ_{mol} , indicate antiferromagnetic ordering of the moments below 17 K. However, the increase of χ_{mol} below 12 K hints towards a change of the type of magnetic ordering.

The magnetization isotherm at 300 K is linear with the applied field with small deviations (Fig. 4.73). The isotherm at 20 K is slightly bent and exhibits significantly larger values of μ/μ_{B} . Finally, magnetization isotherms at 10 and 1.8 K hint towards complex magnetic ordering with multiple transitions. A clear hysteresis can be seen at 1.6 K, but no saturation of the curve, which could be a hint of weak ferromagnetism at very low temperatures. The crystal structure with seven vanadium positions may form a complex spin structure which cannot be determined by magnetization measurements but requires neutron diffraction data.

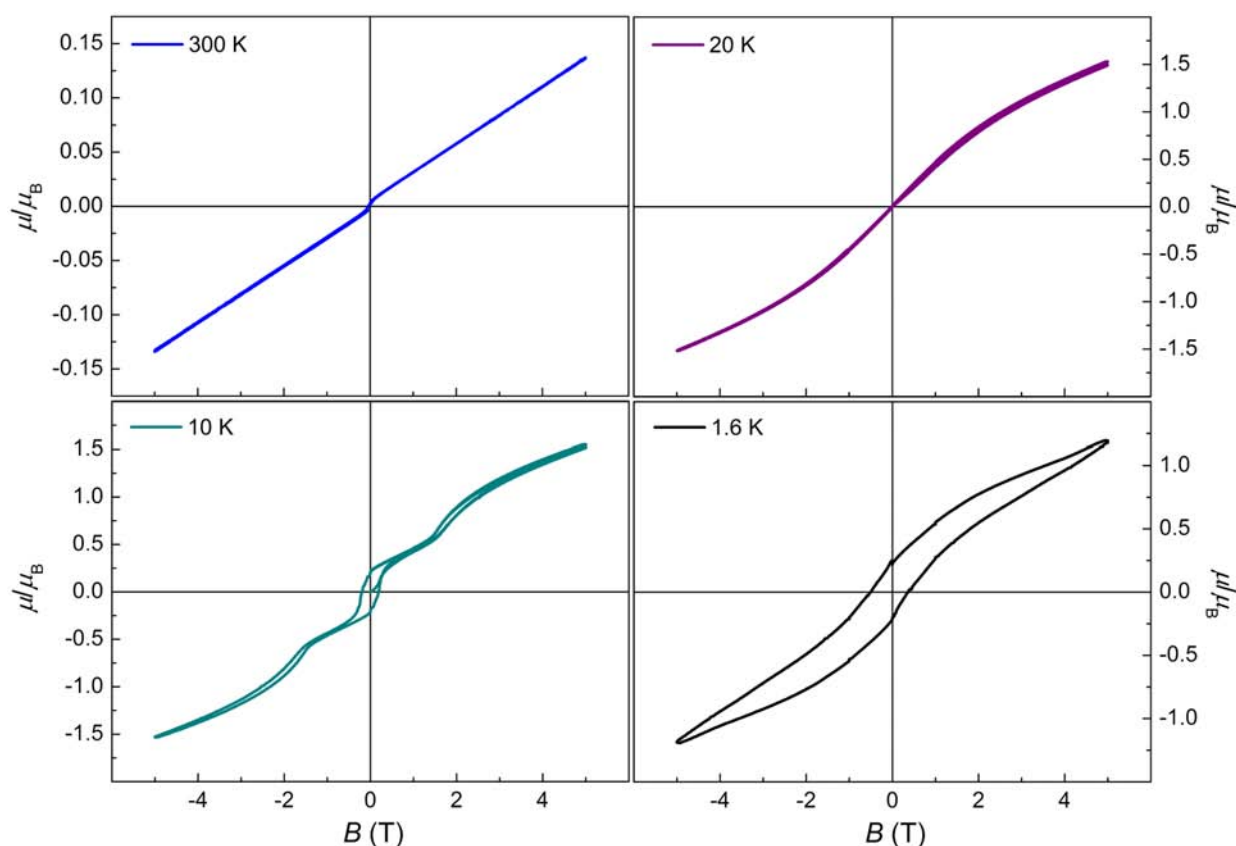


Figure 4.73 Magnetization isotherms of $\text{La}_{13}\text{V}_7\text{Se}_{16}\text{O}_{15}$ at 300 (blue), 20 (purple), 10 (green), and 1.8 K (black).

4.5.5 Conclusion

The first five quaternary lanthanum vanadium oxyselenides could be prepared and characterized. LaVSe_2O and $\text{La}_5\text{V}_3\text{Se}_6\text{O}_7$ adopt literature known structure types, whereas $\text{La}_5\text{V}_3\text{Se}_7\text{O}_5$, $\text{La}_7\text{VSe}_5\text{O}_7$ and $\text{La}_{13}\text{V}_7\text{Se}_{16}\text{O}_{15}$ crystallize in new structure types. The compounds are built

of common building blocks but with different connections between them corresponding to a modular conception. All compounds contain VSe_4O_2 -octahedra and OLa_3V -tetrahedra. Additionally, VSe_5O - and VSe_6 -octahedra, as well as OLa_4 -tetrahedra may exist, which increases the possible connections and opens the door to a huge amount of potential compounds. With the exception of $LaVSe_2O$, all compounds could be prepared in high purity (> 90 wt%) and their magnetic properties were examined. Magnetic measurements indicate a complicated behaviour in most cases, which may be based on the existence of more than one crystallographically unique vanadium position in complex crystal structures. The most frequent oxidation number of vanadium in these materials is +III, whereas $La_5V_3Se_6O_7$ and $La_{13}V_7Se_{16}O_{15}$ are mixed valent compounds with vanadium in different oxidation states.

4.6 Synthesis and Crystal Structures of New Lanthanum Titanium Oxyselenides

4.6.1 Introduction

Quaternary oxyselenides involving both a *d*- and an *f*-block element have not been explored extensively. The first quaternary RE-Ti-Se-O compounds, $RE_{3,67}Ti_2Se_6O_3$ ($RE = Ce, Nd, Sm$), were reported by *Tougait* et al. in 2000.^[19] Only few other examples have been reported in the following years, including $La_4Ti_2Se_5O_4$, $La_6Ti_3Se_9O_5$, $RE_3Ti_3Se_2O_8$ ($RE = Nd, Sm$) and $RE_4TiSe_4O_4$ ($RE = Sm, Gd-Er, Y$).^[20,22,23,34,35] The crystal structures of these compounds contain similar building blocks as found in the new vanadium materials discussed in the previous chapter, namely fluorite-like ribbons of edge-sharing OLa_4 - and OLa_3Ti -tetrahedra, linked by chains of distorted edge-sharing $TiSe_4O_2$ - and $TiSe_5O$ -octahedra. $RE_3Ti_3Se_2O_8$ ($RE = Nd, Sm$) is a more oxygen rich composition and contains TiO_6 and $TiSeO_5$ -octahedra as an exception. As there exist no Se-Se, Se-O or O-O bonds in these compounds, the oxidation numbers of RE/Se/O can be assigned to +3/-2/-2. However, some of the mentioned materials are mixed-valence compounds regarding the oxidation state of titanium, e.g. $La_6Ti_3Se_9O_5$, $RE_3Ti_3Se_2O_8$ and $RE_{3,67}Ti_2Se_6O_3$ contain both, Ti(III) and Ti(IV) cations. Magnetic properties of these compounds are rarely reported. $RE_{3,67}Ti_2Se_6O_3$ ($RE = Ce, Nd, Sm$) display paramagnetic behaviour down to 5 K.^[19] In contrast, magnetic susceptibilities of $RE_4TiSe_4O_4$ ($RE = Gd-Ho$) indicate antiferromagnetic ordering of the rare-earth moments at low temperatures. Moreover, the compounds with Gd and Tb show evidence of ferromagnetism due to spin canting prior to the onset of full antiferromagnetic order.^[23] Here, we present the synthesis and crystal structures of two new lanthanum titanium oxyselenides with some structural building blocks that have not been observed in the RE-Ti-Se-O family before.

4.6.2 Experimental Details

Single crystals of $La_{12}Ti_{13}Se_9O_{32}$ and $La_{15}Ti_6Se_{10}O_{26-x}$ were isolated from the attempt to prepare $La_{13}Ti_7Se_{16}O_{15}$ using appropriate amounts of La_2O_3 (dried in dynamic vacuum at 1273 K), freshly filed lanthanum metal, Se and Ti. A NaI/KI flux was used to promote crystal growth. All starting materials were handled in an argon-filled glove box. The reactants

(0.3 g) were mixed intimately and sandwiched in an aluminum crucible between ≈ 1 g of a eutectic mixture of NaI/KI (mass ratio 0.6:0.4, dried in dynamic vacuum at 673 K). The crucibles were sealed in silica ampoules and heated to 1173 K with heating and cooling rates of 50 and 15 K h⁻¹. The flux was removed by washing with deionized water and ethanol. La₁₂Ti₁₃Se₉O₃₂ are black, plate-like single crystals. La₁₅Ti₆Se₁₀O_{26-x} crystallizes as orange, translucent needles. The compounds are stable in moist air for months.

4.6.3 Results and Discussion

4.6.3.1 La₁₂Ti₁₃Se₉O₃₂

Much effort has been made to prepare a La₁₃Ti₇Se₁₆O₁₅ according to the synthesis of La₁₃V₇Se₁₆O₁₅ in the previous chapter. The polycrystalline samples were always inhomogeneous and without the desired product. However, two new La-Ti-Se-O compounds could be characterized via single crystal X-ray diffraction from this approach. A view through the microscope revealed the existence of two different types of crystals. On the one hand, thin, black plates and on the other hand small, orange, translucent needles.

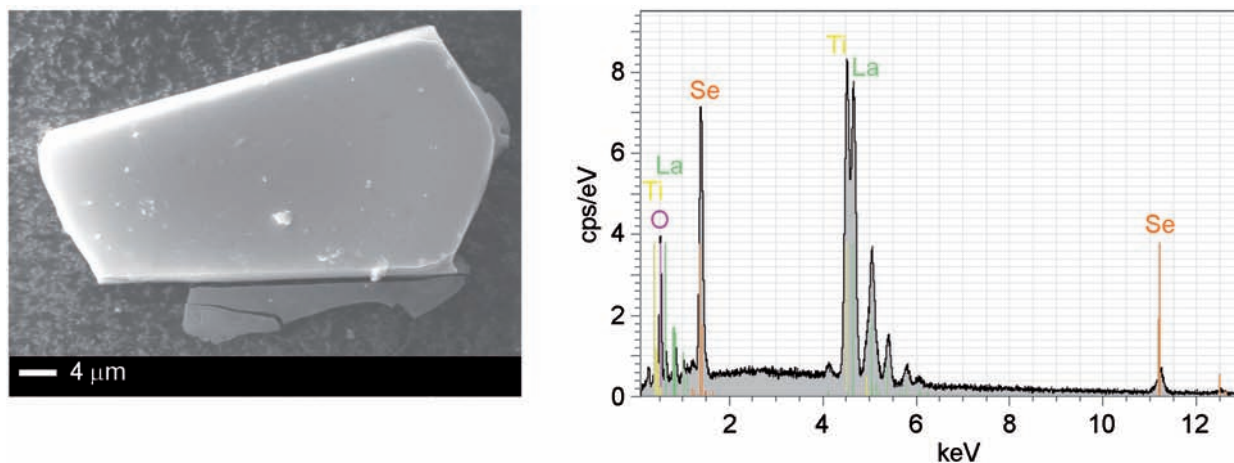


Figure 4.74 Typical plate-like single crystal (left) and EDX spectrum (right) of La₁₂Ti₁₃Se₉O₃₂. Characteristic lines of the elements of the flux are not observed. The peak at ≈ 0.25 keV belongs to carbon from the adhesive conducting carbon film.

EDX-measurements of a black, plate-like single crystal, which is shown in Figure 4.74, indicated atomic percentages of 16.3(1) %, 19.7(2) %, 11.4(1) % and 52.5(3)% for La, Ti, Se and O, which corresponds to La_{12.0}Ti_{14.5(2)}Se_{8.4(1)}O_{38.7(5)}. Single crystal X-ray diffraction experiments revealed the molecular formula La₁₂Ti₁₃Se₉O₃₂, which is in agreement with the

EDX data, with exception of the value for oxygen, which can not be determined reliably via EDX measurements. $\text{La}_{12}\text{Ti}_{13}\text{Se}_9\text{O}_{32}$ crystallizes in a new structure type in space group $R\bar{3}$ (No. 148) with $a = 14.4(1) \text{ \AA}$, $c = 16.7(1) \text{ \AA}$, and $Z = 8$. Crystallographic data are compiled in Table A.16. A view on the ab plane of the structure is depicted in Figure 4.75. The crystal structure includes two crystallographically independent lanthanum atoms, six independent oxygen atoms, and three independent titanium and selenium atoms, respectively.

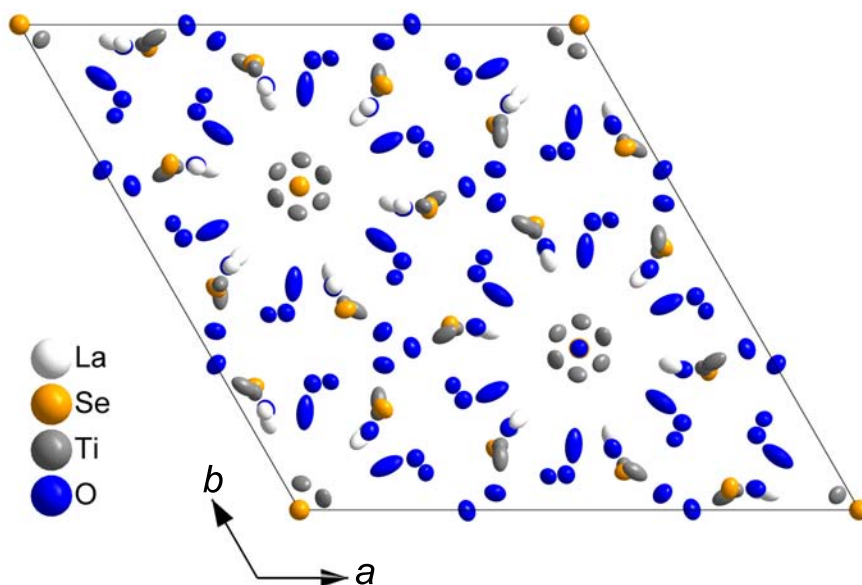


Figure 4.75 View on the ab -plane of the structure of $\text{La}_{12}\text{Ti}_{13}\text{Se}_9\text{O}_{32}$. Ellipsoids represent 90 % probability.

Se(1) is surrounded by six La(1) atoms forming a SeLa_6 -octahedron (Fig. 4.76 A). The Se(1)-La(1) bond length is 323.5(1) pm and the La(1)-Se(1)-La(1) bond angles vary from 88.0–92.0°. Se(2) is in a trigonal prism of three La(1) and three La(2) atoms. The Se(2)-La(1) bond length is 320.9(1) pm and that of Se(2)-La(2) is 323.7(1) pm. The SeLa_6 -octahedron is *trans*-linked to two SeLa_6 -prisms through common trigonal La_3 -planes as shown in Figure 4.76 (A). The second coordination sphere of Se(1) are six Se(3) and two Se(2) atoms in a cubic coordination with bond lengths from 355.8(1)–358.2(1) pm (Fig. 4.76 B). Taking into account the first and the second coordination spheres of Se(1), the resulting coordination environment can be seen as the penetration of an octahedron and a cube (Fig. 4.76 C), which is called the first stellation of a cuboctahedron (Wenninger Model Number 43). However, as the penetration is not complete and the coordination sphere includes two different types of atoms, one should speak of a distorted pseudo-cuboctahedron.

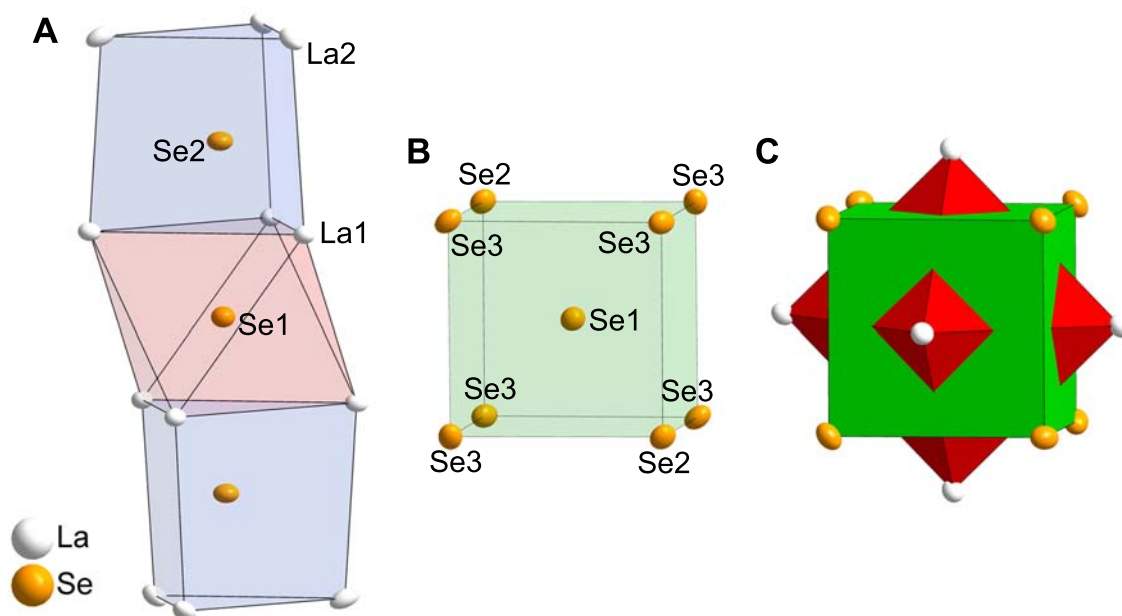


Figure 4.76 Illustration of the coordination environments of selenium in $\text{La}_{12}\text{Ti}_{13}\text{Se}_9\text{O}_{32}$. (A) SeLa_6 -prisms in blue, SeLa_6 -octahedron in red. (B) SeSe_8 -cube in green. (C) Penetration of octahedron and cube. Ellipsoids represent 90 % probability.

$\text{Se}(2)$ in the trigonal SeLa_6 -prisms itself is part of three strongly distorted, octahedral coordination polyhedra of $\text{Ti}(2)\text{Se}_2\text{O}_4$ with $\text{Ti}(2)$ in the center (Fig. 4.77). The $\text{Ti}(2)$ -O and $\text{Ti}(2)$ -Se bond lengths vary from 185.6(1)–197.5(1) pm and 274.1(1)–325.2(1) pm, respectively. Each of these $\text{Ti}(2)\text{Se}_2\text{O}_4$ -octahedra is linked via either a common O-Se edge or a common O corner to two other, distorted $\text{Ti}(1)\text{SeO}_5$ -octahedra, which is shown in Figure 4.78 (A). The $\text{Ti}(1)$ -O bond lengths vary from 195.2(1)–210.7(1) pm and the $\text{Ti}(1)$ -Se bond length is 263.7(1) pm. Six of these $\text{Ti}(1)\text{SeO}_5$ -octahedra are connected via common oxygen atoms forming a sechser ring (Fig. 4.78 A). The six $\text{Ti}(1)$ as well as the six bridging oxygen atoms in the sechser ring have a hexagonal chair conformation as shown in Figure 4.78 (B) and (C). The third crystallographically independent $\text{Ti}(3)$ position is close to the center of the sechser ring. As $\text{Ti}(3)$ is on a general position, the symmetry operations generate six $\text{Ti}(3)$ atoms within the sechser ring with unreasonably large thermal expansion ellipsoids. Free refinement of the occupancy parameter of $\text{Ti}(3)$ results in a value of 0.1660(1), which is close to $\frac{1}{6}$. Therefore, the occupancy of $\text{Ti}(3)$ was fixed to this value. $\text{Ti}(3)$ is coordinated by the six bridging oxygen atoms of the $\text{Ti}(1)\text{SeO}_5$ -octahedra and two oxygen atoms above and below the hexagonal oxygen plane forming a distorted hexagonal bipyramid (Fig. 4.78 B). Equatorial and axial $\text{Ti}(3)$ -O bond lengths are 185.9(1) and 181.6(1) pm, respectively. Fig-

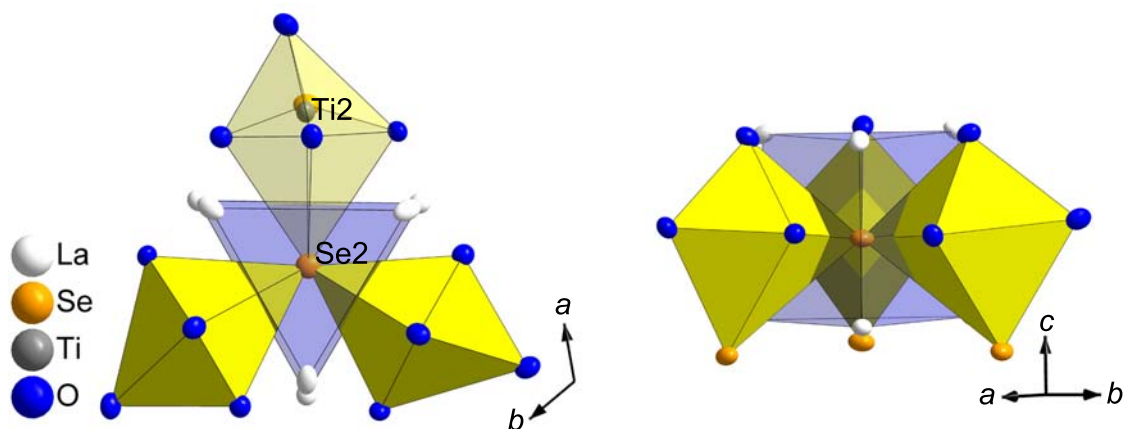


Figure 4.77 Illustration of the coordination environments of Ti(2) in $\text{La}_{12}\text{Ti}_{13}\text{Se}_9\text{O}_{32}$ using two point of views. SeLa_6 -prism in blue, $\text{Ti}(1)\text{Se}_2\text{O}_4$ -octahedra in yellow. Ellipsoids represent 90 % probability.

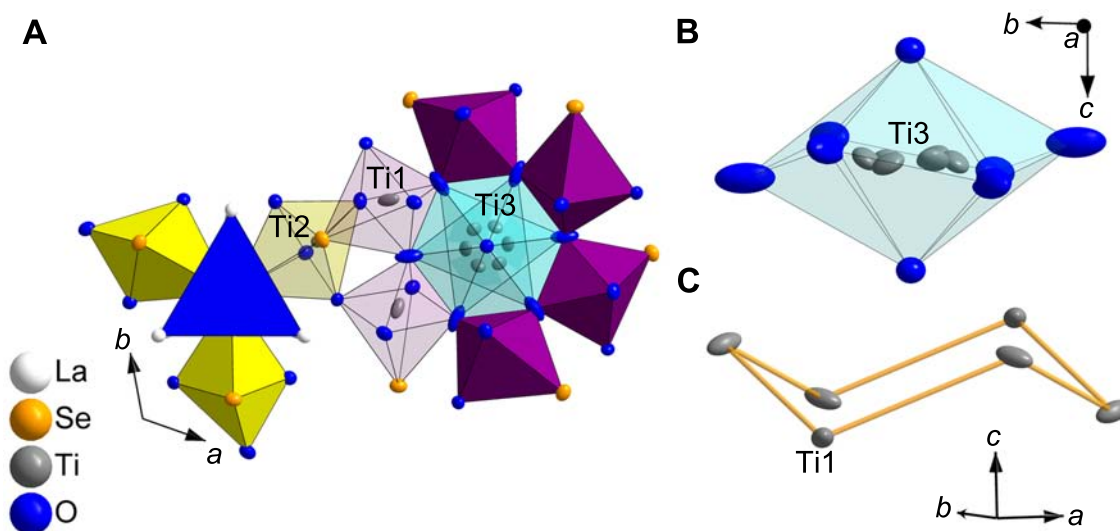


Figure 4.78 (A) Illustration of the connection of the $\text{Ti}(1)\text{Se}_2\text{O}_4$ - (yellow) and the $\text{Ti}(2)\text{SeO}_5$ -octahedra (purple). (B) Coordination environment of Ti(3) in a distorted hexagonal bipyramid. (C) Chair-like arrangement of Ti(2) atoms. Ellipsoids represent 90 % probability.

ure 4.79 (A) shows the arrangement of the discussed building blocks in the unit cell. The crystal structure can be described on the basis of associated strands (Fig. 4.79 B) along c that include all mentioned coordination polyhedra. Each unit cell consists of three of those strands, 4/4 along the cell edges and two within the unit cell.

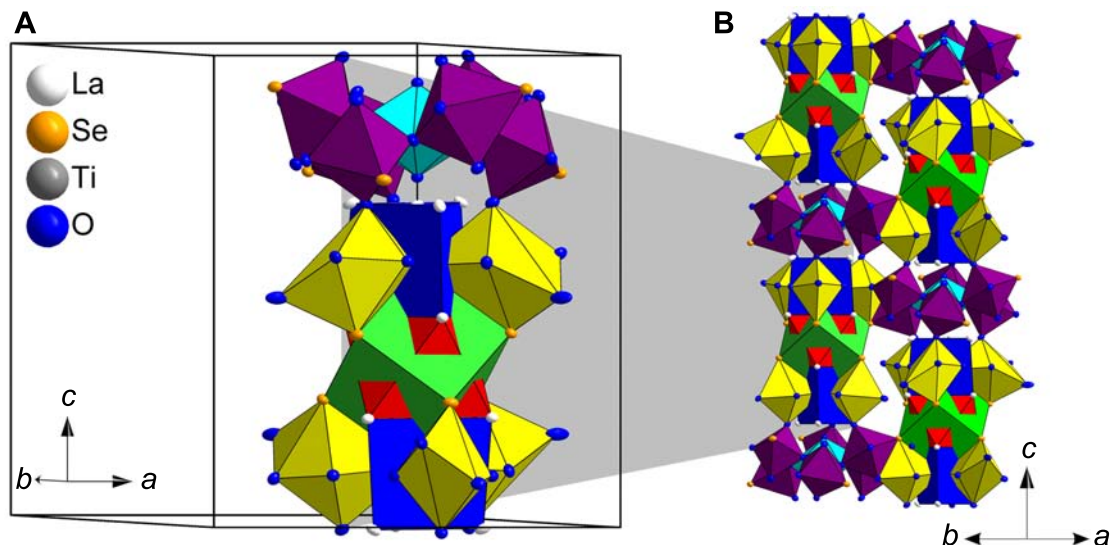


Figure 4.79 (A) Illustration of the assignment of the coordination polyhedra in one unit cell. (B) Linkage of two strands along c . Ellipsoids represent 90 % probability.

$\text{La}_{12}\text{Ti}_{13}\text{Se}_9\text{O}_{32}$ is a mixed valent compound regarding the oxidation state of titanium. The most frequent oxidation states of titanium are +III and +IV. Figure 4.80 shows the coordination environments of the different titanium positions of the new compound. The attribution of the oxidation states to the crystallographically independent titanium positions can be made with regard to the multiplicity and the occupancy of the particular position, which are listed in Table 4.13. Moreover, the Ti-O bond length can act as an indicator for the oxidation state.

Table 4.13 *Wyckoff* site, occupancy, Ti-O bond lengths and assigned oxidation state of the three crystallographically independent titanium positions of $\text{La}_{12}\text{Ti}_{13}\text{Se}_9\text{O}_{32}$.

	<i>Wyckoff</i> site	occupancy	Ti-O bond length (pm)	oxidation state
Ti(1)	18 <i>f</i>	1	195.2(1)–210.7(1)	+III
Ti(2)	18 <i>f</i>	1	185.6(1)–197.5(1)	+IV
Ti(3)	18 <i>f</i>	$\frac{1}{6}$	181.6(1)–185.9(1)	+IV

The Ti-O bond lengths in TiO_2 (rutile) are 194.4–197.6 pm^[49] and that of Ti_2O_3 vary from 199.2–210.3 pm^[50]. Based on the fact that the Ti-O bond lengths of Ti(2) and Ti(3)

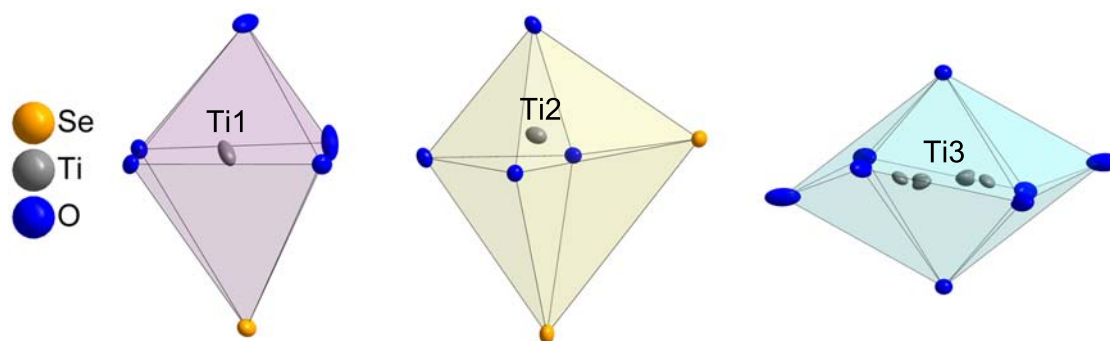


Figure 4.80 Illustration of the coordination environments of the crystallographically independent Ti atoms of $\text{La}_{12}\text{Ti}_{13}\text{Se}_9\text{O}_{32}$. Ellipsoids represent 50 % probability.

are significantly smaller than those of Ti(1), and comparable to Ti^{IV} in rutile, the oxidation number of Ti(2) and Ti(3) should be higher than that of Ti(1). Moreover, the Ti-O bond lengths in the Ti(1) polyhedron is in the range of those in Ti_2O_3 with Ti^{III} . These findings, together with the multiplicities and occupancies listed in Table 4.13, result in the following assignment of oxidation numbers: $\text{La}_{12}\text{Ti}_6(1)^{\text{III}}\text{Ti}_6(2)^{\text{IV}}\text{Ti}_6(3)^{\text{IV}}\text{Se}_9\text{O}_{32}$. Unfortunately, the magnetic properties remain unknown due to the lack of sufficient phase pure samples.

4.6.3.2 $\text{La}_{15}\text{Ti}_6\text{Se}_{10}\text{O}_{26-x}$

In addition to the new compound discussed above, small, orange, translucent needles could be isolated and qualitative analysis uncovered another new quaternary compound. The molecular formula was determined from single crystal X-ray diffraction experiments to be $\text{La}_{15}\text{Ti}_6\text{Se}_{10}\text{O}_{26-x}$. Energy dispersive X-ray spectroscopy of the single crystals (Fig. 4.81) revealed the averaged atomic percentages La 22.3(7) %, Ti 9.2(4) %, Se 14.7(7) % and O 53.8(11) %, which corresponds to $\text{La}_{15.0}\text{Ti}_{6.2(5)}\text{Se}_{9.9(8)}\text{O}_{36.2(20)}$. The values of La, Ti and Se are in good agreement with the data from single-crystal X-ray diffraction experiments. However, the value of oxygen is significantly higher, which could be due to oxidation of the surface of the crystals while removing the flux with water. Moreover, the EDX spectrum (Fig. 4.13) shows no hints of incorporation or inclusion of the elements of the flux.

The compound crystallizes in a new structure type in space group $P\bar{6}2m$ (No. 189) with $a = 16.8(1) \text{ \AA}$, $c = 3.98(1) \text{ \AA}$, and $Z = 3$. The ab -plane of the unit cell, that includes four crystallographically independent lanthanum, one titanium, three selenium and six oxygen atom positions, is shown in Figure 4.82. The crystal structure consists of similar building blocks as in $\text{La}_{12}\text{Ti}_{13}\text{Se}_9\text{O}_{32}$. There exist two types of SeLa_6 -prisms. On the one hand, $\text{Se}(1)$

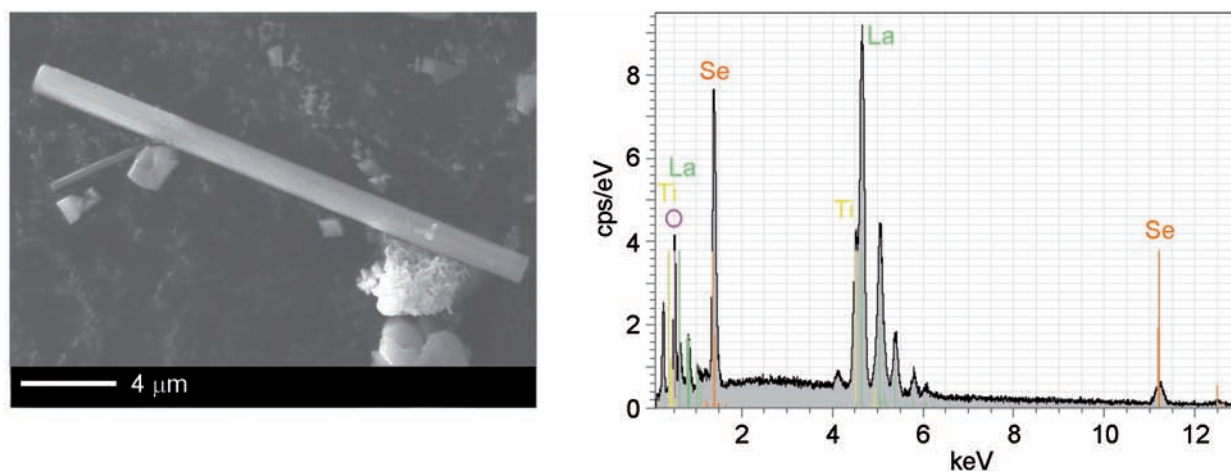


Figure 4.81 Typical needle-like single crystal (left) and EDX spectrum (right) of $\text{La}_{15}\text{Ti}_6\text{Se}_{10}\text{O}_{26-x}$. Characteristic lines of the elements of the flux are not observed. The peak at ≈ 0.25 keV belongs to carbon from the adhesive conducting carbon film.

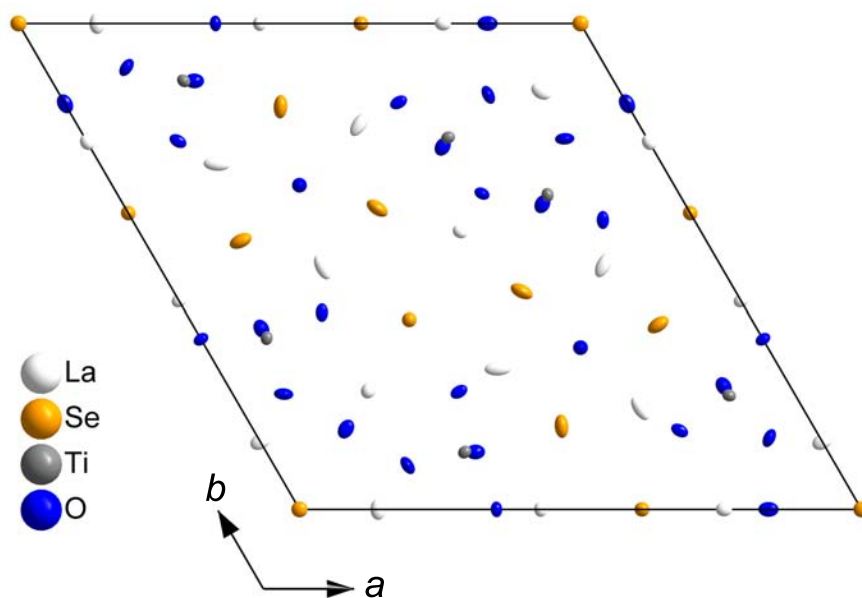


Figure 4.82 View on the ab -plane of the structure of $\text{La}_{15}\text{Ti}_6\text{Se}_{10}\text{O}_{26-x}$. Ellipsoids represent 90 % probability.

is surrounded by La(4) in a SeLa_6 -prism, which build face-sharing strands (blue) along c . Respectively two La(4) atoms in the ab plane are connected to two La(1) atoms outside of the prism forming $\text{O}(4)\text{La}_4$ -tetrahedra (green), which is shown in Figure 4.83. Each tetrahedron is all-side corner-sharing to other tetrahedra, building further strands surrounding the SeLa_6 -prisms. The Se-La bond length is 308.2(1) pm and O-La bond lengths vary from 239.7(1)–259.6(1) pm. La-O-La bond angles are between 103.3(1)–112.5(1)°.

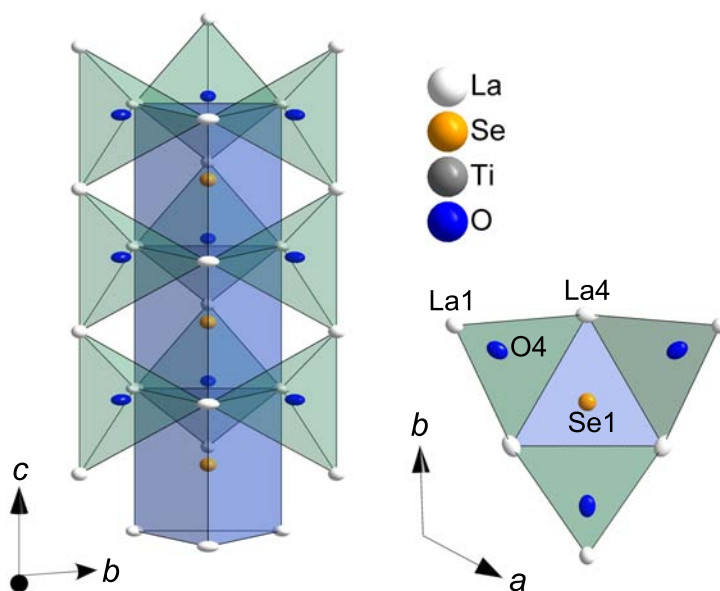


Figure 4.83 Illustration of the connection between the $\text{Se}(1)\text{La}_6$ -prisms (blue) and the OLa_4 -tetrahedra (green) along c . Ellipsoids represent 90 % probability.

On the other hand, Se(3) is in a trigonal SeLa_6 -prism of two La(2) and four La(3), which also expand face-sharing along c (Fig. 4.84). The La-Se bond lengths in this polyhedron vary from 313.3(1)–325.7(1) pm. In contrast to the isolated strands of $\text{Se}(1)\text{La}_6$ -prisms, the $\text{Se}(3)\text{La}_6$ prisms are connected to each other. Three of these prisms are linked to each other via common edges forming a dreier ring. Oxygen is coordinated by three La(3) in the channels of these dreier rings. As the thermal displacement ellipsoid of this oxygen atom was unreasonably large, free refinement of the occupancy of O(6) lead to a value close to $\frac{1}{2}$ (≈ 0.52), which corresponds to the molecular formula $\text{La}_{15}\text{Ti}_6\text{Se}_{10}\text{O}_{25}$. However, the ellipsoid is significantly elongated along c , which may be caused by the poor coordination of this position solely in the ab plane by three lanthanum atoms. As a consequence of the deficiency, the thermal displacement ellipsoids of the coordinating lanthanum atoms La(3) are elongated towards the oxygen position. The dreier rings are connected to six other dreier

rings via common edges forming sechser rings, in which each dreier ring is part of three sechser rings, which is shown in Figure 4.85 (A). The Se(3) atoms within these prisms are part of a distorted TiSeO_5 -octahedron. These octahedra are connected to each other via common oxygen atoms building corner-sharing infinite strands along c and pairs of octahedra in the ab plane as depicted in Figures 4.84 and 4.85 (A). Se(2) is in a distorted trigonal bipyramid of five lanthanum atoms (not shown).

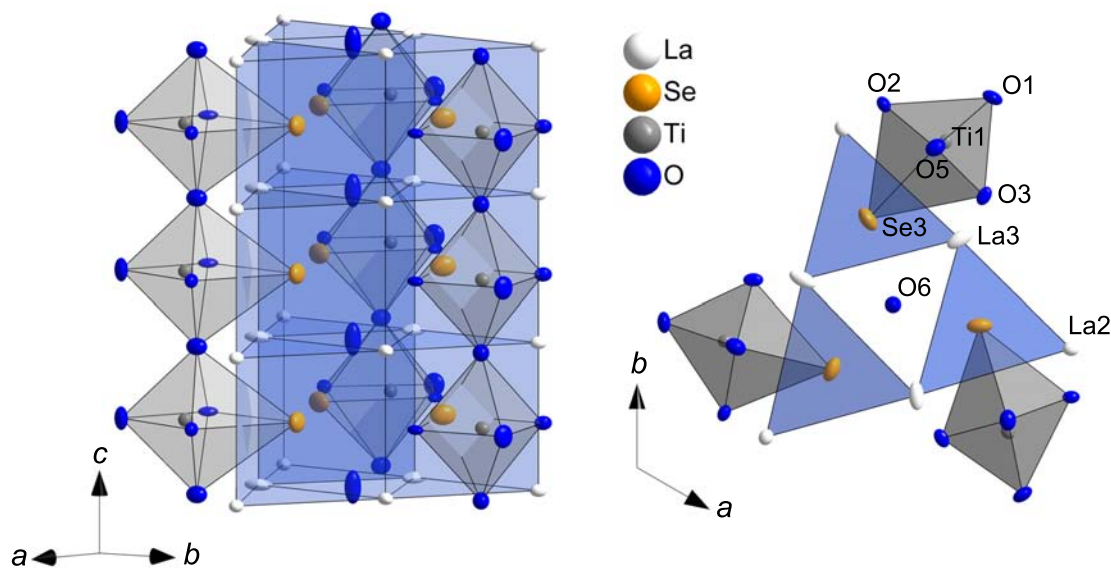


Figure 4.84 Illustration of the connection between the Se(3)La_6 -prisms (blue) and the TiSeO_5 -octahedra (gray) along c . Ellipsoids represent 90 % probability.

The Ti-O bond lengths within the TiSeO_5 -octahedra vary from 175.6(1)–201.9(1) pm and the Ti-Se bond length is 300.3(1) pm. The oxygen atoms O(1–3) and O(5) are not only part of the TiSeO_5 -octahedra but are the central atoms in strongly distorted OLa_3Ti -tetrahedra with Ti-O bond lengths of 175.6(1), 181.9(1), 196.6(1) and 201.9(1) pm. The bond lengths are mostly in the range of those in rutile (194.4–197.6 pm)^[49] but smaller than those in Ti_2O_3 (199.2–210.3 pm)^[50], indicating titanium in the oxidation state +IV. The OLa_3Ti -tetrahedra (red) are connected to each other, to the OLa_4 -tetrahedra (green), and to the SeLa_6 prisms (blue) via common edges as shown in Figure 4.85 (B). As there are no Se-Se, Se-O or O-O bonds, the oxidation numbers for La, Se and O are +3, –2 and –2. The Ti-O bond lengths of 175.6(1)–201.9(1) pm clearly speak for Ti^{IV} . However, the molecular formula, which was obtained from the single-crystal analysis, indicates an oxidation number of Ti larger than +IV (+4.167). EDX measurements gave no hints of foreign atoms (e.g. Na, K, I from the flux). Furthermore, the small residual electron density of +1.01/–1.08, which is spread randomly

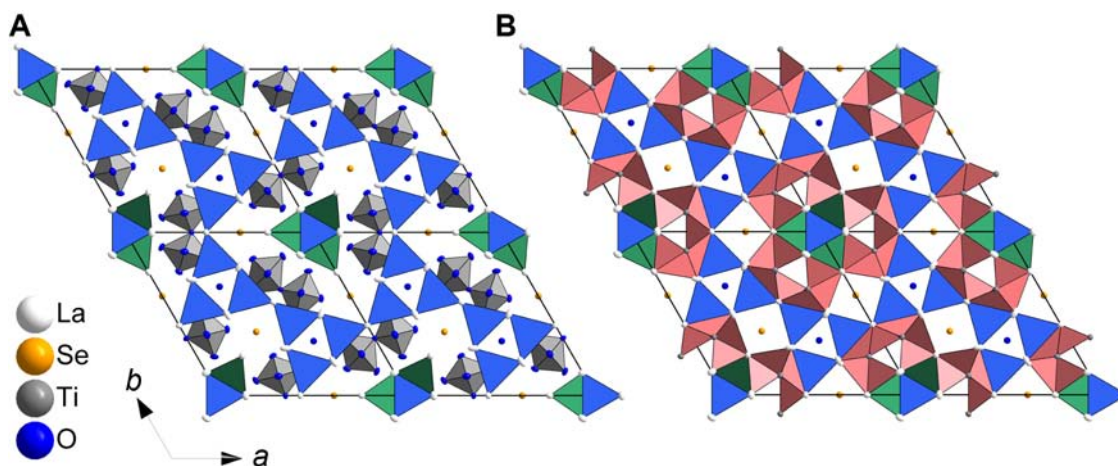


Figure 4.85 Illustration of a $2a \times 2b$ -supercell of $\text{La}_{15}\text{Ti}_6\text{Se}_{10}\text{O}_{26-x}$ with (A) SeLa_6 -prisms in blue, TiSeO_5 -octahedra in gray, OLa_4 -tetrahedra in green and (B) SeLa_6 -prisms in blue, OLa_4 -tetrahedra in green, OLa_3Ti -tetrahedra in red. Ellipsoids represent 99 % probability.

throughout the unit cell, does not indicate any further heavy atoms in the unit cell. Free refinement of the occupational parameters of all atoms except O(6) shows no deviation from a full occupation. Therefore we suggest that the occupation of the O(6)-position is not 50 % but 25 % leading to a molecular formula of $\text{La}_{15}\text{Ti}_6\text{Se}_{10}\text{O}_{24.5}$ and to Ti(IV). However, this can not be clearly verified by X-ray diffraction as deficiencies of light atom positions can not be significantly defined. Neutron diffraction experiments could clarify this problem.

4.6.4 Conclusion

Two new lanthanum titanium oxyselenides have been prepared and characterized using single-crystal X-ray diffraction experiments. $\text{La}_{12}\text{Ti}_{13}\text{Se}_9\text{O}_{32}$ contains three crystallographically unique titanium atoms with a mixture of Ti(III) and Ti(IV) cations for charge balance. Due to the high oxygen content in the molecular formula, there exist no TiSe_4O_2 -octahedra as in many literature known compounds, but TiSeO_5 -octahedra as known from $\text{RE}_3\text{Ti}_3\text{Se}_2\text{O}_8$ ^[34,35]. Furthermore TiSe_2O_4 -octahedra, TiO_8 -hexagonal bipyramids, SeLa_6 -prisms and -octahedra were identified as new structural building blocks in this family. TiSeO_5 -octahedra and SeLa_6 -prisms are also present in $\text{La}_{15}\text{Ti}_6\text{Se}_{10}\text{O}_{26-x}$ beside well-known OLa_4 - and OLa_3Ti -tetrahedra. $\text{La}_{15}\text{Ti}_6\text{Se}_{10}\text{O}_{26-x}$ contains only one unique titanium atom position. The value of x depends on the deficiency of one oxygen position in the unit cell. Single crystal X-ray analysis revealed an occupation of ≈ 50 % leading to $\text{La}_{15}\text{Ti}_6\text{Se}_{10}\text{O}_{25}$ and titanium in the impossible

oxidation state of $+4\frac{1}{6}$. However, a theoretical occupation with 25 % oxygen would lead to $\text{La}_{15}\text{Ti}_6\text{Se}_{10}\text{O}_{24.5}$ and to a more reasonable oxidation state of +IV. As deficiencies of light atom positions can hardly be exactly determined, neutron diffraction experiments would help to clarify this problem.

Although it was not possible to characterize the two materials by magnetic measurements, single crystal X-ray diffraction revealed new interesting structural building blocks that expand the field of imaginable compounds in this quaternary system.

4.7 References

- [1] Y. Kamihara, T. Watanabe, M. Hirano, H. Hosono, *J. Am. Chem. Soc.* **2008**, *130*, 3296.
- [2] H. Hiramatsu, K. Ueda, T. Kamiya, H. Ohta, M. Hirano, H. Hosono, *J. Mater. Chem.* **2004**, *14*, 2946.
- [3] F. Nitsche, R. Niklaus, D. Johrendt, *Z. Anorg. Allg. Chem.* **2014**, *640*, 2897.
- [4] E. E. McCabe, D. G. Free, J. S. O. Evans, *Chem. Commun.* **2011**, *47*, 1261.
- [5] A. J. Tuxworth, E. E. McCabe, D. G. Free, S. J. Clark, J. S. O. Evans, *Inorg. Chem.* **2013**, *52*, 2078.
- [6] I. Ijjaali, K. Mitchell, C. L. Haynes, A. D. McFarland, R. Van Duyne, J. A. Ibers, *J. Solid State Chem.* **2003**, *176*, 170.
- [7] E. E. McCabe, D. G. Free, B. G. Mendis, J. S. Higgins, J. S. O. Evans, *Chem. Mater.* **2010**, *22*, 6171.
- [8] H.-L. Keller, R. Langer, *Z. Anorg. Allg. Chem.* **1994**, *6*, 620.
- [9] *APEX2* (Version 2012.12-0), Bruker AXS Inc., Madison, WI, USA, **2007**.
- [10] G. M. Sheldrick, *SADABS* (Version 2012/1), Bruker AXS Inc., Madison, WI, USA, **2001**.
- [11] V. Petricek, M. Dusek, L. Palatinus, *Jana2006* (Version 26/09/2012), Institute of Physics, Praha, Czech Republic **2006**.
- [12] A. Coelho, *TOPAS-Academic*, Version 4.1, Coelho Software, Brisbane, Australia **2007**.
- [13] P. Kubelka, F. Munk, *Z. Tech. Phys.* **1931**, *12*, 593.
- [14] C. M. Ainsworth, C.-H. Wang, M. G. Tucker, J. S. O. Evans, *Inorg. Chem.* **2015**, *54*, 1563.
- [15] F. Nitsche, A. Jesche, E. Hieckmann, T. Doert, M. Ruck, *Phys. Rev. B* **2010**, *82*, 134514.
- [16] S. Peschke, F. Nitsche, D. Johrendt, *Z. Anorg. Allg. Chem.* **2015**, *641*, 529.
- [17] C.-H. Wang, C. M. Ainsworth, C. M. Gui, E. E. McCabe, M. G. Tucker, I. R. Evans, J. S. O. Evans, *Chem. Mater.* **2015**, *27*, 3121.

- [18] C. Ainsworth, C.-H. Wang, H. E. Johnston, E. E. McCabe, M. G. Tucker, H. E. A. Brand, J. S. O. Evans, *Inorg. Chem.* **2015**, *54*, 7230.
- [19] O. Tougait, J. A. Ibers, *Chem. Mater.* **2000**, *12*, 2653.
- [20] O. Tougait, J. A. Ibers, *J. Solid State Chem.* **2001**, *157*, 289.
- [21] N. H. Dung, V. Tien, *C. R. Acad. Sci. Ser. 2* **1981**, *293*, 933.
- [22] A. Meerschaut, A. Lafond, V. Meignen, C. Deudon, *J. Solid State Chem.* **2001**, *162*, 182.
- [23] A. J. Tuxworth, J. S. O. Evans, *J. Solid State Chem.* **2014**, *210*, 188.
- [24] S. Strobel, A. Choudhry, P. K. Dorhout, C. Lipp, T. Schleid, *Inorg. Chem.* **2008**, *47*, 4936.
- [25] S. Peschke, V. Weippert, A. Senyshyn, M. J. Mühlbauer, O. Janka, R. Pöttgen, S. Holenstein, H. Luetkens, D. Johrendt, *Inorg. Chem.* **2017**, *56*, 2241.
- [26] S. Peschke, D. Johrendt, *Z. Kristallogr.* **2016**, *231*, 89.
- [27] S. Peschke, D. Johrendt, *Inorganics* **2017**, *5*, 9.
- [28] M. Wintenberger, J. Dugué, M. Guittard, N. H. Dung, V. Tien, *J. Solid State Chem.* **1987**, *70*, 295.
- [29] Heinz Maier-Leibnitz Zentrum et al. (2015). SPODI: High resolution powder diffractometer. *Journal of large-scale research facilities*, *1*, A5. <http://dx.doi.org/10.17815/jlsrf-1-24>
- [30] J. Rodriguez-Carvajal, *Physica B* **1993**, *192*, 55.
- [31] A. Suter, B. M. Wojek, *Physics Procedia* **2010**, *30*, 69.
- [32] R. Kraft, T. Fickenscher, G. Kotzyba, R.-D. Hoffmann, R. Pöttgen, *Intermetallics* **2003**, *11*, 111.
- [33] A. Yaouan, P. D. de Rotier, *Muon Spin Rotation, Relaxation and Resonance*, Oxford University Press **2011**.
- [34] H. Person, W. Urland, *J. Alloys Compd.* **2001**, *323*, 57.
- [35] V. Meignen, C. Deudon, A. Lafond, C. Boyer-Candalen, A. Meerschaut, *Solid State Sci.* **2001**, *3*, 189.

- [36] W. J. Zhu, Y. Z. Huang, C. Dong, Z. X. Zhao, *Mater. Res. Bull.* **1994**, *29*, 143.
- [37] O. Tougait, J. A. Ibers, *J. Solid State Chem.* **2000**, *154*, 564.
- [38] P. J. Dugué, T. Vovan, P. Laruelle, *Acta Cryst. C* **1985**, *41*, 1146.
- [39] V. Petricek, M. Dusek, L. Palatinus, *Z. Kristallogr.* **2014**, *229*, 345.
- [40] G. M. Sheldrick, *Acta Crystallogr. Sect. A* **2008**, *64*, 112.
- [41] *SmartSEM*, v. Version 5.07 Beta, Carl Zeiss Microscopy Ltd., **2014**.
- [42] *Quantax 200*, v. Version 1.9.4.3448, Bruker Nano GmbH, **2013**.
- [43] P. Rozier, A. Ratuszna, J. Galy, *Z. Anorg. Allg. Chem.* **2002**, *628*, 1236.
- [44] Y. Ohno, H. Watanabe, A. Kawata, S. Nakai, C. Sugiura, *Phys. Rev. B* **1982**, *25*, 815.
- [45] E. Rost, L. Gjertsen, *Z. Anorg. Allg. Chem.* **1964**, *328*, 299.
- [46] G. Andersson, *Acta Chem. Scand.* **1954**, *8*, 1599.
- [47] S. Andersson, A. Sundholm, A. Magnéli, *Acta Chem. Scand.* **1959**, *13*, 989.
- [48] N. H. Hur, S. H. Kim, K. S. Yu, Y. K. Park, J. C. Park, *Solid State Comm.* **1994**, *92*, 541.
- [49] R. Restori, D. Schwarzenbach, J. R. Schneider, *Acta Crystallogr. B* **1987**, *43*, 251.
- [50] M. E. Straumanis, T. Ejima, *Acta Crystallogr.* **1957**, *10*, 789.

Chapter 5

Summary

The focus of the present thesis lays on syntheses of rare-earth transition-metal oxypnictides and oxychalcogenides covering metathesis reactions as well as flux-mediated solid state reactions. Hereby, the first part concentrates on the analysis of magnetic and superconducting properties of the $REFeAsO_{1-x}F_x$ ($RE = \text{La, Pr, Nd, Sm, Gd-Dy}$) family of iron-based superconductors, whereas the main focus of the second part is the synthesis of new compounds in the quaternary $RE-T\text{-Se-O}$ system ($RE = \text{La-Nd}$; $T = \text{Ti-Mn}$). The obtained compounds were characterized in terms of their crystal structures as well as optical and physical properties using a broad range of experimental methods. An overview over the different materials discovered and investigated within this thesis is given in Figure 5.1 and short summaries of the particular chapters are given below.

LaFeAsO_{1-x}F_x

Superconducting samples of $\text{LaFeAsO}_{1-x}\text{F}_x$ ($0.05 \leq x \leq 0.15$) were successfully synthesized via a solid state metathesis reaction. The solubility limit of fluorine using this synthesis method was determined to be 20–25 %. Samples with $x > 0.15$ are non-superconducting because of over-doping with electrons. Remarkably, superconductivity re-emerges in the solid solutions $(\text{La}_{1-x}\text{RE})_x\text{FeAsO}_{0.8}\text{F}_{0.2}$ ($RE = \text{Pr, Nd, Sm}$) in spite of constant electron doping. T_c depends strongly on the unit cell volume which indicates that, beside electronic influence, structural parameters may play a decisive role for the emergence of superconductivity in this system.

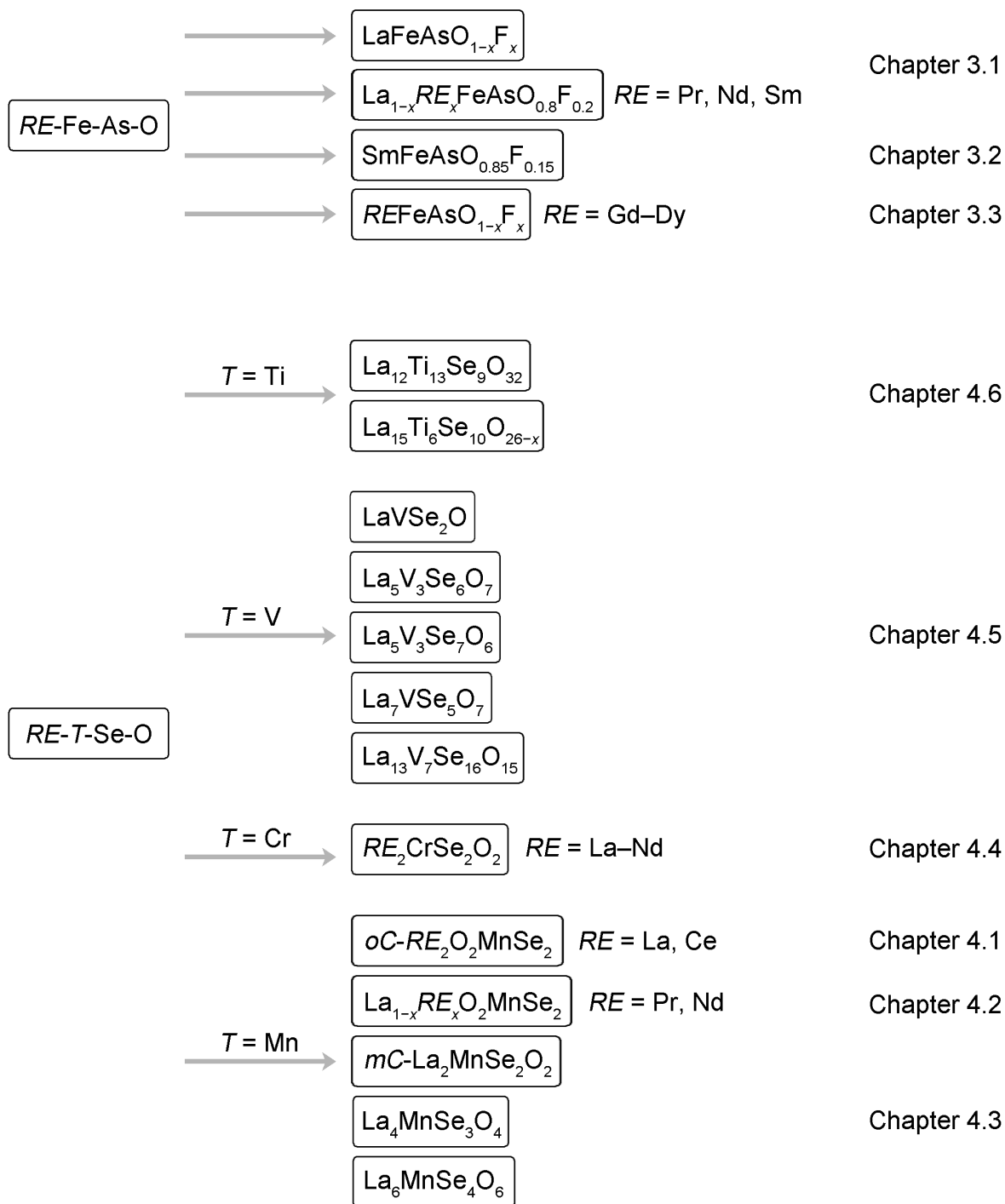


Figure 5.1 Overview over the different materials discussed in the present thesis.

SmFeAsO_{1-x}F_x

High quality samples of optimally doped SmFeAsO_{0.85}F_{0.15} with $T_c \approx 55$ K were prepared and sintered at different temperatures between 1173–1373 K. Measurements of the global critical current density were performed in cooperation with *Dr. A. Malagoli* (CNR-SPIN, Genova, Italy). Sintering of the samples increases the density but continuously degrades the sample quality due to increased formation of impurity phases. The estimated values of J_c^{global} are between 200–250 A/cm², which is comparable to values of hot isostatic pressed samples from the literature. Intragranular critical current densities are significantly higher in the range of 10⁶–10⁷ A/cm². As J_c^{global} is limited by the connection across grain boundaries, the weak connection between the grains due to intragranular gaps or impurities may be the reason for the huge difference between intragranular und intergranular current densities.

REFeAsO_{1-x}F_x (RE = Gd–Dy)

A series of the REFeAsO_{1-x}F_x (RE = Gd–Dy) compounds was successfully prepared using the solid state metathesis reaction. Bulk superconductivity was found for GdFeAsO_{1-x}F_x ($x > 0.05$) as well as for TbFeAsO_{0.85}F_{0.15} and DyFeAsO_{0.85}F_{0.15}. The critical temperature of 50.3 K of GdFeAsO_{0.75}F_{0.25} is the highest T_c observed in the Gd system aside from syntheses at high pressure. Furthermore, we observed bulk superconductivity in the terbium and dysprosium system at ≈ 27 K and ≈ 15 K for the first time using a normal pressure synthesis route. However, T_c of the samples with RE = Tb and Dy are significantly lower than those of high pressure synthesized samples from the literature. A look at the lattice parameters revealed a significant discrepancy between ours and the high pressure synthesized samples, which leads to the conclusion that structural parameters play an important role regarding the superconducting properties.

Flux Synthesis, Modulated Crystal Structures, and Physical Properties of RE₂O₂MnSe₂ (RE = La, Ce)

The selenide oxides RE₂O₂MnSe₂ (RE = La, Ce) were synthesized in a NaI/KI flux, and their modulated crystal structures determined by X-ray single crystal diffraction. The crystal structures are related to the ZrCuSiAs-type structure and uncovered so far unknown motifs of ordered vacancies in the [MnSe₂]²⁻ layers with a mixture of edge- and corner-sharing MnSe_{4/2}-tetrahedra. The resulting modulations are described using superspace group $Cmme(\alpha 0 \frac{1}{2})0s0$

and can be approximated by $5\sqrt{2}a_{\text{subcell}} \times \sqrt{2}b_{\text{subcell}} \times 2c_{\text{subcell}}$ and $19\sqrt{2}a_{\text{subcell}} \times \sqrt{2}b_{\text{subcell}} \times 2c_{\text{subcell}}$ supercells of $\text{La}_2\text{O}_2\text{MnSe}_2$ and $\text{Ce}_2\text{O}_2\text{MnSe}_2$, respectively. Manganese site ordering changes seem to be a key mechanism for strain relief which is necessary because of an inherent size mismatch between the $[\text{RE}_2\text{O}_2]^{2+}$ and the $[\text{MnSe}_2]^{2-}$ layers. Low temperature diffraction experiments revealed no change of the modulation of the lanthanum compound and small changes in case of the cerium compound. Both compounds are insulators with band gaps of 2.13 and 2.01 eV determined from the Kubelka-Munk function, respectively. Magnetic measurements indicate antiferromagnetic ordering of the Mn^{2+} moments with Néel points well above room temperature.

The Modulated Structures of $\text{La}_{2-x}\text{Pr}_x\text{O}_2\text{MnSe}_2$ and $\text{La}_{2-x}\text{Nd}_x\text{O}_2\text{MnSe}_2$

High purity samples of the solid solutions $\text{La}_{2-x}\text{Pr}_x\text{O}_2\text{MnSe}_2$ ($0 \leq x \leq 1$) and $\text{La}_{2-x}\text{Nd}_x\text{O}_2\text{MnSe}_2$ ($0 \leq x \leq 0.6$) were prepared using a NaI/KI flux synthesis. The crystal structures are described with a (3+1)D model in superspace group $Cmme(\alpha 0 \frac{1}{2})0s0$. The modulation vector component α can be controlled by the partial substitution of lanthanum by the smaller rare-earth metals praseodymium and neodymium via the unit cell volume. $(\text{La}_{0.55}\text{Pr}_{0.45})_2\text{O}_2\text{MnSe}_2$ represents a unique case in this solid solution where α adopts a value of $\alpha = \frac{1}{6}$, which allows a simple commensurate model with a sixfold a axis. Comparing the solid solutions $\text{La}_{2-x}\text{RE}_x\text{O}_2\text{MnSe}_2$ ($\text{RE} = \text{Ce}, \text{Pr}, \text{Nd}$) leads to the conclusion that α is affected equally in a wide range with respect to the effective relative radii of the rare-earth metal. However, α decreases stronger than expected in the range $0 \leq x < 0.2$ which is not an effect of the structural changes but an intrinsic effect of the solid solutions.

Flux Synthesis, Crystal Structures, and Magnetism of the Series $\text{La}_{2n+2}\text{MnSe}_{n+2}\text{O}_{2n+2}$ ($n = 0-2$)

Three members of the series $\text{La}_{2n+2}\text{MnSe}_{n+2}\text{O}_{2n+2}$ ($n = 0-2$) were prepared in a NaI/KI flux and characterized by single crystal and powder X-ray diffraction as well as magnetic measurements. mC - $\text{La}_2\text{MnSe}_2\text{O}_2$ adopts the $\text{Pb}_2\text{HgCl}_2\text{O}_2$ -type structure and represents, beside the literature known oA - $\text{La}_2\text{MnSe}_2\text{O}_2$ and the modulated compound oC - $\text{La}_2\text{MnSe}_2\text{O}_2$, a third polymorph in this manganese family. $\text{La}_4\text{MnSe}_3\text{O}_4$ and $\text{La}_6\text{MnSe}_4\text{O}_6$ crystallize in new structure types which are closely related to that of mC - $\text{La}_2\text{MnSe}_2\text{O}_2$. The crystal structures solely differ in the number of La_2SeO_2 -units between chains of edge-sharing MnSe_4O_2 -octahedra.

Magnetic measurements indicate antiferromagnetic ordering of the Mn^{2+} moments below $T_N = 15$ K in all compounds.

Flux Synthesis, Crystal Structures, and Magnetic Ordering of the Rare-Earth Chromium(II) Oxyselenides $RE_2\text{CrSe}_2\text{O}_2$ ($RE = \text{La-Nd}$)

The rare-earth chromium(II) oxyselenides $RE_2\text{CrSe}_2\text{O}_2$ ($RE = \text{La-Nd}$) were synthesized in eutectic NaI/KI fluxes. Single crystal X-ray diffraction identified the $\text{Pb}_2\text{HgCl}_2\text{O}_2$ structure type in space group $C2/m$. Main building blocks are chains of edge-sharing CrSe_4O_2 -octahedra linked together by two edge-sharing $ORE_3\text{Cr}$ -tetrahedra forming infinite ribbons. The *Jahn-Teller* instability of divalent Cr^{2+} (d^4) leads to structural phase transitions at 200 and 130 K in $\text{La}_2\text{CrSe}_2\text{O}_2$ and $\text{Ce}_2\text{CrSe}_2\text{O}_2$, respectively. Magnetometry revealed Curie-Weiss paramagnetism and indicated antiferromagnetic order below $T_N \approx 14$ –17 K. $\text{Pr}_2\text{CrSe}_2\text{O}_2$ shows an antiferromagnetic-to-ferromagnetic spin reorientation (metamagnetism) at higher magnetic fields. Muon spin rotation experiments with $\text{La}_2\text{CrSe}_2\text{O}_2$ confirm a second order transition into a commensurate magnetic structure, which is proved by 4 K neutron powder diffraction data. The magnetic structure is G-type antiferromagnetic with an ordered Cr^{2+} moment of $3.40(4) \mu_B$ at 4 K.

Flux Synthesis, Crystal Structures, and Physical Properties of New Lanthanum Vanadium Oxyselenides

The first five quaternary lanthanum vanadium oxyselenides, LaVSe_2O , $\text{La}_5\text{V}_3\text{Se}_6\text{O}_7$, $\text{La}_5\text{V}_3\text{Se}_7\text{O}_5$, $\text{La}_7\text{VSe}_5\text{O}_7$ and $\text{La}_{13}\text{V}_7\text{Se}_{16}\text{O}_{15}$ were prepared in a NaI/KI flux. Their crystal structures were determined using single crystal X-ray and powder diffraction. Beside new structure types of $\text{La}_5\text{V}_3\text{Se}_7\text{O}_5$, $\text{La}_7\text{VSe}_5\text{O}_7$ and $\text{La}_{13}\text{V}_7\text{Se}_{16}\text{O}_{15}$, the compounds LaVSe_2O and $\text{La}_5\text{V}_3\text{Se}_6\text{O}_7$ adopt literature known structure types. The compounds are built-up of common building blocks, e.g. VSe_4O_2 -octahedra and OLa_3V -tetrahedra, but with different connections between them leading to a modular conception of chemical building blocks. Magnetic measurements indicate various types of ordering, among them antiferromagnetism for $\text{La}_5\text{V}_3\text{Se}_6\text{O}_7$, ferromagnetism for $\text{La}_7\text{VSe}_5\text{O}_7$, metamagnetism for $\text{La}_5\text{V}_3\text{Se}_7\text{O}_5$ and a more complicated behavior for $\text{La}_{13}\text{V}_7\text{Se}_{16}\text{O}_{15}$.

Synthesis and Crystal Structures of New Lanthanum Titanium Oxyselenides

Two new quaternary La-Ti-Se-O compounds have been prepared and characterized via single crystal X-ray diffraction. $\text{La}_{12}\text{Ti}_{13}\text{Se}_9\text{O}_{32}$ and $\text{La}_{15}\text{Ti}_6\text{Se}_{10}\text{O}_{26-x}$ crystallize in new structure types in space group $R\bar{3}$ and $P\bar{6}2m$, respectively. In contrast to literature known compounds of this family, the crystal structures of the new compounds contain no TiSe_4O_2 - but TiSe_2O_4 - and TiSeO_5 -octahedra, which can be attributed to the high oxygen content of these compounds. Additionally, new coordination polyhedra such as TiO_8 -hexagonal bipyramids as well as SeLa_6 -prisms and -octahedra expand the structural diversity in this field of quaternary materials. Regarding the oxidation number of titanium, $\text{La}_{12}\text{Ti}_{13}\text{Se}_9\text{O}_{32}$ is a mixed valent compound with Ti^{III} and Ti^{IV} , whereby titanium in $\text{La}_{15}\text{Ti}_6\text{Se}_{10}\text{O}_{26-x}$ ($x = 1.5$) exhibits solely the oxidation state +IV.

Conclusion

The present thesis includes two different quaternary systems that have been studied extensively. On the one hand, several samples of the $REFeAsO_{1-x}F_x$ family of iron-based superconductors were prepared using a novel solid state metathesis reaction, which also provided a possibility to prepare late rare-earth compounds of this family at ambient pressure. Comparison of structural and physical properties of those samples with samples from conventional solid state and high pressure syntheses revealed both, commonalities as well as striking differences. The observations gave reason to the conclusion that superconducting properties strongly depend, beside electronic influence, on the structural parameters.

On the other hand, the quaternary system $RE-T$ -Se-O with $T = \text{Ti-Mn}$ was investigated using a NaI/KI flux mediated synthesis route. It has been shown that oC - $\text{La}_2\text{O}_2\text{MnSe}_2$ is exclusively accessible in sufficient purity by the use of a flux material. Therefore, further syntheses in this quaternary system were performed by a flux mediated synthesis route leading to a large amount of new materials. Among them, a new polymorph mC - $\text{La}_2\text{O}_2\text{MnSe}_2$ which forms, together with $\text{La}_4\text{MnSe}_3\text{O}_4$ and $\text{La}_6\text{MnSe}_4\text{O}_6$, the series $\text{La}_{2n+2}\text{MnSe}_{n+2}\text{O}_{2n+2}$. In addition, the alternative preparation method also enabled a large scale synthesis of the first examples of rare-earth chromium oxyselenides with chromium in the oxidation state +II, namely $RE_2\text{CrSe}_2\text{O}_2$ ($RE = \text{La-Nd}$), which opened the door to study their magnetism in detail by powder neutron diffraction and muon spin rotation techniques. Research into the La-V-Se-O system revealed the first five quaternary compounds of this family with interesting magnetic properties including ferromagnetism, antiferromagnetism, metamagnetism and more complex behaviour. In addition, the crystal structure of two new quaternary titanium containing oxyselenides were identified and revealed unique structural building blocks that have not been observed in these systems before.

The results of this thesis demonstrate not only the power of alternative preparation methods, but also the still increasing structural variety in the discussed quaternary systems. Strategic research in the field of transition-metal oxypnictides and oxychalcogenides, which still include a multiplicity of unknown materials, revealed numerous compounds with interesting physical properties and further investigations will probably uncover also new superconducting materials.

Appendix A

A.1 Crystallographic data of $\text{La}_2\text{O}_2\text{MnSe}_2$

Table A.1 Crystallographic data of $\text{La}_2\text{O}_2\text{MnSe}_2$ at 300 K.

Formula weight/g mol ⁻¹	522.7					
Space group	$Cmme(\alpha 0 \frac{1}{2}) 0s0$					
α, Z	$\frac{1}{5}, 2$					
$a, b, c/\text{pm}$	573.7(1), 573.7(1), 915.0(1)					
$V/\text{\AA}^3, \rho_{\text{X-ray}}/\text{g cm}^{-3}$	301.2(1), 5.76					
Crystal size/mm ³	$0.04 \times 0.04 \times 0.005$					
Diffractometer	Bruker D8 QUEST					
Radiation λ/pm	71.073					
Absorption coeff. μ/mm^{-1}	28.0					
2θ range/°	8.90–70.00					
Index range ($hklm$)	$h \pm 9, -6 \leq k \leq 9, l \pm 15, m \pm 1$					
No. reflections collected	5582					
No. unique data, $R_{\text{int}}, R_{\sigma}$	654, 0.03, 0.02					
No. data with $I > 3\sigma(I)$	558					
No. parameters	20					
R factors of main reflections						
$R_1(\text{obs/all})$	0.015/0.015					
$wR_2(\text{obs/all})$	0.036/0.036					
R factors of first order satellites						
$R_1(\text{obs/all})$	0.029/0.049					
$wR_2(\text{obs/all})$	0.059/0.063					
$\Delta\rho_{\text{max}}, \Delta\rho_{\text{min}}/\text{e}\text{\AA}^{-3}$	0.77/−1.04					
Atomic and displacement parameters						
	Site	x, y, z	U_{11}	U_{22}	U_{33}	Occupancy
La	$4g$	$\frac{1}{2}, \frac{1}{4}, 0.1347(1)$	0.0051(1)	0.0053(1)	0.0061(2)	1
Mn	$4b$	$\frac{1}{4}, 0, \frac{1}{2}$	0.0126(5)	0.0134(5)	0.0086(5)	0.5
Se	$4g$	$0, \frac{1}{4}, 0.3257(1)$	0.0102(2)	0.0123(2)	0.0089(2)	1
O	$4a$	$\frac{1}{4}, 0, 0$	0.0053(13)	0.0065(13)	0.0072(15)	1
Crenel function	Width	Center				
Mn	0.5	0.25				

Table A.2 Crystallographic data of $\text{La}_2\text{O}_2\text{MnSe}_2$ at 100 K.

Formula weight/g mol ⁻¹	522.7					
Space group	$Cmme(\alpha 0\frac{1}{2})0s0$					
α, Z	$\frac{1}{5}, 2$					
$a, b, c/\text{pm}$	572.6(1), 571.9(1), 912.8(1)					
$V/\text{\AA}^3, \rho_{\text{X-ray}}/\text{g cm}^{-3}$	301.2(1), 5.76					
Crystal size/mm ³	0.04 × 0.04 × 0.005					
Diffractometer	Bruker D8 QUEST					
Radiation λ/pm	71.073					
Absorption coeff. μ/mm^{-1}	28.2					
2θ range/ $^\circ$	9.40–72.72					
Index range ($hklm$)	$-9 \leq h \leq 6, -9 \leq k \leq 8, l \pm 15, m \pm 1$					
No. reflections collected	4556					
No. unique data, R_{int}, R_σ	645, 0.05, 0.04					
No. data with $I > 3\sigma(I)$	479					
No. parameters	20					
R factors of main reflections						
$R_1(\text{obs/all})$	0.014/0.015					
$wR_2(\text{obs/all})$	0.034/0.034					
R factors of first order satellites						
$R_1(\text{obs/all})$	0.047/0.097					
$wR_2(\text{obs/all})$	0.080/0.090					
$\Delta\rho_{\text{max}}, \Delta\rho_{\text{min}}/\text{e}\text{\AA}^{-3}$	1.16/−1.24					
Atomic and displacement parameters						
	Site	x, y, z	U_{11}	U_{22}	U_{33}	Occupancy
La	4g	$0, \frac{1}{4}, 0.1351(1)$	0.0025(2)	0.0025(2)	0.0046(1)	1
Mn	4b	$\frac{1}{4}, 0, \frac{1}{2}$	0.0082(7)	0.0045(6)	0.0058(8)	0.5
Se	4g	$\frac{1}{2}, \frac{1}{4}, 0.3261(1)$	0.0046(3)	0.0061(3)	0.0057(3)	1
O	4a	$\frac{1}{4}, 0, 0$	0.003(2)	0.002(2)	0.002(2)	1
Crenel function		Width	Center			
	Mn	0.5	0.75			

A.2 Crystallographic data of Ce₂O₂MnSe₂

Table A.3 Crystallographic data of Ce₂O₂MnSe₂ at 300 K.

Formula weight/g mol ⁻¹	525.1					
Space group	<i>Cmme</i> ($\alpha 0\frac{1}{2}$) <i>0s0</i>					
α , <i>Z</i>	0.1573(2), 2					
<i>a</i> , <i>b</i> , <i>c</i> /pm	568.6(1), 568.3(1), 910.9(1)					
<i>V</i> /Å ³ , $\rho_{X\text{-ray}}$ /g cm ⁻³	294.4(1), 5.92					
Crystal size/mm ³	0.02 × 0.02 × 0.002					
Diffractometer	Bruker D8 QUEST					
Radiation λ /pm	71.073					
Absorption coeff. μ /mm ⁻¹	29.6					
2θ range/°	8.94–74.20					
Index range (<i>hklm</i>)	$h \pm 9, -9 \leq k \leq 6, l \pm 15, m \pm 1$					
No. reflections collected	5315					
No. unique data, R_{int} , R_{σ}	314, 0.07, 0.06					
No. data with $I > 3\sigma(I)$	256					
No. parameters	20					
<i>R</i> factors of main reflections						
$R_1(\text{obs/all})$	0.013/0.013					
$wR_2(\text{obs/all})$	0.030/0.030					
<i>R</i> factors of first order satellites						
$R_1(\text{obs/all})$	0.032/0.054					
$wR_2(\text{obs/all})$	0.055/0.058					
$\Delta\rho_{\text{max}}$, $\Delta\rho_{\text{min}}$ /eÅ ⁻³	0.52/−0.51					
Atomic and displacement parameters						
	Site	<i>x</i> , <i>y</i> , <i>z</i>	U_{11}	U_{22}	U_{33}	Occupancy
Ce	4 <i>g</i>	$\frac{1}{2}, \frac{1}{4}, 0.1335(1)$	0.0053(3)	0.0044(3)	0.0088(3)	1
Mn	4 <i>b</i>	$\frac{1}{4}, 0, \frac{1}{2}$	0.0141(9)	0.0125(8)	0.0111(10)	0.5
Se	4 <i>g</i>	$0, \frac{1}{4}, 0.3236(1)$	0.0109(4)	0.0120(4)	0.0118(4)	1
O	4 <i>a</i>	$\frac{3}{4}, 0, 0$	0.006(2)	0.002(2)	0.008(3)	1
Crenel function	Width	Center				
	Mn	0.5	0.75			

Table A.4 Crystallographic data of Ce₂O₂MnSe₂ at 100 K.

Formula weight/g mol ⁻¹	525.1					
Space group	<i>Cmme</i> ($\alpha 0\frac{1}{2}$)0 <i>s</i> 0					
α, Z	0.1603(2), 2					
$a, b, c/\text{pm}$	567.0(1), 567.0(1), 905.4(1)					
$V/\text{\AA}^3, \rho_{\text{X-ray}}/\text{g cm}^{-3}$	291.1(1), 5.99					
Crystal size/mm ³	0.02 × 0.02 × 0.002					
Diffractometer	Bruker D8 QUEST					
Radiation λ/pm	71.073					
Absorption coeff. μ/mm^{-1}	29.9					
2θ range/°	8.94–74.20					
Index range ($hklm$)	$-9 \leq h \leq 7, -7 \leq k \leq 9, -14 \leq l \leq 13, m \pm 1$					
No. reflections collected	3666					
No. unique data, $R_{\text{int}}, R_{\sigma}$	308, 0.04, 0.04					
No. data with $I > 3\sigma(I)$	240					
No. parameters	21					
R factors of main reflections						
$R_1(\text{obs/all})$	0.012/0.012					
$wR_2(\text{obs/all})$	0.030/0.030					
R factors of first order satellites						
$R_1(\text{obs/all})$	0.028/0.067					
$wR_2(\text{obs/all})$	0.052/0.065					
Twin fraction	0.404(2)					
Twin matrix	$\begin{pmatrix} 0 & 1 & 0 \\ \bar{1} & 0 & 0 \\ 0 & 0 & 1 \end{pmatrix}$					
$\Delta\rho_{\text{max}}, \Delta\rho_{\text{min}}/\text{e\AA}^{-3}$	0.53/−0.75					
Atomic and displacement parameters						
	Site	x, y, z	U_{11}	U_{22}	U_{33}	Occupancy
Ce	4 <i>g</i>	$\frac{1}{2}, \frac{1}{4}, 0.1342(1)$	0.0014(6)	0.0032(6)	0.0030(3)	1
Mn	4 <i>b</i>	$\frac{1}{4}, 0, \frac{1}{2}$	0.0061(13)	0.0074(14)	0.0031(9)	0.5
Se	4 <i>g</i>	$0, \frac{1}{4}, 0.3239(1)$	0.0046(10)	0.0075(11)	0.0037(4)	1
O	4 <i>a</i>	$\frac{1}{4}, 0, 0$	0.002(7)	0.004(7)	0.003(2)	1
Crenel function	Width	Center				
	Mn	0.5	0.75			

A.3 Crystallographic data of $(\text{La}_{0.55}\text{Pr}_{0.45})_2\text{O}_2\text{MnSe}_2$

Table A.5 Crystallographic data of $(\text{La}_{0.55}\text{Pr}_{0.45})_2\text{O}_2\text{MnSe}_2$.

Formula weight/g mol ⁻¹	524.7					
Space group	$Cmme(\alpha 0\frac{1}{2})0s0$					
α, Z	$\frac{1}{6}, 2$					
$a, b, c/\text{pm}$	569.2(1), 569.2(1), 912.3(1)					
$V/\text{\AA}^3, \rho_{\text{X-ray}}/\text{g cm}^{-3}$	295.7(1), 5.89					
Crystal size/mm ³	$0.03 \times 0.03 \times 0.01$					
Diffractometer	Bruker D8 QUEST					
Radiation λ/pm	71.073					
Absorption coeff. μ/mm^{-1}	29.4					
2θ range/ $^\circ$	8.94–86.24					
Index range ($hklm$)	$h \pm 11, k \pm 9, -17 \leq l \leq 15, m \pm 1$					
No. reflections collected	8186					
No. unique data, $R_{\text{int}}, R_{\sigma}$	924, 0.02, 0.03					
No. data with $I > 3\sigma(I)$	743					
No. parameters	21					
R factors of main reflections						
$R_1(\text{obs/all})$	0.018/0.019					
$wR_2(\text{obs/all})$	0.046/0.046					
R factors of first order satellites						
$R_1(\text{obs/all})$	0.042/0.081					
$wR_2(\text{obs/all})$	0.081/0.088					
Twin fraction	0.369(3)					
Twin matrix	$\begin{pmatrix} 0 & 1 & 0 \\ \bar{1} & 0 & 0 \\ 0 & 0 & 1 \end{pmatrix}$					
$\Delta\rho_{\text{max}}, \Delta\rho_{\text{min}}/\text{e}\text{\AA}^{-3}$	1.48/−2.56					
Atomic and displacement parameters						
	Site	x, y, z	U_{11}	U_{22}	U_{33}	Occ.
RE	$4g$	$0, \frac{1}{4}, 0.1333(1)$	0.0057(2)	0.0041(2)	0.0066(1)	1
Mn	$4b$	$\frac{1}{4}, 0, \frac{1}{2}$	0.0131(6)	0.0110(6)	0.0085(2)	0.5
Se	$4g$	$\frac{1}{2}, \frac{1}{4}, 0.3240(1)$	0.0102(4)	0.0119(4)	0.0085(2)	1
O	$4a$	$\frac{1}{4}, 0, 0$	0.002(2)	0.008(2)	0.010(1)	1
Crenel function		Width	Center			
	Mn	0.5	0.75			

A.4 Crystallographic data of mC -La₂MnSe₂O₂

Table A.6 Crystallographic data of mC -La₂MnSe₂O₂.

Formula weight/g mol ⁻¹	522.7					
Space group, Z	$C2/m$, 2					
a , b , c /pm	1166.2(1), 397.2(1), 720.5(1)					
β /°	121.7(1)					
$V/\text{Å}^3$, $\rho_{\text{X-ray}}/\text{g cm}^{-3}$	284.1(1), 6.11					
Crystal size/mm ³	0.06 × 0.02 × 0.01					
Diffractometer	Bruker D8 QUEST					
Radiation λ /pm	71.073					
Absorption coeff. μ/mm^{-1}	29.6					
2θ range/°	6.64–107.76					
Index range (hkl)	$-19 \leq h \leq 25$, $k \pm 8$, $-16 \leq l \leq 14$					
No. reflections collected	5770					
No. unique data, R_{int} , R_{σ}	1731, 0.02, 0.03					
No. data with $I > 3\sigma(I)$	1441					
No. parameters	23					
$R_1(\text{obs/all})$	0.024/0.036					
$wR_2(\text{obs/all})$	0.048/0.051					
$\Delta\rho_{\text{max}}$, $\Delta\rho_{\text{min}}/\text{eÅ}^{-3}$	1.92/−2.53					
Atomic and displacement parameters						
	Site	x , y , z	U_{11}	U_{22}	U_{33}	Occ.
La	$4i$	0.6923(1), 0, 0.2430(1)	0.0073(1)	0.0058(1)	0.0059(1)	1
Mn	$2d$	0, $\frac{1}{2}$, $\frac{1}{2}$	0.0063(2)	0.0141(2)	0.0137(2)	1
Se	$4i$	0.9405(1), 0, 0.1797(1)	0.0087(1)	0.0088(1)	0.0080(1)	1
O	$4i$	0.8028(2), $\frac{1}{2}$, 0.4187(1)	0.0059(1)	0.0077(7)	0.0081(6)	1

A.5 Crystallographic data of $\text{La}_4\text{MnSe}_3\text{O}_4$

Table A.7 Crystallographic data of $\text{La}_4\text{MnSe}_3\text{O}_4$.

Formula weight/g mol ⁻¹	911.4					
Space group, Z	$P2/m, 1$					
$a, b, c/\text{pm}$	900.6(1), 401.9(1), 719.5(1)					
$\beta/^\circ$	109.7(1)					
$V/\text{Å}^3, \rho_{\text{X-ray}}/\text{g cm}^{-3}$	245.1(1), 6.17					
Crystal size/mm ³	$0.04 \times 0.02 \times 0.01$					
Diffractometer	Bruker D8 QUEST					
Radiation λ/pm	71.073					
Absorption coeff. μ/mm^{-1}	29.4					
2θ range/°	4.80–69.96					
Index range (hkl)	$h \pm 14, -6 \leq k \leq 5, l \pm 11$					
No. reflections collected	6887					
No. unique data, $R_{\text{int}}, R_{\sigma}$	1210, 0.03, 0.02					
No. data with $I > 3\sigma(I)$	1017					
No. parameters	39					
$R_1(\text{obs/all})$	0.023/0.032					
$wR_2(\text{obs/all})$	0.050/0.056					
$\Delta\rho_{\text{max}}, \Delta\rho_{\text{min}}/\text{eÅ}^{-3}$	3.85/−1.71					
Atomic and displacement parameters						
	Site	x, y, z	U_{11}	U_{22}	U_{33}	Occ.
La1	$2n$	0.2245(1), $\frac{1}{2}$, 0.1732(1)	0.0053(1)	0.0056(1)	0.0046(1)	1
La2	$2m$	0.6430(1), 0, 0.3496(1)	0.0053(1)	0.0044(1)	0.0048(1)	1
Mn1	$1f$	0, $\frac{1}{2}$, $\frac{1}{2}$	0.0120(6)	0.0113(5)	0.0115(5)	1
Se1	$1e$	$\frac{1}{2}$, $\frac{1}{2}$, 0	0.0072(3)	0.0062(3)	0.0048(3)	1
Se2	$2m$	0.0627(1), 0, 0.7971(1)	0.0078(2)	0.0095(2)	0.0079(2)	1
O1	$2m$	0.3651(4), 0, 0.3114(5)	0.0048(16)	0.0069(16)	0.0082(16)	1
O2	$2n$	0.2317(4), $\frac{1}{2}$, 0.5070(5)	0.0046(16)	0.0057(15)	0.0079(16)	1

A.6 Crystallographic data of $\text{La}_6\text{MnSe}_4\text{O}_6$

Table A.8 Crystallographic data of $\text{La}_6\text{MnSe}_4\text{O}_6$.

Formula weight/g mol ⁻¹	1300.2					
Space group, Z	$C2/m, 2$					
$a, b, c/\text{pm}$	2476.0(1), 403.6(1), 718.5(1)					
$\beta/^\circ$	104.2(1)					
$V/\text{\AA}^3, \rho_{\text{X-ray}}/\text{g cm}^{-3}$	696.2(1), 6.20					
Crystal size/ mm^3	$0.03 \times 0.02 \times 0.01$					
Diffractometer	Bruker D8 QUEST					
Radiation λ/pm	71.073					
Absorption coeff. μ/mm^{-1}	29.3					
2θ range/ $^\circ$	5.84–70.20					
Index range (hkl)	$-40 \leq h \leq 38, k \pm 6, l \pm 11$					
No. reflections collected	8892					
No. unique data, R_{int}, R_σ	1375, 0.05, 0.05					
No. data with $I > 3\sigma(I)$	957					
No. parameters	53					
$R_1(\text{obs/all})$	0.023/0.049					
$wR_2(\text{obs/all})$	0.041/0.049					
$\Delta\rho_{\text{max}}, \Delta\rho_{\text{min}}/\text{e}\text{\AA}^{-3}$	1.65/–1.70					
Atomic and displacement parameters						
	Site	x, y, z	U_{11}	U_{22}	U_{33}	Occ.
La1	$4i$	0.0788(1), $\frac{1}{2}$, 0.1453(1)	0.0050(2)	0.0060(2)	0.0049(2)	1
La2	$4i$	0.2263(1), 0, 0.2665(1)	0.0045(2)	0.0044(2)	0.0043(2)	1
La3	$4i$	0.1261(1), 0, 0.6051(6)	0.0056(2)	0.0045(2)	0.0052(2)	1
Mn1	$2d$	0, $\frac{1}{2}$, $\frac{1}{2}$	0.0110(9)	0.0110(7)	0.0100(8)	1
Se1	$4i$	0.8252(1), $\frac{1}{2}$, 0.0613(1)	0.0069(3)	0.0067(3)	0.0048(3)	1
Se2	$4i$	0.4781(1), $\frac{1}{2}$, 0.2116(1)	0.0076(4)	0.0095(3)	0.0075(4)	1
O1	$4i$	0.2752(2), $\frac{1}{2}$, 0.3975(6)	0.004(2)	0.009(2)	0.006(2)	1
O2	$4i$	0.1288(2), 0, 0.2662(7)	0.007(2)	0.007(2)	0.007(2)	1
O3	$4i$	0.0823(2), $\frac{1}{2}$, 0.4801(6)	0.003(2)	0.005(2)	0.010(2)	1

A.7 Crystallographic data of $\text{La}_2\text{CrSe}_2\text{O}_2$

Table A.9 Crystallographic data of $\text{La}_2\text{CrSe}_2\text{O}_2$.

Formula weight/g mol ⁻¹	519.7					
Space group, Z	$C2/m$, 2					
a , b , c /pm	1153.8(1), 396.7(1), 717.8(1)					
β /°	121.6(1)					
$V/\text{Å}^3$, $\rho_{\text{X-ray}}/\text{g cm}^{-3}$	279.7(1), 6.17					
Crystal size/mm ³	0.05 × 0.02 × 0.01					
Diffractometer	Bruker D8 QUEST					
Radiation λ /pm	71.073					
Absorption coeff. μ/mm^{-1}	29.8					
2θ range/°	6.66–69.96					
Index range (hkl)	$h \pm 18$, $k \pm 6$, $l \pm 11$					
No. reflections collected	4383					
No. unique data, R_{int} , R_{σ}	679, 0.03, 0.02					
No. data with $I > 3\sigma(I)$	607					
No. parameters	23					
$R_1(\text{obs/all})$	0.015/0.019					
$wR_2(\text{obs/all})$	0.039/0.040					
$\Delta\rho_{\text{max}}$, $\Delta\rho_{\text{min}}/\text{eÅ}^{-3}$	0.78/−1.05					
Atomic and displacement parameters						
	Site	x , y , z	U_{11}	U_{22}	U_{33}	Occ.
La	$4i$	0.6932(1), 0, 0.2428(1)	0.0068(1)	0.0055(10)	0.0058(1)	1
Mn	$2d$	0, $\frac{1}{2}$, $\frac{1}{2}$	0.0052(4)	0.0112(4)	0.0105(4)	1
Se	$4i$	0.9428(1), 0, 0.1840(1)	0.0083(2)	0.0125(2)	0.0091(2)	1
O	$4i$	0.8054(3), $\frac{1}{2}$, 0.4197(4)	0.0038(11)	0.0084(11)	0.0075(11)	1
Selected bond lengths and bond angles						
La-O	234.5(1)–241.4(1) pm		Cr-O	200.6(1) pm		
La-Se	312.2(1)–334.5(1) pm		Cr-Se	281.9(1) pm		
La-O-La	104.8(1)–115.5(1)°		La-O-Cr	107.1(1)–111.9(1)°		
Se-Cr-O	89.2(1)–90.8(1)°		Se-Cr-Se	89.5(1)–90.5(1)°		

Table A.10 Crystallographic data of $\text{La}_2\text{CrSe}_2\text{O}_2$ at 4 and 20 K obtained by neutron powder diffraction experiments.

Temperature /K	4	20		
Diffractometer	SPODI	SPODI		
Wavelength /nm	1.548	1.548		
Space group	$P\bar{1}$	$P\bar{1}$		
a, b, c /pm	1152.3(1), 395.8(1), 716.1(1)	1152.2(1), 395.9(1), 715.9(1)		
α, β, γ /°	89.10(1), 121.58(1), 89.87(1)	89.15(1), 121.58(1), 89.87(1)		
Cell volume /Å ³	278.2(1)	278.1(1)		
Data points	3020	2833		
Reflections (all phases)	2525	1288		
Refined parameters	66	62		
R_p, wR_p, χ	0.027, 0.033, 2.90	0.027, 0.034, 3.20		
Atomic parameters				
<i>Wyckoff</i>	x, y, z	x, y, z	U_{iso} (pm ²)	
La1	2i	0.8054(6), -0.0046(11), 0.2529(7)	38(2)	
La2	2i	0.6901(6), -0.4924(10), -0.2642(7)	38(2)	
Se1	2i	0.5589(6), 0.0209(15), 0.3199(8)	38(2)	
Se2	2i	0.0558(6), 0.5189(15), 0.3132(8)	38(2)	
Cr1	1a	1, 0, 0	66(6)	
Cr2	1e	$\frac{1}{2}, -\frac{1}{2}, 0$	66(6)	
O1	2i	0.6953(6), -0.4881(13), 0.0862(9)	56(3)	
O2	2i	0.8065(6), 0.0139(12), -0.0752(9)	56(3)	
				U_{iso} (pm ²)
				38(2)
				38(2)
				40(2)
				40(2)
				58(6)
				58(6)
				66(3)
				66(3)

A.8 Crystallographic data of LaVSe₂O

Table A.11 Crystallographic data of LaVSe₂O.

Formula weight/g mol ⁻¹	363.8					
Space group, Z	$C2/m$, 4					
a , b , c /pm	1171.1(1), 388.6(1), 843.6(1)					
β /°	90.19(1)					
$V/\text{Å}^3$, $\rho_{\text{X-ray}}/\text{g cm}^{-3}$	383.9(1), 6.29					
Crystal size/mm ³	0.04 × 0.02 × 0.02					
Diffractometer	Bruker D8 QUEST					
Radiation λ /pm	71.073					
Absorption coeff. μ/mm^{-1}	32.1					
2θ range/°	4.82–70.14					
Index range (hkl)	$h \pm 18$, $-5 \leq k \leq 6$, $l \pm 13$					
No. reflections collected	5307					
No. unique data, R_{int} , R_{σ}	943, 0.03, 0.02					
No. data with $I > 3\sigma(I)$	866					
No. parameters	34					
$R_1(\text{obs/all})$	0.018/0.020					
$wR_2(\text{obs/all})$	0.046/0.054					
$\Delta\rho_{\text{max}}$, $\Delta\rho_{\text{min}}/\text{eÅ}^{-3}$	1.86/−2.38					
Atomic and displacement parameters						
	Site	x , y , z	U_{11}	U_{22}	U_{33}	Occ.
La1	$4i$	0.2303(2), 0, 0.1979(1)	0.0058(1)	0.0050(1)	0.0047(1)	1
Se1	$4i$	0.9531(1), 0, 0.1994(1)	0.0063(2)	0.0065(2)	0.0043(2)	1
Se2	$4i$	0.1407(1), $\frac{1}{2}$, 0.4648(1)	0.0061(2)	0.0067(2)	0.0060(2)	1
V1	$2b$	0, $\frac{1}{2}$, 0	0.0037(4)	0.0069(4)	0.0050(4)	1
V2	$2c$	0, 0, $\frac{1}{2}$	0.0059(4)	0.0082(4)	0.0052(4)	1
O1	$4i$	0.1629(1), $\frac{1}{2}$, 0.0582(1)	0.0052(11)	0.0082(12)	0.0052(11)	1

A.9 Crystallographic data of $\text{La}_5\text{V}_3\text{Se}_6\text{O}_7$

Table A.12 Crystallographic data of $\text{La}_5\text{V}_3\text{Se}_6\text{O}_7$.

Formula weight/g mol ⁻¹	1433.1					
Space group, Z	$Pm\bar{m}n$, 2					
a , b , c /pm	1817.4(1), 391.1(1), 1046.7(1)					
$V/\text{\AA}^3$, $\rho_{\text{X-ray}}/\text{g cm}^{-3}$	774.0(3), 6.40					
Crystal size/mm ³	$0.05 \times 0.01 \times 0.005$					
Diffractometer	Bruker D8 QUEST					
Radiation λ /pm	71.073					
Absorption coeff. μ/mm^{-1}	30.5					
2θ range/ $^\circ$	5.94–70.00					
Index range (hkl)	$-28 \leq h \leq 29$, $-6 \leq k \leq 5$, $l \pm 16$					
No. reflections collected	20542					
No. unique data, R_{int} , R_σ	1514, 0.06, 0.04					
No. data with $I > 3\sigma(I)$	1233					
No. parameters	69					
$R_1(\text{obs/all})$	0.023/0.036					
$wR_2(\text{obs/all})$	0.047/0.050					
$\Delta\rho_{\text{max}}$, $\Delta\rho_{\text{min}}/\text{e}\text{\AA}^{-3}$	2.44/–2.96					
Atomic and displacement parameters						
	Site	x , y , z	U_{11}	U_{22}	U_{33}	Occ.
La1	4f	0.3851(2), $\frac{1}{2}$, 0.0207(1)	0.0063(2)	0.0039(2)	0.0078(2)	1
La2	2b	$\frac{1}{2}$, 0, 0.7740(1)	0.0052(2)	0.0041(2)	0.0063(2)	1
La3	4f	0.1654(2), $\frac{1}{2}$, 0.5898(1)	0.0073(2)	0.0054(2)	0.0067(2)	1
Se1	2b	$\frac{1}{2}$, 0, 0.1386(1)	0.0078(4)	0.0058(4)	0.0051(4)	1
Se2	2b	0, $\frac{1}{2}$, 0.5341(1)	0.0070(4)	0.0063(4)	0.0049(4)	1
Se3	4f	0.1179(1), 0, 0.3578(1)	0.0066(3)	0.0052(3)	0.0058(3)	1
Se4	4f	0.2345(3), $\frac{1}{2}$, 0.8571(1)	0.0065(3)	0.0062(3)	0.0056(3)	1
V1	2a	0, 0, 0.6896(1)	0.0051(6)	0.0083(7)	0.0075(7)	1
V2	4f	0.3065(1), 0, 0.7500(1)	0.0060(5)	0.0075(5)	0.0046(4)	1
O1	4f	0.2480(1), 0, 0.6042(1)	0.0054(19)	0.007(2)	0.011(2)	1
O2	2a	$\frac{1}{2}$, $\frac{1}{2}$, 0.9003(1)	0.008(3)	0.008(3)	0.003(3)	1
O3	4f	0.3782(1), 0, 0.8847(1)	0.0087(19)	0.006(2)	0.008(2)	1
O4	4f	0.0993(1), 0, 0.7090(1)	0.007(2)	0.010(2)	0.013(2)	1

A.10 Crystallographic data of $\text{La}_5\text{V}_3\text{Se}_7\text{O}_5$

Table A.13 Crystallographic data of $\text{La}_5\text{V}_3\text{Se}_7\text{O}_5$.

Formula weight/g mol ⁻¹	1480.1					
Space group, Z	$Pnma$, 4					
a , b , c /pm	1650.4(1), 390.1(1), 2475.7(1)					
$V/\text{\AA}^3$, $\rho_{\text{X-ray}}/\text{g cm}^{-3}$	1594.0(3), 6.17					
Crystal size/mm ³	0.07 × 0.01 × 0.01					
Diffractometer	Bruker D8 QUEST					
Radiation λ /pm	71.073					
Absorption coeff. μ/mm^{-1}	30.7					
2θ range/°	4.94–70.16					
Index range (hkl)	$h \pm 26$, $-6 \leq k \leq 5$, $l \pm 39$					
No. reflections collected	41381					
No. unique data, R_{int} , R_{σ}	3959, 0.06, 0.04					
No. data with $I > 3\sigma(I)$	2958					
No. parameters	121					
$R_1(\text{obs/all})$	0.024/0.045					
$wR_2(\text{obs/all})$	0.042/0.047					
$\Delta\rho_{\text{max}}$, $\Delta\rho_{\text{min}}/\text{e}\text{\AA}^{-3}$	2.88/−2.84					
Atomic and displacement parameters						
	Site	x , y , z	U_{11}	U_{22}	U_{33}	Occ.
La1	4c	0.0340(2), $\frac{3}{4}$, 0.0880(1)	0.0073(1)	0.0045(1)	0.0058(1)	1
La2	4c	0.1802(2), $\frac{1}{4}$, 0.1778(1)	0.0083(1)	0.0046(1)	0.0061(1)	1
La3	4c	0.0021(2), $\frac{3}{4}$, 0.2474(1)	0.0094(1)	0.0042(1)	0.0054(1)	1
La4	4c	0.1993(2), $\frac{1}{4}$, 0.8867(1)	0.0064(1)	0.0045(1)	0.0060(1)	1
La5	4c	0.3621(2), $\frac{3}{4}$, 0.9650(1)	0.0071(1)	0.0043(1)	0.0063(1)	1
Se1	4c	0.5711(1), $\frac{3}{4}$, 0.1329(2)	0.0066(2)	0.0061(2)	0.0069(2)	1
Se2	4c	0.8887(1), $\frac{1}{4}$, 0.0243(2)	0.0092(2)	0.0092(3)	0.0062(2)	1
Se3	4c	0.4481(1), $\frac{1}{4}$, 0.0467(2)	0.0079(2)	0.0067(2)	0.0069(2)	1
Se4	4c	0.2663(1), $\frac{3}{4}$, 0.0816(1)	0.0065(2)	0.0061(2)	0.0083(2)	1
Se5	4c	0.2610(1), $\frac{1}{4}$, 0.7730(2)	0.0097(2)	0.0067(2)	0.0062(2)	1
Se6	4c	0.9302(1), $\frac{1}{4}$, 0.1620(2)	0.0079(2)	0.0063(2)	0.0068(2)	1
Se7	4c	0.3844(1), $\frac{1}{4}$, 0.1810(2)	0.0099(2)	0.0074(2)	0.0076(2)	1
V1	4c	0.1964(1), $\frac{1}{4}$, 0.0297(1)	0.0064(4)	0.0082(4)	0.0059(3)	1
V2	4c	0.1529(1), $\frac{1}{4}$, 0.3183(1)	0.0074(4)	0.0076(4)	0.0047(3)	1
V3	4c	0.4160(1), $\frac{3}{4}$, 0.1136(1)	0.0070(4)	0.0091(4)	0.0076(3)	1
O1	4c	0.2779(1), $\frac{3}{4}$, 0.8830(1)	0.0031(15)	0.0065(16)	0.0050(14)	1
O2	4c	0.0821(1), $\frac{1}{4}$, 0.2567(1)	0.0046(16)	0.0078(17)	0.0073(15)	1
O3	4c	0.1119(1), $\frac{1}{4}$, 0.0843(1)	0.0052(16)	0.0063(17)	0.0044(14)	1
O4	4c	0.1012(1), $\frac{3}{4}$, 0.1712(1)	0.0070(17)	0.0042(16)	0.0070(15)	1
O5	4c	0.2753(1), $\frac{1}{4}$, 0.9712(1)	0.0068(17)	0.0056(17)	0.0054(15)	1

A.11 Crystallographic data of $\text{La}_7\text{VSe}_5\text{O}_7$

Table A.14 Crystallographic data of $\text{La}_7\text{VSe}_5\text{O}_7$.

Formula weight/g mol ⁻¹	1530.1					
Space group, Z	$Cmcm$, 4					
a, b, c /pm	398.6(1), 1286.3(1), 3229.0(1)					
$V/\text{\AA}^3, \rho_{\text{X-ray}}/\text{g cm}^{-3}$	1655.5(1), 6.14					
Crystal size/mm ³	$0.04 \times 0.005 \times 0.005$					
Diffractometer	Bruker D8 Venture					
Radiation λ /pm	71.073					
Absorption coeff. μ/mm^{-1}	29.2					
2θ range/ $^\circ$	6.47–49.99					
Index range (hkl)	$h \pm 4, k \pm 14, l \pm 38$					
No. reflections collected	6698					
No. unique data, $R_{\text{int}}, R_{\sigma}$	854, 0.05, 0.03					
No. data with $I > 2\sigma(I)$	769					
No. parameters	54					
$R_1(\text{obs/all})$	0.032/0.037					
$wR_2(\text{obs/all})$	0.074/0.079					
$\Delta\rho_{\text{max}}, \Delta\rho_{\text{min}}/\text{e}\text{\AA}^{-3}$	1.77/−1.97					
Atomic and displacement parameters						
	Site	x, y, z	U_{11}	U_{22}	U_{33}	Occ.
La1	4c	0, 0.0580(1), $\frac{1}{4}$	0.0075(6)	0.0092(6)	0.0046(6)	1
La2	8f	$\frac{1}{2}$, 0.8655(1), 0.3131(1)	0.0084(5)	0.0101(5)	0.0033(4)	1
La3	8f	0, 0.0359(1), 0.3862(1)	0.0083(5)	0.0097(5)	0.0048(4)	1
La4	8f	$\frac{1}{2}$, 0.8205(1), 0.4372(1)	0.0087(5)	0.0103(5)	0.0045(4)	1
Se1	8f	0, 0.7241(1), 0.3680(1),	0.0118(8)	0.0111(8)	0.0081(7)	1
Se2	4c	$\frac{1}{2}$, 0.2468(2), $\frac{1}{4}$	0.0112(11)	0.0110(11)	0.0072(10)	1
Se3	8f	$\frac{1}{2}$, 0.8787(1), 0.5302(1)	0.0138(8)	0.0128(8)	0.0044(7)	1
V1	4a	0, 0, $\frac{1}{2}$	0.0103(19)	0.0139(19)	0.0020(16)	1
			U_{iso}			
O1	4c	$\frac{1}{2}$, 0.9654(10), $\frac{1}{4}$		0.003(3)		1
O2	8f	0, 0.0824(8), 0.5511(3)		0.006(2)		1
O3	8f	$\frac{1}{2}$, 0.9394(8), 0.3823(3)		0.008(2)		1
O4	8f	0, 0.9763(8), 0.3172(3)		0.009(2)		1

A.12 Crystallographic data of La₁₃V₇Se₁₆O₁₅

Table A.15 Crystallographic data of La₁₃V₇Se₁₆O₁₅.

Formula weight/g mol ⁻¹	3665.7					
Space group, <i>Z</i>	<i>Cmc</i> 2 ₁ , 4					
<i>a</i> , <i>b</i> , <i>c</i> /pm	393.8(1), 5400.9(1), 1834.9(1)					
<i>V</i> /Å ³ , ρ _{X-ray} /g cm ⁻³	3902.9(1), 6.24					
Crystal size/mm ³	0.03 × 0.02 × 0.005					
Diffractometer	Bruker D8 QUEST					
Radiation λ/pm	71.073					
Absorption coeff. μ/mm ⁻¹	30.4					
2θ range/°	4.68–70.02					
Index range (<i>hkl</i>)	−5 ≤ <i>h</i> ≤ 6, −83 ≤ <i>k</i> ≤ 86, <i>l</i> ± 29					
No. reflections collected	73357					
No. unique data, <i>R</i> _{int} , <i>R</i> _σ	6370, 0.05, 0.04					
No. data with <i>I</i> > 2σ(<i>I</i>)	5694					
No. parameters	263					
<i>R</i> ₁ (obs/all)	0.017/0.023					
<i>wR</i> ₂ (obs/all)	0.036/0.038					
Δρ _{max} , Δρ _{min} /eÅ ⁻³	0.81/−1.12					
Atomic and displacement parameters						
	Site	<i>x</i> , <i>y</i> , <i>z</i>	<i>U</i> ₁₁	<i>U</i> ₂₂	<i>U</i> ₃₃	Occ.
La1	4 <i>a</i>	0, 0.1582(1), 0.0370(1)	0.0039(3)	0.0079(3)	0.0061(3)	1
La2	4 <i>a</i>	0, 0.1586(1), 0.2709(1)	0.0045(3)	0.0075(3)	0.0063(3)	1
La3	4 <i>a</i>	0, 0.3509(1), 0.2632(1)	0.0053(3)	0.0066(3)	0.0067(3)	1
La4	4 <i>a</i>	$\frac{1}{2}$, 0.1139(1), 0.1546(1)	0.0043(1)	0.0058(2)	0.0045(1)	1
La5	4 <i>a</i>	$\frac{1}{2}$, 0.0399(1), 0.2835(1)	0.0047(3)	0.0056(3)	0.0068(3)	1
La6	4 <i>a</i>	0, 0.4724(1), 0.1566(1)	0.0056(1)	0.0070(2)	0.0090(2)	1
La7	4 <i>a</i>	0, 0.0630(1), 0.4493(1)	0.0044(3)	0.0076(3)	0.0063(3)	1
La8	4 <i>a</i>	0, 0.2670(1), 0.8183(1)	0.0066(3)	0.0066(3)	0.0079(3)	1
La9	4 <i>a</i>	$\frac{1}{2}$, 0.2319(1), 0.9875(1)	0.0062(3)	0.0072(3)	0.0078(3)	1
La10	4 <i>a</i>	0, 0.9367(1), 0.3567(1)	0.0047(3)	0.0066(3)	0.0094(3)	1
La11	4 <i>a</i>	$\frac{1}{2}$, 0.9597(1), 0.5251(1)	0.0047(3)	0.0055(3)	0.0063(3)	1
La12	4 <i>a</i>	$\frac{1}{2}$, 0.3021(1), 0.1531(1)	0.0041(1)	0.0058(2)	0.0058(1)	1
La13	4 <i>a</i>	0, 0.3493(1), 0.0396(1)	0.0046(3)	0.0084(3)	0.0061(3)	1
Se1	4 <i>a</i>	$\frac{1}{2}$, 0.0163(1), 0.4899(1)	0.0083(6)	0.0065(5)	0.0061(5)	1
Se2	4 <i>a</i>	0, 0.1210(1), 0.4226(1)	0.0077(6)	0.0067(5)	0.0092(5)	1
Se3	4 <i>a</i>	$\frac{1}{2}$, 0.1811(1), 0.3890(1)	0.0066(6)	0.0066(5)	0.0060(5)	1
Se4	4 <i>a</i>	0, 0.3199(1), 0.4161(1)	0.0065(6)	0.0063(5)	0.0066(5)	1
Se5	4 <i>a</i>	0, 0.2767(1), 0.0338(1)	0.0059(6)	0.0066(5)	0.0057(5)	1
Se6	4 <i>a</i>	$\frac{1}{2}$, 0.2433(1), 0.1524(1)	0.0070(2)	0.0054(3)	0.0070(3)	1
Se7	4 <i>a</i>	$\frac{1}{2}$, 0.1808(1), 0.1539(1)	0.0050(2)	0.0059(3)	0.0082(3)	1
Se8	4 <i>a</i>	0, 0.0843(2), 0.0537(1)	0.0063(6)	0.0063(5)	0.0082(5)	1

Continued on next page

Atomic and displacement parameters

	Site	x, y, z	U_{11}	U_{22}	U_{33}	Occ.
Se9	4a	0, 0.0199(1), 0.1550(1)	0.0082(3)	0.0093(3)	0.0088(3)	1
Se10	4a	0, 0.2775(1), 0.2717(1)	0.0062(6)	0.0056(5)	0.0073(5)	1
Se11	4a	$\frac{1}{2}$, 0.3719(1), 0.1484(1)	0.0070(3)	0.0050(3)	0.0096(4)	1
Se12	4a	0, 0.0844(2), 0.2571(1)	0.0065(6)	0.0069(5)	0.0078(5)	1
Se13	4a	0, 0.8784(1), 0.3896(1)	0.0061(6)	0.0089(6)	0.0072(5)	1
Se14	4a	0, 0.4114(2), 0.2525(1)	0.0059(4)	0.0111(4)	0.0070(4)	1
Se15	4a	0, 0.4215(2), 0.0700(1)	0.0072(4)	0.0140(4)	0.0069(4)	1
Se16	4a	$\frac{1}{2}$, 0.9833(1), 0.3216(1)	0.0073(6)	0.0056(5)	0.0074(5)	1
V1	4a	$\frac{1}{2}$, 0.2989(1), 0.3459(1)	0.0089(1)	0.0055(8)	0.0042(8)	1
V2	4a	$\frac{1}{2}$, 0.2975(1), 0.9600(1)	0.0067(1)	0.0040(8)	0.0075(9)	1
V3	4a	0, 0.2133(2), 0.1537(1)	0.0079(4)	0.0063(5)	0.0044(4)	1
V4	4a	$\frac{1}{2}$, 0.1048(1), 0.3429(1)	0.0070(1)	0.0053(9)	0.0060(9)	1
V5	4a	0, 0.9997(1), 0.4048(1)	0.0080(4)	0.0047(4)	0.0068(4)	1
V6	4a	$\frac{1}{2}$, 0.8954(1), 0.4664(1)	0.0111(1)	0.0037(9)	0.0063(9)	1
V7	4a	$\frac{1}{2}$, 0.4181(1), 0.1623(1)	0.0064(5)	0.0051(5)	0.0101(8)	1
				U_{iso}		
O1	4a	$\frac{1}{2}$, 0.1323(1), 0.2769(1)		0.0072(2)		1
O2	4a	$\frac{1}{2}$, 0.3248(1), 0.2746(1)		0.0078(2)		1
O3	4a	0, 0.9687(15), 0.4553(1)		0.0102(2)		1
O4	4a	$\frac{1}{2}$, 0.0708(1), 0.3831(1)		0.0055(2)		1
O5	4a	$\frac{1}{2}$, 0.9287(1), 0.4250(1)		0.0059(2)		1
O6	4a	0, 0.0314(1), 0.3527(1)		0.0042(2)		1
O7	4a	0, 0.1373(1), 0.1548(1)		0.0065(1)		1
O8	4a	0, 0.3257(1), 0.1501(1)		0.0056(1)		1
O9	4a	$\frac{1}{2}$, 0.2700(1), 0.8992(1)		0.0059(2)		1
O10	4a	0, 0.2097(1), 0.0535(1)		0.0089(2)		1
O11	4a	$\frac{1}{2}$, 0.3232(1), 0.0308(1)		0.0076(2)		1
O12	4a	$\frac{1}{2}$, 0.8674(1), 0.5328(1)		0.0055(1)		1
O13	4a	$\frac{1}{2}$, 0.4534(1), 0.1832(1)		0.0143(2)		1
O14	4a	$\frac{1}{2}$, 0.2708(1), 0.4037(1)		0.0095(2)		1
O15	4a	0 0.2096(1), 0.2506(1)		0.0088(2)		1

A.13 Crystallographic data of $\text{La}_{12}\text{Ti}_{13}\text{Se}_9\text{O}_{32}$

Table A.16 Crystallographic data of $\text{La}_{12}\text{Ti}_{13}\text{Se}_9\text{O}_{32}$.

Formula weight/g mol ⁻¹	3511.9					
Space group, Z	$R\bar{3}$, 8					
a, c /pm	1438.8(1), 1671.3(1)					
$V/\text{\AA}^3, \rho_{\text{X-ray}}/\text{g cm}^{-3}$	2996.4(3), 5.83					
Crystal size/mm ³	0.05 × 0.05 × 0.01					
Diffractometer	Bruker D8 QUEST					
Radiation λ /pm	71.073					
Absorption coeff. μ/mm^{-1}	23.2					
2θ range/°	5.66–70.16					
Index range (hkl)	$-21 \leq h \leq 23, -21 \leq k \leq 23, -26 \leq l \leq 27$					
No. reflections collected	30297					
No. unique data, $R_{\text{int}}, R_{\sigma}$	1913, 0.04, 0.02					
No. data with $I > 3\sigma(I)$	1690					
No. parameters	108					
$R_1(\text{obs/all})$	0.014/0.019					
$wR_2(\text{obs/all})$	0.036/0.039					
$\Delta\rho_{\text{max}}, \Delta\rho_{\text{min}}/\text{e}\text{\AA}^{-3}$	0.69/−1.18					
Atomic and displacement parameters						
	Site	x, y, z	U_{11}	U_{22}	U_{33}	Occ.
La1	18f	0.8365(1), 0.0400(1), 0.1078(1)	0.0080(1)	0.0076(1)	0.0056(1)	1
La2	18f	0.5136(2), 0.8118(1), 0.0105(1)	0.0147(1)	0.0115(1)	0.0076(1)	1
Se1	3a	0, 0, 0	0.0096(2)	0.0096(2)	0.0073(3)	1
Se2	6c	$\frac{2}{3}, \frac{1}{3}, 0.1204(1)$	0.0113(2)	0.0113(2)	0.0061(2)	1
Se3	18f	0.6218(1), 0.0796(1), 0.2618(2)	0.0128(2)	0.0088(1)	0.0067(2)	1
Ti1	18f	0.5876(1), 0.8927(1), 0.2079(1)	0.0103(3)	0.0202(3)	0.0063(3)	1
Ti2	18f	0.0411(1), 0.2422(1), 0.2351(1)	0.0066(2)	0.0081(3)	0.0135(3)	1
Ti3	18f	0.3570(1), 0.6360(1), 0.1651(1)	0.010(7)	0.009(8)	0.0049(12)	$\frac{1}{6}$
O1	18f	0.8934(2), 0.1538(2), 0.2290(1)	0.0091(10)	0.0084(10)	0.0077(10)	1
O2	18f	0.6330(2), 0.9651(2), 0.0941(1)	0.0106(10)	0.0082(10)	0.0088(10)	1
O3	18f	0.7358(2), 0.9234(2), 0.2240(1)	0.0073(10)	0.0081(10)	0.0095(10)	1
O4	18f	0.0440(2), 0.2069(2), 0.3476(1)	0.0085(10)	0.0106(10)	0.0083(11)	1
O5	18f	0.4439(2), 0.8676(1), 0.1826(1)	0.0165(12)	0.0337(14)	0.0088(11)	1
O6	6c	$\frac{1}{3}, \frac{2}{3}, 0.0670(1)$	0.0083(10)	0.0083(10)	0.0065(17)	1

A.14 Crystallographic data of $\text{La}_{15}\text{Ti}_6\text{Se}_{10}\text{O}_{25}$

Table A.17 Crystallographic data of $\text{La}_{15}\text{Ti}_6\text{Se}_{10}\text{O}_{25}$.

Formula weight/g mol ⁻¹	3560.4					
Space group, Z	$P\bar{6}2m$, 3					
a , c /pm	1683.0(1), 398.6(1)					
$V/\text{\AA}^3$, $\rho_{\text{X-ray}}/\text{g cm}^{-3}$	977.9(1), 6.05					
Crystal size/mm ³	$0.02 \times 0.005 \times 0.005$					
Diffractometer	Bruker D8 QUEST					
Radiation λ /pm	71.073					
Absorption coeff. μ/mm^{-1}	26.5					
2θ range/ $^\circ$	5.58–79.62					
Index range (hkl)	$-28 \leq h \leq 30$, $-30 \leq k \leq 24$, $-6 \leq l \leq 7$					
No. reflections collected	12971					
No. unique data, R_{int} , R_{σ}	1343, 0.06, 0.04					
No. data with $I > 3\sigma(I)$	1231					
No. parameters	65					
$R_1(\text{obs/all})$	0.019/0.022					
$wR_2(\text{obs/all})$	0.038/0.039					
$\Delta\rho_{\text{max}}$, $\Delta\rho_{\text{min}}/\text{e}\text{\AA}^{-3}$	1.01/−1.08					
Atomic and displacement parameters						
	Site	x , y , z	U_{11}	U_{22}	U_{33}	Occ.
La1	3 <i>f</i>	0.7553(1), 0, 0	0.0089(2)	0.0072(2)	0.0058(2)	1
La2	3 <i>g</i>	0.4289(1), 0, $\frac{1}{2}$	0.0065(2)	0.0081(2)	0.0047(2)	1
La3	6 <i>k</i>	0.7104(1), 0.2080(1), $\frac{1}{2}$	0.0067(2)	0.0196(2)	0.0042(2)	1
La4	3 <i>g</i>	0, 0.1397(1), $\frac{1}{2}$	0.0158(3)	0.0102(2)	0.0040(2)	1
Se1	1 <i>a</i>	0, 0, 0	0.0093(4)	0.0093(4)	0.0060(7)	1
Se2	3 <i>g</i>	0.6094(1), 0, $\frac{1}{2}$	0.0081(3)	0.0077(4)	0.0104(4)	1
Se3	6 <i>j</i>	0.5519(1), 0.1714(1), 0	0.0093(3)	0.0200(4)	0.0129(4)	1
Ti1	6 <i>j</i>	0.8820(1), 0.2349(1), 0	0.0060(5)	0.0054(5)	0.0058(5)	1
O1	6 <i>j</i>	0.9094(1), 0.1470(1), 0	0.011(2)	0.012(2)	0.016(3)	1
O2	3 <i>f</i>	0, 0.3505(1), 0	0.009(3)	0.006(2)	0.006(3)	1
O3	6 <i>j</i>	0.7577(1), 0.1626(1), 0	0.0071(19)	0.007(2)	0.0028(19)	1
O4	3 <i>g</i>	0.8345(1), 0, $\frac{1}{2}$	0.013(2)	0.008(3)	0.004(3)	1
O5	6 <i>k</i>	0.8817(1), 0.2538(1), $\frac{1}{2}$	0.008(2)	0.012(2)	0.009(2)	1
O6	2 <i>d</i>	$\frac{2}{3}$, $\frac{1}{3}$, $\frac{1}{2}$	0.008(5)	0.008(5)	0.033(11)	$\frac{1}{2}$

A.15 Supporting Information - $\text{La}_{2n+2}\text{MnSe}_{n+2}\text{O}_{2n+2}$

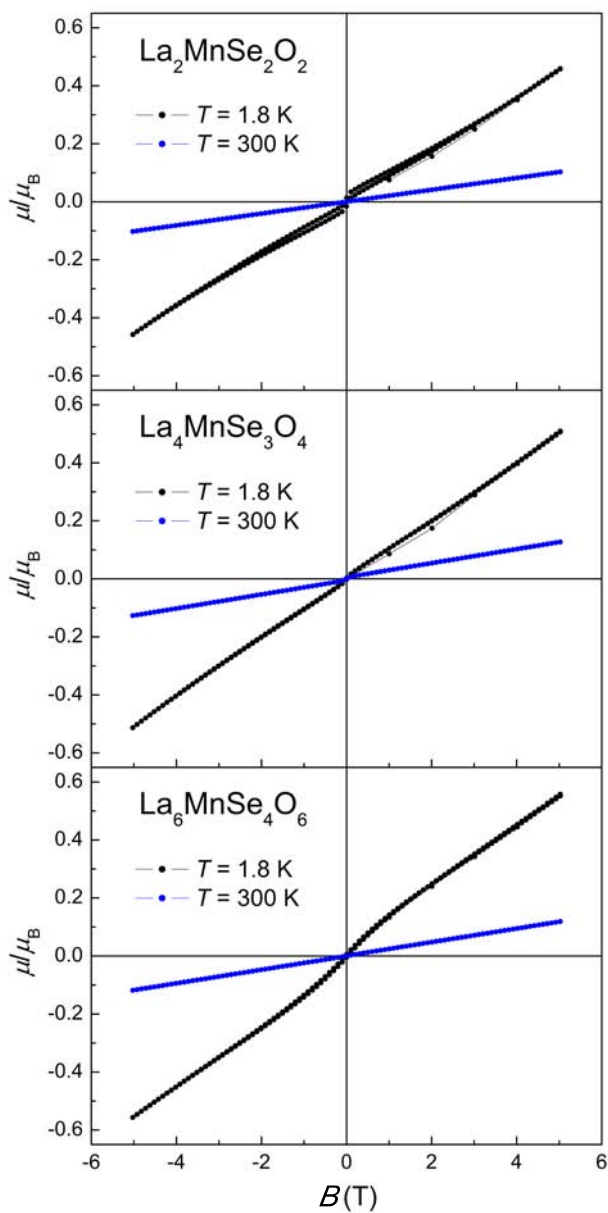


Figure A.1 Isothermal magnetizations at 1.8 (black) and 300 K (blue) of *mC*- $\text{La}_2\text{MnSe}_2\text{O}_2$ (top), $\text{La}_4\text{MnSe}_3\text{O}_4$ (middle) and $\text{La}_6\text{MnSe}_4\text{O}_6$ (bottom).

A.16 Supporting Information - $RE_2CrSe_2O_2$

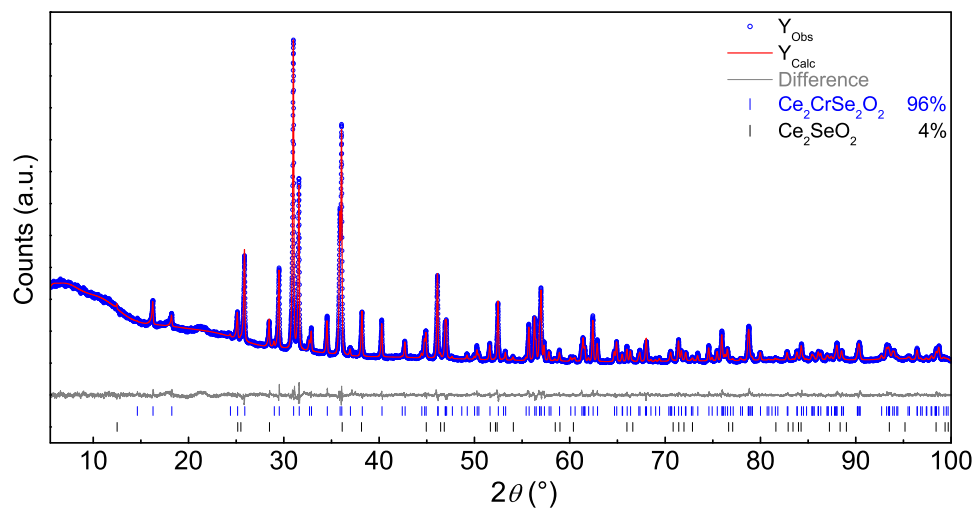


Figure A.2 X-ray powder pattern of $Ce_2CrSe_2O_2$ (blue) with Rietveld fit (red) and difference plot (gray).

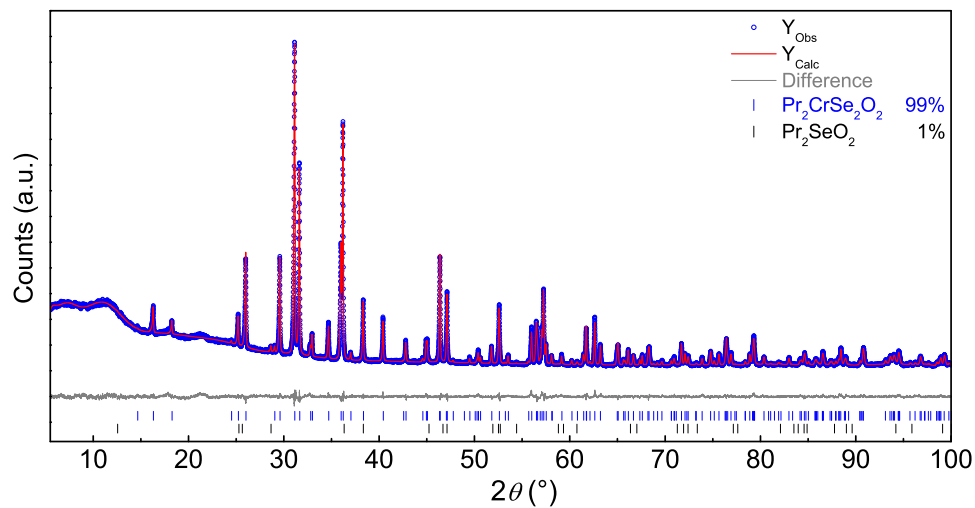


Figure A.3 X-ray powder pattern of $Pr_2CrSe_2O_2$ (blue) with Rietveld fit (red) and difference plot (gray).

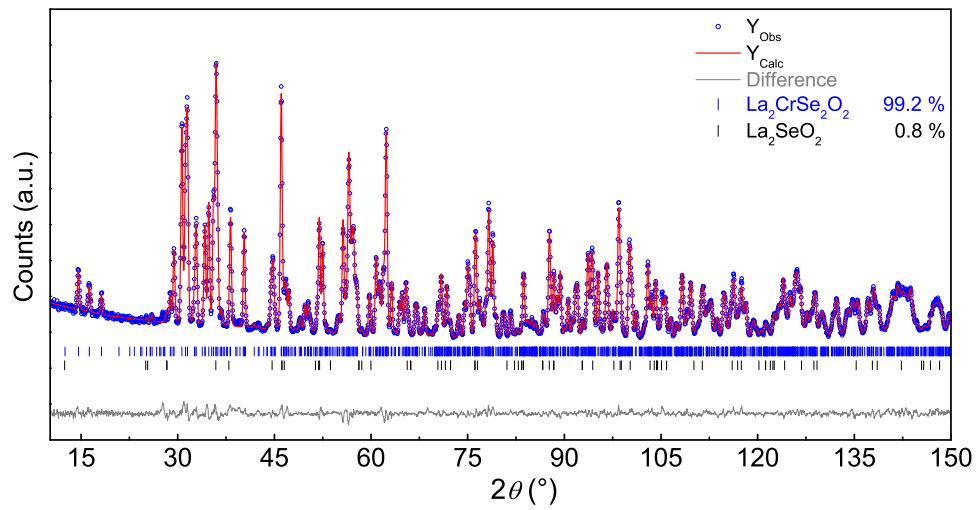


Figure A.4 Neutron powder pattern of $\text{La}_2\text{CrSe}_2\text{O}_2$ (blue) with Rietveld fit (red) and difference plot (gray) at 20 K.

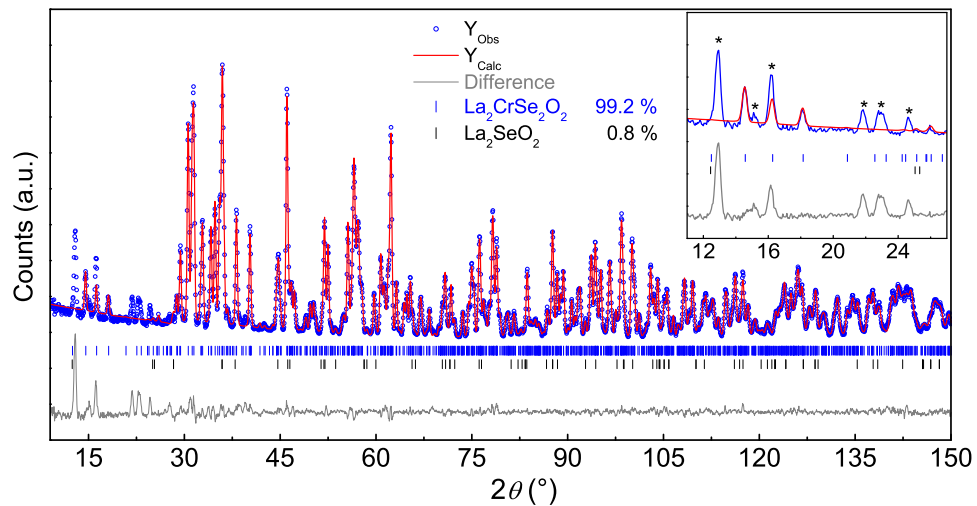


Figure A.5 Neutron powder pattern of $\text{La}_2\text{CrSe}_2\text{O}_2$ (blue) with Rietveld fit (red) and difference plot (gray) at 4 K without magnetic model. Inset: Magnification of the pattern. Reflection marked with asterisks are magnetic Bragg reflections.

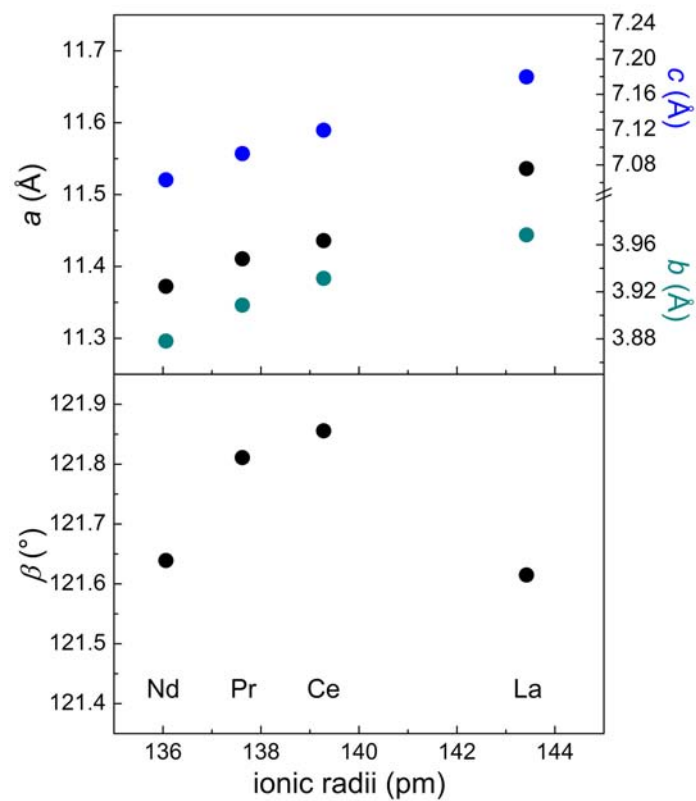


Figure A.6 Plot of the lattice parameters a , b and c (top) and the monoclinic angle β (bottom) versus the effective ionic radii of the RE atom in $RE_2CrSe_2O_2$ ($RE = La-Nd$).

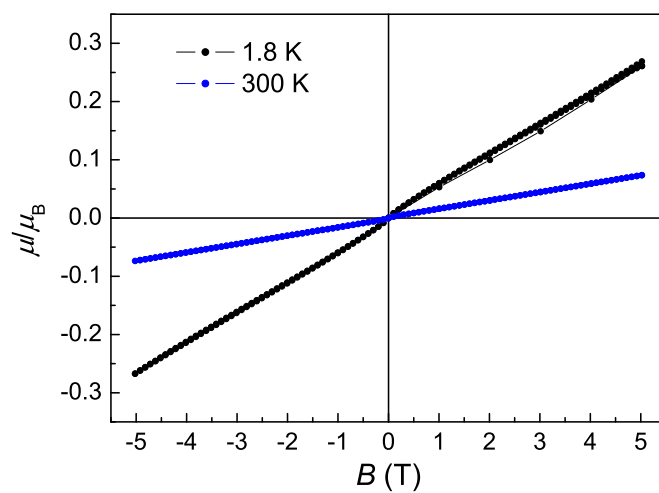


Figure A.7 Isothermal magnetizations at 1.8 (black) and 300 K (blue) of $La_2CrSe_2O_2$.

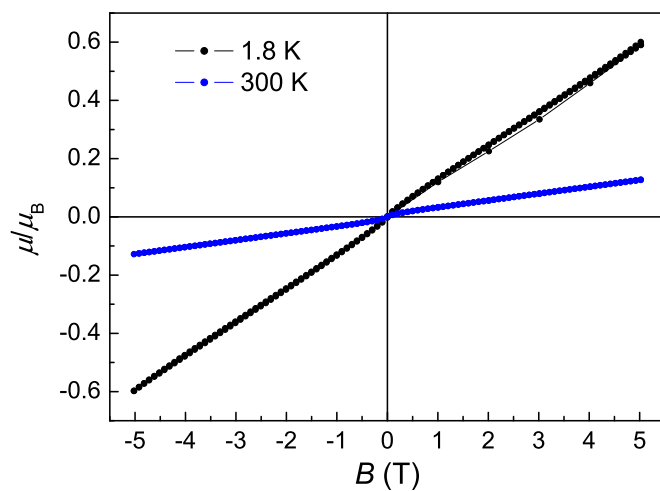


Figure A.8 Isothermal magnetizations at 1.8 (black) and 300 K (blue) of $\text{Ce}_2\text{CrSe}_2\text{O}_2$.

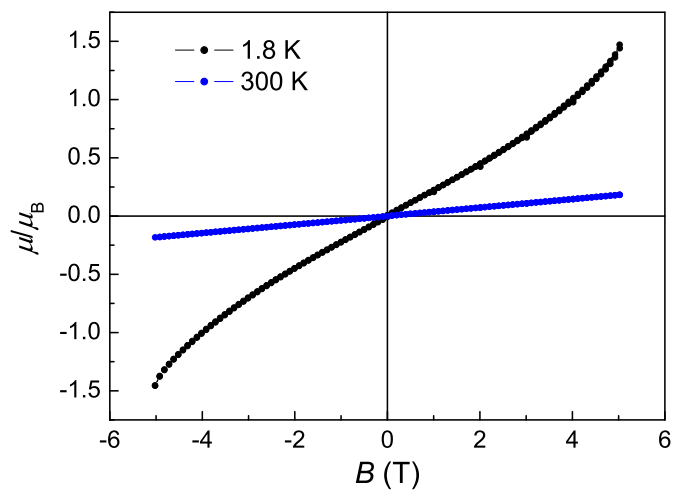


Figure A.9 Isothermal magnetizations at 1.8 (black) and 300 K (blue) of $\text{Pr}_2\text{CrSe}_2\text{O}_2$.

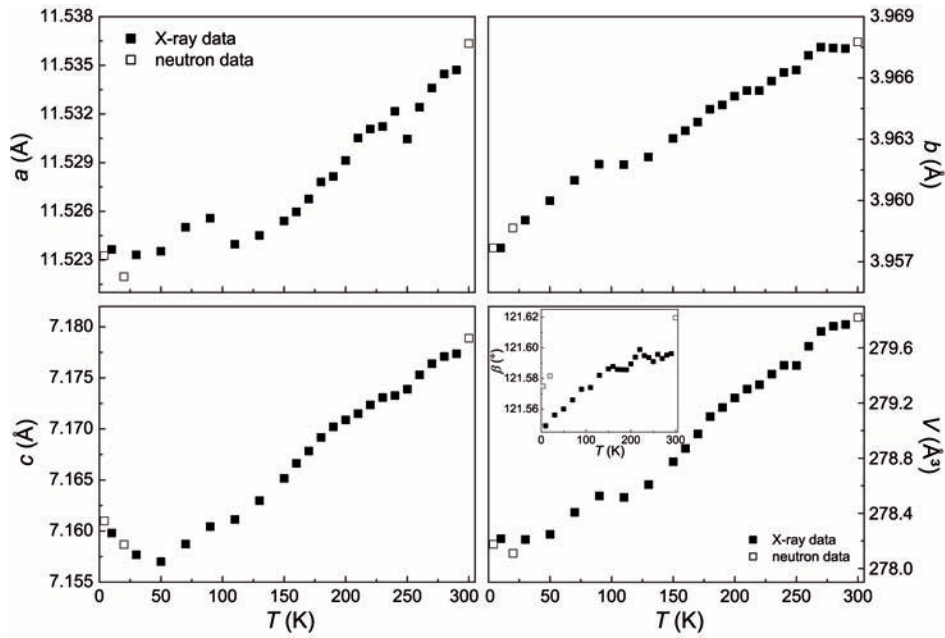


Figure A.10 Plots of the lattice parameters a , b , c , β (inset) and the cell volume V of $\text{La}_2\text{CrSe}_2\text{O}_2$ against the temperature between 4 and 300 K. Filled symbols are data from X-ray powder diffraction, unfilled symbols are from neutron powder diffraction experiments. Error bars are smaller than the data points.

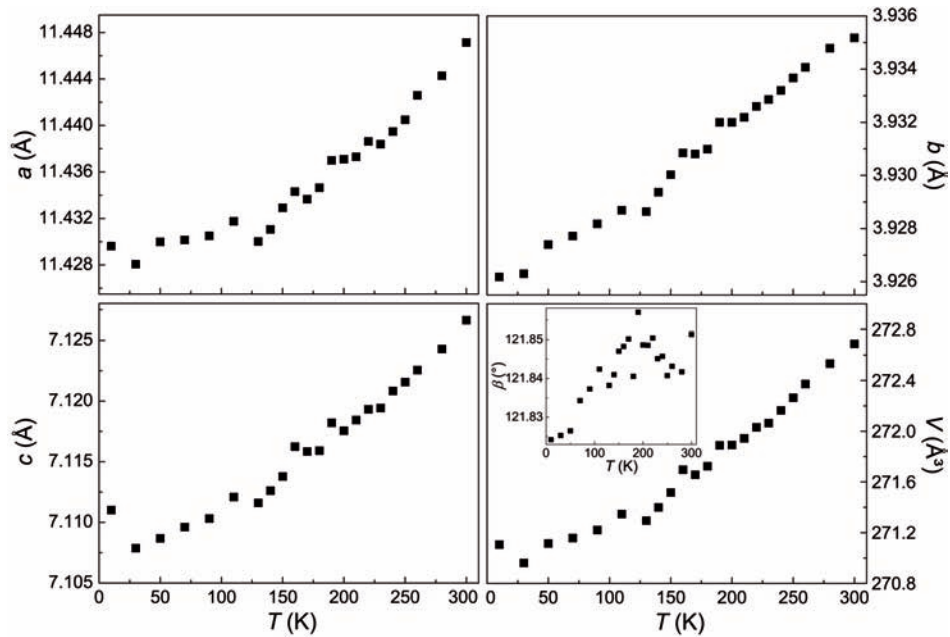


Figure A.11 Plots of the lattice parameters a , b , c , β (inset) and the cell volume V of $\text{Ce}_2\text{CrSe}_2\text{O}_2$ against the temperature between 4 and 300 K. Error bars are smaller than the data points.

Abbreviations

A	Alkaline metal
a, b, c	Unit cell axes
a^*, b^*, c^*	Reciprocal unit cell axes
α, β, γ	Unit cell angles
AC	Alternating Current
AFM	Antiferromagnetic
at%	Atom percent
a.u.	Arbitrary units
B	Magnetic flux density
B_i	Internal magnetic field
C	<i>Curie</i> constant
°C	Degree Centigrade
χ	Magnetic susceptibility
χ_{mol}	Molar susceptibility
D	Demagnetization factor
d	Distance
e	Electron
EA	Alkaline earth metal
EDX	Energy Dispersive X-ray Spectroscopy
E_g	Band gap energy
et al.	et alii (and others)
eV	Electron Volt
eq.	Equivalent
f_i	Precession frequency

Continued on next page

Fig.	Figure
FRM II	Forschungs Reaktor München II
γ	Gyromagnetic ratio of a muon
H	Magnetic field
H_a	Applied field
$H_c; H_{cr}$	Critical field
h	hours
HIP	Hot Isostatic Pressing
$h k l$	<i>Miller</i> Indices
J_c^{global}	Global critical current density
J_c^{intra}	Intragranular critical current density
K	Kelvin
\mathbf{k}	Propagation vector
$K(\lambda)$	Absorption coefficient
λ	Wave length
λ_i	Transverse relaxation rate
λ_L	Spin-lattice relaxation rate
m	Mass
m	Satellite order of a <i>Bragg</i> reflection
M_a, M_b, M_c	Magnetization vectors along the unit cell axes
m_R	Remanent moment
MPMS	Magnetic Property Measurement System
μ	Magnetic moment in <i>Bohr</i> magnetons
μ_0	Vacuum permeability
μ_B	<i>Bohr</i> magneton
μ_{eff}	Effective magnetic moment in <i>Bohr</i> magnetons
μSR	Muon Spin Rotation
Occ.	Occupation
Oe	Oersted
PID	Proportional-Integral-Derivative

Continued on next page

Pn	Pnictogen
ppm	Parts per million
PPMS	Physical-Property-Measurement-System
$P(t)$	Muon spin polarization
Q	Chalcogen
\mathbf{q}	Modulation wave vector
R	Residual factor
R_∞	Diffuse reflectance
r	Radius
r_{eff}	Effective radius
$r_{\text{eff,rel}}$	Relative effective radius
RE	Rare-Earth metal
Ref.	Reference
RM	Remanent Magnetization
ρ	Density
ρ	Electrical resistivity
ρ	Electron density
S	Goodness of fit
$s(\lambda)$	Scattering coefficient
SAED	Selected Area Electron Diffraction
SSM	Solid-State Metathesis
SEM	Scanning Electron Microscopy
SPODI	Structure Powder Diffractometer
SQUID	Superconducting Quantum Interference Device
σ	Standard deviation
T	Tesla
T	Temperature
T	Transition-metal
t	Phase of the modulation wave
Tab.	Table

Continued on next page

T_C	<i>Curie</i> temperature
T_c	Critical temperature of a superconductor
T_N	<i>Néel</i> temperature
T_{tr}	Transition temperature
θ	Diffraction angle
θ	<i>Weiss</i> constant
U_{ij}	Thermal displacement parameter
U_{iso}	Isotropic thermal displacement parameter
V	Unit cell volume
VSM	Vibrating Sample Magnetometer
wR	Weighted residual factor
wt%	Weight percent
wTF	Weak Transverse Field
ω	Thickness of the sample
X	S, Se
XRD	X-Ray Diffraction
x_i	Superspace axes
Z	Number of empirical formulas per unit cell
ZF	Zero field
$4\pi\chi_V$	Magnetic (e.g. superconducting) volume fraction

Scientific contributions

Publications

- **Flux Synthesis, Crystal Structures, and Physical Properties of New Lanthanum Vanadium Oxyselenides**

S. Peschke, L. Gamperl, V. Weippert, and D. Johrendt

Dalton Trans. **2017**, *accepted*.

For this publication, synthesis, sample preparation, and single crystal growth were done by Simon Peschke with assistance of Lisa Gamperl and Valentin Weippert. Single crystal X-ray data was measured by Ursula Pachmayr. Structure elucidation and refinement were performed by Simon Peschke. Measurement and interpretation of magnetic data, Rietveld refinement, EDX measurements, literature screening, writing the manuscript, and picture editing were done by Simon Peschke. The manuscript was revised by Dirk Johrendt.

- **Flux Synthesis, Crystal Structures, and Magnetic Ordering of the Rare-Earth Chromium(II) Oxyselenides $RE_2CrSe_2O_2$ ($RE = La-Nd$)**

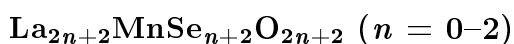
S. Peschke, V. Weippert, A. Senyshyn, M. Mühlbauer, O. Janka, R. Pöttgen, S. Holenstein, H. Luetkens, and D. Johrendt

Inorg. Chem. **2017**, *56*, 2241.

For this publication, synthesis of $RE_2CrSe_2O_2$ and single crystal growth were done by Simon Peschke with the assistance of Valentin Weippert. Single crystal X-ray data was measured by Ursula Pachmayr. Low temperature X-ray powder data measurements were performed by Juliane Stahl. Structure elucidation and refinement were performed by Simon Peschke. Neutron diffraction experiments were done by Martin Mühlbauer and Anatoliy

Senyshyn. Magnetic measurements and interpretation of magnetic data were done by Simon Peschke, Oliver Janka, Rainer Pöttgen, and Dirk Johrendt. Muon spin rotation spectroscopy data measurements and analysis of the data were done by Stefan Holenstein and Hubertus Luetkens. Writing the manuscript main part, literature screening, EDX measurements, picture editing, and Rietveld refinement were done by Simon Peschke. Hubertus Luetkens, Anatoliy Senyshyn, Rainer Pöttgen, and Dirk Johrendt contributed to data analysis and discussion. The manuscript was revised by Martin Mühlbauer, Anatoliy Senyshyn, Rainer Pöttgen, Stefan Holenstein, Hubertus Luetkens, and Dirk Johrendt.

- **Flux Synthesis, Crystal Structures, and Magnetism of the Series**



S. Peschke and D. Johrendt

Inorganics **2017**, 5, 9.

For this publication, synthesis of the series $\text{La}_{2n+2}\text{MnSe}_{n+2}\text{O}_{2n+2}$ ($n = 0-2$), Rietveld refinement, single crystal growth, structure elucidation and refinement, measurement and interpretation of magnetic data, EDX measurements, literature screening, writing the manuscript main part, as well as image editing were done by Simon Peschke. Single crystal X-ray data was measured by Ursula Pachmayr. The manuscript was revised by Dirk Johrendt.

- **Re-Emergence of Superconductivity in $\text{La}_{1-x}\text{RE}_x\text{FeAsO}_{0.8}\text{F}_{0.2}$ ($\text{RE} = \text{Pr-Sm}$)**

S. Peschke, S. Vogel, and D. Johrendt

Z. Anorg. Allg. Chem. **2016**, 642, 1063.

For this publication, synthesis and sample preparation were done by Simon Peschke with assistance of Sebastian Vogel. Rietveld refinement, ac-susceptibility measurements, data analysis, picture editing, and writing the manuscript main part were done by Simon Peschke. The manuscript was revised by Dirk Johrendt.

- **The modulated structures of $\text{La}_{2-x}\text{Pr}_x\text{O}_2\text{MnSe}_2$ ($0 \leq x \leq 1$) and**



S. Peschke and D. Johrendt

Z. Kristallogr. **2015**, 231, 89.

For this publication, synthesis and sample preparation, single crystal growth, structure elucidation, Rietveld refinement, EDX measurements, data analysis, picture editing, literature

screening, and writing the manuscript were done by Simon Peschke. Single crystal X-ray data was measured by Ursula Pachmayr. The manuscript was revised by Dirk Johrendt.

- **Flux Synthesis, Modulated Crystal Structures, and Physical Properties of $RE\text{Mn}_{0.5}\text{SeO}$ ($RE = \text{La}, \text{Ce}$)**

S. Peschke, F. Nitsche, and D. Johrendt

Z. Anorg. Allg. Chem. **2015**, 641, 529.

For this publication, synthesis and sample preparation, as well as single crystal growth and crystal selection were done by Simon Peschke. Single crystal X-ray data was measured by Fabian Nitsche with assistance of Ursula Pachmayr. Structure elucidation was done by Fabian Nitsche with assistance of Simon Peschke and Ursula Pachmayr. EDX measurements were done by Christine Stürzer and Simon Peschke. Rietveld refinement, measurement and interpretation of UV/Vis data, measurement and interpretation of magnetic data, picture editing, literature screening, and writing the manuscript main part was done by Simon Peschke. Fabian Nitsche contributed to data analysis and discussion. The manuscript was revised by Fabian Nitsche and Dirk Johrendt.

- **$\text{Ba}_{1-x}\text{Rb}_x\text{Fe}_2\text{As}_2$ and Generic Phase Behavior of Hole-doped 122-Type Superconductors**

S. Peschke, T. Stürzer, and D. Johrendt

Z. Anorg. Allg. Chem. **2014**, 640, 830.

For this publication, synthesis and sample preparation, as well as single crystal growth and crystal selection were done by Simon Peschke. Single crystal X-ray data was measured by Tobias Stürzer. Structure elucidation was done by Tobias Stürzer with assistance of Simon Peschke. Low temperature X-ray diffraction experiments were performed by Franziska Hummels. Gina Friederichs, Rainer Frankovsky and Simon Peschke performed conductivity and ac-susceptibility measurements. Rietveld refinement, data analysis, picture editing, literature screening, and writing the manuscript main part were done by Simon Peschke. The manuscript was revised by Dirk Johrendt.

Conference contributions

- **Re-emergence of Superconductivity in $\text{La}_{1-x}\text{RE}_x\text{FeAsO}_{0.8}\text{F}_{0.2}$ ($\text{RE} = \text{Pr-Sm}$)**
S. Peschke, S. Vogel, D. Johrendt
18th Vortragstagung Fachgruppe Festkörperchemie und Materialforschung, Innsbruck (Austria), September **2016**. (poster)
- **Titan trifft auf Vanadium**
S. Peschke
Hirschegg-Seminar für Festkörperchemie, Hirschegg (Austria), May **2016**. (talk)
- **Neue La-Mn-Se-O Verbindungen**
S. Peschke
2nd Obergurgl-Seminar Festkörperchemie, Obergurgl (Austria), January **2016**. (talk)
- **Flux Synthesis, Modulated Crystal Structures, and Physical Properties of $\text{La}_2\text{O}_2\text{MnSe}_2$ and $\text{Ce}_2\text{O}_2\text{MnSe}_2$**
S. Peschke, F. Nitsche, D. Johrendt
15th European Conference of Solid State Chemistry (ECSSC 15), Vienna (Austria), August **2015**. (poster)
- **Modulierte Strukturen von $\text{RE}_2\text{O}_2\text{MnSe}_2$ ($\text{RE} = \text{La, Ce}$)**
S. Peschke
Hirschegg-Seminar für Festkörperchemie, Hirschegg (Austria), June **2015**. (talk)
- **Zusammenhang zwischen Löcherkonzentration und Sprungtemperatur in Eisenarsenid-Supraleitern der 122-Familie**
S. Peschke
1st Obergurgl-Seminar Festkörperchemie, Obergurgl (Austria), January **2014**. (talk)

Curriculum vitae

Personal information

Name	Simon Friedrich Peschke
Date of birth	27.02.1988
Place of birth	Rosenheim

Education

Since 02/2013	Ph.D. thesis in inorganic solid-state chemistry in the group of Prof. Dr. Dirk Johrendt, Department Chemistry at the Ludwig-Maximilians-Universität, München; Title of Thesis: <i>Synthesis and characterization of rare-earth oxide transition-metal arsenides and selenides</i>
06/2012–12/2012	Master thesis in the group of Prof. Dr. Dirk Johrendt, Department Chemistry at the Ludwig-Maximilians-Universität, München; Title of Thesis: <i>Synthese, Eigenschaften und Phasendiagramm von $Ba_{1-x}Rb_xFe_2As_2$ ($0 \leq x \leq 1$)</i>
10/2007–12/2012	Bachelor/ Master studies in chemistry and biochemistry at the Ludwig-Maximilians-Universität, München
06/2007	Allgemeine Hochschulreife at the Gymnasium Grafing
09/1998–06/2007	Secondary education, Gymnasium Grafing
09/1994–07/1998	Primary school education at the Grundschule Grafing